Dynamics of the photo-induced desorption and oxidation of CO on Ru(0001) with different (O, CO) coverages

Auguste Tetenoire

Auguste TÊTENOIRE

Dynamics of the photo-induced desorption and oxidation of CO on Ru(0001) with different (O, CO) coverages

Under the supervision of Dr. Maite ALDUCIN and Prof. J.I. JUARISTI

DONOSTIA 2023

Universidad del País Vasco
Euskal Herriko Unibertsitatea

eman ta zabal zazu

Universidad del País Vasco
Euskal Herriko Unibertsitatea

Dynamics of the photo-induced desorption and oxidation of CO on Ru(0001) with different (O, CO) coverages

Auguste TETENOIRE

Supervisors: Dr. Maite ALDUCIN
Prof. J.I. JUARISTI

Committee: President: Dr. Nerea ZABALA UNZALU
Secretary: Dr. Ivor LONCARIC
Vocal 1: Dr. Cristina DIAZ BLANCO

Física de Nanoestructuras y Materiales Avanzados / Physics of Nanostructures and Advanced Materials
Universidad del Pais Vasco / University of the Basque Country

DOCTOR IN PHYSICS

23-03-2023

I dedicate my PhD thesis to the knowledge of Humankind, main purpose of science. All my love goes to the ones who love me, you who supported me in this process... I will never thank you enough for this.

"Tout ce que j'ai affronté était nouveau pour moi. Je n'ai trouvé le courage de surmonter certaines épeuves que parce que j'ignorais les souffrances qu'elles représentaient."

— Mike Horn, Conquérant de l'impossible.

ACKNOWLEDGEMENTS

First of all, I want to thank my advisors Maite Alducin and Iñaki Juaristi for their time, patience and work.

Then, I want to thank those whom I consider part of my scientific family. Credric Crespos, who believed in me, and offered me the opportunity to be a scientist although I was not the best student. We proved together that motivation with benevolent peoples is above the system's trials. Fabio Busnengo, who showed me what is to be passionate, exigent, but also careful with the students. And Pascal Larregaray, who allowed me to step into this PhD. Always here to listen, silent watcher, he never gives you up.

Now I want to thank friends and family, that are not necessarily related to science. In the following acknowledgement, I will name people. Thus, for no double counting, I will name them only once. But consider that some could have appeared in several topics.

First, a special mention to the group which accompany me in my writing, and introduced me to metal bands. Here I quote a part of a song which summarizes well my general spirit in life. The following extract here, traduces my spirit when I arrived in the Basque Country.

‘‘The fire that burns within us
To carry out a dream
Chasing new ambitions
Determined to succeed’’

-A View From the Top of the World-, *Dream Theater (2021)*

When I came to Spain, I packed my stuff from France, drove alone, and started to move my stuff in my new flat. Two Cuban friends were here, first helping me to find a flat, then to move in. Thanks to Ale and Carlos.

Then, Aitor Izura my first flatmate, among so many, has been really kind to me. He showed me the Basque Country, cooked me meals to introduce me to Spanish cuisine, and tried as my Cuban friends, to integrate me here such I could feel comfortable.

Next, I want to thank a friend who put in its own words the feeling to be abroad, but still so close to the border.

‘‘On est loin mais pas trop loin quand même, et on est dans un environnement en même temps très international.’’

M. INFUSO (2019)

Now, I want to thank my friends who integrated me in this new life, and with whom I will remain bounded and grateful. In alphabetical order:

Adam, Alba, Ali and Shagha, Alvaro, Carmen, Che Mikel, Claire, Cris, Cuate, Dani, Giulia, Iker, Jon, Jorge largo, Jordan, Joseba, Marina, Martin, Miguel, Mroczna, Oihana, Paula and Mario, Raoni, Raulillo, Soso, Thomas G., Thomas H., Xavi.

Also my climbing, swimming and running friends (you are quite numerous) that will recognize themselves.

Thanks to the ones who were cooking for me. You saved me a lot of time, and kept me in good health and better humor.

Then, I would like to thank my friends who helped me by reading and making me feedback on parts of my manuscript. By order of revision: Sabine, Raúl B. E., Fer, Alberto S. M. and Laurie.

I thank Aurélie for this pretty book cover she made me.

I want to thank Juliette and Sebastián, who demonstrated that roads can be used on both ways.

Next, I want to give a special thanks to a dear friend who has been here all the time, supportive and motivating me in all matter, personal and professional, even in my darkest hours. Jorge Melillo, you kept me alive.

Then, I warmly thank my sister Leopoldine, who came to visit me in whatever circumstances, every year, even to help me moving in new flats.

Finally, I want to thank all my family. Those years have been tough for everyone. I have been dragged down several times, and you were here, helping me to emerge out of water, again and again. To be separated from you during the pandemic was one of the most awful and traumatic experiences of my actual lifetime. There, I felt how much you counted to me. There, I felt how much I needed you. Nothing values more than the ones you love and who love you.

I hope not to forget anyone, but remember, even though you are not in the acknowledgement, you are in my heart.

To close the section of thanking people, I want to say a word for my grandfather who died in May 2022. He, who was calling me "Futur doctor" never saw me graduated. Do not forget to spend time with your family, time does not wait for you.

‘‘Voilà, c’est fini
On a tant ressassé les mêmes théories
On a tellement tiré chacun de nôtre côté
Que voilà c’est fini’’

-Voilà, c’est fini-, *Jean-Louis Aubert (1989)*

I never felt that Donostia was my home, but I felt happy here. I think home is in the heart of the ones who love you.

Eskerrik asko euskadi, eman didazun hori betiko geratuko da nire bihotzean.

ABSTRACT

The following thesis is dedicated to the study of the photo-induced desorption and oxidation of CO molecules coadsorbed with O adatoms on Ru(0001) with different surface coverages. This thesis is divided in seven chapters summarized in the following.

In the first chapter we begin the manuscript by an introduction which presents the state of the art of the topic, the motivations of the study and the different problematics where this works inscribes.

Carbon monoxide (CO) is colorless, tasteless, and a neuro-toxic gas, therefore oxidation of CO has been seen to be an efficient way to eliminate CO from the air pollutant.[1] The catalytic reaction of CO oxidation at transition metal surfaces is a crucial reaction in various domains, for instance, in automotive exhaust catalysts to convert CO into carbon dioxide and in industrial pollution control.[2] It is considered a heterogeneous reaction because CO is present in gas form and reacts with a solid metallic surface. Also, due to its relative simplicity, it has been the subject of numerous fundamental studies focused on heterogeneous catalytic processes.[3] Great interest has been devoted to the behavior of ruthenium that has been regarded as anomalous when compared to other transition metals (*e.g.*, palladium, platinum, rhodium, and iridium) in the particular case of the CO oxidation reaction. More precisely, it has been found that under Ultra High Vacuum (UHV) conditions Ru is very inactive for CO oxidation.[4;5] Therefore, in the pioneer experimental work of Bonn *et al.*.[6], the authors used a Ru(0001) surface precovered with 0.5 ML of O atoms, and applied on it a CO pressure at 100 K to adsorb CO molecules on the O precovered surface. Next, they promoted the desorption and oxidation of CO by irradiating the surface with a femtosecond laser pulse of 800 nm and record the number of events for each reaction at several time steps after the laser impact. This work showed the opening of a new reaction path for CO oxidation by means of femtosecond laser irradiation.

Accurate simulations of the photo-reaction dynamics are required to give a proper characterization of this kind of experiments. This may give a definite answer to questions about which mechanism is governing each reaction (phonon or electron excitations), which role plays the interadsorbate energy exchange or which specific characteristics of the system dominate the outcome of the experiments. The purpose of this thesis, motivated by the experimental work of Bonn *et al.*.[6], is thus to simulate these experiments with a recently developed theoretical model that incorporates in the adsorbates dynamics both the effect of the laser-induced hot electrons and the concomitant hot phonons. We aspires to complement the knowledge of the oxidation of CO on Ru surfaces by employing recent developed *ab-initio* Molecular Dynamics with Electronic Friction (AIMDEF)[7] simulations, allowing simulations of photo-induced reaction experiment. Then we used modern methods of characterization of reaction paths (Climbing Image Nudged Elastic Band (CI-NEB)[8;9]) and cutting edge technology as neural networks to generate potential energy surfaces.[10]

In the second chapter, we present the theoretical methods that are used in this thesis. First we present the theoretical methods on which the electronic structure calculations applied to the gas-surface systems are based. Then we show the separation of the electronic and nuclear degrees of freedom with the Born-Oppenheimer approximation. Next, we describe the methods for solving the electronic structure problem with Density Functional Theory (DFT), and briefly review the common exchange-correlation functionals. Secondly, we introduce Molecular Dynamics (MD) methods and present the specific case of AIMDEF for photo-induced reaction dynamics. Thirdly, we introduce the Neural Network (NN) and present the general method to generate a Neural Network Potential Energy Surface (NN-PES). For this we introduce the Atomistic Neural Network (ANN) model and its use in Embedded Atom Neural Network (EANN). Finally, we present additional tools used to characterize the system during this thesis.

In the third chapter, we present the results of a complete DFT characterization of different (O, CO) mixed coverages on Ru(0001) that consist of a fixed 0.5 ML of O combined with three different CO coverages (0.25 ML, 0.375 ML, and 0.5 ML). It is organized such that we first introduce the Ru surfaces under study and the simulation box. We also explain the choice of the functional used for the DFT calculations. Second, we present the protocol used to find the important intermediate states of the path for recombinative desorption of CO and O. Third, we provide and discuss the results obtained for each of the three coverages considered. In each case, we start with a systematic search of the energetically most stable configuration that is compatible with the surface preparation reported in refs.[6;11;12;13]. Once the optimized arrangement is identified, we perform a full characterization of the desorption and oxidation of CO on this specific overlayer by calculating the corresponding reaction energies and, importantly, the minimum energy reaction paths for each process. The comparative analysis of their energy diagrams is later shown to understand the competition between CO desorption and oxidation that is observed in experiments. The dependence of this competitive reaction on the three coverages considered here is discussed. Fourth, we present further analysis of the three coverages, with the Bader charge analysis in order to describe the adsorption character of the specie of interest. Finally, we use the Density Of State (DOS) calculation to present a study of the Molecular Orbitals (MOs) at the zero coverage limit, in order to study the effect of the adsorption of $CO_{2(gas)}$ molecules on Ru surfaces.

In the fourth chapter, we present the results of the AIMDEF simulations of the low surface coverage. First, we analysis the probabilities of desorption and oxidation of CO. Second, we study the reaction path of the CO oxidation, and show the complexity to reach the transition state region. Third, we analyze and compare a calculated O-K X-Ray adsorption spectra with the interpretation made in ref.[13]. Finally, we conclude on the creation of the CO_2 molecule in the transition state region, and the competition between formation of CO_2 and desorption of CO.

In the fifth chapter, we present in more details the results of the AIMDEF simulations for all the three different surface coverages, and the two different types of simulations (with and without motion of the surface). First, we analyze the CO desorption and oxidation probabilities for the different surface coverages, and the two types of simulations. Second, we analyze the variation of the kinetic energy of the adsorbates. To give more insight, we show the distribution of the kinetic energy in the translational component, and in the vertical and in-plane kinetic energy. Third, we analyze the variation of the

vertical motion of the adsorbates during the AIMDEF simulations. Here we identify the creation of several species during the simulation, and characterize them. Fourth, we analyze the variation of the in-plane motion of the adsorbates. Finally, we present and study the mechanism of oxidation of the CO found during our AIMDEF simulations.

In the sixth chapter, we present the two methodologies used to generate a NN-PES based on the AIMDEF DFT data. The two NN-PES have been constructed with different selection methods when forming the configurations sets. First, we present the process of training and testing for the development of an accurate NN-PES for the low coverage, with the first method of configuration selection. Afterward we present the results of MD simulation using this NN-PES. Secondly, we present the second process of selection and training, but for the intermediate coverage. We perform some new test to check the accuracy of this NN-PES and its transferability in order to predict correctly the configurational space of the different coverages. Then, we show the limits of the model and training scheme. In the end, we present the results of MD simulations performed with this last NN-PES for the three coverages.

And finally, in the seventh chapter, we present the conclusions of this thesis, and the future work that can be done to improve.

RESUMEN

La siguiente tesis está dedicada al estudio de la desorción y oxidación foto-inducida de moléculas de CO coadsorbidas con adátomos de O sobre Ru(0001) con distintos recubrimientos de superficie. Esta tesis se divide en siete capítulos que se resumen a continuación.

En el primer capítulo comenzamos el manuscrito con una introducción que presenta el estado del arte del tema, las motivaciones del estudio y las diferentes problemáticas en las que se inscribe este trabajo.

El monóxido de carbono (CO) es incoloro, insípido y un gas neurotóxico, por lo que la oxidación del CO se ha visto como una forma eficiente de eliminarlo del aire.[1] La reacción catalítica de oxidación del CO en superficies de metales de transición es una reacción crucial en diversos ámbitos, por ejemplo, en catalizadores de escape de automóviles para convertir el CO en dióxido de carbono y en el control de la contaminación industrial.[2] Se considera una reacción heterogénea porque el CO está presente en forma de gas y reacciona con una superficie de metal sólido. Además, debido a su relativa simplicidad, ha sido objeto de numerosos estudios fundamentales centrados en procesos catalíticos heterogéneos.[3] Se ha prestado gran interés al comportamiento del rutenio, que se ha considerado anormal en comparación con otros metales de transición (por ejemplo, paladio, platino, rodio e iridio) en el caso particular de la reacción de oxidación del CO. Más concretamente, se ha descubierto que, en condiciones de vacío, el Ru es muy inactivo para la oxidación del CO.[4;5] Por lo tanto, en el trabajo experimental precursor de Bonn *et al.*.[6], los autores utilizaron una superficie de Ru(0001) precubierta con 0,5 ML de átomos de O, y aplicaron sobre ella una presión de CO a 100 K para adsorber moléculas de CO en la superficie precubierta de O. A continuación, promovieron la desorción y oxidación de CO irradiando la superficie con un pulso láser de femtosegundo de 800 nm y registrando el número de eventos para cada reacción en varios pasos temporales tras el impacto láser. Este trabajo demostró la apertura de una nueva vía de reacción para la oxidación del CO mediante la irradiación con láser de femtosegundo.

Se requieren simulaciones precisas de la dinámica de la foto-reacción para caracterizar adecuadamente este tipo de experimentos. Esto puede dar una respuesta definitiva a preguntas sobre qué mecanismo gobierna cada reacción (excitaciones de fonones o de electrones), qué papel juega el intercambio de energía interadsorbato o qué características específicas del sistema dominan el resultado de los experimentos. El propósito de esta tesis, motivada por el trabajo experimental de Bonn *et al.*[6], es por tanto simular estos experimentos con un modelo teórico recientemente desarrollado que incorpora en la dinámica de adsorbatos tanto el efecto de los electrones calientes inducidos por láser como el de los concomitantes fonones calientes. Aspiramos a complementar el conocimiento de la oxidación de CO sobre superficies de Ru empleando simulaciones de dinámica moleculares *ab-initio* incluyendo

fricción electrónica (AIMDEF)[7] recientemente desarrolladas, que permitan simular el experimento de reacción foto-inducida. Luego utilizamos métodos modernos de caracterización de rutas de reacción (CINEB[8;9]) y tecnología de vanguardia como redes neuronales para generar superficies de energía potencial.[10]

En el segundo capítulo presentamos los métodos teóricos que se utilizan en esta tesis. En primer lugar presentamos los métodos teóricos en los que se basan los cálculos de estructura electrónica aplicados a los sistemas gas-superficie. A continuación mostramos la separación de los grados de libertad electrónicos y nucleares con la aproximación Born-Oppenheimer. Después, describimos los métodos para resolver el problema de estructura electrónica con teoría de la funcional densidad (DFT), y revisamos brevemente los funcionales de canje-correlación comunes. En segundo lugar, introducimos los métodos de dinámica molecular y presentamos el caso específico de AIMDEF para la dinámica de reacciones foto-inducidas. En tercer lugar, introducimos las redes neuronales (NN) y presentamos el método general para generar una superficie de energía potencial basada en redes neuronales (NN-PES). Para ello introducimos el modelo de red neuronal atómica (ANN) y su uso en la red neuronal con átomos encastrados (EANN). Finalmente, presentamos herramientas adicionales utilizadas para caracterizar el sistema durante esta tesis.

En el tercer capítulo, presentamos los resultados de una caracterización completa de diferentes recubrimientos mixtos de (O, CO) sobre Ru(0001) que consisten en 0.5 ML de O combinado con tres recubrimientos diferentes de CO (0.25 ML, 0.375 ML, y 0.5 ML). Está organizado de tal manera que primero presentamos las superficies de Ru bajo estudio y la caja de simulación. También explicamos la elección del funcional utilizado para los cálculos DFT. En segundo lugar, presentamos el protocolo utilizado para encontrar los estados intermedios importantes de la ruta de desorción recombinativa de CO y O. En tercer lugar, proporcionamos y discutimos los resultados obtenidos para cada uno de los tres recubrimientos considerados. En cada caso, comenzamos con una búsqueda sistemática de la configuración energéticamente más estable que sea compatible con la preparación de la superficie reportada en refs.[6;11;12;13]. Una vez identificada la disposición optimizada, realizamos una caracterización completa de la desorción y oxidación de CO en este recubrimiento específico calculando las energías de reacción correspondientes y, lo que es más importante, las rutas de reacción de energía mínima para cada proceso. El análisis comparativo de sus diagramas energéticos se muestra posteriormente para entender la competencia entre la desorción y la oxidación de CO que se observa en los experimentos. Luego, se discute la dependencia a los tres recubrimientos considerados aquí, de la competición entre estas reacciones. En cuarto lugar, presentamos un análisis adicional de los tres recubrimientos, con el análisis de carga de Bader para describir el carácter de adsorción de las especies de interés. Finalmente, utilizamos el cálculo de densidad de estados para presentar un estudio de los Orbitales Moleculares (MOs) en el límite de recubrimiento cero, con el fin de estudiar el efecto en ellos de la adsorción de la molécula de $CO_{2(gas)}$ sobre superficies de Ru.

En el cuarto capítulo, presentamos los resultados de las simulaciones AIMDEF del recubrimiento superficial bajo. En primer lugar, analizamos las probabilidades de desorción y oxidación del CO. En segundo lugar, estudiamos la ruta de reacción de la oxidación del CO, y mostramos la complejidad para alcanzar la región del estado de transición. En tercer lugar, analizamos y comparamos un espectro de adsorción de rayos X O-K calculado con la interpretación realizada en ref.[13]. Por último, concluimos

sobre la creación de la molécula CO_2 en la región del estado de transición, y la competencia entre la formación de CO_2 y la desorción de CO.

En el quinto capítulo, presentamos con más detalle los resultados de las simulaciones AIMDEF para los tres diferentes recubrimientos de superficie, y los dos tipos diferentes de simulaciones (con y sin movimiento de la superficie). En primer lugar, analizamos las probabilidades de desorción y oxidación de CO para los distintos recubrimientos de superficies y los dos tipos de simulaciones. En segundo lugar, analizamos la variación de la energía cinética de los adsorbatos. Para dar más información, mostramos la distribución de la energía cinética en la componente traslacional, y en la energía cinética vertical y en el plano. En tercer lugar, analizamos la variación del movimiento vertical de los adsorbatos durante las simulaciones. Aquí identificamos la creación de varias especies durante la simulación, y las caracterizamos. En cuarto lugar, analizamos la variación del movimiento en el plano de los adsorbatos. Finalmente, presentamos y estudiamos el mecanismo de oxidación del CO encontrado durante nuestras simulaciones AIMDEF.

En el sexto capítulo, presentamos las dos metodologías utilizadas para generar una NN-PES basado en los cálculos AIMDEF. Las dos NN-PES se han construido con distintos métodos de selección a la hora de formar los conjuntos de configuraciones. En primer lugar, presentamos el proceso de entrenamiento y prueba para el desarrollo de una NN-PES preciso para el recubrimiento de superficie bajo, con el primer método de selección de configuraciones. A continuación, presentamos los resultados de la simulación con esta NN-PES. En segundo lugar, presentamos el segundo proceso de selección y entrenamiento, pero para el recubrimiento de superficie intermedio. Realizamos algunas nuevas pruebas para comprobar la precisión de esta NN-PES y su transferibilidad en predecir correctamente el espacio configuracional de los distintos recubrimientos de superficie. A continuación, mostramos los límites del modelo y del esquema de entrenamiento. Finalmente, presentamos los resultados de las simulaciones realizadas con este último tipo para los tres recubrimientos de superficie.

Y por último, en el séptimo capítulo, presentamos las conclusiones de esta tesis, y el trabajo futuro que se puede hacer para mejorarla.

RESUMÉ

Cette thèse est dédiée à l'étude de la désorption et de l'oxydation photo-induites de molécules de monoxyde de carbone (CO) coadsorbées en présence d'adatomes d' oxygène (O) sur la surface de Ru(0001) avec différents taux de couverture. Cette thèse est divisée en sept chapitres résumés comme suit.

Dans le premier chapitre nous commençons le manuscrit par une introduction qui présente l'état de l'art du sujet, les motivations de l'étude et les différentes problématiques dans lesquelles s'inscrit ce travail.

Le CO est un gaz incolore, inodore et neurotoxique. C'est pourquoi l'oxydation du CO a été considérée comme un moyen efficace de l'éliminer du l'air ambiant.[1] La réaction catalytique d'oxydation du CO produite en surface des métaux de transition est une réaction cruciale dans divers domaines, par exemple, dans les pots catalytiques des voitures qui convertissent le CO en CO_2, comme dans la lutte contre la pollution industrielle.[2] Elle est considérée comme une réaction hétérogène car le CO est présent sous forme de gaz et réagit avec une surface métallique à l'état solide. De plus, en raison de sa relative simplicité, elle a fait l'objet de nombreuses études fondamentales axées sur les processus catalytiques hétérogènes.[3] Il a été dévoué un grand intérêt au comportement du ruthénium (Ru), considéré comme anormal par rapport aux autres métaux de transition (palladium, platine, rhodium et iridium) dans le cas particulier de la réaction d'oxydation du CO. Plus précisément, il a été constaté que dans des conditions d'ultra haut vide, le Ru est particulièrement inactif quant à l'oxydation du CO.[4;5] Dans un article précurseur, Bonn *et al.*[6] montrent expérimentalement qu'il est possible d'activer l'oxydation du CO en irradiant une surface de Ru(0001) pré-couverte d'atomes d'O et de CO avec une laser infra rouge. Techniquement, ils ont déposés 0,5 ML d'atomes de O sur une surface de Ru(0001), puis ont appliqués sur elle une pression de CO à 100 K pour adsorber les molécules de CO. Ensuite, en irradiant la surface avec un laser a impulsion femtoseconde de 800 nm de longueur d'onde, ils ont provoqués la desorption et l'oxydation du CO. Ce travail a démontré l'ouverture d'une nouvelle voie de réaction pour l'oxydation du CO.

Pour caractériser correctement ce type d'expérience, il est nécessaire de faire des simulations précises de la dynamique de la photo-réaction de ce type d'expérience. Grâce à cela, nous pourrions donner une réponse définitive aux questions concernant le mécanisme qui gouverne chaque réaction (excitations phononiques ou électroniques), sur le rôle joué par l'échange d'énergie entre les adsorbats ou les caractéristiques spécifiques du système qui dominent les résultats des expériences. Motivée par le travail expérimental de Bonn *et al.*.[6], l'objectif de cette thèse est donc de simuler ces expériences avec un modèle théorique qui à récemment été développé, et qui incorpore dans la dynamique moléculaire à la fois l'effet des électrons chauds induits par laser et des phonons chauds concomitants.

Nous aspirons à compléter la connaissance autour de l'oxydation du CO sur les surfaces de Ru en employant des simulations de dynamique moléculaire ab-initio incluant les effets de la friction électronique (AIMDEF),[7] permettant de simuler les expériences de réactions photo-induite. Ensuite, nous avons utilisé des méthodes modernes de caractérisation des chemins de réaction (CINEB[8;9]) et une technologie de pointe telle que les réseaux neuronaux pour générer des surfaces d'énergie potentielle.[10]

Dans le deuxième chapitre, nous présentons les méthodes théoriques que nous avons utilisées dans cette thèse. Tout d'abord, nous présentons les méthodes théoriques sur lesquelles sont basés les calculs de structure électronique appliqués aux systèmes gaz-surface. Ensuite, nous montrons la séparation des degrés de liberté électroniques et nucléaires avec l'approximation de Born-Oppenheimer. Ensuite, nous décrivons les méthodes de résolution du problème de structure électronique grâce à la DFT, et passons brièvement en revue les fonctions d'échange-corrélation courantes. Ensuite, nous introduisons les méthodes de dynamique moléculaire (MD) et présentons le cas spécifique de l'AIMDEF pour la dynamique des réactions photo-induites. Troisièmement, nous introduisons les réseaux neuronaux (NN) et présentons la méthode générale pour générer une surface d'énergie potentielle fitée par réseau neuronal (NNPES). Pour cela, nous introduisons le modèle de réseau neuronal atomique (ANN) et son utilisation dans le modèle d'atome incorporé dans un réseau neuronal (EANN). Enfin, nous présentons les outils supplémentaires utilisés pour caractériser les systèmes au cours de cette thèse.

Dans le troisième chapitre, nous présentons les résultats après la caractérisation complète grâce à la DFT de différents taux de couvertures mixtes de (O, CO) sur Ru(0001) qui consistent en un 0.5 ML fixe d'O combiné à trois taux de couverture différente de CO (0.25 ML, 0.375 ML, et 0.5 ML). Le chapitre est organisé de telle sorte que nous présentons d'abord la surface de Ru étudiée et la boîte de simulation. Nous expliquons également le choix de la fonctionnelle de densité utilisée pour les calculs DFT. Deuxièmement, nous présentons le protocole utilisé pour trouver les états intermédiaires importants du chemin de réaction de l'oxydation du CO par un atome d'O. Troisièmement, nous fournissons et discutons les résultats obtenus pour chacun des trois taux de couvertures considérés. Dans chaque cas, nous commençons par une recherche systématique de la configuration énergétique la plus stable et compatible avec la préparation de surface rapportée dans refs.[6;11;12;13]. Une fois l'arrangement optimisé identifié, nous effectuons une caractérisation complète de la désorption et de l'oxydation du CO de chaque taux de couverture en calculant les énergies de réaction correspondantes et, surtout, les chemins de réaction à énergie minimale pour chaque processus. L'analyse comparative de leurs diagrammes énergétiques permet ensuite de comprendre la compétition entre la désorption et l'oxydation du CO qui est observée pendant les expériences. Puis nous discutons du lien entre le taux de couverture et la compétition entre la désorption et l'oxydation du CO. Quatrièmement, nous présentons une autre analyse des trois taux de couvertures, avec l'analyse de la charge de Bader afin de décrire le caractère d'adsorption de l'espèce d'intérêt. Enfin, nous utilisons le calcul de densité d'état (DOS) pour présenter une étude des orbitales moléculaires (MOs) au taux de couverture minimum, afin d'étudier l'effet de l'adsorption d'une molécule de $CO_{2(gas)}$ sur la surface de Ru(0001) sur ses MOs.

Dans le quatrième chapitre, nous présentons les résultats des simulations AIMDEF du taux de couverture dit « low ». Premièrement, nous analysons les probabilités de désorption et d'oxydation du CO. Deuxièmement, nous étudions le chemin réactionnel de l'oxydation du CO, et montrons la

complexité pour atteindre la région de l'état de transition. Troisièmement, nous analysons et comparons un spectre d'adsorption aux rayons X O-K calculé, avec les interprétations faites dans ref.[13]. Enfin, nous analysons comment se crée la molécule de CO_2 dans la région de l'état de transition, et la compétition entre la formation de CO_2 et la désorption du CO.

Dans le cinquième chapitre, nous présentons plus en détail les résultats des simulations AIMDEF pour les trois différents taux de couverture, et les deux différents types de simulations (avec et sans mouvement de la surface). Premièrement, nous analysons les probabilités de désorption et d'oxydation du CO pour les différents taux de couverture de surface et les deux types de simulations. Ensuite, nous analysons les variations de l'énergie cinétique des adsorbats. Pour mieux comprendre, nous décomposons l'énergie cinétique dans sa composante translationnelle, en énergie perpendiculaire et parallèle au plan de la surface. Troisièmement, nous analysons les variations du mouvement vertical des adsorbats pendant les simulations AIMDEF. Nous identifions ici la création de plusieurs espèces pendant la simulation, et nous les caractérisons. Quatrièmement, nous analysons les variations du mouvement des adsorbats dans le plan. Enfin, nous présentons et étudions les mécanismes d'oxydation du CO rencontrés lors de nos simulations AIMDEF.

Dans le sixième chapitre, nous présentons les deux méthodologies utilisées pour générer une NNPES à partir des données AIMDEF calculées avec la DFT. Nous avons construit deux NNPES avec des méthodes de sélection différentes lors de la formation des ensembles de configurations. Nous présentons d'abord le processus de formation et de test pour le développement d'une NNPES pour le taux de couverture « low », avec la première méthode de sélection des configurations. Ensuite, nous présentons les résultats de la simulation MD utilisant cette NNPES. Puis, nous présentons le deuxième processus de sélection et d'entraînement de la NNPES, mais pour le taux de couverture « intermediate ». Nous effectuons de nouveaux tests pour vérifier la précision de ce NNPES et sa transférabilité quant à la prédiction de l'espace configurationnel des différents taux de couvertures. Ensuite, nous montrons les limites du modèle et de la méthode de sélection. Enfin, nous présentons les résultats des simulations effectuées avec cette dernière NNPES pour les trois taux de couvertures.

Finalement, dans le septième chapitre, nous présentons les conclusions de cette thèse, et les travaux futurs qui peuvent être effectués.

LIST OF PUBLICATIONS

1. **A. Tetenoire**, J. I. Juaristi, and M. Alducin, *Insights into the Coadsorption and Reactivity of O and CO on Ru(0001) and Their Coverage Dependence*, Journal of Physical Chemistry C, 125 (23), 12614-12627 (2021), DOI: 10.1021/acs.jpcc.1c01618

2. **A. Tetenoire**, C. Ehlert, J. I. Juaristi, Peter Saalfrank, and M. Alducin, *Why Ultrafast Photoinduced CO Desorption Dominates over Oxidation on Ru(0001)*, Journal of Physical Chemistry Letters, 13 (36), 8516-8521 (2022), DOI: 10.1021/acs.jpclett.2c02327

3. **A. Tetenoire**, J. I. Juaristi, and M. Alducin *Photo-induced CO desorption dominates over oxidation on different O+CO covered Ru(0001) surfaces*, in preparation

TABLE OF CONTENTS

LIST OF FIGURES

LIST OF TABLES

List of Acronyms

2TM Two Temperatures Model

AIMD *ab-initio* Molecular Dynamics

AIMDEF *ab-initio* Molecular Dynamics with Electronic Friction

ANN Atomistic Neural Network

BOA Born-Oppenheimer approximation

CI-NEB Climbing Image Nudged Elastic Band

CM Center of Mass

DFT Density Functional Theory

DIMET Desorption Induced by Multiple Electronic Transitions

DoF Degrees of Freedom

DOS Density Of State

EAM Embedded Atom Method

EANN Embedded Atom Neural Network

fcc Face Centered Cubic

FEG Free Electron Gas

FS Final State

GGA Generalized Gradient Approximation

GTOs Gaussian-type orbitals

hcp Hexagonal Close Packed

HEG Homogeneous Electron Gas

HF Hartree-Fock

HK Hohenberg-Kohn

HOMO Highest Occupied Molecular Orbital

IS Initial State

KS Kohn-Sham

LDA Local Density Approximation

LDFA Local Density Friction Approximation

LEPS London-Eyring-Polanyi-Sato

LUMO Lowest Unoccupied Molecular Orbital

MAE Mean Absolute Error

MD Molecular Dynamics

MEP Minimum Energy Path

MO Molecular Orbital

NEB Nudged Elastic Band

NH Nosé-Hoover

NN Neural Network

NN-PES Neural Network Potential Energy Surface

NNP-MD Neural Network Potential Molecular Dynamics

PAW Projector Augmented Wave

PBC periodic boundaries conditions

PDOS Projected Density Of State

PES Potential Energy Surface

RMSE Root Mean Square Error

TS Transition States

UHV Ultra High Vacuum

VASP Vienna *Ab initio* Simulation Package

vdW van der Waals

XAS X-ray Absorption Spectroscopy

***xc*-functional** exchange correlation functional

XES X-ray Emission Spectroscopy

CHAPTER 1

INTRODUCTION

"Science sans conscience n'est que ruine de l'âme."

— François RABELAIS, Pantagruel.[1]

The catalytic reaction of carbon monoxide oxidation at transition metal surfaces is a crucial reaction in various domains, for instance, in automotive exhaust catalysts to convert CO into carbon dioxide and in industrial pollution control.[2] It is considered a heterogeneous reaction because CO is present in gas form and reacts with a solid metallic surface. More generally, since CO is colorless, tasteless, and a neuro-toxic gas oxidation of CO has been seen to be an efficient way to eliminate CO from the air pollutant.[1] This reaction has been widely studied[23] within the context of emission control (atmosphere purification for hydrogen gas fuel in fuel cells as well[24;25]) and maintenance of clean air (*e.g.*, respiratory protection systems for military, mining, and space devices[26]). Also, due to its relative simplicity, it has been the subject of numerous fundamental studies focused on heterogeneous catalytic processes.[3] Great interest has been devoted to the behavior of ruthenium that has been regarded as anomalous when compared to other transition metals (*e.g.*, palladium, platinum, rhodium, and iridium) in the particular case of the CO oxidation reaction. More precisely, it has been found that under UHV conditions Ru is very inactive for CO oxidation.[4;5] However, at high gas pressures Ru has been found to be a much more active catalyst for CO oxidation than Pd, Pt, Rh and Ir.[27;28;29] These results have motivated numerous experimental and theoretical studies devoted to the understanding and characterization of the adsorption and coadsorption of O_2 and CO on Ru surfaces, as well as their interaction with this metal. This thesis aspires to complement the knowledge of the oxidation of CO on Ru surfaces by employing recent developed AIMDEF[7] simulations to understand the reactions dynamics and modern methods of characterization of reaction paths (CI-NEB[8;9]).

The main interest of this thesis is to gain insight from a theoretical point of view into the femtosecond laser induced desorption and oxidation of CO, disentangling among other things, the contribution that the laser-induced hot electrons and concomitant hot phonons have in these reaction processes. The pioneer experimental work by Bonn *et al.*[6] is the leading reference that motivated this study. In that experiment, the authors used a Ru(0001) surface precovered with 0.5 ML of O atoms. Next, they applied a CO pressure at 100 K to adsorb CO molecules on the O precovered surface. The

[1] *"Science without awareness is doom of the soul."* —François RABELAIS, Pantagruel.

desorption and oxidation of CO were promoted by irradiating the surface with a femtosecond laser pulse of 800 nm and the number of events for each reaction were recorded at several time steps after the laser impact. Therefore, in this thesis we have studied the desorption and oxidation of CO on the Ru(0001) surface covered with 0.5 ML of O and different CO coverages that are expected to be stable at different temperatures. This work gives answers to questions as: Which is the most stable adsorbates configuration for the experimental coverage? How is the mechanism of recombination of CO and O?

The study of catalytic reactions is a very vast field of research, even for the particular case of heterogeneous catalysis, in which the oxidation of CO on Ru is inscribed. An early classification of catalytic reactions at surfaces was proposed by Langmuir[30;31], who split them in two types that are denoted nowadays as:

- The "Langmuir–Hinshelwood" (LH) reaction, the most usual case in heterogeneous catalysis, is when the reactants are both adsorbed on the surface prior to reaction.
- The "Eley–Rideal" (ER) reaction, in which the chemical reaction takes place between a gas phase particle (*e.g.*, CO) that scatters at an adsorbed particle (*e.g.*, O).

Figure 1.1 represents schematically the above reactions using CO as projectile in the case of the ER mechanism (left side) and recombination of O with CO for the LH mechanism (right side). The ER reaction mechanism is usually assumed to be less likely because the amount of gas phase particles hitting the surface per site per second, at given temperature and pressure, is typically low compared to the frequency of encounters between two particles already adsorbed on the surface, as it is the case in the LH process. The photo-induced oxidation of CO on Ru(0001) studied in this thesis, could be considered a kind of LH reaction process that, instead of being thermally activated, is promoted by the highly excited electrons created by the laser pulse.

In both previously cited reaction mechanisms, the O is first adsorbed on the metal surface, afterward CO reacts with the atomic O whether being coadsorbed on the metal surface,[6] or by being sent in a supersonic molecular beam.[32] Thus, the first step is to adsorb the atomic O on the surface. This is achieved by dissociative adsorption of O_2. Regarding this reaction on Ru(0001), it has been well established using Low Energy Electron Diffraction (LEED) that under UHV conditions and at room temperature, two ordered phases can be formed, p(2×2)[33] and p(2×1),[34] corresponding to a O coverage of 0.25 and 0.5 ML, respectively. The latter corresponds to the oxygen saturation coverage under these conditions. In both cases the O atoms adsorb in Hexagonal Close Packed (hcp) sites.[33;34] Calculations based on DFT at the Generalized Gradient Approximation (GGA) level showed that, indeed, the hcp site is the energetically most favorable adsorption site for atomic O on Ru(0001) at these coverages.[35] Interestingly, the authors predicted the stability of a complete monolayer of O arranged in a (1×1) phase, with the O atoms also adsorbed on the hcp sites. The existence of this high coverage phase was subsequently corroborated in experiments that used LEED to characterize the surface structure.[36] However, this coverage is not achievable upon O_2 exposure under UHV conditions and requires that the surface is supplied with atomic O. This coverage was attained by the decomposition of NO_2 into adsorbed O and instantly desorbed NO.[36]

It was speculated that this (1×1)-O phase was responsible of the above mentioned high catalytic activity for CO oxidation that Ru exhibits at high pressures.[28] Several DFT-GGA based studies on the

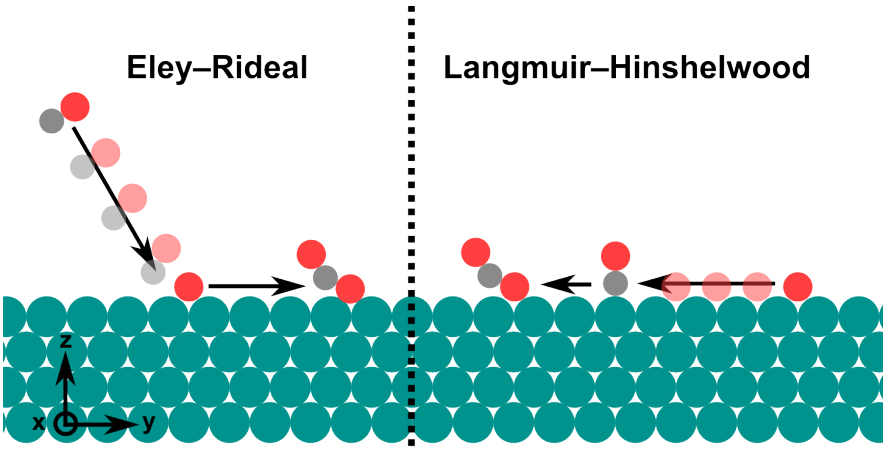

Figure 1.1: Schematic representation of the ER reaction (left side) between CO and O, with CO as projectile, and LH reaction (right side) with O recombination with CO, creating in both cases a CO_2 molecule. The blue, red and gray balls are ruthenium, O and carbon atoms, respectively. The representation is a side view of the surface with the vacuum above in the z direction.

energetics of the reaction at this O coverage seemed to support this idea.[37;38] However, further CO deposition and molecular beam experiments over O precovered Ru(0001) showed that the (1×1)-O overlayer on Ru(0001) is very inactive and that only for O coverages beyond 3 ML the CO/CO_2 conversion is efficient.[32;39;40] Furthermore, after adsorption of 1 ML of O atoms, no more hcp sites are available. This can conduct to either piling up O or to oxidize the ruthenium atoms and form a stable RuO_2 layer.[36;41;42] This oxidation results in the weakening of the bond between ruthenium atoms and adsorbed atomic oxygen atoms.[39] The mechanism of oxidation has been studied in detail in ref.[43] where different O phases are studied during Ru(0001) oxidation. In this work, by means of emission of O_2 and RuO_x ($x < 4$) in thermal desorption spectroscopy, the authors distinguished between the subsurface-O phase and regular oxides. The authors demonstrated that when performing an O exposure below 850 K on Ru(0001), mobile atomic O species is predominantly formed in the subsurface region. Between 900-1150 K, the subsurface O atoms can form a Ru_xO_y phase. In a later study, it has been shown that the active part in the oxidation of CO is in fact an ultrathin RuO_2 surface oxide that grows at high O_2 exposures.[44;45] Finally, the phase diagram of the RuO_2 structure in a constrained equilibrium with O_2 and CO in gas phase has been determined from UHV and low temperature conditions to relevant pressure and temperature.[46]

The oxidized surfaces of ruthenium have been studied more in depth from the late 90s to the beginning of the 2000s in comparison to the Ru(0001) surface, since the oxide has a higher yield of reaction for CO oxidation. Although the information concerning this oxide is relevant, in this thesis we will focus on modeling the pristine ruthenium surface covered with 0.5 ML of O rather than the oxidized one, because the purpose is understanding the oxidation of CO that, although thermally forbidden under UHV conditions on Ru(0001), it can be activated by a femtosecond laser pulse[6].

Yet, we still need to know the corresponding coverage of CO coadsorbed with 0.5ML of O under UHV conditions at low temperatures, and also how the adsorbates are arranged on the surface. In this regard, Kostov *et al.*[11] performed an extensive characterization of the different structures that emerge upon the adsorption of CO on Ru(0001) with different precoverages of O. They used a

battery of techniques such as High Resolution Electron Energy Loss Spectroscopy (HREELS), LEED, Temperature Programmed Desorption (TPD) and measurements of work function changes. One of the important results of this work concerns the CO saturation coverage on the 0.5 ML O precovered surface. First, it was found that at 120 K, CO saturation leads to crowded CO in the empty space of the (2×1)-O layer. However, at 300 K, around one third of the CO has been desorbed so that saturation at this temperature corresponds to a O:CO ratio of roughly 2:1. Interestingly, in this higher temperature structure, the experimental information strongly suggested that half of the O atoms changed place from their equilibrium hcp sites to less stable fcc sites forming a honeycomb structure, in which CO adsorbs vertically on top of the Ru atom located at the center of the O hexagon. This structure had been suggested by a previous study that used Fourier Transform-Infrared Reflection Absorption Spectroscopy (FT-IRAS), LEED, and thermal desorption mass spectroscopy (TDMS).[29] Its existence was finally confirmed by a LEED-IV analysis.[47]

After introducing the different characterized coverages of O and CO on Ru(0001) it is important to review the static properties of such systems (*e.g.*, interactions between each species, activation energies for desorption and for diffusion on the surface *etc.*). When CO or CO_2 molecules adsorb on metal surfaces, they form a bond with this metal. The two processes under study (CO desorption and oxidation) need to break this bond either to desorb or to diffuse on the surface. Thus, it is important to understand the bonding of a molecule to various transition metals. Several studies investigated the bonding between CO and transition metals,[48;49;50] ruthenium alloys,[51;52] and specifically ruthenium surfaces.[53] Different models have been elaborated to explain chemical bonding, starting with the Blyholder model[54] that explains the adsorbate-metal bonding using the Highest Occupied Molecular Orbital (HOMO) and Lowest Unoccupied Molecular Orbital (LUMO) frontier orbitals. More recently, a more advanced model, the π-σ model,[19] has been proposed. This model includes HOMO-1 and LUMO+1 orbitals in addition to the frontier orbitals in its explanation of molecular bonding. Lastly, it is worth to mention a recent extension of the π-σ model that can be additionally applied to describe the bonding between organic molecules and metal alloys.[51]

According to the Blyholder model, the CO HOMO (5σ) creates a dative bond with the surface by exchanging electrons with the metal. The electrons donation through this dative bond is compensated by a back-donation mechanism from the metal to the CO LUMO (2π). The π-σ model provides a more elaborated analysis of the bonding. The Molecular Orbitals (MOs) that couple with the metal are denoted as tilde orbitals to distinguish them from the gas-phase MOs, and the σ system is split into attractive and repulsive parts, still compensated by the π system. In the case of the O adatom, a straightforward description from the π-σ model is that a bond between its *p* orbitals and the *d* orbitals of Ru is created.[55] The type of bonding between CO and the metal surface has a direct impact on the frequency of the CO internal stretch vibrational mode,[53] adsorption energy, and on the different activation barriers of reactions[56] the involve CO.

The bonding of CO on various Ru surfaces was extensively studied by Stampfl *et al.*[56] The authors additionally calculated CO adsorption energies and adsorption activation barriers at different O and CO coverages, including adsorption phases that occur in nature and also model phases not realized in experiments yet. Regarding the 0.5 ML O saturation coverage under UHV conditions, two different phases were studied: (i) the above mentioned honeycomb structure with O atoms equally distributed

between hcp and fcc sites with CO molecules at on-top sites and (ii) an additional structure with O on hcp sites arranged in a p(2×1) structure and the CO molecules adsorbed on hcp sites. However, in both considered structures the O:CO ratio was 2:1, *i.e.*, none of them corresponds to the low temperature CO saturation coverage found experimentally by Kostov *et al.*[11] (the one with crowded CO molecules in the empty space of the (2×1)-O layer). Since coadsorption of Ru(0001)-0.5 ML-O with higher CO coverages has not been theoretically studied, in this thesis we have started by performing a complete DFT characterization of three different CO co-adsorbed coverages, denoted as low, intermediate, and high coverages in the following. Specifically, the low coverage is formed by 0.5 ML O + 0.25 ML CO, the intermediate coverage consists of 0.5 ML O + 0.375 ML CO, and the high coverage is defined by 0.5 ML O + 0.5 ML CO. The low and intermediate coverages have been experimentally achieved in ref.[11], while the high coverage is a theoretical one, interesting to study the limits of CO adsorption on O precovered surface.

In the works discussed above,[11;56] the activation energies for the different processes were also provided. With these data, one could perform a kinetic Monte Carlo (kMC) study, or apply transition state theory to calculate the kinetic of reactions. However, no such studies has been found in literature for pristine Ru surfaces. Notwithstanding, there exist some of these studies for ruthenium oxide. The results and conclusions of those studies are interesting in connection to our work. Reuter and coworkers[57] studied the oxidative reaction of CO on RuO_2 oxide using transition state theory and kMC simulations. They examined the reaction from UHV to several atmosphere pressures, using two different temperatures (350 K and 600 K). As a first conclusion, they showed the dependence of the oxidative reaction on the temperature and pressure of the O_2 and CO gases. They demonstrated that for a specific temperature, the optimum pressure of each gas (O_2 and CO) must be controlled to maximize the CO oxidation. They also evidenced the rarity of this reaction due to the high amount of other possible reactions. This is a very important conclusion that is transferable to the CO desorption/oxidation competition problem for CO and O on the Ru(0001) surface. In other words, the chemical reaction with the most favorable energy barrier contributes only to a small amount of the overall CO_2 production at maximum activity conditions. The authors stated that, although the process itself has very suitable properties for catalysis, it can only occur too rarely considering all possible events (*e.g.*, 8 processes of O and CO diffusion, 6 processes of adsorption/desorption, and 4 other processes) to have a significant effect on the observable macroscopic functionality. In ref.[58] the authors remarked the importance of considering the lateral interactions between CO molecules in a kMC study of CO oxidation on RuO_2 surface. Finally, a theoretical study using kMC investigates the diffusion of O on the CO saturated Ru(0001) surface.[59] This study showed a concurring movement between the O and CO diffusion.

We will now turn our attention to what mechanisms can be used to activate the desorption and oxidation of CO on the Ru(0001) surface. In general there are several ways to activate a reaction, namely, acid/base catalytic processes, the use of metal catalysts, thermal catalysis, photocatalysis, electrocatalysis and even plasma catalysis.[60] In ref.[11], it was shown that CO oxidation cannot be thermally activated under UHV conditions in the flat Ru surface. However, it was later shown that the reaction can be efficiently propelled by exciting the system with femtosecond laser pulses under the same UHV conditions.[6]

In thermal reactions on a metal surface, the needed energy to drive the system across the activation barrier in the electronic ground state comes from the excited phonons. However, as demonstrated in ref.[6], electrons in the high-energy tail of a thermal Fermi-Dirac distribution can also induce chemical transformations by transient population of normally unoccupied states. Phonon and electron-mediated processes are fundamentally different, but cannot be distinguished when electrons and phonons are in equilibrium. Thus, with the use of a femtosecond laser excitation, the strong nonequilibrium between electrons and phonons can be used to separate electron- from phonon- induced processes allowing to establish their implication in the reaction process. The predominant coupling path can be determined by means of a two-pulse correlation measurement (2PC). In such experiments, the photo-reaction yield is measured as a function of the delay between two pulses of equal intensity. Because of the fast electron-phonon coupling, high electronic temperatures resulting from the combined effect of the two pulses can only be reached when the two pulses are separated by a time-span that does not exceed the electron-phonon equilibration time of $\sim$1 ps. Therefore, one expects a fast response of a few picoseconds in the 2PC if the reaction is electron-mediated. In contrast, a slow response indicates a predominant coupling to phonons, because the cooling of phonons is much slower ($\sim$50 ps). Using this technique, several experimental groups investigated the effects and the implication of phonons and hot-electrons in different reaction processes, including pure desorption of the adsorbed molecules and recombination of different adsorbates prior desorbing.[6;61;62;63;64;65;66] Later, various theoretical groups simulated these experiments in order to gain insight into the experimental findings and conclusions.[7;13;13;67;68;69]

In what follows we will first present the experimental studies of CO photo-desorption, followed by a literature review on the oxidation of CO, which is the competing process to CO desorption.

Experimentally, the photodesorption of CO from the Cu(111) and Cu(100) surfaces was considered to be electron mediated.[70;71] However, both electrons and phonons were expected to contribute efficiently in the desorption of CO from Pd(111).[64] In the case of Ru(0001), the results from 2PC experiments suggested that CO desorption is predominantly phonon mediated.[62] The same conclusion was obtained in a work in which the transition of CO into a weakly adsorbed precursor state prior to desorption (occurring on a time scale $>$2ps) was found to be phonon-mediated.[72] Notwithstanding, there are also several studies combining both experiment and theory suggesting that the CO photo-desorption from Ru is not only phonon mediated. In ref.[73], the authors studied femtosecond laser-induced desorption of CO from Ru(0001) using intense near-infrared and visible femtosecond laser pulses. In this case, they found that both hot electrons and phonons contribute to the desorption process. Although previously studied in ref.[72], the authors of ref.[67] provided a microscopic interpretation of this phenomenon, supported by experiments. They also provide *ab-initio* Molecular Dynamics (AIMD) simulations of CO adsorbed on Ru(0001) at 1500 K and 3000 K. In this work, the authors established that after an optical laser excitation, a two-step mechanism leads to CO desorption. Subpicosecond electron-driven dynamics leads to excitation of CO external vibrational modes and diffusion, which, in combination with slower phonon-driven ($>$2ps) dynamics, leads to the population of the precursor state prior to desorption. The effect of the non-thermal electrons on the internal stretch and frustrated rotation of CO adsorbed on Ru surfaces has been confirmed in a theoretical study.[74] Later, in ref.[75], the authors performed a theoretical study with DFT calculations of CO desorption

from Ru(0001), which also predicts a weakly bound state prior to desorption when non-local correlation effects are included. Moreover, the authors included the entropic contribution in the calculations to obtain the finite temperature potential-energy surface through the potential of mean force. They found that at elevated temperature, the chemisorbed state is separated from the precursor state by a barrier that increases as the temperature increases.

Electron and phonon mediated processes for CO desorption from Ru(0001) under UHV conditions were theoretically investigated in ref.[76], where the authors presented molecular dynamics simulations of the femtosecond laser induced diffusion and desorption of CO in the Ru(0001) surface. They found that the photo-induced reaction yields are for both diffusion and desorption considerably larger than those obtained by thermal activation. The authors also computed 2PC simulations that indicated that aside the laser-induced hot electrons, the excited phonons also play an important role in the laser-induced dynamics.

In the works discussed above, the CO desorption from Ru surfaces was studied on only purely CO covered surfaces. However, CO oxidation on the surface requires the presence of coadsorbed O atoms. In this respect, there are also studies of CO desorption, but from an O precovered Ru(0001) surface. In ref.[77], the authors showed experimentally that coadsorbed O atoms in the honeycomb structure have a dramatic effect on the CO desorption dynamics. In contrast to the precursor-mediated desorption mechanism on Ru(0001),[75] the presence of O adsorbates modifies significantly the Ru(0001) electronic structure such that CO desorption occurs predominantly via a direct pathway. The co-adsorption of CO with O is inducing a reduction of the dative 5σ bond of CO with the metal, which makes the desorption step more facile because of the smaller free energy barrier. This bond-breaking process has been corroborated by AIMD simulations of CO desorption from the Ru(0001) surface with coadsorbed O in the honeycomb structure.[77]

After this short description about CO desorption on transition metal surfaces, but specifically Ru(0001), we will briefly review the oxidation process of CO on metallic surfaces.

The complex reaction path of CO oxidation on metal surfaces has been studied for various flat metal surfaces (Fe, Co, Ni and Cu),[78;79] for bimetallic alloys,[80] and for stepped Pt surfaces.[81] In all cases the formation of one or several intermediate states is observed. The most important intermediate state is the anionic CO_2^- (also called bent CO_2) which has been revealed of important interest,[79;82] for instance, in the hydrogenation of CO_2 and its transformation to methanol on a metal oxide,[83] and as a precursor state to the linear adsorbed CO_2.[82] Also seen as a very important mechanism, previous studies have reported the importance of the diffusion of the adsorbates on the surface in CO_2 oxidation.

In the case of Ru surfaces, energy barriers and minimum energy paths for CO oxidation have been studied for different adsorbate structures and coverages. They included the p(2×2)-(O, CO) structure,[84;85;86] the p(2×1)-O with CO in hcp sites in a O:CO ratio of 2:1,[12;86] the 0.5 ML O honeycomb structure,[12;13] and two very low coverage phases in a 5×5 cell consisting of one O and one CO in one case and of four O and one CO in the other case.[87] The same group studied also the effect of steps in Ru surfaces on the CO oxidation MEP for one CO and one O in the same cell.[88] A general result of these studies was that the main responsible for the activation barrier that hinders CO oxidation is the energy required to destabilize and move the atomic O from its adsorption site. In most cases, it was also found that the adsorption energy of CO was larger than the corresponding activation

energy for CO oxidation, with the exception of the very low coverage results of ref.[87]. Yet no report of the CO_2^- intermediate state has been done for Ru(0001).

Until our days, not much work has been done to unravel the importance of electrons or phonons in the oxidation process of CO on Ru surfaces. Although some experiments have been done, yet no full theoretical work has been reported. We previously reviewed the effects of electrons and phonons on CO desorption, therefore we will now cover their effect on CO oxidation.

Bonn *et al.*[6] demonstrated for coadsorbed O/CO-Ru(0001) that electrons can chemically activate adsorbates, thus opening a new reaction pathway for CO oxidation. The novelty of this work is to make use of hot electrons to promote a reaction that could not be initiated by thermal activation and to show the existence of this new pathway by conducting 2PC experiments. In a later work,[13] the authors confirmed that the CO molecules reached the transition state (TS) of CO_2 formation by means of O K-edge X-ray absorption spectroscopy prior to CO oxidation. They measured that after 1 ps after arrival of the femtosecond laser pulse, 10% of the CO populates the TS region, which is consistent with their predictions. In a similar experiment of CO oxidation induced by fs-laser pulses on Ru(0001) with coadsorbed CO and O in the honeycomb structure, the authors found that a shorter wavelength excitation reduces the branching ratio between CO oxidation and desorption (from 1:31 with the 800 nm laser pulse to 1:9 in the case of the 400 nm pulse).[12] They also evidenced discrepancies between activation energies calculated from DFT and values extracted from experiments, which suggested both a mixture between different adsorbed phases and the importance of non-adiabatic effects on the effective barrier for oxidation. They also found (as in ref.[67]) that the excitation of CO vibrations, which leads to subsequent desorption of CO, occurs on the time scale of thermalization of electrons for CO on bare Ru(0001).

Concerning the oxidation pathway of CO, the authors of ref.[12] also simulated the reaction using a kinetic model that combines the two-temperature model for the laser-induced energy transfer to the substrate with a friction model for the coupling to adsorbate vibrations. They studied the surface coverage containing 0.25 ML of CO and 0.5 ML of O with two different arrangements, the already mentioned honeycomb structure and another one with O adsorbed on HCP sites in a p(2×1) structure and CO adsorbed on near-atop site. In both coverage structures, the access to the TS configuration requires initial displacement of an O atom towards the adjacent bridge site with CO moving towards the O atom. By using two different wavelengths for exciting the electrons from the metal (400 nm and 800 nm), the authors showed the effect of the electrons in the high-energy tail of a thermal Fermi-Dirac distribution on the chemical bonding. The unoccupied O-Ru antibonding is located at 1.8 eV above the Fermi level. Thus populating this state with the electrons in the tail of the thermal Fermi-Dirac distribution allows to activate the motion of the O atom by weakening the bond with ruthenium (as predicted in ref.[6]). The O atom can be expected to come out from the hollow site due to this bond weakening and access the transition state of the oxidation reaction.[13] The effect of non-thermalized electrons is expected to be smaller for CO desorption since the M-CO $\tilde{\pi}^*$ state, which is antibonding between the adsorbate and the surface,[49] is located around 3.6 eV above the Fermi level and neither single-photon excitation using 1.55 nor 3.1 eV photons will reach this level. Finally, it is worth to mention that, recently, a higher selectivity in favor of the oxidative reaction has been achieved by a direct excitation of the O atoms by means of intense THz pulses[89] and X-ray femtosecond laser

pulses in resonance with the O 1s excitation.[90] The three last cited experiments are emphasizing the importance of electrons to selectively activate a chemical bond or a stretching mode to initiate a reaction.

Accurate simulations of the photo-reaction dynamics are required to give a proper characterization of this kind of experiments. This may give a definite answer to questions about which mechanism is governing each reaction (phonon or electron excitations), which role plays the interadsorbate energy exchange or which specific characteristics of the system dominate the outcome of the experiments. The purpose of this thesis is thus to simulate these experiments with a recently developed theoretical model that incorporates in the adsorbates dynamics both the effect of the laser-induced hot electrons and the concomitant hot phonons.

The response of the metal to the laser pulse has been successfully described in terms of coupled electronic and phononic excitations characterized by two time dependent electronic and phononic temperatures.[14] When femtosecond lasers of large fluence ($>$0.6m J/cm^2) are used for photodesorption, the process occurs through multiple electronic transitions (Desorption Induced by Multiple Electronic Transitions (DIMET) process).[91] As shown in ref.[91], the DIMET process can be described by MD which includes electronic frictions. This approach was introduced by Tully and co-workers.[92] In this method, the nuclear motion is treated classically, whereas the electronic degrees of freedom are hidden in a generalized Langevin formalism in the form of friction and fluctuating forces. However, up to now, this calculation scheme has not been applied to the CO oxidation, among other reasons, due to the high dimensionality involved in the reaction. Only very recently, the development of AIMDEF[93;94;95] has allowed to treat the multidimensional nonadiabatic dynamics of this kind of photo-induced reaction at the DFT level,[7;68;69] taking into account the coupling of the adsorbates to both excited electronic and phononic systems,[7;69] as well as the interadsorbate energy exchange.[7;68] In this thesis, we will use this model to investigate the problem of photodesorption and oxidation of CO coadsorbed with O atoms on Ru(0001).

As it is generally the case for AIMD simulations (and also for AIMDEF simulations), each simulation is computationally very demanding, both in time and resources. In computer simulations for chemical reactions, alternatives have been developed to decrease the amount of time and resources needed that consist in constructing accurate Potential Energy Surfaces (PESs) that are based on fitting or interpolation methods and permit us a very efficient calculation of the adiabatic forces. In the 2000s, in the gas/surface interaction research field, reduced six dimensional[96] PESs were used to simulate the dynamics of diatomic molecules interacting with static metal surfaces. Later, Force Fields (FF) parametrizations, and in particular Reactive Force Fields (RFF), allowed in some systems to access to PESs with more dimensions.[97] Another solution has been proposed in the last decade. It is to use Neural Networks (NNs) to create a PES by fitting DFT energies and reach a full multidimensional PES called NN-PES. Multidimensional interpolation methods were already used in order to access PESs, but the NN method allows us to automatize the process without the need of a hand parametrization. A generalized NN method for constructing accurate DFT-based PES able to describe every type of bonding, the so-called atomistic neural network,[98] has been proposed. The resulting NN-PES can be used in systems of arbitrary size. In this model, a general NN contains specific NNs for each atomic element (the atomic NN). These specific NNs describe the neighboring environment of this atomic

species. Thus, the general NN describes the whole system by the use of several local environments. Recently, it has been proposed to use the Embedded Atom Method (EAM) in combination with atomistic NN to create a novel NN-PES called EANN.[10] This NN differs from the precedent one because it uses a different way to decompose the configurational space of the atomic NN, by making use of EAM and Gaussian type orbitals.

In this thesis, a preliminary NN-PES has been developed making used of the previously calculated AIMDEF configurations. Although this NN-PES has to be improved, it allows us to compute thousands more MD simulations, in order to increase the statistic of occurring processes, and also to compute larger systems with reasonable computational resources.

Chapter description

This thesis is structured as follows:

- In Chapter 2 we present the theoretical methods that are used in this thesis. First we present the theoretical methods on which the electronic structure calculations applied to the gas-surface systems are based. Then we show the separation of the electronic and nuclear degrees of freedom with the Born-Oppenheimer approximation. Next, we describe the methods for solving the electronic structure problem with DFT, and briefly review the common exchange-correlation functionals. Secondly, we introduce MD methods and present the specific case of AIMDEF for photo-induced reaction dynamics. Thirdly, we introduce the NN and present the general method to generate a NN-PES. For this we introduce the ANN model and its use in EANN. Finally, we present additional tools used to characterize the system during this thesis.

- In Chapter 3 we present the results of a complete DFT characterization of different (O, CO) mixed coverages on Ru(0001) that consist of a fixed 0.5 ML of O combined with three different CO coverages (0.25 ML, 0.375 ML, and 0.5 ML). It is organized such that we first introduce the Ru surfaces under study and the simulation box. We also explain the choice of the functional used for the DFT calculations. Second, we present the protocol used to find the important intermediate states of the path for recombinative desorption of CO and O. Third, we provide and discuss the results obtained for each of the three coverages considered. In each case, we start with a systematic search of the energetically most stable configuration that is compatible with the surface preparation reported in refs.[6;11;12;13]. Once the optimized arrangement is identified, we perform a full characterization of the desorption and oxidation of CO on this specific overlayer by calculating the corresponding reaction energies and, importantly, the minimum energy reaction paths for each process. The comparative analysis of their energy diagrams is later shown to understand the competition between CO desorption and oxidation that is observed in experiments. The dependence of this competitive reaction on the three coverages considered here is discussed. Fourth, we present further analysis of the three coverages, with the Bader charge analysis in order to describe the adsorption character of the specie of interest. Finally, we use the DOS calculation to present a study of the MOs at the zero coverage limit, in order to study the effect of the adsorption of $CO_{2(gas)}$ molecules on Ru surfaces.

- In Chapter 4 we present the results of the AIMDEF simulations of the low surface coverage. First, we analysis the probabilities of desorption and oxidation of CO. Second, we study the reaction path of the CO oxidation, and show the complexity to reach the transition state region. Third, we analyze and compare a calculated O-K X-Ray adsorption spectra with the interpretation made in ref.[13]. Finally, we conclude on the creation of the CO_2 molecule in the transition state region, and the competition between formation of CO_2 and desorption of CO.

- In Chapter 5 we present in more detail the results of the AIMDEF simulations for all the three different surface coverages, and the two different types of calculation (with and without motion of the surface). First, we analyze the CO desorption and oxidation probabilities for the different surface coverages, and the two types of calculation. Second, we analyze the variation of the kinetic energy of the adsorbates and its coverage dependence. Third, we analyze the variation of the vertical motion of the adsorbates during the AIMDEF simulations. Here we identify the creation of several species during the simulation, and characterize them. Fourth, we analyze the variation of the in-plane motion of the adsorbates. Finally, we present and study the mechanism of oxidation of the CO found during our AIMDEF simulations.

- In Chapter 6 we present the two methodologies used to generate a NN-PES based on the AIMDEF DFT data. The two NN-PES have been constructed with different selection methods when forming the configurations sets. First, we present the process of training and testing for the development of an accurate NN-PES for the low coverage, with the first method of configuration selection. Afterwards we present the results of MD simulations using this NN-PES. Secondly, we present the second process of selection and training, but for the intermediate coverage. We perform some new tests to check the accuracy of this NN-PES and its transferability in order to predict correctly the configurational space of the different coverages. Then, we show the limits of the model and training scheme. At the end, we present the results of MD simulations performed with this last NN-PES for the three coverages.

- In Chapter 7 we present the conclusions of this thesis.

CHAPTER 2

THEORETICAL METHODS

"Mais ce n'est rien. Cela va finir. -Il sourit avec effort.- C'est fini."

— Edmond ROSTAND, Cyrano de Bergerac.[1]

In this chapter we present the theoretical background and methods that have been utilized to simulate the photo-induced dynamics of adsorbates on metal surfaces. It starts by describing in Section 2.1 the important Born-Oppenheimer approximation (BOA) that allows us to treat separately the nuclei and electronic wavefunctions. DFT is used to calculate the electronic ground state of the gas-surface systems under consideration and it will be briefly introduced in Sections 2.2 and 2.3. In Section 2.4, we explain the theoretical framework that has been used to simulate the complex dynamics induced by femtosecond laser pulses. We start justifying the use of classical dynamics for the nuclei motion. Next, we explain the Two Temperatures Model (2TM), which describes the excitations created by the laser pulse in the system by means of two coupled heat thermal baths, the Langevin dynamics that describes the coupling of the adsorbates to the laser-induced hot electrons, and the Nosé-Hoover thermostat, used to additionally account for the hot lattice created by the hot electrons. In this thesis all the dynamics simulations are ab-initio, *i.e.*, the adiabatic forces are calculated directly from DFT. However, taking advantage of the ab initio data generated in these simulations, we have also started the calculation of a Neural Network Potential Energy Surface (NN-PES) that could be used to calculate the adiabatic forces at a considerably lower computational cost. The basics of the NN framework applied in this thesis is given in Section 2.5. Finally, in Section 2.6, we describe diverse theoretical tools that have been used in this thesis to analyze the results from our electronic structure calculations and dynamics simulations.

2.1 The Born-Oppenheimer approximation

The system conformed by interacting gas-phase atoms/molecules and a metal surface is a many-body quantum system. It contains n electrons and N nuclei, being their total energy described by the

[1] *"It is nothing. It is going to end. -He smiles with effort.- It is ended."* —Edmond ROSTAND, Cyrano de Bergerac.

following Hamiltonian,

$$H = T_{\mathrm{n}} + T_{\mathrm{e}} + V_{\mathrm{ee}} + V_{\mathrm{en}} + V_{\mathrm{nn}}\,, \tag{2.1}$$

where T_{e} and T_{n} are, respectively, the kinetic energy of the electrons and the nuclei. The potential energy terms V describe the electron-electron interaction (V_{ee}), the nucleus-nucleus interaction (V_{nn}), and the electron-nucleus interaction (V_{en}). Neglecting the spin and using atomic units ($\hbar = m_{\mathrm{e}} = e = 1$), the terms of the non-relativistic Hamiltonian are:

kinetic energy of nuclei:
$$T_{\mathrm{n}} = \sum_{k=1}^{N} -\frac{1}{2M_k}\nabla^2_{\mathbf{R}_k}\,, \tag{2.2}$$

kinetic energy of electrons:
$$T_{\mathrm{e}} = \sum_{i=1}^{n} -\frac{1}{2}\nabla^2_{\mathbf{r}_i}\,, \tag{2.3}$$

electron-electron electrostatic interaction:
$$V_{\mathrm{ee}} = \frac{1}{2}\sum_{\substack{i,j=1\\ i\neq j}}^{n} -\frac{1}{|\mathbf{r}_i - \mathbf{r}_j|}\,, \tag{2.4}$$

electron-nucleus electrostatic interaction:
$$V_{\mathrm{en}} = -\sum_{i=1}^{n}\sum_{k=1}^{N}\frac{Z_k}{|\mathbf{r}_i - \mathbf{R}_k|}\,, \tag{2.5}$$

nucleus-nucleus electrostatic interaction:
$$V_{\mathrm{nn}} = \frac{1}{2}\sum_{\substack{k,k'=1\\ k\neq k'}}^{N}\frac{Z_k Z_{k'}}{|\mathbf{R}_k - \mathbf{R}_{k'}|}\,, \tag{2.6}$$

with the sets of electronic coordinates written as $\mathbf{r}_i (i = 1,...,n)$ and nuclear coordinates written as $\mathbf{R}_k (k = 1,...,N)$, which will be denoted as $\{\mathbf{r}\}$ and $\{\mathbf{R}\}$, respectively. Here Z_k and M_k are, respectively, the charge and mass of the k^{th} nucleus.

Now, let us consider a stationary state described by the wavefunction of the system $\Psi(\{\mathbf{r}\},\{\mathbf{R}\})$ whose eigenstate satisfies the time-independent Schrödinger equation:

$$H\Psi(\{\mathbf{r}\},\{\mathbf{R}\}) = E\Psi(\{\mathbf{r}\},\{\mathbf{R}\})\,. \tag{2.7}$$

Although, one can solve the Schrödinger equation for one electron atomic species such as H and He^+ and get the exact solution, it is extremely hard to solve it when considering more Degrees of Freedom (DoF), as it is the case of the gas-surface systems with $(3n+3N)$ DoF that are studied in this thesis. Fortunately, there are different approximations that allow us to tackle this issue,[99;100;101] being the first important one the BOA.[102]

The BOA consists in separating the ionic and electronic degrees of freedom. The justification for this common approximation is that even for the lightest atom (hydrogen), the electron is ~ 2000 times lighter than the nucleous. Note, in our case, that the lightest atom used is carbon, which is at least an order of magnitude heavier than hydrogen. Due to this mass difference, electrons move much faster than nuclei, and from the electronic frame of reference the nuclei appear to be static. In practice, the BOA implies that the Schrödinger equation of the full system (eq.(2.7)) can be separated into the Schrödinger equation of the electrons interacting with the nuclei fixed at the position $\{\mathbf{R}_0\}$ and the Schrödinger equation of the nuclei. Thus, denoting the electronic wavefunction as Ψ_{e}, the electronic

Schrödinger equation for a given fixed configuration of the nuclei reads,

$$H_{\mathrm{e}}\Psi_{\mathrm{e}}(\{\mathbf{r}\},\{\mathbf{R}_0\}) = E_{\mathrm{e}}(\{\mathbf{R}_0\})\Psi_{\mathrm{e}}(\{\mathbf{r}\},\{\mathbf{R}_0\})\,, \tag{2.8}$$

where the electronic Hamiltonian H_{e} for fixed nuclear coordinates $\{\mathbf{R}_0\}$ (the latter acting as a parameter, not as a variable) is defined as

$$H_{\mathrm{e}} = T_{\mathrm{e}} + V_{\mathrm{ee}} + V_{\mathrm{en}} + V_{\mathrm{nn}}\,. \tag{2.9}$$

And the Schrödinger equation of the nuclei is,

$$[T_{\mathrm{n}} + E_{\mathrm{e}}(\{\mathbf{R}\})]\Psi_{\mathrm{n}}(\{\mathbf{R}\}) = E_{\mathrm{n}}\Psi_{\mathrm{n}}(\{\mathbf{R}\})\,, \tag{2.10}$$

with Ψ_{n} the nuclear wavefunction. From this equation, it is clear that $E_{\mathrm{e}}(\{\mathbf{R}\})$ plays the role of a potential in which the nuclei evolve. It is the so-called, BO-PES. The BOA is very successful in the description of many processes on solid surfaces. However, it remains now to solve the electronic problem for a particular nuclear configuration. The most complicated part of any electronic structure calculation is due to the electron-electron interaction. A wide variety of wavefunction based methods have been developed to solve the electronic Schrödinger equation, such as, Hartree-Fock (HF), Configuration Interaction (CI) theory and Möller-Plesset perturbation theory (MP2). Within these formalisms, the wavefunctions of an electronic system will depend on $3n$ coordinates, that is, on all the electronic DoF. Therefore, as the size of the system increases, the number of DoF increases and the use of these methods becomes numerically intractable. This drawback motivated the development of a theory to reduce the total number of DoF involved in the calculation, namely, the DFT that is briefly introduced next.

2.2 Density Functional Theory

The central idea of DFT is to replace the complicated n-electron wavefunction $\Psi_{\mathrm{e}}(\{\mathbf{r}\},\{\mathbf{R}_0\})$ (which depends on the $3n$ electronic DoF for fixed $\{\mathbf{R}_0\}$) by the electron density $\rho(\mathbf{r})$, which depends only on three spacial coordinates, and it is defined as

$$\rho(\mathbf{r}) = n\int |\psi(\mathbf{r},\mathbf{r}_2...,\mathbf{r}_n)|^2 d\mathbf{r}_2,...,d\mathbf{r}_n\,. \tag{2.11}$$

This idea was originally formulated independently by Thomas [103] and Fermi [104] in the 1920s. In their original work, they proposed an expression for the total electronic energy where the kinetic, exchange, and correlation contributions were taken from the Homogeneous Electron Gas (HEG), for which good approximations were known. However, there are two major drawbacks in the Thomas-Fermi theory. First, it does not describe the molecular binding and, second, it is of poor accuracy. After countless modifications and improvements, Hohenberg and Kohn provided the fundamental theorems showing that for the ground state, the Thomas-Fermi model can be seen as an approximation to the exact theory of DFT.

The Hohenberg and Kohn theorems

There are two fundamental theorems demonstrated by Hohenberg-Kohn (HK)[105;106] which are the basis of DFT. The first theorem states that

Theorem 2.2.1 *For any system of interacting particles in an external potential $v_{\text{ext}}(\mathbf{r})$, the potential $v_{\text{ext}}(\mathbf{r})$ is determined uniquely, except for a constant , by the ground state particle density $\rho_0(\mathbf{r})$*

In other words, there is a one-to-one correspondence between the external potential and the ground state density of a gas of interacting electrons. So, the density uniquely defines the electronic Hamiltonian and therefore the energy of the electronic system. In the present case, the external potential is the electron-nucleus electrostatic interaction.

The second theorem of HK states that

Theorem 2.2.2 *For a trial density $\rho'(\mathbf{r})$ such that $\rho'(\mathbf{r}) \geq 0$ at any $\mathbf{r}$, the electron density obeys a variational principle $E_{\text{HK}}[\rho'(\mathbf{r})] \geq E_0$ where E_0 is the true ground state energy and where $E_{\text{HK}}[\rho'(\mathbf{r})]$ is the energy functional*

Therefore, the exact ground-state density is the density that minimizes E_0. In principle, E_0 can be obtained by minimizing the energy within the constraint that $\rho(\mathbf{r})$ integrates to n (the number of electrons) using the Rayleigh-Ritz variational principle[107]:

$$E_0 \leq \frac{\langle \Psi_{\text{e}} | H_{\text{HK}} | \Psi_{\text{e}} \rangle}{\langle \Psi_{\text{e}} | \Psi_{\text{e}} \rangle} \,. \tag{2.12}$$

Accordingly to the first HK theorem, the electronic energy can be written as a functional of the density $\rho(\mathbf{r})$

$$E_{\text{HK}}[\rho(\mathbf{r})] = V_{\text{en}}[\rho(\mathbf{r})] + T_{\text{e}}[\rho(\mathbf{r})] + V_{\text{ee}}[\rho(\mathbf{r})] = V_{\text{en}}[\rho(\mathbf{r})] + F_{\text{HK}}[\rho(\mathbf{r})] \,, \tag{2.13}$$

where the electronic kinetic energy $T_{\text{e}}[\rho(\mathbf{r})]$ and the *e-e* potential $V_{\text{ee}}[\rho(\mathbf{r})]$ of eq.(2.13) are universal, *i.e.*, they do not depend on the external potential and they are generic for a given Coulomb interaction. These two terms define the HK functional term $F_{\text{HK}}[\rho(\mathbf{r})]$ in eq.(2.13). However, the exact analytical form of the $F_{\text{HK}}[\rho(\mathbf{r})]$ functional is not known and approximations have to be used.

The Kohn-Sham equations

To tackle this problem, Kohn and Sham introduced the concept of a non-interacting reference system.[108] According to this scheme, it is possible to find a system of non-interacting electrons subject to an effective (fictitious) potential v_{eff}, whose density $\rho'(\mathbf{r})$ is the same as the density of the interacting system $\rho(\mathbf{r})$. Thus, the wavefunction associated to the non-interacting particles is a Slater determinant constructed from a set of orbitals ϕ_i^{KS}, the so-called KS orbitals. The corresponding electron density is given by

$$\rho'(\mathbf{r}) = \sum_{i=1}^{n} |\phi_i^{\text{KS}}(\mathbf{r})|^2 = \rho(\mathbf{r}) \,. \tag{2.14}$$

The electron-electron interaction potential V_{ee} can be separated in two terms:

$$V_{\mathrm{ee}}[\rho(\mathbf{r})] = E_{\mathrm{H}}[\rho(\mathbf{r})] + G_{\mathrm{xc}}[\rho(\mathbf{r})]\,, \tag{2.15}$$

where $E_{\mathrm{H}}[\rho(\mathbf{r})]$ is the Coulomb potential energy, *i.e.*, the classical part of $V_{\mathrm{ee}}[\rho(\mathbf{r})]$:

$$E_{\mathrm{H}}[\rho(\mathbf{r})] = \frac{1}{2}\int \frac{\rho(\mathbf{r})\rho(\mathbf{r}')}{|\mathbf{r}-\mathbf{r}'|} d\mathbf{r} d\mathbf{r}' \tag{2.16}$$

and $G_{\mathrm{xc}}[\rho(\mathbf{r})]$ is the exchange and correlation term containing the quantum many-body effects.

Similarly, the kinetic energy functional T_{e} of interacting particles can be separated into a non-interacting contribution $T_{\mathrm{s}}[\rho(\mathbf{r})]$, *i.e.*, the kinetic energy of non-interacting electrons moving in the effective potential v_{eff}

$$T_{\mathrm{s}}[\rho(\mathbf{r})] = -\frac{1}{2}\sum_{i=1}^{n}\int d\mathbf{r}[\phi_i^{\mathrm{KS}}(\mathbf{r})]^*\nabla^2\phi_i^{\mathrm{KS}}(\mathbf{r}) \tag{2.17}$$

and an unknown component $T_{\mathrm{c}}[\rho(\mathbf{r})]$ that contains corrections due to the quantum many-body effects. The HK functional F_{HK} (eq.(2.15)) is now rewritten as

$$F_{\mathrm{HK}}[\rho(\mathbf{r})] = T_{\mathrm{s}}[\rho(\mathbf{r})] + E_{\mathrm{H}}[\rho(\mathbf{r})] + E_{\mathrm{xc}}[\rho(\mathbf{r})]\,, \tag{2.18}$$

where the exchange correlation functional $E_{\mathrm{xc}}[\rho(\mathbf{r})]$ accounts for the missing quantum mechanical interaction of the electrons in the aforementioned non-interacting reference system, *i.e.*, the exchange and correlation contributions to the kinetic and *e-e* interaction energies, not captured by T_{s} and E_{H}. Then it can formally be written as

$$E_{\mathrm{xc}}[\rho(\mathbf{r})] = G_{\mathrm{xc}}[\rho(\mathbf{r})] + T_{\mathrm{c}}[\rho(\mathbf{r})]\,. \tag{2.19}$$

Taking into account all the above definitions, the total energy functional can be written as

$$E_{\mathrm{HK}}[\rho(\mathbf{r})] = T_{\mathrm{s}}[\rho(\mathbf{r})] + V_{\mathrm{en}}[\rho(\mathbf{r})] + E_{\mathrm{H}}[\rho(\mathbf{r})] + E_{\mathrm{xc}}[\rho(\mathbf{r})]\,. \tag{2.20}$$

Finding the ground state of the KS auxiliary system consists in minimizing eq.(2.20) with respect to the density $\rho(\mathbf{r})$. In doing so we arrive to the KS equations:

$$\left(-\frac{1}{2}\nabla^2 + v_{\mathrm{en}} + v_{\mathrm{H}} + v_{\mathrm{xc}}\right)\phi_i^{\mathrm{KS}}(\mathbf{r}) = \varepsilon_i\phi_i^{\mathrm{KS}}(\mathbf{r})\,, \tag{2.21}$$

where:

$$v_{\text{en}} = -\sum_{i=1}^{N} \frac{Z_i}{|\mathbf{r}-\mathbf{R}_i|}\,, \tag{2.22}$$

$$v_{\text{H}}[\rho(\mathbf{r})] = \int \frac{\rho(\mathbf{r}')}{|\mathbf{r}-\mathbf{r}'|} d\mathbf{r}'\,, \tag{2.23}$$

$$v_{\text{xc}}[\rho(\mathbf{r})] = \frac{\delta E_{\text{xc}}[\rho(\mathbf{r})]}{\delta\rho(\mathbf{r})}\,. \tag{2.24}$$

The sum of the terms v_{en}, $v_{\text{H}}[\rho(\mathbf{r})]$, and $v_{\text{xc}}[\rho(\mathbf{r})]$ is known as the KS effective potential v_{eff}^{KS}.

The eigenvalues ε_i of the KS equations are called KS orbital energies. The ground state total energy is given by the sum of the occupied orbital energies and the correction to avoid double-counting contributions to the total energy

$$E_{\text{DFT}}[\rho(\mathbf{r})] = \sum_{i=1}^{n} \varepsilon_i - E_{\text{H}}[\rho(\mathbf{r})] + E_{\text{xc}}[\rho(\mathbf{r})] - \int v_{\text{xc}}[\rho(\mathbf{r})]\rho(\mathbf{r}) d\mathbf{r}\,. \tag{2.25}$$

Since the exchange-correlation functional contains everything that is unknown, if we could know the precise expression for it, DFT would be an exact theory. Therefore, the exchange-correlation functional is a central quantity in DFT. It remains now to find the exchange-correlation term v_{xc} (eq.(2.25)), which can be done by different types of approximations.

Exchange correlation functional

Within DFT there exist several levels of approximation of the exchange-correlation functional, summarized in the Jacob's ladder introduced by Perdew *et al.* in ref.[109]. The first level of approximation is the Local Density Approximation (LDA). It assumes that the exchange-correlation energy at each point in the system is the same as that of an HEG of the same density. It is written as

$$E_{\text{xc}}^{\text{LDA}} = \int d\mathbf{r}\rho(\mathbf{r})\varepsilon_{\text{xc}}^{\text{LDA}}[\rho(\mathbf{r})]\,, \tag{2.26}$$

where $\varepsilon_{\text{xc}}^{\text{LDA}}$ is the exchange-correlation energy per electron in a HEG with electron density ρ, which is split into the exchange and correlation contributions, *i.e.*,

$$\varepsilon_{\text{xc}}^{\text{LDA}} = \varepsilon_x^{\text{LDA}} + \varepsilon_c^{\text{LDA}}\,. \tag{2.27}$$

In the HEG, the exchange energy per electron $\varepsilon_x^{\text{LDA}}$ is exactly known.[110] The correlation part $\varepsilon_{\text{c}}^{\text{LDA}}$ can be calculated numerically with accurate quantum Monte Carlo methods.[111] These results have been parametrized by different authors to obtain an analytical expression.[112;113;114] Even though the rules of LDA are very simple, it has been proved to work well in many cases. Still, it is not accurate enough to describe the chemical bonding, in particular, the cohesive and bonding energies are usually overestimated.

A natural improvement over LDA is to use the gradient of the electronic density, $\nabla\rho(\mathbf{r})$, that takes into account its spatial variation. This constitutes the second level of approximation called GGA and

written as:

$$E_{\mathrm{xc}}^{\mathrm{GGA}} = \int d\mathbf{r}\rho(\mathbf{r})\varepsilon_{\mathrm{xc}}^{\mathrm{GGA}}\left[\rho(\mathbf{r},\nabla\rho(\mathbf{r}))\right] . \tag{2.28}$$

The choice of the function $\varepsilon_{\mathrm{xc}}^{\mathrm{GGA}}[\rho(\mathbf{r},\nabla\rho(\mathbf{r}))]$ gives rise to different GGA parametrizations.[114;115;116;117]

Often, current GGA functionals seem to give reliable results for various chemical properties: chemical bonds (ionic, covalent, metallic), polarizability and hyperpolarizability, *etc*... However, the GGA functionals fail to describe correctly the van der Waals (vdW) dispersion interaction. This interaction is very important in our case because the possible presence of physisorption wells during the molecular adsorption/desorption reaction paths are expected to affect the outcome of the reaction dynamics. Therefore, a higher level of precision including van der Waals interactions in the exchange correlation functional is needed for the systems studied in this thesis.

Nowadays there are two ways to correct the total energy. Either we apply a correction after calculating self consistently the electronic energy, which gives a non-self consistent result, or we introduce the correction into $\varepsilon_{\mathrm{xc}}$. As an example of the first type of vdW corrections, we present DFT-D3(BJ)[118] (Grimme *et al.*) which is an atom pairwise sum over C_6R^{-6} potential method, and introduces a correction of the form:

$$E_{\mathrm{DFT-D3(BJ)}} = E_{\mathrm{KS-DFT}} - E_{\mathrm{disp}} , \tag{2.29}$$

with $E_{\mathrm{KS-DFT}}$ being the self-consistent KS energy and E_{disp} the dispersion correction split as a sum of two-body and three-body terms.

Then, as an example of the second type of introduction of the dispersion forces in functionals, we present the vdW-DF proposed by Dion *et al.*.[119] This functional introduces one of the three vdW interactions,[120] the instantaneous dipole-induced dipole-induced interaction, also called London dispersion force, by expressing the exchange-correlation energy such:

$$E_{\mathrm{xc}} = E_{\mathrm{x}}^{\mathrm{GGA}} + E_{\mathrm{c}}^{\mathrm{new}} , \tag{2.30}$$

where $E_{\mathrm{x}}^{\mathrm{GGA}}$ is the exchange energy of the selected functional (originally rev-PBE[121] for vdW-DF) and $E_{\mathrm{c}}^{\mathrm{new}}$ is the new approach of the correlation energy that is split in two terms:

$$E_{\mathrm{c}}^{\mathrm{new}} = E_{\mathrm{c}}^{LDA} + E_{\mathrm{c}}^{\mathrm{nl}} , \tag{2.31}$$

where E_{c}^{LDA} is the correlation energy of LDA and $E_{\mathrm{c}}^{\mathrm{nl}}$ the nonlocal correction. Different forms of the nonlocal correction has been proposed. The one proposed by Dion *et al.* consists in expanding the exact value of $E_{\mathrm{c}}^{\mathrm{nl}}$ up to second order in S, defined in terms of the dielectric function as $S \equiv 1-\varepsilon^{-1}$. Thus,

$$E_{\mathrm{c}}^{\mathrm{nl}} \approx \int_0^{\infty} \frac{du}{4\pi} \mathrm{tr}\left[S^2 - \left(\frac{\nabla S\cdot\nabla V}{4\pi}\right)^2\right] , \tag{2.32}$$

where u is the imaginary frequency, and V is the interelectronic Coulomb interaction. Note that this functional does not include spin polarizability. One can argue that there is double counting of the energy because of the split in two terms, however, LDA does not take long range interactions into account, thus for a uniform system, E_c^{nl} vanishes.

2.3 DFT in practice

After describing the theoretical basics of KS-DFT to find the electronic ground state of a general system, in this section we present how to solve in practice the KS equations.

The first step is to select a basis set in order to represent the KS orbitals ϕ_i. There exist various basis functions that can be used to represent the KS wavefunction, such as the localized Gaussian orbitals and Slater-type orbitals, for example. There are also non-localized basis sets, like plane waves. Their natural periodicity makes them convenient for representing the potential in ideal crystal like metallic surfaces, but have disadvantages for the localize potential of gas molecules. All the DFT calculations presented in this thesis have been done with the Vienna *Ab initio* Simulation Package (VASP) code that uses the plane wave basis set.

In a periodic structure, the potential is also a periodic function with the period of the corresponding lattice. Thus in the KS eq.(2.21), the effective single-electron potential v_{eff}, has the periodicity of the lattice. In such a case, Bloch's theorem [122] states that the eigenstates (in our case KS orbitals) of a periodic potential can be written as a product of a plane wave $e^{i\mathbf{kr}}$ and a function with the periodicity of the lattice,

$$\phi_{i,\mathbf{k}}(\mathbf{r}) = u_{i,\mathbf{k}}(\mathbf{r})e^{i\mathbf{k}\cdot\mathbf{r}}, \tag{2.33}$$

$$u_{i,\mathbf{k}}(\mathbf{r}) = u_{i,\mathbf{k}}(\mathbf{r}+\mathbf{R}), \tag{2.34}$$

where $\mathbf{k}$ is a wavevector within the first Brillouin zone and $\mathbf{R}$ is any vector of the Bravais lattice defined by $\mathbf{R} = n_1a_1 + n_2a_2 + n_3a_3$ (where a_1, a_2 and a_3 are the linearly independent three dimensional primitive vectors of the Bravais lattice). By expanding $u_{i,\mathbf{k}}$ in the plane wave basis set (Fourier series), KS orbitals can be written as

$$\phi_{i,\mathbf{k}}(\mathbf{r}) = \frac{1}{\sqrt{\Omega}}\sum_{\mathbf{G}} C_{\mathbf{k}}(\mathbf{G})e^{i(\mathbf{k}+\mathbf{G})\cdot\mathbf{r}}, \tag{2.35}$$

where $\mathbf{G}$ are reciprocal lattice vectors and $\frac{1}{\sqrt{\Omega}}$ is a normalization factor. Inserting eq.(2.35) in eq.(2.21), one obtains a matrix equation for the coefficients $C_{\mathbf{k}}$

$$\sum_{\mathbf{G}'}(\frac{1}{2}|\mathbf{k}+\mathbf{G}|^2 + \tilde{v}_{eff}(\mathbf{G}-\mathbf{G}'))C_{\mathbf{k}}(\mathbf{G}') = C_{\mathbf{k}}(\mathbf{G})\varepsilon_{\mathbf{k}}, \tag{2.36}$$

where $\tilde{v}_{\text{eff}}$ is the Fourier transform of v_{eff} presented in eq.(2.22). In practice, the number of plane waves that represent the wavefunction cannot be infinite. Thus, the number of plane waves is limited by the

use of a cutoff kinetic energy

$$\frac{1}{2}(\mathbf{k}+\mathbf{G}) \leq E_{\text{cut\_off}}\,. \tag{2.37}$$

To determine a suitable $E_{\text{cut\_off}}$ one should perform several calculations with increasing $E_{\text{cut\_off}}$ and stop when the property of the interest (*e.g.* energy) converges.

As we previously said, the advantage of the plane wave basis set is also its disadvantage. Indeed, it is very convenient for periodic systems, while for a localized wavefunctions, a tremendous amount of plane waves is necessary to describe the large oscillations of wavefunctions close to the nuclei. However, core electrons described by those wavefunctions almost do not participate in the interaction with the other atoms. Therefore, it is possible to remove these electrons from explicit consideration by making use of the *pseudopotential* approximation, and conserve the valence electrons, which are the ones contributing to the description of the chemical bonding. In this way, the associated pseudowavefunction reproduces the true valence wavefunction outside a certain cutoff radius r_c, whereas inside, the nodal structure is suppressed, thus reducing the required $E_{\text{cut\_off}}$. One of the most general and accurate pseudopotential is the Projector Augmented Wave (PAW)[123] method, which is the one used in this thesis.

A second bottleneck of these calculations is the continuous sampling of the Brillouin zone, because now we have to compute a finite number of eigenstates, at an infinite number of **k**–points, in a single unit cell. However, in the limit of large volume, the **k**–points become a dense continuum and in this case, electronic wavefunctions in **k**–points that are close together can be roughly considered the same. Thus, it is possible to represent the wavefunction in a region of the **k**–space by the wavefunctions on a single **k**–point

$$\frac{1}{V_{\text{BZ}}}\int_{\text{BZ}} d\mathbf{k} \approx \frac{1}{(2\pi)^3}\sum_{\mathbf{k}} w_{\mathbf{k}}\,. \tag{2.38}$$

Here, only **k**-points from the irreducible Brillouin zone weighted by a symmetry factor w need to be computed. In this thesis we use the Monkhorst and Pack[124] scheme to divide and generate a **k**-point grids.

The study of periodic gas/surface system is usually computed with the supercell approach. In this method, the surface is represented by a finite number of atoms arranged in layers and constituting the slab. This slab is separated to its top periodic replication by a vacuum. The slab must be thick enough to ensure that its top and bottom layers do not interact. In the ideal case, the atoms in the middle of the slab should have the properties of bulk atoms. Since we will compute molecular adsorption, we construct a supercell that is laterally large enough to avoid spurious interactions between isolated molecules in adjacent cells. Then, because we study molecular desorption process, the vacuum region between the slab and its top replication must be large enough to avoid any interaction between slabs. In the case of gas/surface dynamics, it is recommended to use a vacuum layer at least twice as thick as the slab. Finally, one has to find a compromise between the size of the system and the computational cost. Consider more atoms will increase the precision and the numerical cost while too few will not represent the system accuratey.

The KS equation is solved self-consistently as shown in the scheme represented in Fig. 2.1 and following the variational principle expressed in eq.(2.12). To initiate the electronic self consistent convergence cycle, one first gives an initial guess of the electron density. Then, one evaluates the effective potential, and solve the KS equations. If the value of the energy varies less than the defined threshold, then the cycle stops, otherwise, the new density is reintroduced in the loop to construct the new KS operator and continue the cycle until convergence.

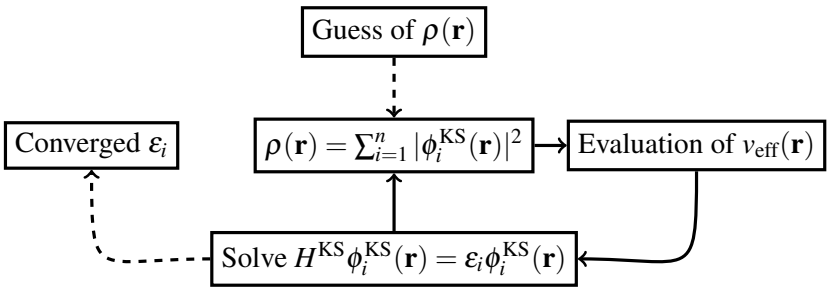

Figure 2.1: Scheme of the electronic self consistent cycle for convergence of the DFT energy using KS equation. Full lines represent the steps of the cycle, while the dash lines are unique steps. With the KS Hamiltonian $H^{\mathrm{KS}} = \left(-\frac{1}{2}\nabla^2 + v_{\mathrm{en}} + v_{\mathrm{H}} + v_{\mathrm{xc}}\right)$.

As technical details, all the DFT calculations in this thesis for the relaxation process have been carried out with the following parameters. For each atomic configuration, the electronic ground state is determined by minimizing the system total energy up to a precision of 10^{-6} eV. In this process, integration in the Brillouin zone is performed using Γ-centered Monkhorst-Pack grids of special **k**-points[124] ($11\times11\times11$ for bulk Ru and later $3\times6\times1$ for pristine and (O,CO)-covered Ru(0001)) and the Methfessel and Paxton scheme of first order with a broadening of 0.1 eV to describe partial occupancies of each state.[125] The latter are expanded in a plane-wave basis set with an energy cutoff of 400 eV, whereas the electron-core interaction is treated with the PAW method[123] implemented in VASP.[126;127;128]

2.4 Molecular dynamics

Although it is very important to catch the static properties of a system, MD simulations are necessary to understand the reaction mechanisms. In this section we start justifying the use of classical dynamics to describe the movement of the nuclei. Next we will describe the theoretical model used in this thesis to simulate the dynamics of femtosecond laser-induced reactions of adsorbates on metal surfaces.

2.4.1 Classical Dynamics

Our objective is to simulate the dynamics of carbon monoxide and atomic oxygen adsorbed on Ru(0001). In principle, the motion of atoms/molecules should be treated quantically by solving the corresponding time-dependent nuclear Schrödinger equation to obtain the time evolution of the nuclei wavefunctions. However, an alternative is the use of a correspondence between the classical and quantum world by means of the Ehrenfest theorem[129] that provides the time evolution of the mean

values of the position **R** and momentum **P** operators as follows:

$$\frac{d\langle \mathbf{R} \rangle}{dt} = \frac{1}{m}\langle \mathbf{P} \rangle \,, \tag{2.39}$$

$$\frac{d\langle \mathbf{P} \rangle}{dt} = -\langle \nabla V(\mathbf{R}) \rangle \,. \tag{2.40}$$

These two equations remind the form of the classical Hamilton-Jacobi equations for a particle. If the center of the wave packet is sufficiently localized then we can use classical mechanics to move the nuclei. It is justified if the difference between the expected value of the gradient of the potential at the position **R** ($\langle \nabla V_{\mathrm{e}}(\mathbf{R}) \rangle$) and its value in classical mechanics ($[\nabla V_{\mathrm{e}}(\mathbf{r})]_{\mathbf{r}=\langle \mathbf{R} \rangle}$) evaluated at the same position, is negligible. In other words, the motion of the wave packet is practically that of a classical particle of mass m placed in the potential $V(\mathbf{r})$. This allows us to reduce this quantum problem to a simple Newton's equation:

$$\frac{d\mathbf{P}}{dt} = m\frac{d^2}{dt^2}\mathbf{r} = -\nabla_{\mathbf{R}_\alpha} V_{\mathrm{e}}(\mathbf{r}) \,. \tag{2.41}$$

Therefore, considering this approximation, simulations become tractable. This equation can be solved by standard numerical integration schemes like Runge-Kutta, Bulirsh-Stoer, and predictor-corrector methods.[130] In this thesis we use the Beeman algorithm[131], which is closely related to the Verlet algorithm,[132] but provides more accurate velocities. In our case this is particularly important because, as it is discussed in the next section, the dynamics of the adsorbates will be described by means of Langevin equations that explicitly depend on the velocity. Let us finally remark that the time step to perform the simulation has to be chose carefully according to computational resources and needed accuracy.

2.4.2 Photo-induced reaction dynamics

Surface femtochemistry can be initiated by ultrashort-laser pulse excitation of an adsorbate-covered metal surface, resulting in dynamical processes as diffusion, desorption and reaction. After irradiation by a femtosecond laser pulse of wavelength between UV and near-IR, the response of the metal surface can be described within the 2TM[14]. In this model the laser-induced electronic and concomitant (electron-induced) phononic excitations are represented by two coupled heat thermal baths (shown in Fig. 2.2) that are respectively characterized by two distinct time-dependent temperatures, the electronic temperature T_{e} and the lattice temperature T_{ph} (Fig. 2.2 lower panel). However, the use of T_{e} to describe the electronic excitation has to be done with caution because of the following.

After laser irradiation the distribution of excited electrons is non-thermal, and in principle, cannot be described by a Fermi-Dirac distribution and an electronic temperature. However, due to electron-electron scattering, energy redistribution takes place leading to the thermalization of the electronic system. For the Ru(0001) surface at 100 K and laser fluences below 0.6 mJ/cm2 (with $\lambda = 800$nm), it has been shown that up to $\sim$500 fs after pulsed-laser excitation, deviations from a Fermi-Dirac distribution can occur.[133] Nevertheless, in the same experiment, it has also been shown that after 100fs, 80% of the electrons are well described by a Fermi-Dirac distribution. In addition, as the

laser fluence increases, the excitation density increases, which in metals leads to an increase of the electron-electron scattering rate and the subsequent decrease of the thermalization time.[134] For that reason, considering the properties of the laser used in this thesis being 20mJ/cm^2 as fluence, 110fs as FWHM and a wavelength of 800nm, the distinction between thermalized and non-thermal electrons is not no longer relevant, and at early time the electronic system may again be described by an effective electron temperature. Then, the use of the 2TM is well justified in our case. Thus, as a first step, we solve the following coupled equations

$$C_{\mathrm{e}}\frac{\partial T_{\mathrm{e}}}{\partial t} = \frac{\partial}{\partial z}\kappa\frac{\partial T_{\mathrm{e}}}{\partial z} - g(T_{\mathrm{e}} - T_{\mathrm{ph}}) + S(z,t)\,, \tag{2.42}$$

$$C_{\mathrm{ph}}\frac{\partial T_{\mathrm{ph}}}{\partial t} = g(T_{\mathrm{e}} - T_{\mathrm{ph}})\,, \tag{2.43}$$

where $C_{\mathrm{e}} = \gamma T_{\mathrm{e}}$ is the electron heat capacity and γ the corresponding specific heat. C_{ph} is the phonon heat capacity taken from the Debye model, κ is the electronic thermal conductivity and g is the electron-phonon coupling constant. In this model, lateral diffusion can be neglected because the beam diameter of the exciting laser pulse on the surface is much larger than the electron diffusion length. Therefore, in equation (2.42) only the distance along the surface normal z is considered. $S(z,t)$ is the absorbed laser power per unit volume that depends on the shape, wavelength, and fluence of the applied pulse, described as

$$S(z,t) = \frac{I(t)e^{-\alpha z}}{1-e^{-\alpha d}}\,, \tag{2.44}$$

where $I(t)$ is the absorbed fraction of the laser pulse intensity, α^{-1} the optical penetration depth, and d the metal thickness. One can calculate α^{-1} using the laser wavelength λ and the imaginary part of the refractive index of the surface k as $\alpha^{-1} = \lambda/(4\pi k)$. In equation (2.42) and (2.43) we see that the variation of the electronic and lattice temperature are linked, such that the electronic temperature decreases when lattice temperature increases. This operates a transfer of energy between the electronic bath to the phononic bath. The indicated transfer is modulated by the electron-phonon coupling constant. Thus we see that what is determinant for the heating of phononic bath is the electronic bath, and its capability to absorb the energy of the femtosecond laser. This capability is determined by the electronic thermal conductivity, and $S(z,t)$ which both depends on the characteristics of the metal.

The process of a femtosecond laser exciting metal surface electrons is schematically described in Fig. 2.2 top panel. It starts with the excitation of the electronic system that is driven out of equilibrium by the laser radiation. The pulse energy is deposited into the electron system, and due to the small heat capacity of the electrons (compared to the lattice), T_{e} rises within the pulse width to levels far above the melting point of the lattice. This increase is represented in the bottom part of Fig. 2.2, where we show the 2TM calculated with previous mentioned laser characteristics. Next, this electronic excitation energy is then dissipated either by electron diffusion into the bulk or by energy transfer into the phonon subsystem via electron-phonon coupling.[135;136] This gives rise to an increase of the lattice temperature, T_{ph}, however, on a much slower time scale than the electronic response (Fig. 2.2). Within a time span of approximately the electron-phonon coupling time of the substrate, both the electron and phonon

heat baths equilibrate. The adsorbate system can either be vibrationally excited by the hot electrons or the phonons. Depending on which of this two bath excites the adsorbates, the processes will occur in different time scales. This difference is rather important for the identification of whether a process is due to electrons or to phonons. Note that the adsorbates can also be excited by a combination of electrons and phonons.

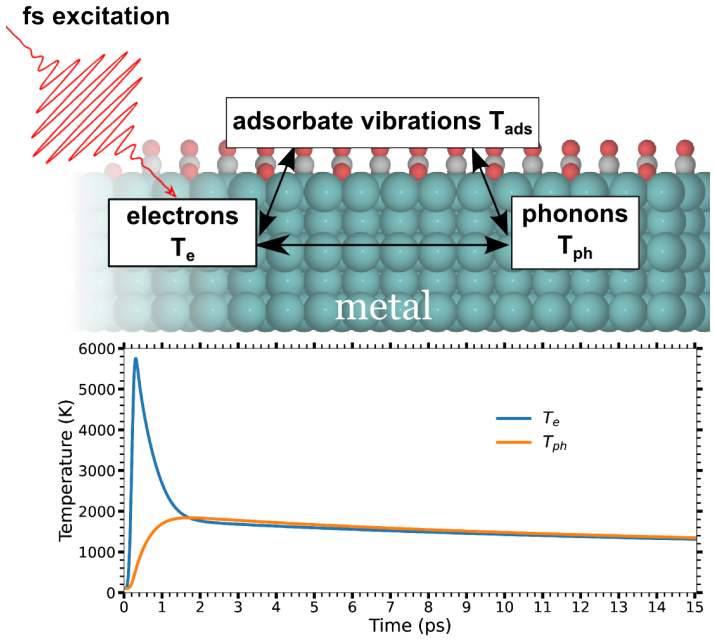

Figure 2.2: (Top) Schematic diagram of the energy flow at metal surfaces after femtosecond-laser excitation. The femtosecond-laser radiation excites the electronic system of the substrate, which next equilibrates with the lattice phonons on the order of the electron-phonon coupling time. Surface reactions can be driven either by electronic coupling or by lattice phonons. (Bottom) Transient temperature for the electron and phonon heat baths with temperatures T_{e} and T_{ph}, respectively, calculated with the two-temperature model [14] here for Ru as the substrate metal. The parameters of the exciting laser pulse are FWHM=110 fs and 20 mJ/cm^2 at 800 nm center wavelength.

Adsorbates Dynamics

The effect of the laser-excited electrons on the adsorbates is described through the following Langevin equation [7]

$$m_i \frac{d^2\mathbf{R}_i}{dt^2} = -\nabla_{\mathbf{R}_i} V(\mathbf{R}_1,...,\mathbf{R}_N) - \eta_{\mathrm{e},i}(\mathbf{R}_i)\frac{d\mathbf{R}_i}{dt} + \mathcal{R}_{e,i}[T_{\mathrm{e}}(t),\eta_{\mathrm{e},i}(\mathbf{R}_i)]\,, \tag{2.45}$$

where m_i, $\mathbf{R}_i$ and $\eta_{\mathrm{e},i}$ are the mass, position vector, and electronic friction coefficient of the i^{th} atom conforming the set of adsorbates. The first term on the right hand side of the equation represents the adiabatic force that depends on the position of all (adsorbates and surface) atoms. Its calculation will be explained in Section 2.4.3. The third term $\mathcal{R}_{e,i}$ is the random fluctuating force that mimics the effect of the hot metal electrons, described by the electronic temperature T_{e}, on the adsorbates. This force

is related to the electronic friction force (second term) through the fluctuation-dissipation theorem. Specifically, $\mathcal{R}_{e,i}$ is modeled by a Gaussian white noise with variance

$$\mathrm{Var}[\mathcal{R}_{e,i}(T_\mathrm{e},\eta_{\mathrm{e},i})] = \frac{2k_\mathrm{B}T_\mathrm{e}(t)\eta_{\mathrm{e},i}(\mathbf{R}_i)}{\Delta t}\,, \tag{2.46}$$

where k_B and Δt are the Boltzmann constant and the time-integration step, respectively. Let us remark that the Langevin dynamics, with different levels of approximations, is widely applied in studies of photo-induced desorption processes.[68;137;138;139;140;141;142;143;144] The electronic friction coefficient for each atom in each adsorbate $\eta_{\mathrm{e},i}$ is calculated within the original Local Density Friction Approximation (LDFA)[145;146] that in the case of molecular adsorbates treats the molecule as formed by independent atoms (independent atom approximation, IAA).

LDFA assumes that $\eta_{\mathrm{e},i}(\mathbf{R}_i)$ is equal to the friction coefficient that the same atom i would experience in case of being moving within a homogeneous Free Electron Gas (FEG)s of density $\rho_0 = \rho_\mathrm{sur}(\mathbf{R}_i)$, where $\rho_\mathrm{sur}(\mathbf{R}_i)$ is the electron density of the bare metal surface at the position $\mathbf{R}_i$.[147] The calculation of the stopping power on an atom traveling through a FEG of density ρ_0 is performed in terms of the LDA DFT potential of an impurity embedded in a jellium. It can be expressed in terms of the transport cross-section and for very small projectile velocities $\mathbf{v}$ (adiabatic limit) it reduces to a mere frictional force proportional (and antiparallel) to the projectile velocity:

$$\mathcal{F}_\mathrm{diss} = -\eta\mathbf{v} = -\rho_0 k_\mathrm{F}\sigma_{tr}(k_\mathrm{F})\mathbf{v}\,, \tag{2.47}$$

where k_F is the Fermi momentum and σ_{tr} is the transport cross section at the Fermi level. Note that the friction coefficient reads $\eta = \rho_0 k_\mathrm{F}\sigma_{tr}(k_\mathrm{F})$. The transport cross section is calculated to all orders in the nuclear charge of the atom in terms of the scattering phase-shifts at the Fermi level ($\delta_l(k_\mathrm{F})$):

$$\sigma_{tr}(k_\mathrm{F}) = \frac{4\pi}{k_\mathrm{F}^2}\sum_{t=0}^{\infty}(l+1)\sin^2[\delta_l(k_\mathrm{F}) - \delta_{l+1}(k_\mathrm{F})]\,. \tag{2.48}$$

Thus we obtain the friction coefficient

$$\eta_{\mathrm{e},i}(\mathbf{R}_i) = \frac{4\pi\rho_\mathrm{sur}(\mathbf{R}_i)}{k_\mathrm{F}}\sum_{t=0}^{\infty}(l+1)\sin^2[\delta_l(k_\mathrm{F}) - \delta_{l+1}(k_\mathrm{F})]\,. \tag{2.49}$$

In practice, the method to calculate $\rho_\mathrm{sur}(\mathbf{R}_i)$ will be different depending on whether the adiabatic forces are calculated at each integration step with DFT or with a precalculated PES, as it will be described later in Section 2.4.3.

Surface atoms dynamics

In order to incorporate the effect of the excited lattice indirectly created by the laser pulse, the surface atoms are coupled to a time-dependent thermostat characterized by the lattice temperature T_ph. We choose the Nosé-Hoover thermostat to introduce T_ph in the system because it has been proved to sample the canonical ensemble.[148] This thermostat was first proposed by Nosé[149], in a preliminary form, but we use the one improved by Nosé[150] and Hoover[148] later on. The idea in the Nosé-Hoover[148]

thermostat formulation is to extend the real system by addition of an artificial dynamic variable $\tilde{s}$ which plays the role of a time-scaling parameter. This variable is associated to a parameter Q which has the dimensions of $[E] \times [t]^2$. In ref.[151] it is shown that by defining a new quantity $\xi = \dot{\tilde{s}} = Q^{-1} s p_s$, the equations of motion of the ions becomes:

$$m_j \frac{d^2 \mathbf{R}_j}{dt^2} = -\nabla_{\mathbf{R}_j} V(\mathbf{R}_1, ..., \mathbf{R}_N) - m_j \xi \frac{d\mathbf{R}_j}{dt}, \tag{2.50}$$

$$\frac{d\xi}{dt} = \frac{1}{Q}(\sum_j m_j |\frac{d\mathbf{R}_j}{dt}|^2 - 3Nk_B T_{ph}), \tag{2.51}$$

where N is the number of moving atoms. The first term in the first equation above is the adiabatic force depending on the position of each atom composing the system. Note that the lattice temperature is introduced in $\frac{d\xi}{dt}$ (second equation). When the moving atoms temperature is below target temperature T_{ph}, ξ is negative and the heat of the heat bath flows to the real system to increase the temperature. In the reverse case, when the temperature is above T_{ph}, ξ becomes positive and the heat flows from the real system to the fictitious one. This leads to temperature oscillations that are controlled by the parameter Q. Hence, this parameter must be chosen with care. On the one hand, if its value is too large, *i.e.*, weak coupling, the canonical distribution will be reached after a very long simulation time, which introduces many systematic energy drift due to numerical error. On the other hand, if the value of Q is too low, *i.e.*, strong coupling, the oscillation of the temperature will be very fast and will result to an off resonance with real system, which decouple from the physical DoF. For gas/surface simulation, it is recommended to use a value of Q in the order of the surface phonon frequency.

2.4.3 Adiabatic forces and electronic density

We left on purpose out of Section 2.4.2 the explanation of the calculation of the adiabatic force, and the details about the electronic density, because for the same Langevin equation, we proceed with two different methods to calculate those terms which we will explain in detail in the following. The first method, which is the most expensive in time and resources, is to compute AIMDEF simulations in which the adiabatic forces are obtained by means of the Hellmann-Feynman theorem. In AIMDEF simulations the electronic density at the position of the atoms required to compute the electronic forces are calculated on-the-fly in terms of the self-consistent system electronic density as explained below. The second method is much cheaper in time and resources than the first one, however, it needs an extensive database of AIMDEF calculations. In the second case the adiabatic forces are calculated using a NN-PES built using the AIMDEF calculation data. An additional procedure is needed to calculate the friction forces that will be described in Section 2.5.

AIMD calculation of adiabatic forces and Hirshfeld partitioning for density

We demonstrated previously in 2.4.1, that the motion of nuclei can be treated with classical mechanics. Still, to compute equations 2.45 and 2.50, one has to get the adiabatic and non-adiabatic forces that are acting on the ions in the simulation. During AIMDEF the adiabatic forces can be calculated with the help of the Hellmann-Feynman theorem.[152;153] This theorem states that the derivative of the potential

energy with respect to a parameter (here the nucleus position $\mathbf{R}_\alpha$) is equal to the expected value of the derivative of the Hamiltonian with respect to the same parameter:

$$\mathbf{F}_\alpha = -\nabla_{\mathbf{R}_\alpha} V_{\mathrm{e}}(\mathbf{R}) = -\langle \Psi(\mathbf{r},\mathbf{R}) | \nabla_{\mathbf{R}_\alpha} H_{\mathrm{e}}(\mathbf{R}) | \Psi(\mathbf{r},\mathbf{R}) \rangle \,. \tag{2.52}$$

It remains now to calculate the electronic density of the surface atoms, $\rho_{\mathrm{sur}}(\mathbf{r}_i)$, to compute the friction coefficient. During AIMDEF, the total system density is calculated self consistently at each time step. The difficulty remains in extracting from the total electronic density the contribution of the surface atom only. Various methods have been developed in ref.[147] to overcome this problem. In this thesis we used the method based on the Hirshfeld partitioning scheme [154] to evaluate the density of the substrate that a given adsorbate is experiencing. This allows us to take into account the deformation of the surface by calculating on-the-fly the specific electronic density in which each adsorbate is evolving at each time step of the simulation.

The idea is to use the Hirshfeld partitioning scheme [154] in order to subtract the contribution of the gas-phase atoms from the self-consistent density of the whole system $\rho_{\mathrm{sur}}(\mathbf{r}_i)$. More precisely, the bare surface electron density is approximated at each t by

$$\rho^{\mathrm{H}}_{\mathrm{sur}}(\mathbf{r}_i,t) = \rho^{\mathrm{SCF}}(\mathbf{r}_i,t)[1 - \sum_{n=1}^{N_{\mathrm{A}}} w_n(\mathbf{r}_i,t)] \,, \tag{2.53}$$

$$w_n(\mathbf{r}_i,t) = \frac{\rho_n^{\mathrm{atom}}(\mathbf{r}_i,t)}{\sum_{m=1}^{N} \rho_m^{\mathrm{atom}}(\mathbf{r}_i,t)} \,. \tag{2.54}$$

where the indexes m and n run, respectively, over the total numbers of atoms in the system N and in the adsorbate N_{A}. In this equation, the Hirshfeld weighting factor $w_n(\mathbf{r}_i,t)$ represents the contribution of the n^{th} atom to the electron density of the whole system at $\mathbf{r}_i$. Thus the factor $[1 - \sum_{n=1}^{N_{\mathrm{A}}} w_n(\mathbf{r}_i,t)]$ defines the weight corresponding to the system without the contribution of the adsorbate.

NN-PES calculation of adiabatic forces and fit of Hirshfeld partitioned density

After several AIMDEF calculations, we end up with a large number of configurations for which we know the potential energy and the forces on each of the atoms of the system. These data can be fitted with a multidimensional NN to create a PES (details about the NN are given in the Section 2.5). Thus, with a well converged NN-PES we can calculate the energy and, hence, the adiabatic forces acting on the atom simply by providing the coordinates of the atoms in the simulation to our NN-PES.

Furthermore, we need to calculate the surface electronic density to obtain the electronic friction force acting on each adsorbate. In the case of NN-PES we cannot follow the Hirshfeld partitioning scheme described above because we do not have access to the total electronic density of the system since we are not performing any self-consistent DFT calculation. It is desirable that the process of calculation of the electronic density is as fast as the process of calculation of the forces, otherwise it cancels the main purpose of using NN-PES. Thus, as proposed in ref.[155], we used a fit of the surface electronic density that was explored (and stored) during the AIMDEF calculations. First, we write the metal electron density at the position of each adsorbate of the system $\rho(\mathbf{r}_{\mathrm{A}})$ as a sum of the electronic

densities contributed by individual surface atoms at this position

$$\rho^{\mathrm{H}}_{\mathrm{sur}}(\mathbf{r}_{\mathrm{A}}) = \sum_{\mathrm{M}} \rho(|\mathbf{r}_{\mathrm{A}} - \mathbf{r}_{\mathrm{M}}|)\,. \tag{2.55}$$

This allows to create a relation between the metal electronic density at the adsorbate position $\mathbf{r}_{\mathrm{A}}$ and the distance between the adsorbate A and the metal atoms M of total number N_{M}. Then we assume that $\rho(|\mathbf{r}_{\mathrm{A}} - \mathbf{r}_{\mathrm{M}}|)$ can be described by two exponentially decaying functions

$$\rho(\mathbf{r}_{\mathrm{A}}, \mathbf{r}_{\mathrm{M}}) = ae^{(-b|\mathbf{r}_{\mathrm{A}} - \mathbf{r}_{\mathrm{M}}|)} + ce^{(-d|\mathbf{r}_{\mathrm{A}} - \mathbf{r}_{\mathrm{M}}|)}\,, \tag{2.56}$$

The fitting parameters are presented in appendix I

2.5 Neural Network Potential Energy Surface

In the previous section, we mentioned that AIMDEF calculations are very costly in resources and time. In computer simulation for chemical reactions, alternatives have been developed to decrease the amount of time and resource that one needs to perform MD. In the last decade, the use of NN to create a PES by fitting the result of DFT calculations and reach a full multidimensional PES has been popularized. As stated in ref.[156], artificial neurons are born in 1943, proposed by McCulloch and Pitts[157] to be a simple mathematical tool for modeling signal processing in nervous system. Later, in 1958, Rosenblatt connected several artificial neurons organized as an input and output layer to establish the first artificial neural network, called perceptron.[158] Hidden layers were added in this structure by Minsky and Papert[159] in 1969, which significantly improved the capabilities of the NN. Because of the complexity of the system, NNs were not used in chemistry to create PES but for spectra analysis. The use of NNs as PESs (called NN-PES) in chemistry appeared in the middle and late 90's. In this section we will present the general scheme of a NN-PES. Next, we will present the atomistic-NN proposed by Behler and Parinello,[160] and finish the section with the presentation of EANN proposed by the group of B. Jiang.[10]

2.5.1 General structure of neural networks

One of the most popular approach to construct a PES based on NN is the feed-forward NN. It consists in artificial neurons, also called nodes, which are arranged in layers as shown in Fig. 2.3. The first layer is the input layer, the last one is the output layer, and all layers in between those two are called hidden layers. The number of layers and nodes per layer defines the analytic form of the NN, by constructing a relation between the input vector $\mathbf{G} = \{G_i\}$ and the output value of energy E. As the number of nodes and layers of the NN are increased, we increase its flexibility and capability to represent a complex system. However, we will see later that this number of nodes has a limit and drawbacks that one has to balance by making good compromises. Each node is connected to those of the previous and next layers by weights, *e.g.*, weight $a^{j-1\,j}_{ki}$ is connecting node k in layer $j-1$ with node i in layer j. With N_{j-1} the number of nodes in the preceding layer, the numerical value of a node i in layer j, y^j_i, is then

calculated from the values of the nodes y_k^{j-1} in the previous layer $j-1$ according to

$$y_i^j = f_i^j(x_i^j) = f_i^j(b_i^j + \sum_{k=1}^{N_{j-1}} a_{k,i}^{j-1,j} y_k^{j-1}), \tag{2.57}$$

with f_i^j being the activation function described later. Note that the node is also connected to a bias node by a bias weight b_i^j, see Fig. 2.3. The bias node has a constant value of one, and the bias weight can be further used as an adjustable offset to shift the input of the node. Following eq.(2.57), the NN could be expressed as simple linear combination, however it would not reflect the topology of the PES. Therefore, the activation function is a non-linear function that provides the capability to the NN to fit arbitrary functions. It is usually a non-linear function asymptotically converging to small numbers for very positive and very negative input values (*e.g.* sigmoidal function). Some of these activation functions are represented in Fig. 2.4.

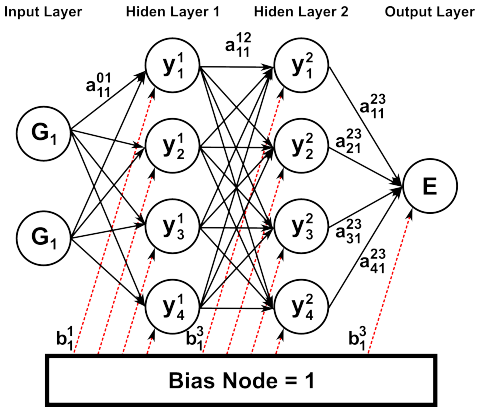

Figure 2.3: Schematic structure of a feed-forward NN. The nodes are arranged in layers and the goal is to establish a functional relation between the energy output E and the structure described by a vector of input coordinate.

The activation function to the output layer is linear to avoid any restriction in the range of the NN energy value output. Note that if only linear activation functions were used for hidden layers, then one layer will have the same effect as various layers, since the result of eq.(2.57) would be a linear combination of x_i^j which are also linear combinations. The weight a_{ki}^{j-1j} are optimized using a training set and an algorithm to give the best fit as output value. Typically they are initialized with random numbers, then, they are optimized iteratively to minimize the error of a set of N_{struct} known energies. This optimization is called training in the NN community, and an iteration is called epoch. The fitting process corresponds to the minimization of an error function, *e.g.*, root mean square error

$$\text{RMSE} = \sqrt{\frac{1}{N_{\text{struct}}} \sum_{i=1}^{N_{\text{struct}}} (E_{i,\text{ref}} - E_{i,\text{NN}})^2}, \tag{2.58}$$

with reference energies $E_{i,\text{ref}}$ that are the target energies of a set of atomic configurations, which have been obtained in electronic structure calculations, and $E_{i,\text{NN}}$ the energies evaluated with NN-PES. A wide range of optimization algorithms can be used to determine the set of weights minimizing this function. In the case of NNs, in particular, the backpropagation algorithm,[161] the limited-memory

BFGS method,[162] or the Levenberg Marquardt algorithm[163] are frequently used. As a general scheme for the training, we first give an input value from DFT calculation, next the optimization algorithm minimizes the output error regarding to the input value by changing the weight coefficients, and repeat the process iteratively for all the values of the training set. Thus, the error is minimized for all input parameters of the training set. Afterwards, a test set is given to the NN to verify the total error with data not used in the training procedure. The test set must be different to the training set, therefore one can compare the resulting error between training and testing data. One can compare the root mean square error and maximum error obtained with the training and test sets to check the validity of the NN-PES.

NN can be summarized as automated multidimensional fitting, being a "black box" to which we give an input value and it gives back an output value. Although it is possible to extract the exact analytical equation from the weight coefficients, an important drawback of the NN-PES is that the fundamental form of the NN is not physically motivated. Note that due to its "non-physical" form, the NN gives poor results for extrapolation, and it may only be used confidently in the range of the trained configurational space.

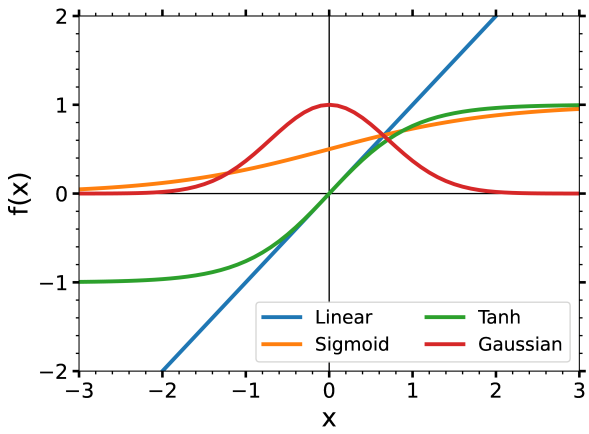

Figure 2.4: Typical activation functions used in feed-forward NNs.

The architecture of the NN is given in terms of the number of nodes and activation function. Thus, the name of the NN in Fig. 2.3 considering the hyperbolic tangent (labeled t) as activation function is 3-5-5-1 ttl, with l being the label for the linear activation function. The structure of the NN is of great importance because if too many nodes are given, the NN will be too flexible and it might give rise to spurious features in the PES. If there are too few, the fit cannot represent the PES corrugation. One has to test the different NN architectures and select the best architecture that provides a good compromise between errors and computational cost.

In practice, to use a NN-PES, one provides as input the position of the ions in the simulation cell and their species, then gets as an output the total energy of the system. However, this gives rise to three major drawbacks. First, by increasing the number of atoms in the simulation cell, we increase the number of inputs, and with more inputs, we decrease the efficiency of the NN. Second, the positional coordinates do not allow to reuse a trained NN for a system containing the same type but different amount of atoms. The problem is that there is an input node for each atom, thus if we change the

number of atom, the we must change the number of input node, thus change the structure of the NN. Third, positional coordinates are not symmetry invariant. This prohibits to substitute two atoms of the same species in the inputs, as this input node has been trained for this particular atom, and not atom type. This makes the NN unique for one system, which reduces greatly its uses. The solution is to use as input, not the position coordinates, but some symmetry functions that are invariant to changes like rotation and translation. Thus, the system is defined in a more general way. In the following we will present the atomistic-NN[156] and EANN[10] which are two ways of construct a NN-PES but with different manners to decompose the system in symmetry functions.

2.5.2 Atomistic neural networks

In the first NN-PESs that were developed, when we exchanged the position of two atoms of the same species, we changed the input coordinate vector, which changed the output energy. This is the problem of invariance.[156] To solve this problem, it has been first proposed to train the NN with a replicated training set to include all possible representations of the system.[164;165] However, this method is very resources consuming, especially for large systems. We also already mentioned that if we change the nature of one ion from the input data, we must retrain the whole NN. This specificity problem and the fact of not being symmetry invariant are both great inconveniences. A solution has been presented with the ANN.[98] The problem of being not symmetric invariant is solved by replacing the NN representing the total energy by a set of atomistic-NNs.[160;166] Thus, every NN provides the contribution E_i of an atom i to the total energy of the system such as:

$$E = \sum_i E_i \,. \tag{2.59}$$

The E_i depends on the chemical environment of the atom, which is defined by the positions of all neighbors inside a sphere of cutoff radius R_c. Therefore, for each different chemical species, an atomistic-NN is trained. To do so, the position vector $\mathbf{R}_i = (X_i, Y_i, Z_i)$ of an atom is processed by several symmetry functions $\mathbf{G}_{i,j}$ into suitable input coordinates. The index $j = 1..,M_i$ stands for the name of the symmetry functions that will be presented later. Therefore, by decomposing $\mathbf{R}_i$ in such a way, the energy only depends on the environment of the atom and no more on the position coordinates. Then, the output of $\mathbf{R}_i$ processed by $\mathbf{G}_{i,j}$ is used as input into a neural network, as shown in Fig. 2.3. The symmetry functions represent structural fingerprints of the atoms. These fingerprints are later used in the high-dimensional neural network potential to compute the energy of an atom depending on its environment. This atomistic-NN can be associated to a lower-dimensional PES. Now, to compute the energy of a system, one simply has to give the position coordinate of an atom to its specific at-NN. Then, its coordinates are decomposed by the symmetry functions and input into the atomistic-NN that outputs an energy, and the sum of the energy of all atoms that compose the system gives the total energy. This scheme is shown in Fig. 2.5.

The symmetry functions are the core of the new method to create a NN-PES. Here we describe these functions and their prerequisites in the case of atomistic-NN.

They first have to be suitable for giving a correct description of the symmetry of the PES. Then, they must respect two mathematical properties: continuity and derivability in analytical form, since

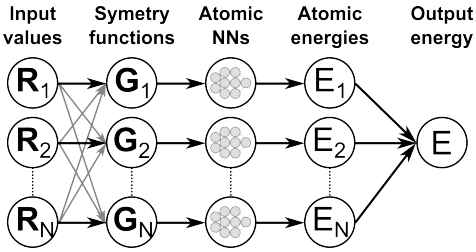

Figure 2.5: Example of high-dimensional NNP for a four-atom system. Each line represents one atom i. Starting from the Cartesian coordinate vector $\mathbf{R}_i$ first a transformation to a symmetry function vector $\mathbf{G_i}$ is performed. This represents the input for the atomic NN yielding E_i. Finally ,all atomic energies are added to obtain the (short-range) energy E.

they are later used to calculate atomic forces. Finally, it is numerically advantageous that for large interatomic distances the symmetry functions decay to zero. The general idea of the symmetry function is to decompose the environment of an atom comprised in a cutoff sphere $f_c(R_{ij})$ of a cutoff radius R_{ij} by constructing a many-body symmetry function which simultaneously depends on the positions of all atoms inside the cutoff sphere. The cutoff function is of the form:

$$f_c(\mathbf{R}_{ij}) = \begin{cases} 0.5\left[\cos(\frac{\pi \mathbf{R}_{ij}}{R_c}) + 1\right] & \text{for } \mathbf{R}_{ij} \leq R_c \\ 0 & \text{for } \mathbf{R}_{ij} > R_c \end{cases}, \tag{2.60}$$

with $\mathbf{R}_{ij}$ the distance between atom i and j. If $\mathbf{R}_{ij} > R_c$, then $f_c(\mathbf{R}_{ij}) = 0$, which implies discontinuity in the second derivative. This problem becomes very minor in MD if we select a cutoff radius large enough. To ensure that no atom outside the cutoff sphere is taken into account in the symmetry function, the latter is multiplied by one or multiple cutoff functions. For the sake of clarity, the followings many-body functions will be called instead: radial and angular functions. Radial functions are constructed as sums of two-body terms, while angular functions contains an additional term as the sums of three-body terms. Behler and Parinello proposed three radial symmetry functions for describing the radial environment of an atom i:

$$G_i^1 = \sum_j f_c(\mathbf{R}_{ij}), \tag{2.61}$$

$$G_i^2 = \sum_j e^{-\eta\left(\mathbf{R}_{ij} - R_s\right)^2} f_c(\mathbf{R}_{ij}), \tag{2.62}$$

$$G_i^3 = \sum_j \cos(\kappa \mathbf{R}_{ij}) f_c(\mathbf{R}_{ij}). \tag{2.63}$$

Function G^1 is the sum of the cutoff functions with respect to all neighboring atoms j. Function G^2 is a sum of Gaussian functions multiplied by a cutoff function. The parameters η and R_s control respectively the width and the center of the Gaussian functions. One can shift the center of G^2 to describe a spherical shell around the reference atom. For small values of η and considering $R_s = 0$, G^2 is reduced to the function G^1. Finally, the radial function G^3 represents damped cosine functions where κ allows to adjust the period length. Therefore, the description of radial distribution of neighbors can be described well by: G^1 functions with different cutoff radii, G^2 functions with different cutoff and/or

η parameters, and, G^3 functions with different values of κ. However, due to the positive and negative oscillation of the values of G^3, some neighbors can be canceled, thus, the advice in ref.[98] is to use this function in combination with the other. Additionally, two types of angular functions are proposed. They are summations of cosine functions of the angles $\theta_{ijk} = \text{acos}(\mathbf{R}_{ij}\mathbf{R}_{ik}/R_{ij}R_{ik})$ centered at atom i. They are defined as

$$G_i^4 = 2^{1-\xi} \sum_{j,k\neq i}^{all} \left(1+\lambda\cos\theta_{ijk}\right)^{\xi} e^{-\eta(\mathbf{R}_{ij}^2+\mathbf{R}_{ik}^2+\mathbf{R}_{jk}^2)} f_c(\mathbf{R}_{ij}) f_c(\mathbf{R}_{ik}) f_c(\mathbf{R}_{jk}), \tag{2.64}$$

$$G_i^5 = 2^{1-\xi} \sum_{j,k\neq i}^{all} \left(1+\lambda\cos\theta_{ijk}\right)^{\xi} e^{-\eta(\mathbf{R}_{ij}^2+\mathbf{R}_{ik}^2)} f_c(\mathbf{R}_{ij}) f_c(\mathbf{R}_{ik})). \tag{2.65}$$

Both functions are similar, they only differ on their angular part. The parameter λ can have the value +1 or -1 shifting the maxima of the cosine function to $\theta_{ijk} = 0^\circ$ or $\theta_{ijk} = 180^\circ$. To give a reference of the number of symmetry function used in the NN-PES, they mention in ref.[98] that for a single chemical element about 50 functions were used. This covers more than the useful degrees of freedom of the element, however, it ensures that the interactions are well represented. Such amount of symmetry functions are well managed by the NN.

2.5.3 Embedded atom neural networks

In 2019, Bin Jiang and coworkers proposed a new framework for NN named EANN,[10] which is based on the EAM,[167;168] explained in the following. This NN is also an atomistic-NN, but it uses different symmetry functions to describe the system. The proposed functions follow the ideas behind the quasi-atom theory[169], which assumes that the embedding energy of an impurity in a host is a functional of the electron density of the unperturbed host without impurity,*i.e.*, $E_i = \mathcal{F}|\rho(\mathbf{r})|$. Note that the density-functional $\mathcal{F}$ is unknown and non-trivial. Secondly, if one assumes that the impurity feels a locally uniform electron density,[169] the embedding energy can be approximated as a function of the scalar local electron density at the impurity site, to which we sum up an electrostatic interaction. The EAM considers all atoms in the system as impurities embedded in the electron gas created by other atoms so that the total energy of an N atom system is simply the sum over all individual impurity energies, written as

$$E = \sum_{i=1}^{N} E_i = \sum_{i=1}^{N} [F_i(\rho_i) + \frac{1}{2}\sum_{j\neq i}\phi_{ij}(\mathbf{R}_{ij})], \tag{2.66}$$

F_i and ρ_i are respectively, the embedding function and the embedded electron density at the position of atom i given by the superposition of the densities of surrounding atoms. In this approximation, the embedding function F_i, is the energy to embed an atom of type i into the background electron density at site i, ρ_i is a pair interaction between atoms i and j whose separation is given by $\mathbf{R}_{ij}$. ϕ_{ij} is the short-range repulsive potential between atoms i and j depending on their distance $\mathbf{R}_{ij} = |\mathbf{R}_i - \mathbf{R}_j|$. The Cartesian position vectors of atoms i and j are defined as: $\mathbf{R}_i = (x_i, y_i, z_i)$ and $\mathbf{R}_j = (x_j, y_j, z_j)$. EAM has a limited accuracy because the exact form of the function F_i is unknown, and therefore has to be approximated with experimental or computed values. In the EANN, in order to improve the

EAM expression of the embedded density, the embedding background density is expressed in term of Gaussian-type orbitals (GTOs)s[170] centered at each atom, *i.e.*,

$$\varphi^{\alpha,r_s}_{l_x l_y l_z}(\mathbf{R}_i - \mathbf{R}_j) = e^{-\alpha|\mathbf{R}_{ij}-r_s|^2}\left[(x_i - x_j)^{l_x}(y_i - y_j)^{l_y}(z_i - z_j)^{l_z}\right]. \tag{2.67}$$

The width and the center of the Gaussian-like term are respectively α and r_s. Then, l_x, l_y, and l_z are the values of the orbital angular momentum in each coordinate, and their sum is equal to the total angular momentum L, *i.e.*, $L = 0, 1$, and 2 correspond to s, p, and d orbitals. The individual electron density contribution with equivalent L, α and r_s are evaluated as follows:

$$\rho^i_{L,\alpha,r_s} = \sum_{l_x,l_y,l_z}^{l_x+l_y+l_z=L} \frac{L!}{l_x!l_y!l_z!}\left(\sum_{j=1}^{n_a} f_c(\mathbf{R}_{ij}) c_j \varphi^{\alpha,r_s}_{l_x l_y l_z}(\mathbf{R}_i - \mathbf{R}_j)\right)^2. \tag{2.68}$$

There are n_a atoms j located within a radius r_c from the embedded atom i. $f_c(\mathbf{R}_{ij})$ is the cutoff function as defined in the precedent section, and c_j is the expansion coefficient of an orbital of the atom j. It is worth to mention that the elements and orbital-dependent weights[171] are adjusted during the NN_i training. Next, the embedding function F is replaced by an atomistic-NN. Since the core-core repulsion $\phi_{ij}(\mathbf{R}_{ij})$ also depends on the internuclear distance $\mathbf{R}_{ij}$, this contribution is automatically incorporated in the NN and requires no extra terms. Thus, eq.(2.66) can be rewritten as

$$E(\{\mathbf{R}_k\}) = \sum_{i=1}^{N} E_i(\{\mathbf{R}_k\}) = \sum_{i=1}^{N} NN_i(\rho^i), \tag{2.69}$$

NN_i is the atomistic-NN depending on the chemical species of the i^{th} atom in the system, ρ^i is the orbital-dependent density components defined in eq.(2.68). As said previously, ρ^i can be assimilated to a set of local atomic density descriptors as introduced by ref.[160]. As a result, the EANN method overcomes the intrinsic approximation on the uniform density and pairwise superposition of scalar density contributions in the EAM. The new architecture of the NN is illustrated in Fig. 2.6.

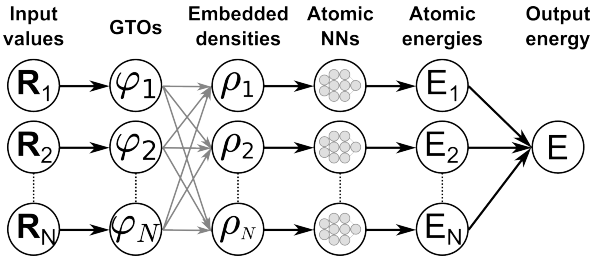

Figure 2.6: Schematic architecture of the embedded atom neural network.

2.6 Miscellaneous methods

In this final section, we describe the Nudged Elastic Band (NEB) method and DOS calculation that we used to analyze diverse adsorption properties of the systems studied in this thesis.

2.6.1 Nudged Elastic Band method

In this thesis, we performed an analysis of the PES by looking for stable adsorption states and minimum energy paths of reaction. The first ones are found by minimization of the forces applied to the system, while the latter are obtained by the NEB method. The NEB [172] method consists in finding the saddle points and MEP between two previously known reactants and product. It works by optimizing a number of intermediate images along a guessed reaction path. Since the reaction path is unknown, we have to propose one, relaying on energetic (diffusion energy, energy barrier...) and physical (bond size, atomic distances...) criteria. In many cases, the coordinates of the atoms in the new images are calculated by linear interpolation between the initial and final reaction state. However, sometimes this interpolation has to be corrected due to periodic boundary conditions or unphysical atomic distances. It has been inspired by London-Eyring-Polanyi-Sato (LEPS) potential model, which mimics the reaction involving three atoms confined to motion along a line. The force acting on image i is represented as:

$$\mathbf{F}_i = -\vec{\nabla} V(\mathbf{R}_i) + \mathbf{F}_i^{\mathrm{s}}\,, \tag{2.70}$$

$$\mathbf{F}_i^{\mathrm{s}} \equiv k_{i+1}(\mathbf{R}_{i+1} - \mathbf{R}_i) - k_i(\mathbf{R}_i - \mathbf{R}_{i-1})\,, \tag{2.71}$$

where $\mathbf{F}_i^{\mathrm{s}}$ is the spring force and k_i the spring constant. Each image finds the lowest energy possible while maintaining equal spacing to neighboring images using the spring force. However, if the force constant k and the number of images are not well tuned, the calculation may converge to a path which either misses the saddle point, or avoids the barrier region and thus diminish the resolution in the critical region. To solve both problems NEB uses the projection of the perpendicular component of the spring force and the parallel component of the true force. Forces thus become:

$$\mathbf{F}_i = -\vec{\nabla} V(\mathbf{R}_i)|_{\perp} + (\mathbf{F}_i^{\mathrm{s}} \cdot \hat{\tau}_{\parallel})\hat{\tau}_{\parallel}\,, \tag{2.72}$$

where $\hat{\tau}_{\parallel}$ is the unit tangent to the path and $\vec{\nabla} V(\mathbf{R}_i)|_{\perp} = \vec{\nabla} V(\mathbf{R})_i - (\vec{\nabla} V(\mathbf{R})_i \cdot \hat{\tau}_{\parallel})\hat{\tau}_{\parallel}$. These projections of the perpendicular and parallel components of the spring force are referred as "nudging". The spring force then does not interfere with the relaxation of the images perpendicular to the path and the relaxed configuration of the images satisfies $\vec{\nabla} V(\mathbf{R}_i)|_{\perp} = 0$, *i.e.*, they lie on the MEP. However, in some occasions like in covalent bond formation or breaking, a problem arises. During such or equivalent events, a rapid change of the energy along the path is observed, while the restoring force on the images perpendicular to the path remains weak. Then, the convergence of the minimization slows down, and the estimation of the local tangent can become problematic. To solve this issue, a smooth switching function is introduced to gradually turn on the perpendicular component of the spring force where the path becomes distorted:

$$\mathbf{F}_i^{\mathrm{NEB}} = \mathbf{F}_i^0 + f(\phi_i)(\mathbf{F}_i^{\mathrm{s}} - (\mathbf{F}_i^{\mathrm{s}} \cdot \hat{\tau}_{\parallel})\hat{\tau}_{\parallel})\,, \tag{2.73}$$

$$f(\phi) = \frac{1 + \cos(\pi(\cos(\phi)))}{2}\,. \tag{2.74}$$

The CI-NEB [8;9] method is a modification of the traditional NEB method. In the latter, one has to interpolate the energies to get the transition state energy. With CI-NEB, one has directly the transition

state image converged. To get so, after few iterations of the regular NEB, the image with the highest energy $i_{\max}$ is identified. Then, the forces on this image are not given by eq.(2.72) but rather by:

$$\mathbf{F}_{i_{\max}} = -\vec{\nabla}V(\mathbf{R}_{i_{\max}}) + 2(\vec{\nabla}V(\mathbf{R}_{i_{\max}}) \cdot \hat{\tau}_{\| i_{\max}})\hat{\tau}_{\| i_{\max}} \,. \tag{2.75}$$

Since the image with the highest energy does not feel anymore the spring force constant and is moved to the saddle point, the spacing between images will be different. This image will climb the potential energy surface along the elastic band, and descend the potential energy surface perpendicular to the band. As well as the CI-NEB method converges, the climbing image is a saddle point.[173] In some cases, it is possible to use variable spring constants to reduce the number of iterations before convergence.[8] In this thesis, in order to find some transition state, we had to use this feature.

2.6.2 Calculation of Density of States

In this thesis, we also computed the DOS of the system under study in order to have further information on the possible hybridization between the substrate and the adsorbates electronic states. The DOS is defined as the number of states that are within the energy range ε and $\varepsilon + d\varepsilon$. The equation in terms of energy is written as[110]

$$\rho(\varepsilon) = \frac{1}{N_{\mathbf{k}}} \sum_{n,\mathbf{k}} \delta(\varepsilon_{n,\mathbf{k}} - \varepsilon) \,, \tag{2.76}$$

where, for independent particle states, $\rho(\varepsilon)$ is the number of independent particle states per unit energy, $\varepsilon_{n,\mathbf{k}}$ is the energy of the electronic $(n,\mathbf{k})$ state, $\mathbf{k}$ is the k-points in the full Brillouin's zone, $N_{\mathbf{k}}$ is the amount of k-points in the full Brillouin's zone and n is the band index. To get a more precise information, one can project the DOS onto an atomic orbital of one or various species of the system to get its contribution on the total DOS. In this thesis, we have calculated the atom-projected DOS as implemented in VASP. In particular, the DOS is projected on spherical harmonics centered in the ion, *i.e.*,

$$\rho_{\alpha,l}(\varepsilon) = \frac{1}{N_{\mathbf{k}}} \sum_{n,\mathbf{k}} f_{n,\mathbf{k}} \sum_{m=-l}^{l} |\langle Y_{l,m}^{\alpha} | \phi_{n,\mathbf{k}}^{\mathrm{KS}} \rangle|^2 \delta(\varepsilon_{n,\mathbf{k}} - \varepsilon) \,, \tag{2.77}$$

where $\phi_{n,\mathbf{k}}^{\mathrm{KS}}$ are the Kohn-Sham orbital of the occupied states, $Y_{l,m}^{\alpha}$ are the spherical harmonics that are non zero within a sphere centered at ion α and $f_{n,\mathbf{k}}$ is the Kohn-Sham occupation number.

2.6.3 Calculation of Bader charge

Another useful property to characterize the binding character of a chemical system is the charge transfer analysis. Richard Bader proposed a method, called Quantum Theory of Atoms in Molecules[174], to divide a system composed of several atoms depending on the electronic charge density. This separation is based on the zero flux surfaces. At the minimums of charge density in a 2D space, we separate the particles. For molecular systems, the charge density is minimum between the atoms. Then it is reasonable to separate the atoms at this point. Moreover, the charge enclosed in Bader volume is a

good approximation of the total electronic charge of an atom. Later in this thesis we will discuss the identification of chemisorbed and physisorbed molecular states using charge transfer analysis. For this, we performed a Bader charge analysis[175] of the different relevant states, using the implementation provided by the Henkelman's group.[176;177;178] From the Bader charge, the charge state of each atom is next calculated as follows:

$$Q = Z - Q_{\mathrm{BC}}\,, \tag{2.78}$$

where Z and Q_{BC} are the atomic number and Bader charge of the considered atom. Note that in using eq.(3.3), negative (positive) values of Q indicate that the atom has captured (lost) $|Q|$ electrons.

2.6.4 Simulation of X-ray absorption spectra

The O K-edge X-ray absorption spectra shown in Chapter 4 have been calculated in collaboration with Prof. P. Saalfrank's group as follows.

For O K-edge X-ray absorption spectra, a transition state potential method in combination with a Delta-Kohn-Sham method has been applied. All calculations are performed with the GPAW program[179], a real-space grid density functional theory program that uses the projector augmented wave (PAW) approach[180]. For each calculation, the initial unit cell was duplicated along the shortest axis, mainly to avoid core-hole/core-hole interactions and the three lowest Ru-layers have been removed from the snapshots. Further, a grid spacing of 0.2Å and the PBE (Perdew-Burke-Ernzerhof)[117;181] exchange-correlation functional have been used. Choosing PBE offers a slight computational performance advantage compared to a non-local van der Waals functional, while the choice of the exchange-correlation functional mainly affects the absolute position of the overall spectrum (we expect by less than 5 eV for the O K-edge). The shape and relative positions of the resonances are less affected (see, for example[182]). All calculations are done at the Γ-point and in a spin polarized fashion to account for an unequal number of spin-up and spin-down electrons during the simulation procedure (see below). To obtain the total absorption cross section, $\sigma_T(\omega, t_n)$, at a single timestep t_n, the following calculations have been done:

1. Ground state calculation, to obtain the electronic ground state energy, E_{gs}.

2. For each excitation center i (unique oxygen atoms in the system), a transition potential calculation is performed. This method utilizes an artificial auxiliary state, where the core-orbital (here oxygen 1s) at a single excitation center is occupied by half an electron. The core orbital occupation number is set by using a pre-generated PAW potential. After the transition potential state is found variationally, the contribution of the i-th excitation center is given by a Fermi's Golden Rule expression:

$$\sigma^i(\omega, t_n) = C\omega \sum_f \sum_{s=x,y,z} \left|\langle \psi_i \mid s \mid \psi_f \rangle\right|^2 \delta(\varepsilon_f - \varepsilon_i - \hbar\omega) \qquad , \tag{2.79}$$

   where C is a constant, $\hbar\omega$ the excitation energy, ψ_i is the initial state (O 1s orbital) at the excitation center "i". ψ_f represents all possible final states (unoccupied bands). ε_i and ε_f

correspond to the orbital (band) energies. $\langle \psi_i \mid s \mid \psi_f \rangle$ are transition dipole matrix elements ($s = x, y, z$). To account for finite experimental resolution, the δ-functions are replaced by Gaussian functions with a full-width at half maximum of 0.5 eV.

3. For each excitation center i, an additional full core-hole calculation is done by using a pre-generated PAW potential. Further, an additional electron is added at the Fermi level. The resulting electronic energy, E^i_{ce} is used to calculate the first core excitation energy:

$$\Delta_i = E^i_{ce} - E_{gs} \quad . \tag{2.80}$$

The spectrum is then shifted such that the first peak coincides with Δ_i.

4. To obtain the total X-ray absorption cross section, we sum over all individual contributions, *i.e.*, all excitation centers:

$$\sigma_T(\omega) = \sum_i \sigma^i(\omega) \, . \tag{2.81}$$

The atom-resolved spectra are obtained by plotting each individual contribution $\sigma^i(\omega, t_n)$ together with the total spectrum $\sigma_T(\omega, t_n)$.

Finally, the time-averaged total spectra shown in Figs. 4.2(a)-(c) as black dashed lines are calculated as:

$$\langle \sigma_T(\omega) \rangle = \sum_i \langle \sigma^i(\omega) \rangle \, , \tag{2.82}$$

where $\langle \sigma^i(\omega) \rangle$ is the time-averaged contribution of atom i (colored curves in Figs. 4.2(a)-(c)), *i.e.*,

$$\langle \sigma^i(\omega) \rangle = \frac{1}{N} \sum_n \sigma^i(\omega, t_n) \, , \tag{2.83}$$

with N the number of time steps included in the n-summation, *i.e.*, in the time interval of interest.

CHAPTER 3

COADSORPTION AND REACTIVITY OF O AND CO ON RU(0001): STATIC ANALYSIS

"Science is not about why, it's about why not !"

— Cave Johnson, Portal 2.[1]

One of the different purposes of this thesis is to simulate the process of desorption and oxidation of carbon monoxide over a ruthenium metallic surface induced by femtosecond laser pulses. However, prior to the dynamic studies that we present in Chapters 4 and 5, we must understand the characteristics of our system from a static point of view. Since we are performing DFT calculations, the first step is to select an exchange-correlation functional which accurately represents the interactions of the system, without requiring excessive calculation time and computational resources. Therefore, in this chapter we will start by presenting how we selected one *xc*-functional according to the quality of its description of the ruthenium bulk and the Ru(0001) slab (Section 3.1). We also verify that the description of the desorption of carbon monoxide is well represented with this selected *xc*-functional.

Subsequently, we present in Section 3.2 the protocol used to find the intermediate states of the reaction, which are essential in the oxidative desorption process of carbon monoxide. Afterwards, we present the core of this chapter in Section 3.3, the static study of the different coverages that we simulate. For each of the four studied coverages, we present a complete study of the lowest energy adsorption state, the potential energy curve for desorbing one CO from the surface and the MEP for CO oxidation. In the last Section 3.4 of this chapter, we present two complementary studies to characterize the states involved in the MEP, the Bader charge analysis in Section 3.4.1 and the analysis of the Projected Density Of State (PDOS) on the atoms composing the CO_2 molecule, which is performed for each relevant step along the CO oxidation reaction. Finally, by making use of the previously calculated PDOS, in Section 3.4.2, we calculate the partial charge densities of these atoms to identify and analyze the MOs of CO_2 molecule at different steps along the CO oxidation process.

3.1 Selecting the exchange correlation functional

The first step when using DFT is to choose the adequate *xc*-functional. Thus, we selected four different *xc*-functionals to find which is the best one to describe the properties of our system. The four *xc*-

[1] *"En science la bonne question n'est pas pourquoi, mais pourquoi pas !"* —Cave Johnson, Portal 2.

functionals selected are: the semi-local PBE[181] and RPBE[183] functionals, that are based on the GGA; the RPBE together with the DFT-D3(BJ) dispersion correction by Grimme with the Becke-Johnson damping[118;184]; and the vdW-DF functional proposed by Dion et al.[119] that naturally includes the vdW interaction.

3.1.1 Analysis of bulk ruthenium

We evaluate for each chosen *xc*-functional how it describes the properties of the ruthenium bulk, as well as the properties of a ruthenium slab in our chosen supercell.

	a	c	c/a
Experimental (ref.[99])	2.70	4.28	1.59
Experimental (ref.[185])	2.75	4.31	1.57
RPBE 4l(5x5) (ref.[87])	2.74	4.33	1.58
PBE 4l(2x2) (ref.[86])	2.72	4.31	1.58
PBE	2.72	4.29	1.57
RPBE	2.73	4.14	1.58
DFT-D3(BJ)	2.62	4.32	1.57
vdW-DF	2.75	4.27	1.57

Table 3.1: Lattice constants of ruthenium bulk from experimental measurements and theoretical calculations. The first four rows correspond to values from literature with the two first ones being experimental values, and the two last ones theoretical values. The values from our calculations with different *xc*-functionals are presented n the last four rows.

Therefore, the first step consists in calculating the lattice parameters of the ruthenium bulk with each selected functional. The ruthenium metal has a hcp structure with lattice parameters $a = b \neq c$.[99] We found in literature various values of the lattice parameters both from experiments[99;185], and theory.[86;87] These values are summarized in the top part of Table 3.1. We observe that in all cases, the ratio c/a is in the range 1.57-1.59. To find the a and c values of the equilibrium configuration of the bulk for each *xc*-functional, we first calculate the potential energy of the bulk with the given functional for these parameters. More precisely, we vary the ratio c/a in the range 1.45-1.70 with a step of 0.05, and the lattice parameter a from 2.5 to 2.9 Å with a step of 0.1 Å. Each calculation gives us a DFT potential energy, that all together form the 2D PES describing the variation of the potential energy with respect to the lattice parameters (a and c). The result of these calculations for the four selected *xc*-functionals is presented in Figure 3.1. The white rectangle in each graphic represents the minimum energy value. The exact values of the lattice parameters corresponding to the white rectangle are given in Table 3.1. The results obtained for the lattice parameters with the different functionals are in good agreement with experiments, exceptions are the value of a in the case of the DFT-D3 (BJ) functional and the value of c in the case of the RPBE that differ in more than 0.1 Å.

The pristine Ru(0001) surface is modeled using a periodic five-layer slab defined by a (4x2) surface unit cell. Next, we determine the z distance of the supercell, in order to leave enough vacuum such that the slab and its top replication (due to periodic boundaries conditions (PBC)) do not interact. Note that we also include enough space to assure that a molecule in the center of the vacuum does not interact with either the surface or the bottom layer of the periodic slab. However, we cannot use a

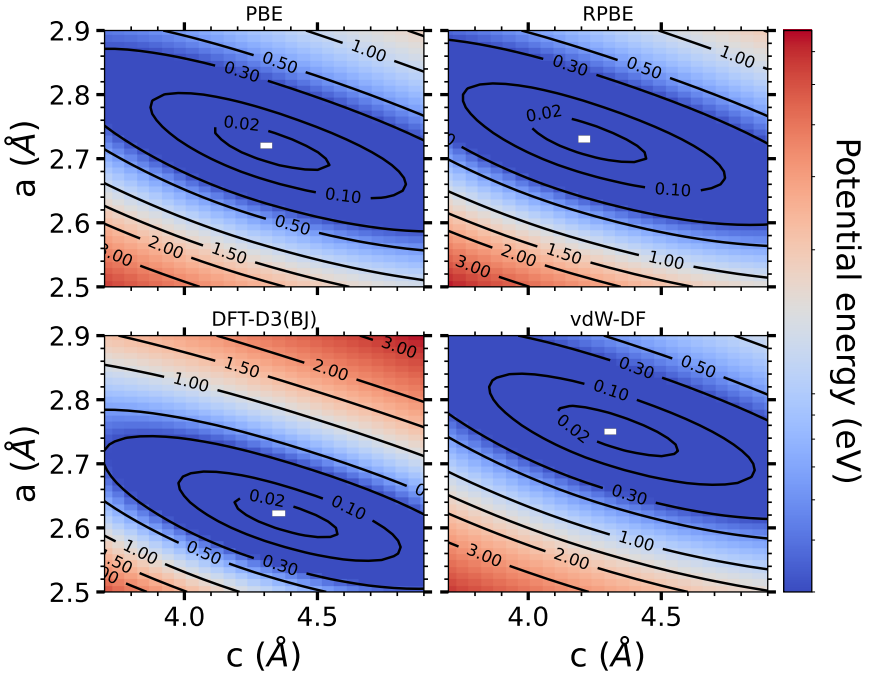

Figure 3.1: Potential energy per unit cell of bulk Ruthenium as a function of the parameters a and c for the selected four different *xc*-functionals. The zero of energy is taken at the equilibrium configuration. Black lines are isovalues of the potential energy. The white rectangle is the minimum value of the potential energy.

too large distance between slabs because the calculation time and resources would increase too much. Therefore, we must find a compromise between resources consumption and accuracy, thus we create two supercells. For one of it we leave the equivalent of 9 layers of ruthenium as vacuum, while for the other system we leave the equivalent of 11 layers of ruthenium as vacuum. Both supercells are shown in Figure 3.2. Then we calculate the potential energy of both systems, and their calculation cost in memory and time. Because the two systems have the same amount and type of atoms, we can directly compare the energy outputs by DFT calculations. We observe that the difference in energy between the two systems is 1.9 meV. Regarding the time of calculation and memory used, the larger system is slower, and uses 10% more memory to converge to the lowest energy configuration. Taking into account the very small variation of energy between both system, we chose to use the smaller supercell to save computing resources, specifically thinking on the AIMDEF simulations that we have planned.

3.1.2 Analysis of Ru(0001) and CO adsorption

Before performing the calculations of relaxation of the forces to find the minimum energy configuration or performing MD, we have tested the performance of the four selected *xc*-functionals to select only the one which describes the best the properties of the system (*i.e.* inter-atomic distances, adsorption energy...) to perform further calculations. As a first examination, we evaluate the obtained interlayer distances between the topmost and second layers, and between the second and third layers, upon relaxation of the Ru(0001) surface. In Table 3.2 we show the values obtained with each functional, together with the relative error (given as a percentage) in relation to the experimental values.[20] In general, the performance of the functionals is very good, with errors well below 2% for the distance

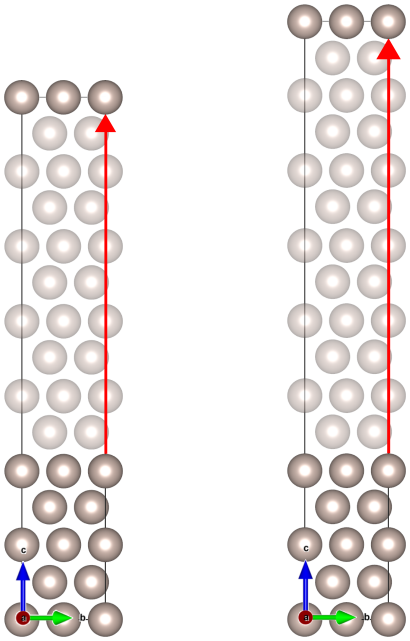

Figure 3.2: Supercell representation with the total size along the $\vec{c}$ coordinate of 14 or 16 layers of ruthenium atoms respectively left and right panel. Brown balls represents ruthenium atoms. Transparent ruthenium atoms represent the number of layer left empty for vacuum space. On the left (right) panel, 9 (11) layers have been left empty, corresponding to 19 Å (23 Å) of vacuum, represented by the red arrow.

between the topmost and second layer, and below 3% for the distance between the second and third layers. Regarding these surface properties, the best agreement with the experiment is obtained with the PBE functional and the largest errors with DFT-D3(BJ).

Functional	$D1$	$D2$
PBE	2.063 (0.10%)	2.157 (0.79%)
RPBE	2.073 (0.39%)	2.168 (1.31%)
vdW-DF	2.089 (1.16%)	2.185 (2.10%)
DFT-D3(BJ)	2.036 (1.40%)	2.083 (2.66%)

Table 3.2: Ru(0001) interlayer distances calculated with different functionals. The experimental interlayer distance between the outermost and second layer is $D1$=2.065±0.02 Å; between the second and third layer, $D2$=2.140±0.025 Å; and the bulk value D_{bulk}=2.141 Å.[20] The errors (given as a percentage) with respect to the experimental values are written in parentheses.

However, describing accurately the interaction between CO and the Ru(0001) surface is very important in our study. For this reason, for each *xc*-functional we computed the binding energy of CO molecule with the ruthenium bare surface (see Fig. 3.3) and compare the obtained energies.

To obtain the binding energy of an adsorbate at the surface, we calculate the energy difference between DFT converged relaxed states. There exist two approaches to calculate such energy difference. Both procedures should give the same value for the adsorption energy, provided that the supercell is large enough to avoid spurious interactions between periodic slabs. The first approach is to calculate

Equation	Energy(eV)
(3.1)	1.666
(3.2)	1.670

Table 3.3: Adsorption energy of CO on the bare Ru(0001) calculated using eqs. (3.1) and (3.2)

the adsorption energy E_{ads} in the following way

$$E_{\text{ads}} = E(\text{A}_{(\text{gas})}/\text{M}) - E(\text{A}_{(\text{ads})}/\text{M})\,, \tag{3.1}$$

where we subtract to the energy of the equilibrium configuration where the adsorbate is in the center of the vacuum of the cell ($E(\text{A}_{(\text{gas})}/\text{M})$), the energy of equilibrium configuration where the adsorbate is adsorbed on the surface of the metal ($E(\text{A}_{(\text{ads})}/\text{M})$). Then the second approach [12;186], widely used, to calculate the binding energy is the following

$$E_{\text{ads}} = E_{\text{M}} + E(\text{A}_{(\text{gas})}) - E(\text{A}_{(\text{ads})}/\text{M})\,, \tag{3.2}$$

where the terms are respectively the energies after relaxation for: $E(\text{A}_{(\text{gas})}/\text{M})$ the system with adsorbate A desorbed in the middle of the vacuum following z coordinate, $E(\text{A}_{(\text{ads})}/\text{M})$ the system with the adsorbate A adsorbed on the surface, E_{M} the system containing only the metal surface, and $E(\text{A}_{(\text{gas})})$ the system containing only the adsorbate (which is thus in gas phase).

To confirm that both methods are equivalent, we computed the value of the desorption of one CO molecule adsorbed on a bare Ru(0001) surface, using the vdW-DF functional for the calculation. The computed values are reported in Table 3.3. The results are equivalent, confirming that the size of the selected vacuum is adequate and, therefore, that both procedures are equally valid to compute adsorption energies. Hereafter, we will use the first approach (eq.(3.1)) to compute energy differences all along this thesis.

Functional	Desorption energy(eV)
PBE	1.923
RPBE	1.656
vdW-DF	1.666
DFT-D3(BJ)	2.293

Table 3.4: Adsorption energy of an isolated CO molecule on the top site of Ru(0001) calculated with different exchange-correlation functionals. The experimental value of the CO adsorption energy is 1.658 eV.[21]

Now that we clarified how to compute energy differences, we return to the comparison of CO adsorption site and binding energy with the different *xc*-functionals. As important results, we note that all four functionals correctly give the top [21;186] site as the most stable adsorption site for CO on Ru(0001). After relaxation of all the forces, in Table 3.4 we give the results of the desorption energy of CO in the bare Ru(0001) surface obtained with these functionals. The experimental value to which these values must be compared is 1.658 eV.[21] Clearly, both the PBE functional and the

DFT-D3(BJ) functionals greatly overestimate the adsorption energy, mostly in the case of the latter for which the overestimation amounts around 0.6 eV. On the other hand, both the RPBE and the vdW-DF functionals provide a very accurate adsorption energy. Motivated by this fact, and since the long range vdW interaction, not included in the RPBE functional, is expected to be very important to describe accurately the system under study, we have selected the vdW-DF functional to perform the calculations presented in this thesis.

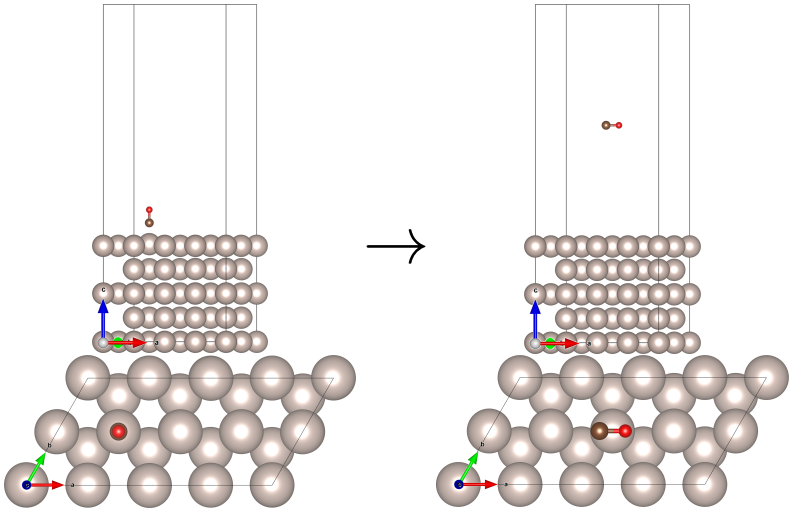

Figure 3.3: Desorption of CO molecule from the bare surface of Ru(0001).

3.2 Protocol to find the intermediate states

The complex chemical reaction consisting in the recombinative desorption of CO and O on the Ru(0001) surface, written $O_{(ads)} + CO_{(ads)} \rightleftharpoons CO_{2(gas)}$, involves several steps. The initial state ($O_{(ads)} + CO_{(ads)}$) is composed of CO and O dissociatively adsorbed on the surface, and the final state is composed of the $CO_{2(gas)}$ desorbed in vacuum. It has been reported in literature that two intermediate states are involved in this reaction of oxidation. These two states consist in the chemisorbed bent CO_2 (bCO_2) and the physisorbed linear CO_2 (lCO_2). The bCO_2 state has also been mentioned in ref.[13] in the low coverage honeycomb structure and in ref.[87] for CO_2 on the bare Ru(0001) slab. Furthermore, refs.[81;187] reported similar states on a bare platinum slab. Thus, to compute the full reaction path, we must find these bCO_2 and lCO_2 states. As a starting point, we must perform the identification of the relevant intermediate CO_2 state in the bare Ru(0001) surface. They will serve as an initial guess when we deal with different coverages of O and CO at the surface. Once we find and characterize well these two states, we obtain the reaction path, including the corresponding transition states, by use of the CI-NEB method.[8;9]

In this section, we present the detailed procedure we employed to identify these intermediate states for each coverage, beginning with the uncovered surface. Since the procedure used is basically the same for both bCO_2 and lCO_2 states, for illustrative purposes we will focus on the bCO_2 state.

3.2.1 The case of uncovered surface

In order to find the intermediate states involved in the recombinative desorption of CO_2, we create a protocol with five different steps. Thus, we ensure a systematic investigation of the intermediate states. The protocol has been developed for the bare surface, then adapted to the covered surface.

The first step consists in finding the intra (C-O distance, $\widehat{OCO}$ angle) and inter (surface to CO_2 distance and angles) coordinates of the bCO_2 states in the supercell. As an example, we show in Figure 3.4 the intra and inter coordinates of the bCO_2 and lCO_2 molecule. The values correspond to the ones calculated in this thesis, not from literature. However, we are starting this investigation from the very beginning, thus we do not have yet access to those values. Hence, we use the information given in the supplementary material of the work of Öström *et al.* [13]. In this article, the authors used a different supercell, coverage and *xc*-functional. We therefore anticipate that the intra coordinate of the bCO_2 in our cell will slightly differ after the relaxation of the forces. Notwithstanding, it remains as an acceptable starting point. Hence, in the work of Öström *et al.* [13] we identify the O1-C of bCO_2 to be located on a near-top site, with its axis slightly tilted so that the C atom point to a bridge site, with the O1 atom oriented toward vacuum. The O2 atom of bCO_2 is located on this bridge where the carbon atom is pointing.

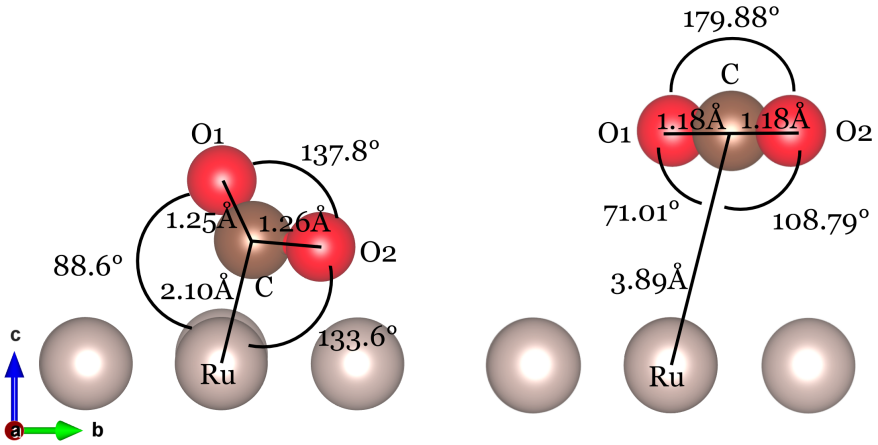

Figure 3.4: Side views of thebCO_2 andlCO_2 states on the bare surface, calculated in this thesis. Labels, angles and distances are given in black.

The second step is to locate the bCO_2 in the supercell. We know that the C atom of the bCO_2 molecule adsorbs on the near-top site, thus we select an empty top site where to locate it. In the case of the bare surface, it is easy since all ruthenium atoms are free from adsorbates and equivalent. Thus, whichever top site is acceptable, therefore we selected the one named A in Figure 3.5.

The third step is to consider different possible orientations of the bCO_2 molecule positioned on the top site in the supercell. In fact, we selected a top site to adsorb the molecule, but we do not know which orientation in the *x*-*y* plane the bCO_2 molecule must have to be in its most sable state. Indeed, from the top site to the bridge site, the bCO_2 molecule crosses either fcc or hcp site. They are not equivalent adsorption sites and would give a different adsorption energy. Although in the work of Öström *et al.* [13] the bCO_2 molecule was oriented above a hcp site, with an oxygen adatom from fcc site, we want to consider more possible options. Thus, we estimate that it is possible for the bCO_2

molecule to adsorb with an initial position oriented along fcc, hcp or bridge sites. With this aim, we consider different initial orientations of the bCO_2 by taking rotations centered in the chosen top site. In Figure 3.5 we depict in black the circle of rotation centered on the top site. The azimuthal angle (φ) describes this rotation relative to the z-axis of the surface plane, with $\varphi = 0$ defined as the alignment with the x-axis The angular step of the rotations is $\frac{\pi}{6}$, which, in principle, implies 12 different initial orientations. However, out of the 12 orientations some are equivalent by symmetry. Thus we can reduce to a total amount of rotation on the bare surface to only three non-equivalent orientation indicated as black line in Figure 3.5.

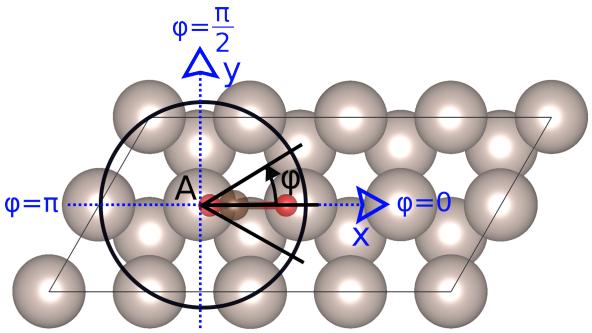

Figure 3.5: Sketch of the projection on the (x,y)-plane of the different possible orientations of bCO_2 and lCO_2. The center of the black circle, named A, is the selected top site of the ruthenium atom where we put the bCO_2 or lCO_2 molecule. Black lines shows the calculated orientation of the molecule. These lines cross at the center of the black circle. The Cartesian coordinate system is represented in blue, with its origin in the center of the circle. The CO_2 molecule is represented shaded (oxygen atoms in red and carbon atom in brown) in its bCO_2 configuration.

The fourth step is to relax the forces applied to the structure. Note that each orientation is a different calculation. This means that for the uncovered surface, we have performed 3 calculations. The relaxation process is done sequentially. Initially, we fix the bCO_2 coordinates and relax the Ru atoms of the topmost three layers. Next, we relax the bCO_2 coordinates and fix the coordinates of the rest of the Ru atoms. Lastly, we relax the coordinates of bCO_2 and the Ru atoms of the topmost three layers.

Finally, the fifth and last step of our protocol is devoted to the analysis of the obtained final states. After the relaxation process, for some initial guesses the final state is still bCO_2, but for some others, the final state can be lCO_2 or desorbed CO_2. We thus classify the final states. We discard orientations leading to a final state different to bCO_2, which is none on the uncovered surface. The most stable orientation in the case of uncovered surface is $\varphi = \frac{\pi}{3}$ with an adsorption energy of 1.53eV.

The same five-step procedure is been employed to obtain the intermediate lCO_2 state, except that for the initial guess we use the intra and inter coordinates of $CO_{2(gas)}$ in the bare surface. Note that upon relaxation no initial lCO_2 ends as bCO_2. Interestingly, for covered and uncovered protocol, when we find the bCO_2 of minimum-energy, the lCO_2 of minimum-energy is the one of the same φ orientation. Thus the key is to find the bCO_2 and use its corresponding lCO_2 to further compute the CI-NEB calculation.

We specify here that the bCO_2 and lCO_2 are respectively confirmed as chemisorbed and physisorbed states by performing a Bader charge analysis as explained later in the Section 3.4.

3.2.2 The case of CO and O covered surfaces

Once the bCO_2 state at the bare surface has been found, we use the following and very similar protocol to obtain the bCO_2 state in the CO and O covered surface.

Like in the case of the uncovered surface, the first step is to find the intra and inter coordinate of the bCO_2 in our cell. As an initial guess, we could use the coordinate of Öström *et al.* [13] as we have done for the uncovered surface. However, we expect the bCO_2 state of the bare surface converged in our supercell, with the same *xc*-functional, to be very close to the one of the covered surface. The intra and inter coordinates calculated after relaxation of the forces for bCO_2 and lCO_2 on ruthenium bare surface in our supercell are given in Figure 3.4. Hence, we are using those intra and inter coordinate as initial guess for the geometry of the bCO_2 for the covered surface.

The second step consists in selecting the pair of atoms that will recombine to form the bCO_2. In the covered surface, because there are different CO molecules and O adatoms, there exist a very large number of possibilities when the choice of the recombining species is to be made. At any rate, it is clearly not possible nor necessary to explore all the possible combinations of adsorbates when looking for the bCO_2 state. Therefore, to discriminate among the numerous possibilities we define two well educated criteria.

- The first criterion relies on the energetics. For each coverage, the energy of reaction is defined as the energy difference between the CO_2 in the gas phase (meaning one O and one CO less at the surface), and the equilibrium structure ($O_{(ads)}$ + $CO_{(ads)}$). This energy depends on the specific adsorbates that recombine. Indeed, regarding their position of desorption on the surface, all adsorbates are not equivalent. In our study, we give preference to the adsorbate combinations for which this reaction energy is low respect to the others.

- The second criterion is related to the relative position of the recombining adsorbates. Even if the reaction energy was low, in some cases the O and CO adsorbates are too far away and separated by other adsorbates, which makes it very difficult to find a tractable reaction path. In these cases, we deem this recombination unlikely and do not include it in our study.

With the help of these two criteria, we are able to select only a few of the numerous possible recombination pairs.

The third step consists in selecting an appropriate top site where the bCO_2 is formed. We make the reasonable assumption that in the covered surface the geometry and position relative to the Ru(0001) surface of the bCO_2 is similar to that found in the bare surface. Still, there exist plenty of different top sites, nonequivalent due to the surrounding arrangement of adsorbates, that can be chosen as the site close to which the bCO_2 is created. Thus, we impose two conditions which must be fulfilled to select the top site:

- First, it should be relatively close to both recombining adsorbates ($\sim$3 Å maximum).

- Second, it must be in a region sufficiently free of other adsorbates in order to form the bCO_2 and to adsorb it in its vicinity.

The selected top sites, with the corresponding pairs of recombination are described for the covered surfaces in appendix C.

Once the adsorbate combination and the adsorption site are selected, the fourth step consists in locating the bCO_2 on the adsorption site and choosing the orientation. In the same way as for the uncovered surface, in order to have a better initial sampling set, we do not restrict ourselves to the equilibrium bCO_2 orientation on the bare surface (appendix C). In the case of the covered surfaces some orientations are irrelevant because they would lead to unphysical distances between the atoms forming the bCO_2 and other adsorbates at the surface, which reduces the total number of considered orientations.

After the initial conditions have been fixed, the fifth step involves the relaxation of the structure. As for the uncovered surface, we do it sequentially. First, we fix the bCO_2 coordinates and relax all other adsorbates and the Ru atoms of the topmost three layers. Second, we relax the bCO_2 coordinates and fix the coordinates of the rest of the atoms. Finally, we relax the coordinates of bCO_2, the rest of adsorbates and the Ru atoms of the topmost three layers.

The sixth and last step of our protocol is devoted to the analysis of the obtained final states. This step is exactly the same as the step five of the uncovered surface protocol.

3.3 Static study of the different coverages

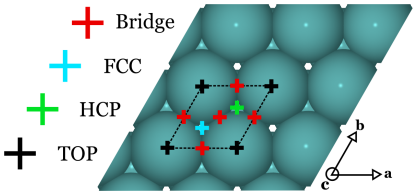

Figure 3.6: Adsorption sites over Ru(0001) surface view along *c* axis. In dashed black line is represented the minimum cell to represent Ru(0001) surface. The different crosses represent the adsorption site named according to legend. The blue balls are ruthenium atoms.

As stated in the introduction of this chapter, one of the main goals of this thesis is to carry out molecular dynamics of carbon monoxide and oxygen atoms coadsorbed on the surface. However, before performing the dynamics simulations, the first step consists in the characterization of the IS of the system before its excitation with the laser pulse. To choose the coverages to be studied, we recall that we aim to reproduce and understand the experiments of refs.[6;12;13]. In those experiments the Ru(0001) surface is first dosed with oxygen up to saturation, which in the chosen conditions means that a 0.5 ML O coverage is achieved.[11] On the ruthenium surface the oxygen adatoms adsorb on the hcp site[33;34] (see Figure 3.6), and under 0.5 ML coverage they are arranged in a p(2×1) overlayer, creating rows of oxygen on the surface. Subsequently, the system is dosed with CO up to saturation. In refs.[12;13] some theoretical calculations were performed in which it was assumed that the CO coverage was 0.25 ML and two different structures were considered. The first was the honeycomb structure, in which half of the O atoms are adsorbed on hcp sites, the other half on fcc sites and the CO molecules on top sites.[12;13] In the second structure, the O atoms remain in the hcp sites in a p(2×1)-O arrangement and the CO molecules are located near atop sites.[12] However, after surface preparation and before exciting it with the laser pulse, in these experiments the surface is cooled down to 100 K. According to Kostov *et al.*[11], at this temperature the equilibrium structure consists in a p(2×1)-O arrangement with crowded CO at the empty space of the layer. In other words, it cannot be excluded that under the

experimental conditions of refs.[6;12;13] the CO coverage is higher than 0.25 ML. Therefore, it would be interesting to study the different coverages of CO and adsorbate structures, provided they can be considered realistic in the light of the reported surface preparation and the observations of Kostov *et al.*[11].

Motivated by these facts, here we perform a complete DFT characterization of different (O, CO) mixed coverages on Ru(0001). We first study the lowest possible coverage in our simulation cell, named minimum coverage, in order to study the effects of O and CO coadsorption and recombination without perturbation of other adsorbates. In the case of our (4×2) simulation cell, strictly speaking, this corresponds to a 0.125 ML O + 0.125 CO coverage but, as it will be shown later, it represents an excellent approximation of the zero coverage limit. Therefore, we prepare three different coverages that consist of a fixed 0.5 ML of O combined with three different CO coverages, which will be denoted as low, intermediate, and high coverages. Specifically, the low coverage is formed by 0.5 ML O + 0.25 ML CO and it represents the CO saturation coverage found in ref.[11] at 300 K. The intermediate coverage, consisting of 0.5 ML O + 0.375 ML CO, corresponds closely to the CO saturation coverage reported in ref.[11] at temperatures below 120 K. Finally, we also study the high coverage defined by 0.5 ML O + 0.5 ML CO, despite the fact that this mixed ML has not been experimentally observed yet. Here, it will be shown that this high coverage is indeed energetically stable, but unreachable by the sample preparation procedure followed in refs.[6;11;12;13]. It is important to note that the spin of the open-shell O atoms is quenched when adsorbed on Ru(0001),[77;188;189] therefore, all the calculations are based on non spin-polarized DFT.

The study is divided by coverages. In each coverage we start identifying the lowest energy configuration. Once the stable surface structure is known, we calculate the potential energy curve of the desorption of one CO molecule from the surface, we compare the energies of the desorption of one CO and one CO_2 molecule, and finally we analyze the MEP for CO oxidation.

In the case of the hcp structure there are four principal adsorption sites: bridge, fcc, hcp, and top. Their position on the surface are represented in Figure 3.6. In addition to these four adsorption sites, we specify that for the top site, some nuances exist. In fact, when an adsorbate is at the top site, it can be slightly displaced from the center of the top site. Thus, it is oriented toward an hcp, fcc or bridge site. Therefore, to underline this differences, we will refer to these specific adsorption site as top-hcp, top-fcc or top-bridge.

3.3.1 Minimum coverage (0.125ML O + 0.125ML CO on Ru(0001))

Equilibrium configuration and CO desorption

The minimum coverage is composed of the bare surface of Ru(0001), one CO molecule and one O adatom adsorbed. In the case of the minimum coverage, it is important to guarantee that the adsorbed CO and O are far enough in order to be considered as non-interacting isolated adsorbates. Their adsorption site is chosen following the literature that reports that at very low coverage CO adsorbs on top site,[56;76;186;190;191] while O adsorbs on hcp site.[33;34] For the same top site of adsorption of the CO, we propose two different hcp sites for the oxygen, one farther from the CO than the other. After relaxation, we observe that both configurations, denoted α and β in Figure 3.7, are stable. Also we note

that they are energetically equivalent. This means that even for structure α in 3.7, the configuration in which the distance between the O and CO adsorbates is the shortest, the adsorbates can be considered as non-interacting. For this reason, in the following we have used the configuration α to study the energetics of CO desorption and oxidation at the minimum coverage. We have ensured this energetic equivalence by performing calculations with a stricter convergence criteria (energy cut-off of 500 eV and atomic force minimization below 0.001 eV/Å).

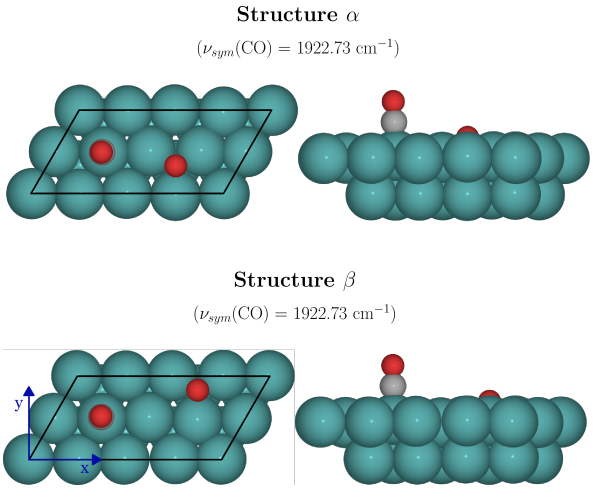

Figure 3.7: Top (left) and side (right) views of the three stable structures obtained for the 0.125 ML O + 0.125 ML CO coverage on Ru(0001). Top panels: the energetically most stable structure. Bottom panels: equivalent structure to prove isolated adsorbates. The frequency of the in-phase C–O stretch mode is specified for each coverage. Color code: O atoms in red, C in gray, and Ru in blue. The black parallelograms show the surface unit cells in the calculations. For clarity, the periodic images of the O and CO adsorbates are not shown and only the two topmost Ru layers are depicted in the side views.

As a first study, we compute the desorption energies of CO and CO_2 at this coverage. These results are shown in Table 3.5. We observe that both process are highly endothermic with very similar desorption energies, 1.59 and 1.63 eV, respectively.

Reaction	Adsorption site	E (eV)
$CO_{(ads)} \rightharpoonup CO_{(gas)}$	CO_{top}	1.590
$O_{(ads)}$+$CO_{(ads)} \rightharpoonup CO_{2(gas)}$	CO_{top}, O_{hcp}	1.633

Table 3.5: Reaction energies E for CO desorption and oxidation from the Ru(0001) surface at the zero coverage limit. The initial adsorption site for each desorbing species is indicated as a subscript in the second column.

Thereafter, we compute the potential curve of desorption of one CO molecule at this coverage. Figure 3.8 shows the potential energy against the CO Center of Mass (CM) height Z_{CO} that is measured from its adsorption position. For comparison, we also show the potential energy curve for CO desorption in the case of the pristine Ru(0001) surface (denoted as CO-Ru(0001) hereafter). We observe on Figure 3.8 that the desorption process presents an activation energy equal to its desorption energy. Thus, there is no energy barrier for the adsorption of one CO on the precovered Ru(0001) with 125ML-O. The value of the two curves is only 0.07eV different, above 1 Å desorption from adsorption position, and has a very similar shape. This emphasizes that the oxygen adatom adsorbed

on the surface has a small effect on the energetic of desorption and almost none on the chemistry of the surface, comparing to the case of isolated CO on bare Ru(0001) surface.

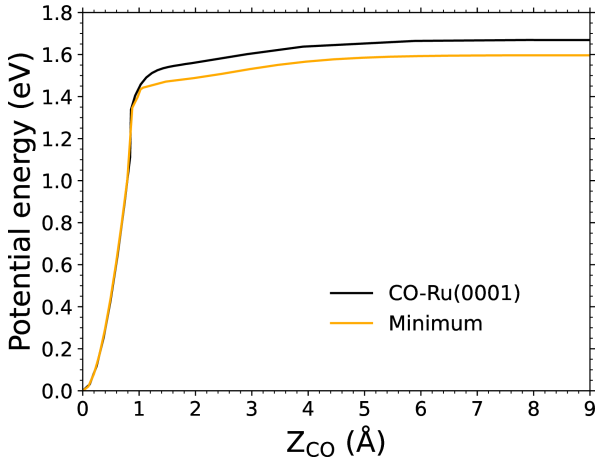

Figure 3.8: Potential energy of a CO molecule as a function of its center of mass height Z_{CO}, measured from its equilibrium adsorption position Z_{CO-Ru}. Results obtained for minimum coverage in yellow, and for the pristine Ru(0001) surface in black. The zero of energy is chosen as that of the equilibrium adsorption position for each coverage.

CO oxidation on structure α

In this section we show the MEP for oxidative desorption of CO at minimum coverage. As initial mandatory step, we identified the intermediate states of the CO oxidation reaction (bCO_2 and lCO_2) as presented in the Section 3.2. Then we performed a CI-NEB calculation between each of the states. The reaction path is split in three parts. From the IS to the bCO_2, from the bCO_2 to the lCO_2 and from the lCO_2 to the $CO_{2(gas)}$. Hence, we computed three CI-NEB calculations with four intermediate images in each. We verified that all transition states that we encountered are saddle points by confirming that only the frequency of the normal mode along the reaction coordinate is imaginary. We present the final calculated energy path in Figure 3.9.

Here the figure shows schematically images of the IS and FS states, the two molecular adsorption states (bCO_2 and lCO_2), and the three Transition States (TS) we find (TS0, TS1 and TS2). In Fig. 3.9 we show the image of an additional state denoted E(diff)). This state has not been relaxed so that it has not been verified to be and equilibrium state, but it appears as a local minimum on the CO+O recombination path in the NEB calculation. The state appears in the diffusion of the oxygen adatom on the surface between hcp sites.

Apart from the features of the oxygen diffusion path discussed above, the oxidation MEP is characterized by two (local) minima that correspond to the chemisorbed bCO_2 and physisorbed lCO_2 states. During the recombination process, the most interesting is the bCO_2, since it is the first stable state that marks the successful recombination of the carbon monoxide with the oxygen. Therefore, the two transition states TS1 and TS2 that surround bCO_2 are every important. TS1 is restricting the access to the bCO_2 state from IS with an energy barrier of 1.67eV and TS2 is restricting the desorption of the CO_2 molecule with an energy barrier of 0.23eV. Analyzing the energies of the different states, we

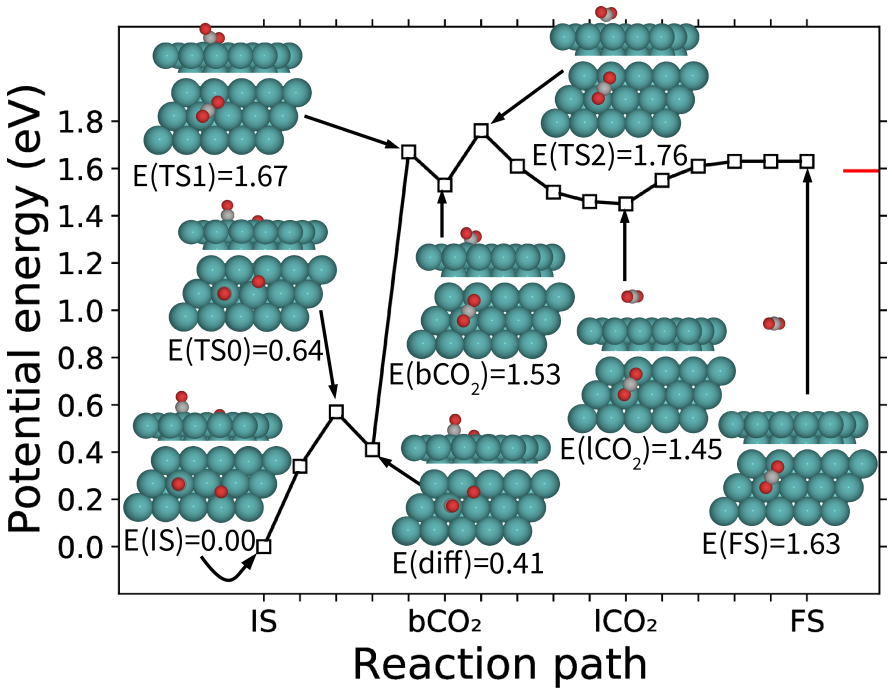

Figure 3.9: CI-NEB calculated minimum energy path for the CO_2 recombinative desorption from Ru(0001)-(0.125 ML O + 0.125 ML CO) coverage. Also are shown the top and side views of the relevant configurations along the path: the initial state $O_{(ads)}$ + $CO_{(ads)}$ (IS), the final state $CO_{2(gas)}$ (FS), the intermediate adsorption states (bCO_2 and lCO_2), and the transition states (TS1 and TS2). Their energies referred to IS are given in eV below each image. For comparison, the energy of the desorbed CO is also given by a red short-line on the top right of the figure. Color code: O in red, C in gray, and Ru in blue.

conclude that the formation of TS2 is the limiting step in the oxidative desorption of carbon monoxide. Note that from the physisorbed lCO_2 state the molecules need to overcome an energy barrier of 0.18 eV to be desorbed. In Fig. 3.9, for comparison, we also show with a red line the desorption energy of CO at the same coverage.

It is meaningful to compare these results to those obtained by Zhao et al.[87] also in the minimum coverage. In that work they used the RPBE-GGA *xc*-functional,[183] which neglects the van der Waals interaction, and a 5×5 simulation cell. The results obtained in our case for the energy of the TS1 and bCO_2 states measured from IS are, considering the different calculation setups, in rather good agreement with those obtained by Zhao *et al.*, with energy differences that amount less than 60 meV. However, their CO_2 desorption energy is 0.48 eV lower than ours, probably due to the too repulsive RPBE functional. Moreover, the lCO_2 and TS2 states were not reported by them. This should be attributed to the neglect of the vdW interaction, which is necessary to describe the physisorption region.

3.3.2 Low coverage (0.5ML O + 0.25ML CO on Ru(0001)

Equilibrium configuration

The honeycomb structure has been confirmed experimentally as the most likely adsorbate arrangement at (0.5ML O + 0.25ML CO) coverage.[11;29;47] In this structure, each CO adsorbs top a Ru atom

and is surrounded by six oxygen atoms that occupy the second nearest hcp and fcc sites forming a honeycomb arrangement (see Fig. 3.10, top panel). We remark that we are not using the minimum unit cell. The purpose of using a bigger unit cell is to be able to simulate out of phase motion of the adsorbates when performing molecular dynamics. To confirm whether the honeycomb structure is indeed the energetically most favorable adsorbate arrangement at this coverage, we additionally study the stability of other possible structures that are compatible with the initial oxygen-saturation coverage of 0.5 ML that is formed in the fs-laser induced reaction experiments prior dosing the surface with CO.[6;12;13] In this respect, it is well established by experiments and theory that at 0.5 ML coverage and in absence of CO adsorbates, the O atoms adsorb preferentially in hcp sites forming a p(2×1) structure.[34;35] Therefore, coadsorbed with p(2×1)-O_{hcp}, we consider four possible p(2×2)-CO structures that correspond to the two CO molecules in our 4×2 unit cell being initially at either top, bridge, fcc, or hcp sites. The results after relaxation with details about initial and final adsorption site of CO molecules are presented in Table 3.6

O-structure	O site	CO initial site	CO final site	E(eV)	Z_{CO-Ru}(Å)
Honeycomb	0.5fcc+0.5hcp	top	top	0.000	2.632
p(2×1)	hcp	top	desorbed	–	–
p(2×1)	hcp	bridge	top-fcc	0.759	2.665
p(2×1)	hcp	fcc	top-fcc	0.759	2.665
p(2×1)	hcp	hcp	hcp	1.118	2.160

Table 3.6: Results from the structural optimization for the 0.5 ML O + 0.25 ML CO coverage on Ru(0001), indicating the structure and adsorption sites of the O atoms, the initial and final adsorption sites of the coadsorbed (2×2)-CO, the potential energy per simulation cell E referred to that of the lowest energy honeycomb structure, and the height of the CO center of mass from the surface (defined as the average heights of the Ru atoms in the topmost layer) Z_{CO-Ru}.

In the case of the p(2×1) oxygen arrangement, coadsorption of CO on top site, which is the preferred adsorption sites in the honeycomb structure,[11;29;47] is unstable since all the CO molecules desorb upon relaxation. Optimization of the two structures in which the CO molecules are initially located on either bridge or fcc sites, leads in both cases to the same p(2×2)-$CO_{top-fcc}$ structure depicted in Fig. 3.10. In this relaxed overlayer, the CO molecules end up with the center of mass in the line joining the top and fcc sites, with their axis slightly tilted towards the nearest O atom. Additionally, the farthest O atoms shift about 0.32 Å along the y direction. This is the most stable structure with the p(2×1) oxygen arrangement, but it is still 0.759 eV higher in energy per simulation cell than the honeycomb structure. Finally, relaxation of the structure with the CO molecules in the unoccupied hcp sites shows that this arrangement is also stable, but 0.359 eV higher in energy per simulation cell than the previous one. In this respect, it is worth to mention that previous DFT studies of the same coverage with the p(2×1) oxygen arrangement had considered different adsorption positions for the CO molecules: the hcp sites in ref.[86] and near atop sites in ref.[12]. Our DFT+vdW-DF results show that for this oxygen arrangement the two proposed structures are stable. Nevertheless, they also suggest that the top-fcc location may be a more realistic adsorption site for the coadsorbed CO, in agreement with ref.[12].

Regarding the energetics, the honeycomb structure is the one with the lowest energy, *i.e.*, it is the equilibrium structure for this coverage. Regarding the structures with the p(2×1) O arrangement, the one with the CO molecules in top-fcc sites is the energetically most favorable, whereas the one with CO molecules in hcp sites represents, among the obtained structures, the highest energy configuration.

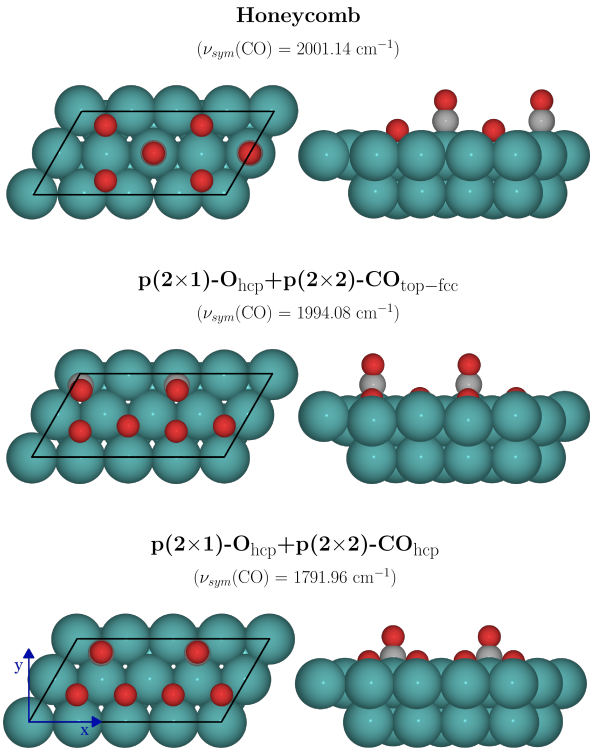

Figure 3.10: Top (left) and side (right) views of the three stable structures obtained for the 0.5 ML O + 0.25 ML CO coverage on Ru(0001). Top panels: the energetically most stable honeycomb structure. Middle panels: p(2×1)-O$_{hcp}$+p(2×2)-CO$_{top-fcc}$. Bottom: p(2×1)-O$_{hcp}$+p(2×2)-CO$_{hcp}$. The frequency of the in-phase C–O stretch mode is specified for each coverage. Color code: O atoms in red, C in gray, and Ru in blue. The black parallelograms show the surface unit cells in the calculations. For clarity, the periodic images of the O and CO adsorbates are not shown and only the two topmost Ru layers are depicted in the side views.

The frequencies of the in-phase C–O internal stretch mode (*i.e.*, when the two CO vibrate in phase) are written in Fig. 3.10 for each optimized structure. The lowest value corresponds to the p(2×2)-CO$_{hcp}$ arrangement, for which the CO molecules locate closer to the surface. The frequencies for the honeycomb and p(2×2)-CO$_{top-fcc}$ only differ in 7 cm^{-1}, showing that the CO adsorption properties are locally similar in both cases.

Next, the analysis concerning the energetics of CO desorption and oxidation on the low coverage will be performed on the honeycomb structure, which is confirmed as the lowest energy configuration.

CO desorption and oxidation on the honeycomb structure

The reaction energies for CO desorption and oxidation on the honeycomb structure are summarized in Table 3.7. The CO desorption energy of 1.569 eV, which is around 0.1 eV less endothermic than on the pristine surface, would be in line with existing DFT calculations that report a decrease in the CO desorption energy as the O coverage increases.[56;86] Nevertheless, the values we obtain in both cases

are rather similar, suggesting that the CO desorption energetics is not much influenced by the presence of O adsorbates. Oxidation on the honeycomb structure is also endothermic irrespective of whether the CO recombines with the O adsorbed at either the fcc site (0.643 eV) or the hcp site (1.206 eV). The lower oxidation energy obtained in the former case is consistent with the higher binding energy of O in the hcp site than in the fcc site.[35;87;192;193] Interestingly, the oxidation energy is in both cases smaller than the desorption energy. Nonetheless, this result alone is insufficient to determine the likeliness of one process over the other, since it may hide the existence of energy barriers along the reaction paths. This is precisely the kind of information provided by the MEPs that we analyze next to further characterize the competition between both processes.

Reaction	Adsorption site	E (eV)
$CO_{(ads)} \rightharpoonup CO_{(gas)}$	CO_{top}	1.569
$O_{(ads)}+CO_{(ads)} \rightharpoonup CO_{2(gas)}$	CO_{top}, O_{fcc}	0.643
	CO_{top}, O_{hcp}	1.206

Table 3.7: Reaction energies E for CO desorption and oxidation from the Ru(0001) surface with 0.5 ML O + 0.25 ML CO coverage in the honeycomb structure. The initial adsorption site for each desorbing species is indicated as a subscript in the second column.

Figure 3.11 shows the potential energy against the CO CM height Z_{CO} that is measured from its adsorption position in the honeycomb structure. For comparison, we also show the curves for the same magnitude corresponding to the minimumn coverage (with only one CO molecule and one O atom in the simulation cell) and for the case in which there is only one CO molecule in the simulation cell already discussed in the previous section (Fig. 3.8). In each curve, the energy reference is taken for the equilibrium configuration with the molecule adsorbed in its adsorption well, on top of a Ru atom. At distances $Z_{CO} > 6$ Å the curves have already reached the asymptotic region and the energy values basically coincide with the desorption energies. All three curves have as common important features the apparent absence of a physisorption well and the absence of energy barriers for CO adsorption. The latter is important regarding experiments in which the coadsorption of O and CO on surfaces is realized by first adsorbing O up to the required coverage and next adsorbing CO under thermal deposition. This is the procedure used, for instance, in refs.[6;11;12;13]. The absence of energy barriers for CO adsorption means that the 0.5 ML O + 0.25 ML CO honeycomb structure is achievable using this procedure.

The energetics of CO oxidation on the honeycomb structure is more involved. For simplicity, we will focus on the reaction between the CO and the O adsorbed in the fcc site, which is the energetically most favorable recombination (see Table 3.7). As above mentioned, the oxidation is assumed to proceed through the two molecular adsorption states that are identified in this system, the chemisorbed bCO_2 and the physisorbed lCO_2. It is worth to remark that intermediate states of similar characteristics have been obtained in the reaction path for CO oxidation on Pt(111)[81;187] and Co(0001).[194] On Ru(0001), Zhao *et al.*[87] at low CO and O coverage and Öström *et al.*[13] for the same honeycomb structure analyzed here, described also the bCO_2 but not the lCO_2 as intermediate state in the MEP for CO oxidation. This is probably due to the fact that the DFT calculations in both references were based

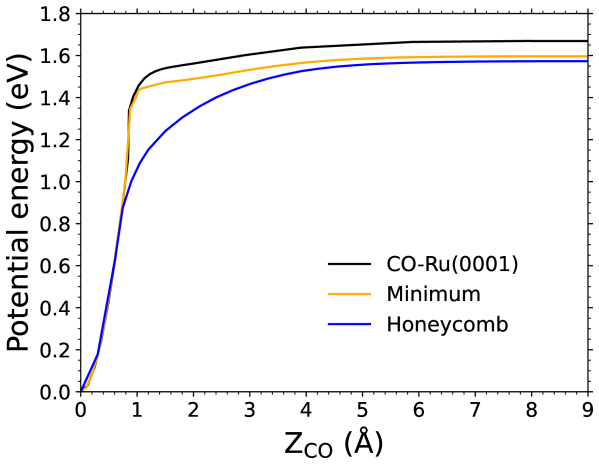

Figure 3.11: Potential energy of a CO molecule as a function of its center of mass height Z_{CO}, measured from its equilibrium adsorption position Z_{CO-Ru}. Results obtained for the honeycomb structure (blue), (O+CO)Ru(0001) in yellow, and for the pristine Ru(0001) surface (black). The zero of energy is chosen as that of the equilibrium adsorption position for each coverage.

on GGA *xc*-functionals. Such functionals, not including van der Waals corrections, are expected to be unable to describe the physisorption region relevant for the characterization of the lCO_2 state.

Figure 3.12 shows the MEP for the oxidation of CO with the O adsorbed in the fcc site. A detailed description of all the calculated states along the MEP are given in Appendix C, following the protocole describe in minimum coverage section. The minimum energy configuration along the CO oxidation MEP is IS. The chemisorbed bCO_2 is a metastable adsorption state. The molecules in this state only require 0.03 eV to desorb through the more stable lCO_2 state and 0.13 eV to dissociate on the surface as $O_{(ads)}$ + $CO_{(ads)}$. In contrast, the physisorbed lCO_2 is rather stable. Energy barriers of 0.39 and 0.94 eV separate this state from desorbing and from dissociating on the surface, respectively. Regarding the oxidation reaction of interest, the overall process is governed by TS1 and it requires an activation energy of 1.19 eV. Note however that this activation energy is still 0.38 eV lower than the energy required to desorb CO (see Table 3.7). Clearly, the dominant desorption over oxidation reported in experiments has to be explained in terms of the complex oxidation process. CO_2 desorption requires destabilization of a strongly bound O atom, diffusion of CO and O at the surface, and the encounter between CO and O under proper geometrical and energy conditions in order to form the molecular bond. As a consequence, among all the configurations of the system that can be explored in a given dynamics, a relatively small number of them are expected to lead to oxidation, *i.e.*, the configurational space for oxidation is much reduced as compared to the direct CO desorption. In this respect, recent experimental and theoretical studies have shown the complexity of O diffusion on a crowded CO Ru(0001) surface.[59;195] The way the energy is provided to the system by exciting directly the adsorbates or indirectly by thermal activation or generating electronic excitations, is also determinant regarding the relative probability for CO and CO_2 desorption. These questions will be further discussed in Chapter 5.

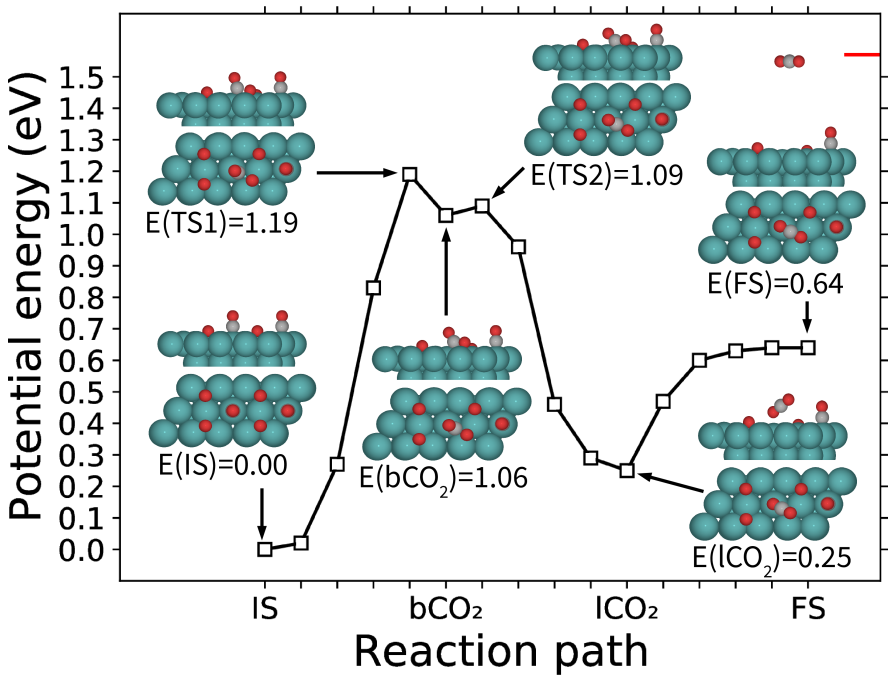

Figure 3.12: CI-NEB calculated minimum energy path for the CO_2 recombinative desorption from Ru(0001)-(0.5 ML O + 0.25 ML CO) in the honeycomb structure. Also are shown the top and side views of the relevant configurations along the path: the initial state $O_{(ads)}$ + $CO_{(ads)}$ (IS), the final state $CO_{2(gas)}$ (FS), the intermediate adsorption states (bCO_2 and lCO_2), and the transition states (TS1 and TS2). Their energies referred to IS are given in eV below each image. For comparison, the energy of the desorbed CO is also given by a red short-line on the top right of the figure. Color code: O in red, C in gray, and Ru in blue.

3.3.3 Intermediate coverage (0.5ML O + 0.375ML CO on Ru(0001)

Equilibrium configuration

The intermediate coverage, which is simulated by four adsorbed O and three adsorbed CO molecules in our 4×2 simulation cell, is very close to the saturation coverage that was identified in experiments performed under UHV and temperatures below 120 K.[11] In this coverage, the O atoms adsorb at hcp sites in a p(2×1) arrangement and the CO molecules occupy the empty space left between the O arrays. However, the precise sites in which the crowded CO are located is experimentally undetermined. Therefore, as a first step, we look for the energetically most favorable CO arrangement that coadsorbs with the p(2×1)-O overlayer. Four different structures are considered in which the three CO are initially adsorbed at either top, fcc, bridge, or hcp positions. After relaxation, only the two final structures, denoted as structure A and structure B, are shown in Fig. 3.13 are obtained. Both are stable structures according to the normal mode analysis. Table 3.8 summarizes the results of our structural search for the intermediate coverage.

In structure B, the CO molecules remain adsorbed in the hcp sites (Fig. 3.13, bottom panel). In this case, the molecules remain in the hcp sites, the central one slightly tilted towards the nearest Ru atom with two adjacent O atoms in hcp sites, and the two lateral ones slightly tilted towards the fcc site that is at the same distance from them as from the remaining empty hcp site.

O-structure	O site	CO initial site	CO final site	E(eV)	Z_{CO-Ru}(Å)
p(2×1)	hcp	fcc	near-top$^{3.8.A}$	0.000	2.6
p(2×1)	hcp	bridge	near-top$^{3.8.A}$	0.000	2.6
p(2×1)	hcp	top	near-top$^{3.8.A}$	0.000	2.6
p(2×1)	hcp	hcp	hcp$^{3.8.B}$	0.251	2.2

Table 3.8: Results from the structural optimization for the 0.5 ML O + 0.375 ML CO coverage on Ru(0001), indicating the structure and adsorption sites of the O atoms, the initial and final adsorption sites of the coadsorbed CO, the potential energy per simulation cell E referred to that of the (lowest energy) structure A, and the height of the CO center of mass from the surface (defined as the average heights of the Ru atoms in the topmost layer) Z_{CO-Ru}.

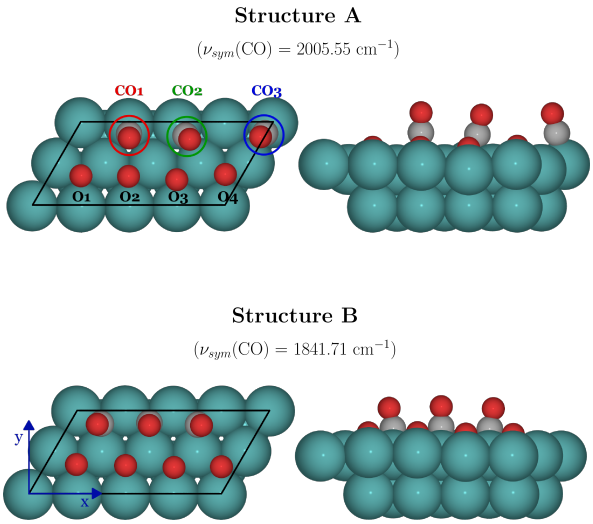

Figure 3.13: Top (left) and side (right) views of the two stable structures obtained for the 0.5 ML O + 0.375 ML CO coverage on Ru(0001). Top panels: Structure A, which is energetically the most stable. Bottom panels: Structure B. The frequency of the in-phase C–O stretch mode is specified for each coverage. Color code: O atoms in red, C in gray, and Ru in blue. The black parallelograms show the surface unit cells in the calculations. For clarity, the periodic images of the O and CO adsorbates are not shown and only the two topmost Ru layers are depicted in the side views. The nomenclature used in the text to denote the different adsorbates in structure A is indicated in the top view. From left to right the adsorbed CO molecules are labeled as CO1, CO2, and CO3 and the adsorbed O atoms as O1, O2, O3, and O4.

The lowest energy arrangement corresponds to structure A (Fig. 3.13, top panel). In this structure, which is the optimized structure when the CO molecules are initially on either top, fcc, or bridge sites, the CO molecules adsorb near the top site. Specifically, the CO molecules labeled as CO2 and CO3 in the figure are located in the line joining the top and bridge sites, with their axes slightly tilted towards the bridge site. *i.e.* top-bridge site. The molecule labeled CO1 is located in the line joining the top and fcc sites and is slightly tilted towards the fcc site, *i.e.* top-fcc site. Note that CO1 is situated between CO2 and the periodic image of CO3 (not shown in the figure). This means that the local coverage is higher around CO1 than around CO2 and CO3 that have an empty site in their vicinity. As a result, none of the O atoms are strictly equivalent and, though they remain very close to the hcp sites, they are slightly displaced along the y direction (see Fig. 3.13). The values of these displacements respect to their initial hcp sites are 0.08 Å, 0.06 Å, −0.124 Å, and 0.158 Å for O1, O2, O3, and O4, following this order.

The frequencies of the in-phase internal stretch mode of the CO overlayer are written in the figure for each structure. As expected, the frequency is larger in structure A than in structure B, *i.e.*, for the CO molecules adsorbed on near-top than in hcp sites. The frequency of 2005.55 cm^{-1} found for structure A compares well (within the expected DFT accuracy) with the intense HREELS peaks at 2089 and 2060 cm^{-1} reported for this coverage in ref.[196] and11, respectively. Furthermore, our calculations suggest that the low intensity peak at 1850 cm^{-1} that is additionally identified in ref.[11], but not in ref.[196], might be related to the presence of very minor domains with, for instance, the structure B arrangement.

Next, the analysis concerning the energetics of CO desorption and oxidation on the intermediate coverage will be performed on the structure A, which is the lowest energy configuration for such coverage.

CO desorption and oxidation on structure A

The study of the reactivity is somewhat more complex than in the previous low coverage case due to the amount of non-equivalent CO and O adsorbates at the surface. After calculating all possible CO+O recombinations, we find however that there exist a number of energetically nearly equivalent recombinations due to the similar reorganization of the adsorbates that remain on the surface. In particular, using the labeling in Fig. 3.13, we obtain the following nearly equivalent recombinations: CO1+O1≅CO1+O3, CO1+O2≅CO1+O4, CO2+O1≅CO3+O2, CO2+O2≅CO3+O3, CO2+O3≅CO3+O4, and CO2+O4≅CO3+O1. The reaction energies for the CO desorption from its chemisorbed and physisorbed states, and for the recombinative desorption of CO_2 are given in Tab. 3.9 for the different types of CO-s and CO+O combinations. Note that the reaction energies between the nearly equivalent recombinations differ in 1 meV at most.

Reaction	Adsorption site	E(eV)
$CO_{(ads)} \rightharpoonup CO_{(gas)}$	CO1	0.580
	CO2 (CO3)	0.730 (0.731)
$CO_{phys} \rightharpoonup CO_{(gas)}$	$CO1_{phys}$	0.178
	$CO2_{phys}$ ($CO3_{phys}$)	0.205 (0.201)
$O_{(ads)}$+$CO_{(ads)} \rightharpoonup CO_{2(gas)}$	CO1+O1 (CO1+O3)	−0.169 (−0.169)
	CO1+O2 (CO1+O4)	−0.678 (−0.679)
	CO2+O1 (CO3+O2)	−0.815 (−0.814)
	CO2+O2 (CO3+O3)	−0.176 (−0.176)
	CO2+O3 (CO3+O4)	0.026 (0.027)
	CO2+O4 (CO3+O1)	−0.584 (−0.584)

Table 3.9: Reaction energies E for CO desorption and oxidation from the Ru(0001) surface with 0.5 ML O + 0.375 ML CO coverage in structure A (Fig. 3.13), calculated for all the possible reactants. The initial adsorption site for each desorbing species and each reaction is indicated in the second column following the labeling defined in Fig. 3.13 for structure A. The desorption energies from the physisorption wells ($CO1_{phys}$, $CO2_{phys}$, $CO3_{phys}$) are also provided. Note that the (energetically) quasiequivalent reactions and their energies are given within parenthesis.

As shown in Table 3.9, CO desorption in structure A is less endothermic than in the honeycomb structure of the low coverage. In particular, the CO1 molecule, which experiences the highest local CO-coverage, has a desorption energy around 0.15 eV smaller than that of CO2/CO3 (0.58 vs 0.73 eV), and around 1 eV smaller than that of CO in the honeycomb structure. As a consequence, upon excitation of the surface, the desorption of CO is expected to be more efficient at this coverage than at the honeycomb low coverage. Remarkably, the oxidation of CO on structure A is exothermic for all possible recombinations, except for the pair (CO2+O3) (and its energetically quasiequivalent (CO3+O4)) that becomes endothermic by less than 30 meV (note that all the corresponding reaction energies in Table 3.9 are negative for the rest).

Since CO1 is the CO adsorbate that requires less energy to be desorbed, one would expect that the energetically most favorable CO_2 desorption should also involve CO1. However, a counter intuitive result is obtained. It is the oxidation of CO2 with O1 (or, equivalently, CO3 with O2) the most exothermic reaction. We attribute this result to the different rearrangement of the adsorbates after CO oxidation. Our calculations for the two rearrangements show that the latter (*i.e.*, without CO2+O1) is 0.136 eV more stable than the former (*i.e.*, without CO1+O2).

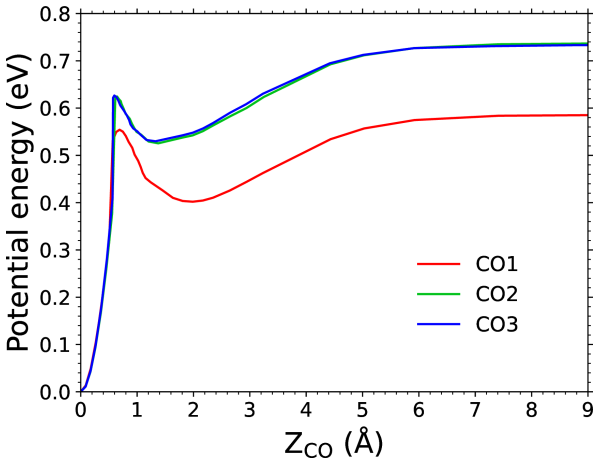

Figure 3.14: Potential energy of a CO molecule as a function of its center of mass height Z_{CO}, measured from its equilibrium adsorption position Z_{CO-Ru}. Results obtained for the 0.5 ML O + 0.375 ML CO covered Ru(0001) surface in structure A (Fig. 3.13), for the CO1 molecule (red), CO2 molecule (green) and CO3 molecule (blue). The zero of energy is chosen for each species as that of its equilibrium adsorption position.

Figure 3.14 shows the potential energy as a function of the distance from their adsorption sites for CO1, CO2, and CO3. The almost coincident CO2 and CO3 curves evidence that these adsorbates are nearly equivalent, as also observed when comparing their respective desorption and oxidation energies in Table 3.9. The most important feature shown by the three curves is the existence of a physisorption well, absent in the case of low CO coverage. Note in passing that this well is not predicted by a GGA xc functional such as PBE, and thus, its existence remarks the importance of using a functional that incorporates the van der Waals interaction for this system. Common to the three curves, there is an incipient energy barrier separating the physisorption state from the chemisorption state. However, this barrier is in the three cases smaller than the corresponding energy barrier to desorption.

In common to the low and zero limit coverage, this result confirms that under the surface preparation followed in refs.[6;11;12;13] the 0.5 ML-O + 0.375-CO coverage is also achievable. Finally note that

the asymptotic region is reached at slightly larger distances than in the low coverage case due to the existence of the physisorption well.

Concerning the MEP, our multiple attempts and strategies to obtain it for the most exothermic oxidative reaction involving the pair CO2+O1 (or equivalently CO3+O2) have been totally unsuccessful. With none of our initial guess images we have been able to find stable intermediate states for this recombination (*i.e.*, bCO_2 and lCO_2). We attribute this apparent lack of molecular adsorption states to the fact that CO2 is actually closely surrounded by the O2, O3, and O4 adsorbates. This situation makes difficult the approach of CO2 to O1 without altering substantially the (O2,O3,O4) arrangement. These considerations suggest the impossibility of this specific reaction or that the actual reaction path traverses through very high energy states. As an alternative, we have calculated the MEP for the energetically second most favorable recombination that involves the pair CO1+O2. The information and conclusions extracted from these results are meaningful, but we acknowledge that we cannot completely exclude the existence of a lower energy path involving the CO2 and O1 species.

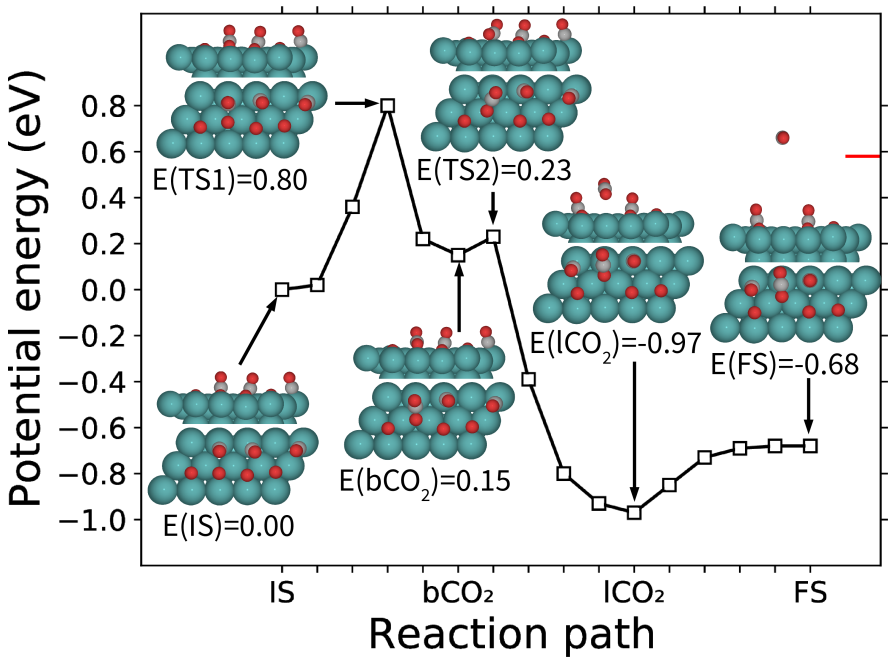

Figure 3.15: CI-NEB calculated minimum energy path for the recombinative desorption of CO1+O2 from structure A of the Ru(0001)-(0.5 ML O + 0.375 ML CO) surface. Also are shown the top and side views of the relevant configurations along the path: the initial state (IS), the final state $CO_{2(gas)}$ (FS), the intermediate adsorption states (bCO_2 and lCO_2), and the transition states (TS1 and TS2). Their energies referred to IS are given in eV below each image. For comparison, the energy of the desorbed CO is also given by a red short-line on the top right of the figure. Color code: O in red, C in gray, and Ru in blue.

Figure 3.15 shows the calculated MEP for the recombinative desorption of CO1 and O2, including images of the main states. As in the low coverage, there are two minima along the MEP that correspond to the molecularly adsorbed states, bCO_2 and lCO_2, and two transition states, TS1 and TS2, that separate bCO_2 from IS and from lCO_2, respectively. The chemisorbed bCO_2 state with an energy of 0.15 eV respect to IS and with energy barriers to escape to lCO_2 and to IS of 0.08 eV and 0.65 eV, respectively, is also metastable in the intermediate coverage. The physisorbed state lCO_2, being -0.97 eV below IS and -0.29 eV below FS, becomes the lowest energy state in the reaction

path at the intermediate coverage. The corresponding physisorption well is located around 1.5 Å above the equilibrium adsorption site of $CO_{(ads)}$. Altogether, the activation barrier for CO oxidation is also governed at this coverage by TS1 and its value is 0.8 eV.

In other words, though, as shown in Table 3.9, the process is exothermic, it is necessary to give, at least, 0.8 eV to the system in order the CO oxidation can take place. In fact, this activation barrier for CO oxidation is larger by 0.22 eV than the energy required to desorb CO, suggesting that CO desorption would dominate over CO oxidation on the intermediate coverage. As for precedent coverage, this problem will be further discussed in the next Chapter 5.

3.3.4 High coverage (0.5ML O + 0.5ML CO on Ru(0001)

Equilibrium configuration

The proposed (O,CO)-mixed monolayer over the Ru(0001) surface, which is simulated by four adsorbed O and four adsorbed CO molecules in our 4×2 simulation cell, has ,as far as we know, not been obtained experimentally yet. However, as we will show below, it is a stable structure. We start studying the stability of those structures that are compatible with the initial p(2×1)-O overlayer that is formed in the experiments prior dosing the surface with CO. Thus, coadsorbed with p(2×1)-O_{hcp}, in which the four O atoms in our 4×2 unit cell adsorb in hcp sites, we consider the six possible p(2×1)-CO arrangements (depicted in Appendix D): adsorption in hcp, fcc, top sites, and three nonequivalent structures (bridge-a, bridge-b and bridge-c) that involve adsorption of the molecules in bridge sites. Note that in the bridge-a and bridge-c structures, the CO molecules are located in equivalent bridge sites, albeit different in each structure. In the bridge-b structure the CO molecules are equally distributed among two nonequivalent bridge sites. In five of these guess structures, all the CO molecules adsorb on equivalent sites, that is, on either hcp, fcc, top, bridge-a, or bridge-c sites. In the sixth structure, denoted bridge-b, the CO molecules are equally distributed among the two nonequivalent bridge sites.

O-structure	O site	CO initial site	CO final site	E(eV)	Z_{CO-Ru}(Å)
p(2×1)	hcp	top	desorbed	–	–
p(2×1)	hcp	hcp	hcp	0.000	2.20
p(2×1)	hcp	bridge-b	hcp	0.000	2.20
p(2×1)	hcp	bridge-c	hcp	0.000	2.20
p(2×1)	hcp	fcc	top-fcc	0.287	2.63
p(2×1)	hcp	bridge-a	top-fcc	0.292	2.63

Table 3.10: Results from the structural optimization for the 0.5 ML O + 0.5 ML CO coverage on Ru(0001), indicating the structure and adsorption sites of the O atoms, the initial and final adsorption sites of the coadsorbed p(2×1)-CO, the potential energy per simulation cell E referred to that of structure C, which is the lowest energy arrangement, and the height of the CO center of mass from the surface (defined as the average heights of the Ru atoms in the topmost layer) Z_{CO-Ru}.

Upon relaxation the adsorbates stabilize into one of the two structures, denoted structure C and D, represented in Fig. 3.16. The only exception is the guess structure with the CO molecules initially

adsorbed in on-top sites that end desorbing. The p(2×1)-(O_{hcp}+CO_{hcp}) structure is obtained when the CO adsorbates are initially on either hcp, bridge-b, or bridge-c. In this structure (hereafter denoted structure C), the CO molecules are located in the hcp sites with the molecular axis slightly tilted. This is the lowest energy structure at the high coverage. The second stable arrangement, p(2×1)-(O_{hcp}+$CO_{top-fcc}$) (hereafter denoted structure D), is found when the CO molecules are initially on either fcc or bridge-a sites. In this case, CO locates in the line joining the top and fcc sites with its molecular axis slightly tilted toward the fcc site. The energy of structure D is around 0.29 eV per simulation cell higher than that of the equilibrium structure C. The results of the structural search for the high coverage are summarized in Tab. 3.10.

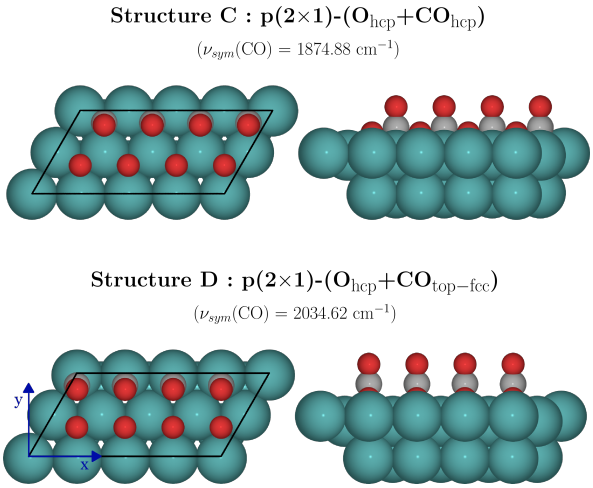

Figure 3.16: Top (left) and side (right) views of the two stable structures obtained for the 0.5 ML O + 0.5 ML CO coverage on Ru(0001). Top panels: the energetically most stable p(2×1)-(O_{hcp}+CO_{hcp}) structure. Bottom panel: p(2×1)-(O_{hcp}+$CO_{top-fcc}$) structure. The frequency of the in-phase C–O stretch mode is specified for each coverage. Color code: O atoms in red, C in gray, and Ru in blue. The black parallelograms show the surface unit cells in the calculations. For clarity, the periodic images of the O and CO adsorbates are not shown and only the two topmost Ru layers are depicted in the side views.

As previously, the distinct frequencies of the in-phase C–O stretch mode are given in the figure for the two optimized structures (Fig. 3.16). In common to the low and intermediate coverages, the highest frequency corresponds to CO adsorbed on near-top position. Interestingly, the high-coverage frequencies are around 30 cm^{-1} larger than the ones found for the intermediate and low coverages at similar adsorption sites. We ascribe this effect to the weaker CO-surface bound formed in the high coverage, that is reflected in the smaller CO adsorption energies that we obtain for this coverage (see below) as compared to the others. This effect, *i.e.*, the increase of the C–O stretch frequency with CO coverage (for the same adsorption site) has been observed and discussed for different metal surfaces.[197;198;199]

CO desorption and oxidation on structure C

Table 3.11 shows the calculated reaction energies for CO desorption and oxidation on structure C of high coverage. Since at this coverage all the CO molecules and all the O adsorbates are equivalent, the oxidation energy is only calculated for a pair of nearest CO and O neighbors. In common to structure

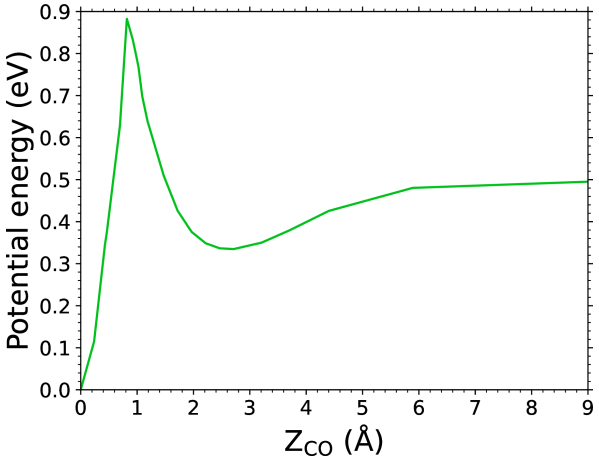

Figure 3.17: Potential energy of a CO molecule as a function of its center of mass height Z_{CO}, measured from its equilibrium adsorption position Z_{CO-Ru}. Results obtained for the 0.5 ML O + 0.5 ML CO coverage in the optimized structure C. The zero of energy is chosen as that of the equilibrium adsorption position.

A of the intermediate coverage, the energy values show that oxidation of CO is exothermic and the desorption endothermic. At the high coverage, the difference between the two reactions energies is around 1.88 eV, which is a notable value. However, as in previous cases, energy barriers could exist in the reaction paths that would imply the existence of activation energies governing the process even in the exothermic cases.

Reaction	adsorption site	E(eV)
$CO_{(ads)} \rightharpoonup CO_{(gas)}$	CO_{hcp}	0.488
$O_{(ads)}+CO_{(ads)} \rightharpoonup CO_{2(gas)}$	CO_{hcp}, O_{hcp}	−1.389
$CO_{(phys)} \rightharpoonup CO_{(gas)}$	CO_{phys}	0.155

Table 3.11: Reaction energies E for CO desorption and oxidation from the Ru(0001) surface with 0.5 ML O + 0.5 ML CO coverage in structure C. The initial adsorption site for each desorbing species is indicated as a subscript. The desorption energy from the physisorption well (CO_{phys}) is also provided.

Figure 3.17 shows the value of the potential energy as one CO desorbs from structure C of high coverage. Since at this coverage all the CO adsorbates are equivalent, only a single curve is calculated. Alike the intermediate coverage, the CO desorption curve confirms the existence of a physisorption well that in this case is located at around 2.7 Å from the chemisorption well. There is a new feature appearing in the high coverage that was not present at the lower coverages. The energy barrier of 0.883 eV separating both adsorption wells is notably larger than the calculated chemisorption energy of 0.488 eV and hence rules the desorption process. Additionally, the existence of this barrier can explain why this high coverage has not been achieved with the usual experimental techniques based on thermal deposition of CO under UHV conditions on the previously O-saturated surface. Indeed, it is extremely unlikely that thermally deposited CO molecules could gain the 0.395 eV required to overcome the barrier when coming from vacuum. In other words, the presence of this barrier is expected to prevent the CO molecules from being chemisorbed, so that this high coverage could be achieved.

The calculated MEP for the oxidation of CO is shown in Fig. 3.18 together with images of the configurations that correspond to the extremes of the path. As in the low and intermediate coverages,

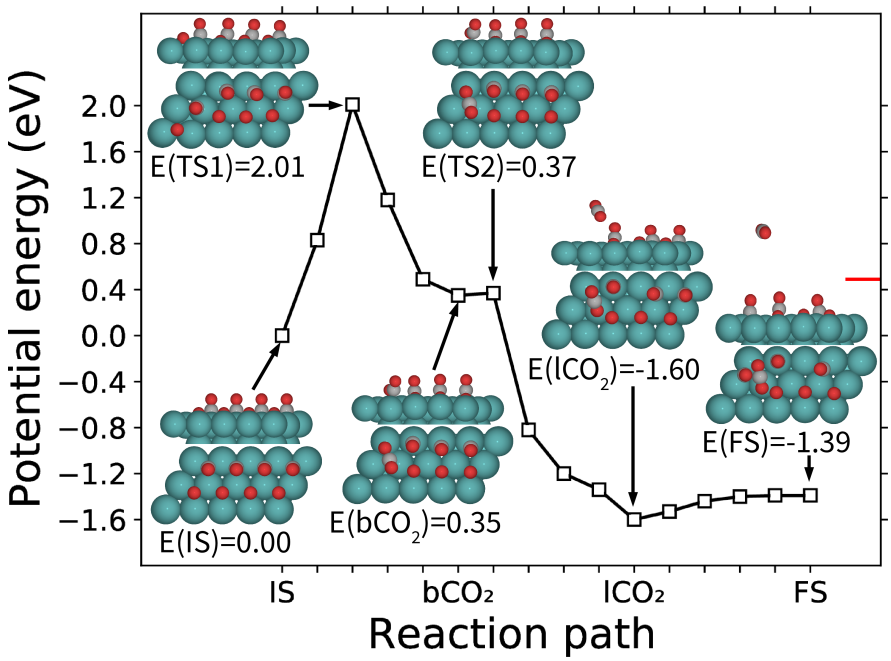

Figure 3.18: CI-NEB calculated minimum energy path (MEP) for the CO_2 recombinative desorption from Ru(0001) with the p(2×1)-(O_{hcp}+CO_{hcp}) coverage. Also are shown the top and side views of the relevant configurations along the path: the initial state $O_{(ads)}$ + $CO_{(ads)}$ (IS), the final state $CO_{2(gas)}$ (FS), the intermediate adsorption states (bCO_2 and lCO_2), and the transition states (TS1 and TS2). Their energies referred to IS are given in eV below each image. For comparison, the energy of the desorbed CO is also given by a red short-line on the top right of the figure. Color code: O in red, C in gray, and Ru in blue.

we identify two molecular adsorption states, the chemisorbed bCO_2 and the physisorbed lCO_2, and the corresponding transition states TS1 and TS2, separating the chemisorbed state from IS and from the physisorbed state, respectively. Qualitatively, the MEP is similar to the one found at the intermediate coverage. In particular, lCO_2 is the lowest energy state in the reaction path with an energy of -1.60 (-0.21) eV respect to IS (FS), while TS1 is the highest energy state located 2.01 eV above IS[2]. As in previous coverages, bCO_2 is metastable, being 1.66 eV and 0.02 eV the energy barriers to escape from this state to the dissociatively adsorbed $O_{(ads)}$ + $CO_{(ads)}$ state and to lCO_2, respectively.

Regarding the comparison with the CO desorption process, we observe that although, as stated previously, CO desorption is endothermic and CO_2 desorption exothermic, the activation barrier for this last process is not only much higher than the energy of the desorbed CO state (0.488 eV), but also much higher than the activation energy for CO desorption (0.883 eV).

3.3.5 Coverage comparison

In this section we compare the CO desorption curves and oxidation MEP between the different presented coverages. The CO desorption curves are compared in Fig. 3.19 for the different coverages. As a general trend, we observe a decrease in the desorption energy as the coverage increases. The

[2]In order to converge the subpath from IS to bCO_2 it was necessary to restrict the degrees of freedom to those of the recombining O+CO, while keeping the rest fixed. The ulterior relaxation of the TS1 configuration reduced the energy to 1.72 eV, but the new configuration is not a saddle point. Therefore, we estimate that the real TS1 must be in the range 1.72-2.01 eV.

energetics of desorption of CO for the cases in which there is only one CO in the simulation cell, and for the minimum coverage, is very similar except for a minor reduction of around 0.076 eV in the desorption energy in the presence of O. Increasing the O and CO coverages to 0.5 ML and 0.25 ML, respectively, causes a further reduction of 0.02 eV in the desorption energy. Clearly, the overall CO desorption energetics is very similar in these three low coverages, which is an indication of the minor influence exerted by the O adsorbates.

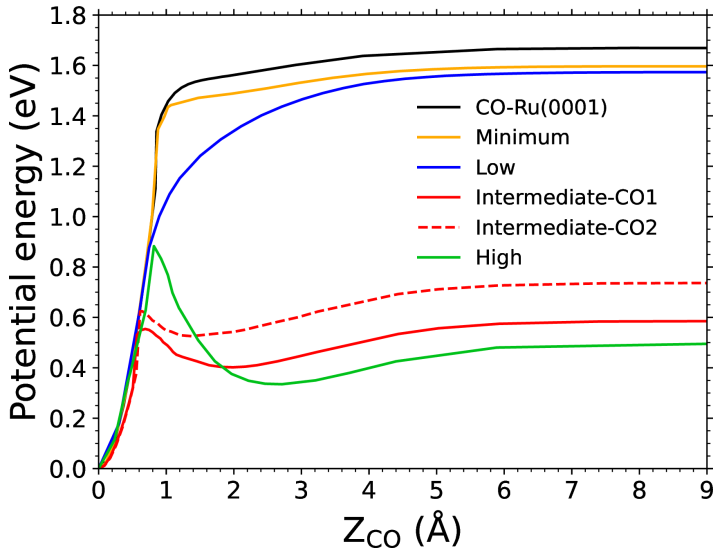

Figure 3.19: Potential energy of a CO molecule as a function of its center of mass height Z_{CO}, measured from its equilibrium adsorption position Z_{CO-Ru} at different coverages in their optimized structure. In all cases, the zero of energy is chosen as that of the corresponding equilibrium adsorption position. In the case of the intermediate coverage results for the nonequivalent CO1 (solid line) and CO2 (dashed line) adsorbates are shown.

In contrast, the CO desorption energy is drastically reduced when increasing the CO coverage from 0.25 ML to 0.375 ML and 0.5 ML, showing the limit at which the CO-CO dipole interaction becomes relevant and competes against the CO-surface binding. This is a common effect widely observed by different authors on different metals.[7;197;198;199;200;201]

Also the appearance of a stable physisorption well at the intermediate and high CO-coverages seems to be a consequence of the CO-CO interaction. The depth of the wells is similar for both coverages (E_{phys}(CO1)=0.178 eV and E_{phys}(CO2)=0.205 eV at the intermediate coverage and E_{phys}=0.155 eV at the high coverage, well depths measured from vacuum), but there are also differences between them. The distance between the minimum of the chemisorption and physisorption wells is 0.7 Å smaller in the case of intermediate-CO1 than at high coverage, and 1.3 Å smaller in the case of intermediate-CO2 than at high coverage. As a result, the energy barrier separating the molecularly chemisorbed and physisorbed states is visibly higher at the high coverage than at the intermediate coverage.

A simplistic explanation can be obtained in terms of a 1D picture of the Lennard-Jones model for chemisorption and physisorption at surfaces, pictured in Figure 3.20. In this figure we represent three potential curves, corresponding to the interaction of an atom/molecule X with a metal surface. In blue we show a potential energy curve with a chemisorption well. In red and green we show potential energy curves with physisoprtion wells at different heights from the surface. More precisely, the physisorption well of the green curve is located at a larger distance from the surface than the one of the red curve.

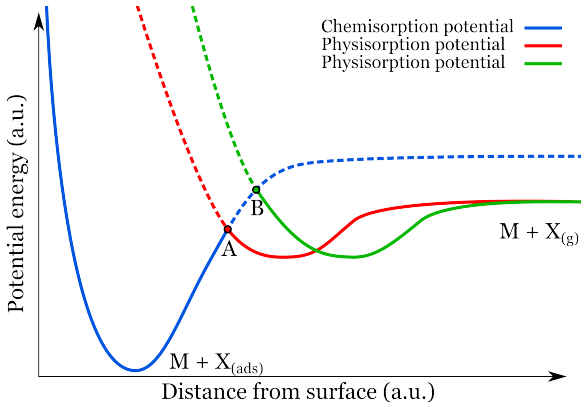

.

Figure 3.20: Scheme of the different potential curve for chemisorption and physisorption wells. The dashed lines represent the full chemisorbed (physisorbed) potential if not intersected by physisorbed (chemisorbed) potential. Inspired by 15;16;17

According to this simplified model, a barrier between physisorption and chemisorption wells appears at the crossing point between the chemisorption and physisorption curves (points A or B in Fig. 3.20). Therefore, due to the repulsive part of the physisorption potential, the energy at this crossing point will increase as the distance between those two wells increases. In the following, we consider the potential energy curves formed by taking together the chemisorption and physisorption potential energy curves (solid lines in Figure 3.20).

First, we consider the blue and red curves. In this case, the energy of the crossing point A between the physisoprtion and chemisorption regions is lower that the energy of the X atom/molecule in vacuum. As a consequence, there is no energy barrier to access the chemisorption well from vacuum. This case is the analogous to the situation at the intermediate coverage, in which there exists a physisorption well and no energy barrier to chemisorption.

Second, when we consider the blue and the green curves. We observe that the energy at the crossing point B is higher than the energy of the desorbed specie. Hence, in this case there exists an energy barrier to the chemisorption well when coming from vacuum. Therefore, this second case is the analogous to the case encountered at high coverage, in which there exists a physisoprtion well and also an energy barrier to chemisorption.

In conclusion, we see that depending on the distance separating the chemisorption and physisorption well, we observe the appearance or not of an adsorption barrier.

Back to our results, note that in both the intermediate and high coverages, the existence of the physisorption well is may limit the access to the chemisorbed state from gas-phase because of the physisorbed meta-stable state, then molecules from vacuum can loses energy and stay trapped in the physisorption well. In addition, completion of the 0.5 ML CO coverage is prevented by a large positive barrier of 0.395 eV (measured from vacuum) and as aforementioned, it explains that this coverage is not formed in the experiments by Kostov et al.[11].

In the diagram of Fig. 3.21 we compare the calculated MEP for the oxidation of CO on the different coverages. The figure shows schematically the energies of the relevant states along each reaction path, namely, the initial (IS) and final (FS) states, the two molecular adsorption states (bCO_2 and lCO_2),

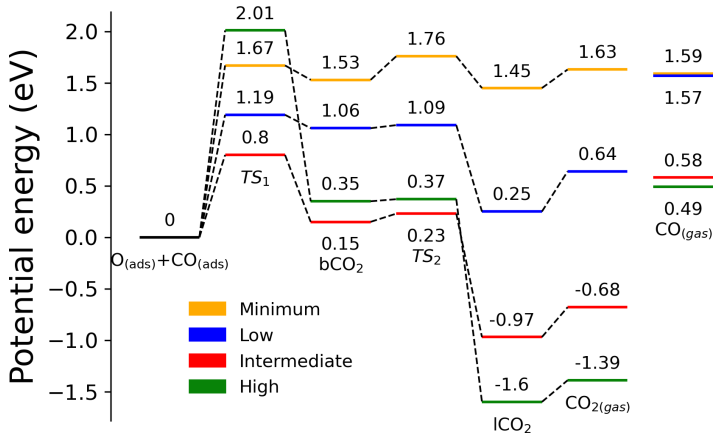

Figure 3.21: Schematic energy diagram comparing the oxidation of CO on the different covered surfaces for the relevant states along the MEP, including the initial (IS) and final (FS) states, as well as the extremes of the paths that are defined by the two molecular adsorption states (bCO_2 and lCO_2) and the two transition states (TS1 and TS2). For comparison the CO desorption energy is also shown for all coverages.

and the two transition states (TS1 and TS2). As observed for the CO desorption energy, the oxidative desorption energy (energy of FS) decreases as the coverage increases, although exhibiting a more monotonic dependence. As a result, the reaction changes from endothermic at the minimum and low coverages to exothermic at the intermediate and high coverages. A similar behavior is detected for oxidation into the lCO_2 state. However, the results for bCO_2, TS1, and TS2 at the high coverage break this tendency, since their corresponding energies are higher at the high coverage than at the intermediate coverage. This sudden increase can be due to the difficulty of forming the bCO_2 on the overcrowded surface, where the near adsorbates are necessarily too close and contribute to the energy increase. As a final observation, note that TS1 is the transition state with the highest energy and, therefore, governs the reaction at the low, intermediate, and high coverages. For the minimum coverage, TS2 is 0.09 eV more energetic than TS1 and constitutes the limiting step for CO oxidation in this case.

3.4 Bader charge, density of states and molecular orbitals analysis

During the process of oxidation of the CO, we observe the creation of different important states. In order to characterize with more precision those states, and shed light on their properties, we have performed two analyses. Those analyses come are complementary to the previous study presented in Section 3.3. The first one, the analysis of the Bader charge, will be carried out for the IS, bCO_2, lCO_2 and FS, and will serve to determine the distribution of the electronic charge. The second analysis will be limited to the minimum coverage and will consist in the calculation of the PDOS of the CO_2 molecule for all the steps in the reaction path presented in Figure 3.21. This will allow us to identify the MO of the CO and CO_2 molecules, and their modification during the oxidation process. We also have performed the PDOS analysis of the CO_2 molecule in the low, intermediate and high coverage, but we will not present the results here. The reason is that, the variation of the MOs of the CO_2 molecule for

the different coverages is minor. Nevertheless, the exist some differences in the MOs when varying the coverage, that will be mentioned in the text.

3.4.1 Bader charge analysis

Regarding to the two intermediate states in the CO oxidation reaction path, it has been previously stated that the bCO_2 and the lCO_2 states correspond to chemisorbed and physisorbed CO_2 states, respectively. A support for this statement can be achieved by the study of the eventual charge transfer between the molecule and the surface. For this reason, we have performed a Bader charge analysis[175] of the different relevant states along the reaction path, using the implementation provided by the Henkelman group.[176;178] Specifically, we perform calculations of the Bader charge of all the O and C atoms in the simulation cell, for the intermediate states bCO_2 and lCO_2, as well as for the adsorbed dissociated state and desorbed CO_2 gas state.

As already described in Chapter 2, the charge state of each atom is calculated as follows,

$$Q = Z - Q_{\mathrm{BC}}\,, \tag{3.3}$$

where Z and Q_{BC} are the atomic number and Bader charge[175] of the considered atom.

The latter is calculated with the implementation by Tang *et al.*[176] and Henkelman *et al.*[177]. Note that in using equation (3.3), negative (positive) values of Q indicate that the atom has captured (lost) $|Q|$ electrons. In the tables we have separated the atoms in three different sets. The first set, formed by two O atoms and one C atom, corresponds to the recombining CO_2 molecule. The second set is formed by the O and C atoms of the adsorbed CO molecules that do not recombine. Finally, the third set is constituted by the three adsorbed O atoms that do not recombine.

Label	atom	O+CO-Ru(0001)			
		IS	bCO_2	lCO_2	$CO_{2(gas)}$
1	O	-0.827	-1.039	-1.065	-1.040
2	O	-1.046	-0.998	-1.060	-1.058
3	C	0.806	1.451	2.085	2.098

Table 3.12: Charge state Q of the atoms forming the CO_2 molecule calculated at different configurations along the oxidative MEP found for the minimum coverage: the initial $O_{(ads)}$ + $CO_{(ads)}$ state (IS), the chemisorbed bCO_2 state, the physisorbed lCO_2 state, and the final $CO_{2(gas)}$ state (FS).

First, we study the minimum coverage case. The Q values associated to this coverage obtained for CO_2 are shown in Table 3.12. In the gas phase CO_2, we observe electronic transfer from the C atom to the O atoms, reflected in the negative charge of the O atoms and the positive charge of the C atom. This transfer amounts to two electrons, one for each oxygen. This is due to the higher electronegativity of O as compared to that of C. In the IS state we also observe electronic transfer between the surface and the adsorbed O atom. Also in this state, a net charge transfer of $0.2e^-$ between the surface and the CO molecule is observed, which is reflected in the fact that the negative charge of the O atom is not compensated by the positive charge around the C atom. Similarly, in the bCO_2 state a charge transfer of $0.6e^-$ exists between the surface and the bCO_2 molecule, this justifies the identification

of this state as a chemisorbed state. On the contrary, in the case of lCO_2 the charge distributions is, roughly, the same as in the case of $CO_{2(gas)}$, *i.e.*, no charge transfer between the lCO_2 state and the surface is observed. Indeed, this is the manifestation of the physisorbed nature of the lCO_2 state.

Label	atom	0.5 ML O + 0.25 ML CO			
		IS	bCO_2	lCO_2	CO2(gas)
1	O	-0.753	-0.895	-1.089	-1.065
2	O	-1.039	-1.021	-1.026	-1.027
3	C	0.936	1.321	2.112	2.092
4	O	-1.046	-1.032	-0.996	-1.015
5	C	0.941	0.912	0.886	0.856
6	O	-0.784	-0.775	-0.830	-0.810
7	O	-0.784	-0.773	-0.795	-0.794
8	O	-0.753	-0.704	-0.743	-0.733

Table 3.13: Charge state Q of the adsorbates calculated at different states along the oxidative MEP for the low coverage honeycomb structure: the initial lcoois state (IS), the chemisorbed bCO_2 state, the physisorbed lCO_2 state, and the final $CO_{2(gas)}$ state (FS). The desorbing CO_2 is formed by atoms 1 to 3, the adsorbed CO by 4 and 5, and the adsorbed O atoms correspond to atoms 6 to 8.

Tables 3.13, 3.14 and 3.15, show the values of the charges Q for the different states along the oxidative desorption MEP for the honeycomb structure of the low coverage, the A structure of the intermediate coverage, and the C structure of the high coverage, respectively. Albeit minor differences in the absolute values of the charges, the same considerations apply to all these coverages.

The first observation is that for the four considered states, the charge distribution around the non recombining O and CO adsorbates is practically the same, irrespective of the state of the CO_2 molecule. As for minimum coverage, the chemisorbed nature of the adsorbed O atoms is apparent from the noticeable electronic transfer from the surface to these atoms that amounts between 0.6 to 0.8 electrons. In the case of the adsorbed CO molecule, apart from the electronic redistribution in the molecular bond which leads to polarized molecules, we also observe electronic transfer from the surface to the molecule (around 0.10-0.20 electrons) that reflects the chemical bond between the CO and the surface.

As noted in minimum coverage, in the desorbed $CO_{2(gas)}$ we observe the transfer of 2 valence electrons of the C atom to the more electronegative O atoms. Interestingly, roughly the same distribution of charge is obtained in the case of the lCO_2 state. This is important, because it definitely shows the absence of charge transfer and the non existence of chemical bond between the lCO_2 and the Ru(0001) surface, and this state is considered as physisorbed independent of the surface coverage.

In contrast, for the the bCO_2 state the charge distribution is quite different. First, the amount of electrons around one of the O atoms is reduced by $\sim 0.1e^-$ as compared to the isolated CO_2 case. It reflects that both oxygens of the CO_2 molecule are not equivalent by symmetry. On the other hand, the C atom experiences an increase in the number of electrons as compared to the isolated $CO_{2(gas)}$ molecule that amounts around 0.6-0.7 electrons. Additionally, the bCO_2 molecule has a whole gain of around 0.6 electrons that are transferred from the surface. This constitutes a clear indication of the existence of a chemical bond between the molecule and the surface, and of the chemisorbed nature of

Label	atom	0.5 ML O + 0.375 ML CO			
		IS	bCO_2	lCO_2	CO2(gas)
1	O	-0.755	-0.929	-1.081	-1.014
2	O	-1.006	-1.045	-1.058	-1.016
3	C	0.958	1.393	2.127	2.030
4	O	-1.044	-1.014	-1.024	-0.992
5	O	-1.051	-1.034	-1.033	-1.061
6	C	0.953	0.932	0.892	0.857
7	C	0.981	0.990	0.936	0.976
8	O	-0.739	-0.729	-0.735	-0.743
9	O	-0.766	-0.774	-0.787	-0.792
10	O	-0.741	-0.739	-0.800	-0.797

Table 3.14: Charge state Q of the adsorbates calculated at the IS, bCO_2, lCO_2, and FS states along the oxidative MEP for structure A of the intermediate coverage. The desorbing CO_2 is formed by atoms 1 to 3, the two adsorbed CO by atoms 4 to 7, and the adsorbed O correspond to atoms 8 to 10.

the bCO_2 state. We thus demonstrate that the identification of the bCO_2 and lCO_2 as chemisorbed and physisorbed states, respectively, is also valid for these higher coverages.

Label	atom	0.5 ML O + 0.5 ML CO			
		IS	bCO_2	lCO_2	CO2(gas)
1	O	-0.682	-0.989	-1.063	-1.038
2	O	-0.935	-1.043	-1.065	-1.046
3	C	0.728	1.517	2.128	2.084
4	O	-0.935	-1.037	-0.987	-0.974
5	O	-0.935	-0.992	-0.983	-1.004
6	O	-0.935	-1.003	-1.009	-0.991
7	C	0.728	1.027	0.701	0.703
8	C	0.728	0.966	0.778	0.782
9	C	0.728	0.935	0.925	0.919
10	O	-0.682	-0.763	-0.748	-0.747
11	O	-0.682	-0.745	-0.723	-0.723
12	O	-0.682	-0.749	-0.761	-0.767

Table 3.15: Charge state Q of the adsorbates calculated at the IS, bCO_2, lCO_2, and FS states along the oxidative MEP for structure C of the high coverage. The desorbing CO_2 is formed by atoms 1 to 3, the three adsorbed CO by atoms 4 to 9, and the adsorbed O correspond to atoms 10 to 12.

3.4.2 Density of states and molecular orbitals analysis

We calculate the PDOS of the CO_2 molecule in order to identify its molecular orbitals and to study how they are modified at different steps along the MEP of CO oxidation reaction. We first calculate the distribution of states as a function of energy of the CO and CO_2 molecules in vacuum. Thus we can recognize the MOs of both molecules without any deformation due to an external perturbation. Secondly, in order to understand the reasons of the deformation of the MOs of the CO_2 when it is adsorbed on the ruthenium surface, we will present the Blyholder model and its improvements with

π-σ model. Third, we calculate for the different surface coverages presented in Section 3.3, the PDOS of each atom composing the CO_2 molecule and identify the MOs of the CO_2 during the reaction. In this way we can study the effect of the ruthenium surface and the coverage on the MOs of the CO_2. Even though, we have performed the same analysis for all coverages, we present here only the results for the minimum coverage. As we observe only small changes between the MOs between the different coverages, we simply mention those differences in the text.

Molecules in vacuum

In Figure 3.22 we present the calculated PDOS of O and C atoms composing the CO molecule in vacuum. For each peak, we calculate the associated charge density corresponding to the MOs of the CO molecule, and represent it as an inset. In this case it is easy to identify the MOs of the molecule because they are well defined in a range of energy. In Figure 3.22, we identify the 3σ, 4σ, 1π, 5σ, $2\pi^*$ MOs of CO denoted respectively from 1 to 5.

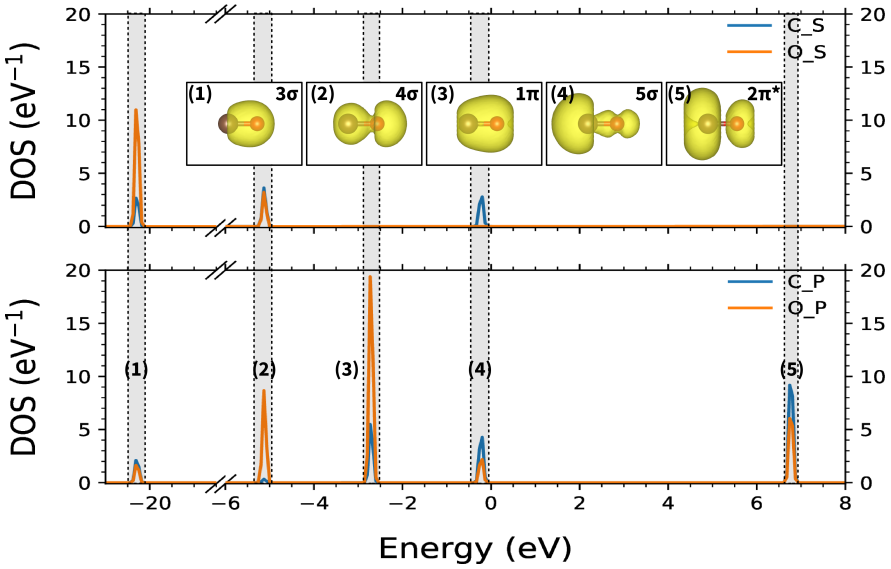

Figure 3.22: Density of state plot of $CO_{(gas)}$ molecule in vacuum, with representation of the calculated charge for the energy range represented in gray area. On energy axis, zero corresponds to Fermi level. Top plot shows the contribution of S orbitals when bottom plot shows the contribution P orbitals. Inset images correspond to the density of charge calculated in the gray area identified with the same number. In blue is the DOS of the carbon atom. In orange is the DOS of the oxygen atom. Molecular orbitals are labeled such 3σ **(1)**, 4σ **(2)**, 1π **(3)**, 5σ **(4)**, $2\pi^*$ **(5)**

In order to differentiate the σ and π orbitals, we define z as the axis oriented along the C-O bond. Thus in Cartesian coordinates the σ bonds/orbitals are the ones oriented along the z axis. In the case of the π bonds/orbitals, they are located in the xz and yz planes. In the absence of an external perturbation, the xz and yz orbitals are equivalent under rotations of 90° around the z axis because they have degenerated energy. We observe for the CO molecule that the two π orbitals 1π, $2\pi^*$ (**(3)** and **(5)** in Figure 3.22) are degenerated. However, in the insets, the two MOs are represented together and, then we cannot differentiate one from the other. We remark that the energetic order of the MOs of the CO is in agreement with literature.[202] The HOMO-3 (3σ) is mostly composed of S atomic orbital

from C and O which makes it more stable and lower in energy. The other MOs are mainly composed of P atomic orbitals of C and O.

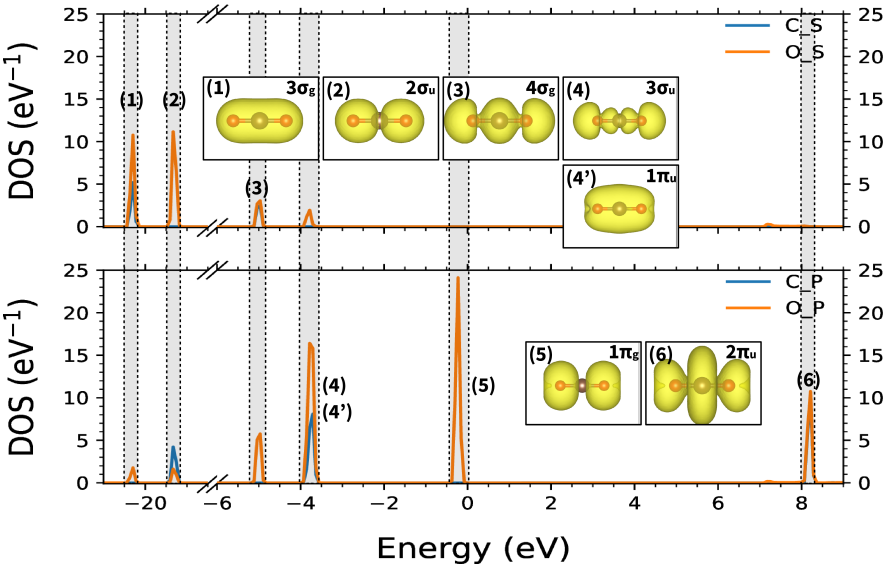

Figure 3.23: Density of state plot of $CO_{2(gas)}$ molecule in vacuum, with representation of the calculated charge for the energy range represented in gray area. On energy axis, zero corresponds to Fermi level. Top plot shows the contribution of S orbitals when bottom plot shows the contribution P orbitals. Inset images correspond to the density of charge calculated in the gray area identified with the same number. In blue is the DOS of the carbon atom. In orange is the DOS of the the sum of both oxygen atoms. Molecular orbitals are labeled such $3\sigma_g$ **(1)**, $2\sigma_u$ **(2)**, $4\sigma_g$ **(3)**, $3\sigma_u$ **(4)**, $1\pi_u$ **(4')** , $1\pi_g$ **(5)**, $2\pi_u$ **(6)**

In Figure 3.23 we present the calculated PDOS of O and C atoms composing the CO_2 molecule in vacuum. We identify the MOs of the $CO_{2(gas)}$ being, $3\sigma_g$, $2\sigma_u$, $4\sigma_g$, $3\sigma_u$, $1\pi_u$, $1\pi_g$, $2\pi_u$ numbered respectively from 1 to 6 in Figure 3.23. The energetic order of the MOs of the CO_2 are in agreement with literature.[18] Compared to $CO_{(gas)}$, in the case of $CO_{2(gas)}$ there are not one but two MOs mostly composed of S atomic orbitals, which are $3\sigma_g$, $2\sigma_u$ (**(1)** and **(2)** in Figure 3.23). Also for CO_2, there are three degenerated π orbitals, which are $1\pi_u$, $1\pi_g$, $2\pi_u$. They are represented in the insets **(4)**, **(5)**, **(6)** of Figure 3.23. We also note that $3\sigma_u$ and $1\pi_u$ are very close in energy, thus we find both MOs in the same range of energy labeled **(4)** and **(4)'**.

The important point of this section is to identify the MOs of the CO and CO_2 molecules. However, we know that during the CO oxidation reaction the CO_2 molecule adopt a bent configuration called bCO_2. The effect of bending a triatomic molecule on its MOs is described by the so-called Renner-Teller effect,[203] and can be represented in a Walsh diagram. For this reason, in Figure 3.24, we present the qualitative Walsh diagram of the CO_2 molecule in linear and bent configurations. On the right-hand side, the insets represent the MOs of the linear CO_2 in vacuum as presented in Figure 3.23, and in the left-hand side the CO_2 molecule bent at $\widehat{OCO} = 157$ °,corresponding to TS2 state of the MEP of CO oxidation on the minimum coverage. In Figure 3.24, we observe that when we bend the CO_2 molecule from 180° to 90°, all energetic levels of the MOs are modified. This bending introduces an asymmetry which causes minor changes for σ MOs, but major ones for π orbitals due to the break of symmetry. This is particularly remarkable for the $2\pi_u$ orbitals, for which the split of the two orbitals creates a huge gap between the two new energy levels named $2b_1$ and $6a_1$. This effect is of great importance

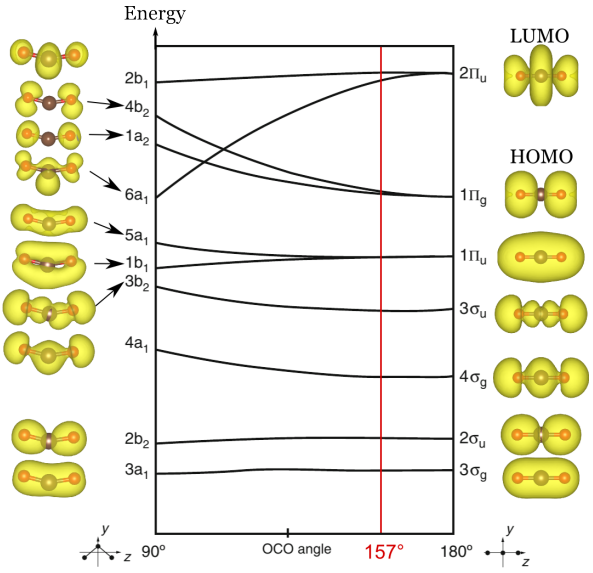

Figure 3.24: Qualitative Walsh diagram for CO_2 molecule. The red line depict the CO_2 molecular angle $\widehat{OCO} = 157°$. As inset on the right side are shown the MOs of the linear CO_2 molecule in vacuum, and on the left side the CO_2 molecule in the chemisorbed well with $\widehat{OCO} = 157$ ° angle. The π MOs for linear CO_2 are the sum of the contribution of the two degenerated MOs. Modified from ref.[18].

because by decreasing the HOMO-LUMO gap, it helps to populate the $2\pi_u$ orbital, with for instance back-bonding[204] as described in the Blyholder[54;205] model (explained in the following Section 3.4.2). Note that in the case of $\widehat{OCO} = 157$ ° there is no level crossing.

Models for molecular orbital interactions with a transition metal surface

In the frontier orbital point of view, the HOMO and the LUMO orbitals are the ones assumed to have the greatest effect on the adsorbate chemistry. This effect can be described using the Blyholder[54;205] model first presented in 1964. In the case of the CO molecule, the HOMO and LUMO orbitals are the 5σ and the $2\pi^*$. In the Blyholder model, when a CO molecule adsorbs on transition metal surface, it forms a dative bond between the 5σ of the CO and a metal state with σ symmetry, leading to a charge donation of 2 electrons from CO to the metal. This donation is partially compensated by a back-donation of the metal through its π orbitals into the empty CO $2\pi^*$. Figure 3.25 shows a sketch of the Blyholder model for the dative bond in the left-hand panel and the π back-bonding in the right-hand panel. In this model, the population of the $2\pi^*$ orbital of the CO leads to a weakening of the C-O bond, and creation of Ru-C bond.

The simple description of the Blyholder model was improved later by Nillson and Pettersson in their $\pi - \sigma$ model,[19] in order to take into account the 1π and 4σ orbitals that have been neglected in the former model (HOMO-1 and HOMO-2 of the CO molecule in vacuum). They introduce the concept of tilde molecular orbitals, that are MOs hybridized with the d-bands of the metal. They used X-ray Emission Spectroscopy (XES) and spacial charges calculations to corroborate their model.[19] They observe, for the CO molecule, that the π system of the molecule is bonding to the transition metal, while the σ system is repulsive, which contrast with the Blyholder model where the σ system is

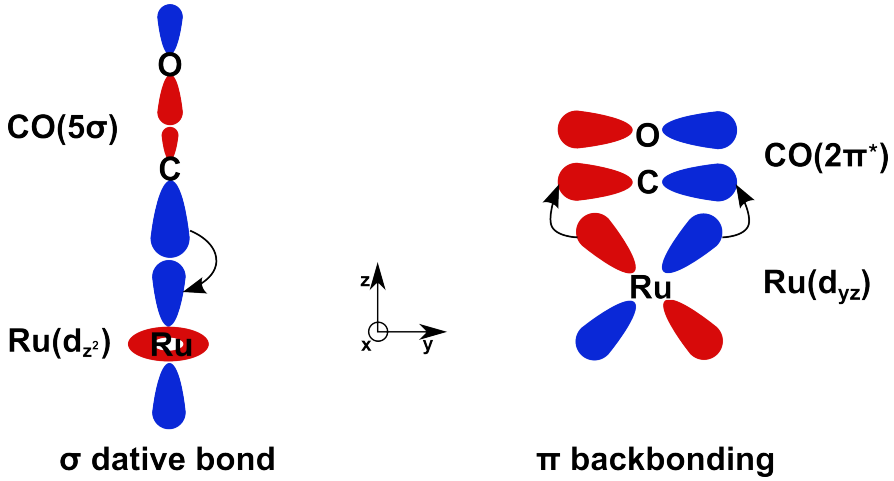

Figure 3.25: Representation of the Blyholder model for CO adsorbed molecule on Ru. In blue and red are represented the orbitals of the atom. The arrows represent an exchange of electron. Left: dative bonding (sigma donation) scheme between CO 5σ orbital and Ru d_{z^2}. Right: represent back donation scheme between Ru d_{yz} and CO $2\pi^*$ depending on orientation.

bonding. They also observed that according to their model, this effect of bonding/repulsion increases with the coordination number between the CO molecule and the metal atom. In the $\pi - \sigma$ model, the repulsive σ system is composed of the $\tilde{d_\sigma}$ orbital defined as a hybrid of the unperturbed 5σ of the CO molecule and the d_{z^2} of the metal. It is somehow the equivalent of the dative bond in the Blyholder model, but repulsive in this case. Also composing the σ system, the $4\tilde{\sigma}$ and $5\tilde{\sigma}$ are hybrids of the 4σ and 5σ orbitals with the d-band of the metal. In the case of the π bonding system, it is composed of three CO hybrid orbitals $1\tilde{\pi}$, $\tilde{d_\pi}$ and $2\tilde{\pi}^*$. Those tilde orbitals are such that, $\tilde{d_\pi}$ is a hybrid of the unperturbed 1π and $2\pi^*$ orbitals of the CO and $d_{xz,yz}$ of the metal. An "indirect" back-donation effect is comprised in the hybridization of the $2\pi^*$ and $d_{xz,yz}$. Generally, the $\tilde{d_\pi}$ intensities are in the energy range between the $5\tilde{\sigma}$ and the Fermi level. Then, the $1\tilde{\pi}$ and $2\tilde{\pi}^*$ are respectively hybrid orbitals of the 1π and $2\pi^*$ with the d-band of the metal.

In the Figure 3.26 we show the XES spectra of CO molecule in the gas phase (in the bottom panels) and adsorbed on Cu(100) transition metal (in the top panels). This figure is obtained using the data presented in ref.[19]. The spectra are plotted on a common binding energy scale relative to the Fermi level, obtained by subtracting the C or O 1s core-level photoemission binding energies of the two atoms, from the emission energies of the corresponding atom. On the top panels, we see the $\tilde{d_\pi}$ and $\tilde{d_\sigma}$ orbitals when the CO adsorbs on the surface. We observe for the adsorbed molecule a shift of $1\tilde{\pi}$ towards the Fermi level as compared to the energy position of the 1π orbital of $CO_{(gas)}$. Additionally, in the left panels of Figure 3.26 we see that the non-perturbed 4σ and 5σ MOs of the CO molecule in gas phase are respectively at higher and lower energies than the perturbed $4\tilde{\sigma}$ and $5\tilde{\sigma}$ of the CO adsorbed on Cu(100). We do not observe the $2\tilde{\pi}^*$ in XES spectra because this orbital is empty, then one should perform X-ray Absorption Spectroscopy (XAS) to visualize it.

In Figure 3.27 we present the contour plots of the σ and π orbitals of the CO molecule when the molecule is in the gas phase and when it adsorbs on Cu(100) (modified figure from ref.[19]). The effect of the CO adsorption can be visualized in the contour plot of the $5\tilde{\sigma}$ MO. This orbital couples to

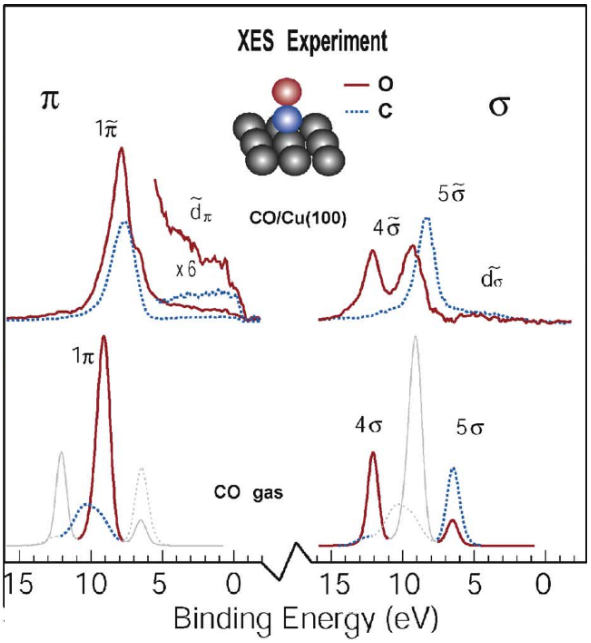

Figure 3.26: XES spectra of CO in gas phase and adsorbed on Cu(100). On left (right) panel is represented the π (σ) system. Light gray curve in the $CO_{(gas)}$ spectra are the corresponding σ or π peaks position. Modified from ref.[19].

the metal surface which induces an inversion of its polarization. In the case of the $2\tilde{\pi}^*$ we also see an intense coupling with the surface.

With the help of this model, we will examine the energetic levels of the MOs for the CO oxidation on the Ru(0001) in the minimum coverage case, and the deformation of their MOs.

CO and CO_2 MOs on the Ru(0001) surface

Here, we study the variation of the MOs of the CO_2 along the 6 steps of the MEP of the CO oxidation reaction on the Ru(0001) for the minimum coverage case. In Figure 3.28 we present the PDOS and MOs of the CO an O adatom composing the CO_2 molecule for each step of the MEP as introduced in Subsection 3.3.1, but in the reverse order (FS, lCO_2, TS2, bCO_2, TS1, IS) in order to go from the (non-deformed) gas-phase MOs to the (deformed) hybridized MOs. This figure is separated in six panels, from A to F, with each panel corresponding to a different step of the MEP of CO oxidation. As an example, the first panel A shows in blue the sum of the PDOS of the atoms composing the initial CO molecule, and in orange the PDOS of the initial O adatom. In the top (bottom) panel, we illustrate the PDOS on the atomic S (P) orbitals. We also calculate the charge density corresponding to the finite energy ranges depicted by grey rectangles. The associated picture of the MO is added as a numbered inset in the figure.

Figure 3.28.A shows the results for the FS of the CO oxidation MEP corresponding to the minimum coverage case. We observe that the MOs and the PDOS of the CO_2 molecule resemble the ones in Figure 3.23 when the CO_2 molecule is in vacuum. In the following, we use panel A as a reference for non-deformed PDOS and MOs of the CO_2 molecule in gas phase. In addition, all panels share the same Fermi energy, so that we can compare them directly with panel A.

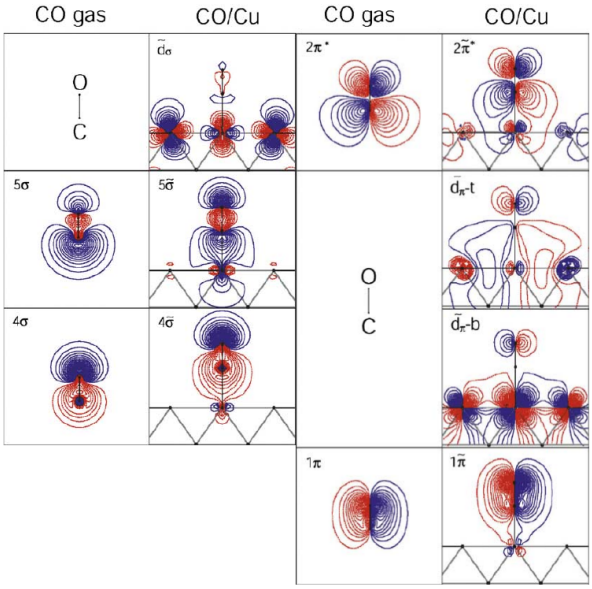

Figure 3.27: Contour plot σ and π systems of CO in gas phase and adsorbed on Cu(100). On left (right) panel is represented the σ (π) system. Modified from ref.[19]

Figure 3.28.B shows the results in the lCO_2 state. We first note that the CO_2 molecule remains in a linear configuration. Secondly, we note that in the PDOS the peaks corresponding to the orbitals $4\sigma_g$, $3\sigma_u$, $1\pi_u$ and $2\pi_u$ (respectively **(3)**, **(4)**, **(4')**, **(6)** in Figure 3.28.B) are split into two peaks close in energy. We attribute this variation of the PDOS to the long-range vdW interactions in the physisorption well.

Figure 3.28.C shows results for TS2. Let us remark that the CO_2 molecule is bent. As a result, as shown in the Walsh diagram presented in Figure 3.24, mainly the π orbitals change their shape. The peak corresponding to the $1\pi_g$ orbital (HOMO) is now split into two peaks forming the $1a_2$ and $4b_2$ orbitals. At the same time, the $1\pi_u$ orbital is separated into $1b_1$ and $5a_1$ (respectively **(4)** and **(5)** in Figure 3.28.C). Additionally, $3\sigma_u$ is modified into $3b_2$ (numbered **(4')** in Figure 3.28.C), which is higher in energy and hence closer to the $1b_1$ orbital. The latter explains why we find $1b_1$ and $3b_2$ in the same range of energy in the PDOS. Also the LUMO, originally $2\pi_u$, splits into $2b_1$ and $6a_1$ orbitals. Thus we see in the PDOS the increase of the gap between the two peaks corresponding to the $2\pi_u$ orbitals according to the Renner-Teller effect and the Walsh diagram (Fig. 3.24). Our results for bCO_2 in vacuum are in good agreement with ref.[82;206]. We note in the PDOS that the energies corresponding to $6a_1$ are spread over an energy range of about 1 eV. This behavior has also been observed by Chernyshova and coworkers.[79] It is important to remember that although the molecule in TS2 is close to the surface, it is still not bonding to the surface.

Figure 3.28.D shows results for the bCO_2 state. We observe that the σ MOs $3a_1$ and $2b_2$ (**(1)** and **(2)** in Figure 3.28.D) are higher in energy than for the TS2 configuration. In the PDOS we find that the energy position of $4a_1$ is the same as in TS2, but we observe an hybridization of this orbital with the d_{z^2} of the surface. This leads to a change in the orbital shape that can be observed in the inset **(3)** of Figure 3.28.D. The new hybridized orbital is denoted $4\tilde{a}_1$. Note also that the gap between $1b_1$ and $5a_1$ in the PDOS is increased. This is due to the hybridization of $1b_1$ with the ruthenium d_{z^2} orbitals to

form $1\tilde{b}_1$, which is also confirmed by the change in the orbital shape (see inset **(4)** of Figure 3.28.D). Hybridization of the (gas-phase) $4b_2$, $5a_1$, and $1a_2$ MOs with the Ru d_{z^2}, which is also observed in the Ru-projected PDOS (not presented here), gives rise to the new $4\tilde{b}_2$, $5\tilde{a}_1$ and $1\tilde{a}_2$ MOs, respectively. Finally, hybridization of the $2b_1$ MO with the Ru $d_{xz,yz}$ leads to the new $2\tilde{b}_1$ MO. The hybridization of all those MOs is due to the fact that the molecule is in a chemisorbed state. In the case of the minimum coverage, we did not distinguish the $6a_1$ state in the PDOS. However, in the intermediate and high coverage cases, we observe the $6a_1$ orbital and that it hybridizes with the surface forming the $6\tilde{a}_1$ orbital. It is worth to mention that Chernyshova *et al.*[79] have also observed the $6\tilde{a}_1$ MO when CO_2 is adsorbed on the Cu(111) surface in its bCO_2 state with an extra Na atom bound to it.

Figure 3.28.E shows the results for TS1. In the case of the minimum coverage, there are no significant differences between the results obtained for TS1 and bCO_2 for both the PDOS and the orbital shapes of the CO_2 molecule. However, we observe differences between bCO_2 and TS1 in the case of the low, intermediate, and high coverages. Specifically, CO_2 $3\sigma_u$ orbital is still not formed in any of the corresponding TS1 configurations. Instead, for these three higher coverages, we observe the CO 3σ MO and the S orbital of the O adatom, *i.e.*, the orbitals from which the CO_2 $3\sigma_u$ will be formed. We attribute the differences between the higher coverages and the minimum surface coverage to the fact that the distance between CO and O in TS1 is larger for the former cases than for the latter.

Finally, Figure 3.28.F shows the results for IS. As a first observation note that the orbitals corresponding to the peaks **(2)** and **(6)** in the PDOS of Figure 3.28.F are completely located on the oxygen adatom. We identify the one corresponding to peak **(2)** as the S atomic orbital of the oxygen adatom. The one corresponding to the peak **(6)** is the P atomic orbital of the same oxygen with some contribution of the ruthenium d-band. Second, we note that the lowest energy orbital is the 3σ as in the case of $CO_{(gas)}$. Third, the hybridized $4\tilde{\sigma}$ orbital reverts its polarization respect to that of the 4σ $CO_{(gas)}$, since there is more electronic density around the C atom than around O (compare the insets **(3)** between Figs. 3.28.F and 3.28.A). This change is consistent with the π-σ model (Fig. 3.27). The same result has been observed by Fohlisch and coworkers.[49] Fourth, the 5σ orbital (**(4)** in Figure 3.28.F) is similar to the 5σ orbital of $CO_{(gas)}$ but modified due to some transfer of charge to the ruthenium surface. Indeed, there exists a coupling between the d_{z^2} orbital of the ruthenium with the 5σ orbital of CO, leading to the $5\tilde{\sigma}$ orbital, shown in Fig. 3.27. A fifth and very interesting observation is that the 1π orbitals is the HOMO-1 in the IS instead of being the HOMO as it was the case for $CO_{(gas)}$. This is the result of a level crossing between the 1π orbital and the $5\tilde{\sigma}$ orbital, which is a behavior described by the π-σ model when CO adsorbs on a transition metal surface. The π-σ model also describes the hybridization of the 1π orbital with the metal *d* electrons that we observe, and that results in the $1\tilde{\pi}$ orbital. Several experimental and theoretical works[12;67;72] have also observed this level crossing for CO adsorbed on Ru(0001). Finally, we observe that the degenerated $2\pi^*$ orbitals (**(7)** and **(7')**) in Figure 3.28.F are spread in an energy range of 2 eV, noticeably wider than when the CO is in vacuum. The reason is that those orbitals hybridize with the $d_{xz,yz}$ orbitals of the ruthenium surface and become $2\tilde{\pi}^*$ orbitals. Our results are in good agreement with Fohlisch *et al.*[49], who find that both the σ- and π-electronic structures of the adsorbate result from the hybridization of the initial CO orbitals with the metal states, leading to a significant modification of the orbital structure in comparison to free CO.

It should be mention that for the IS we find at the high coverage one important difference not observed in the other cases. The polarization of $5\tilde{\sigma}$, that is not reversed for the other coverages, it is completely reversed in the high coverage case. These change of polarization of the repulsive sigma system, can be related to the lower adsorption energy of CO at the high coverage.

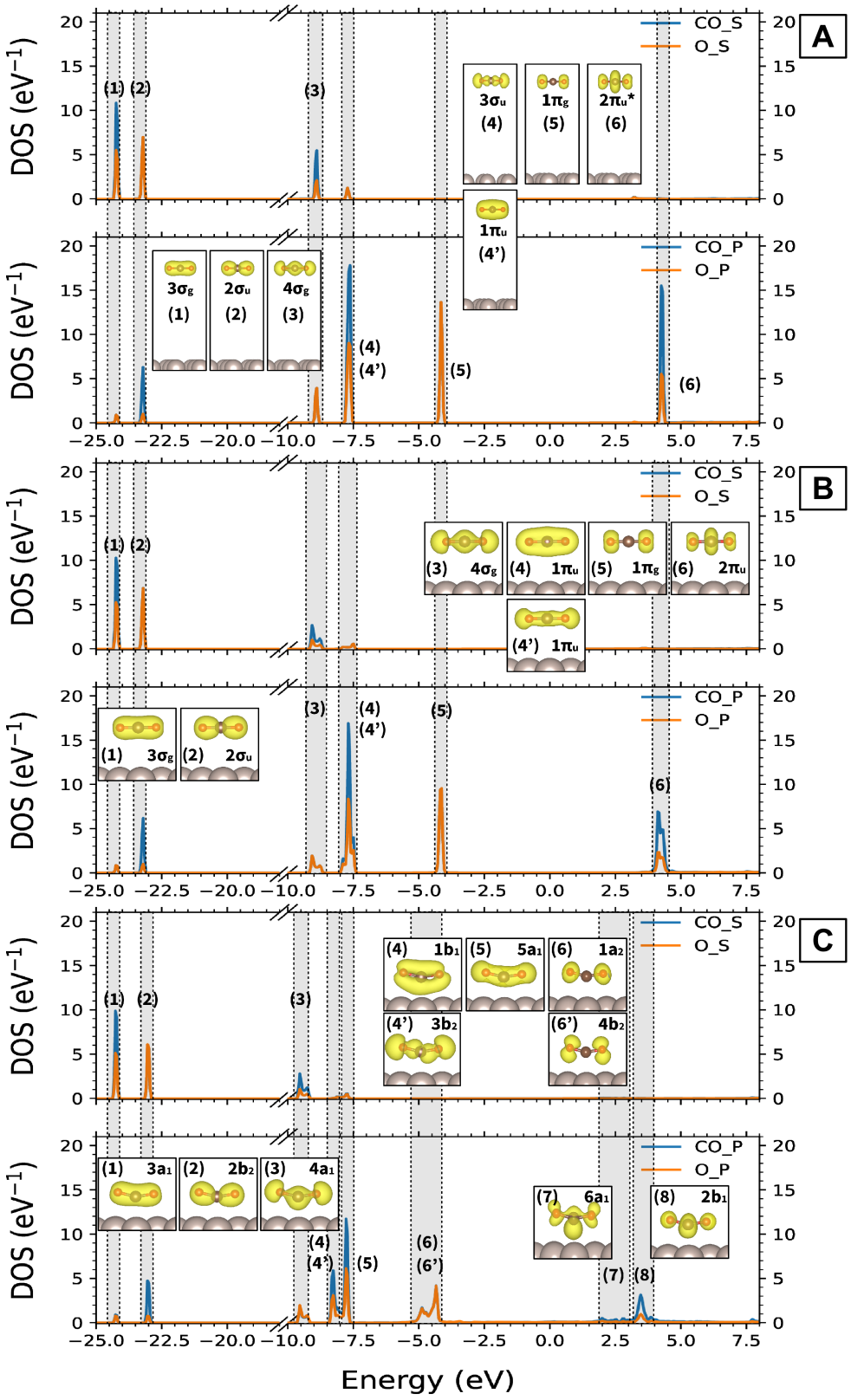

Figure 3.28: Projected density of states (PDOS) calculated at different states along the MEP for $O_{(ads)} + CO_{(ads)}$ recombination in the minimum coverage: (A) FS, (B) lCO_2 and (C) TS2. The zero energy corresponds to the Fermi level. For each state, the top and bottom PDOS show the contribution of S and P atomic orbitals, respectively. Blue curves shows the sum of the PDOS of the C and O atoms forming the CO molecule and orange curves the PDOS of the O adatom. Each image in the inset corresponds to the partial electronic density calculated within the energy range marked by the gray area that is identified with the same number.

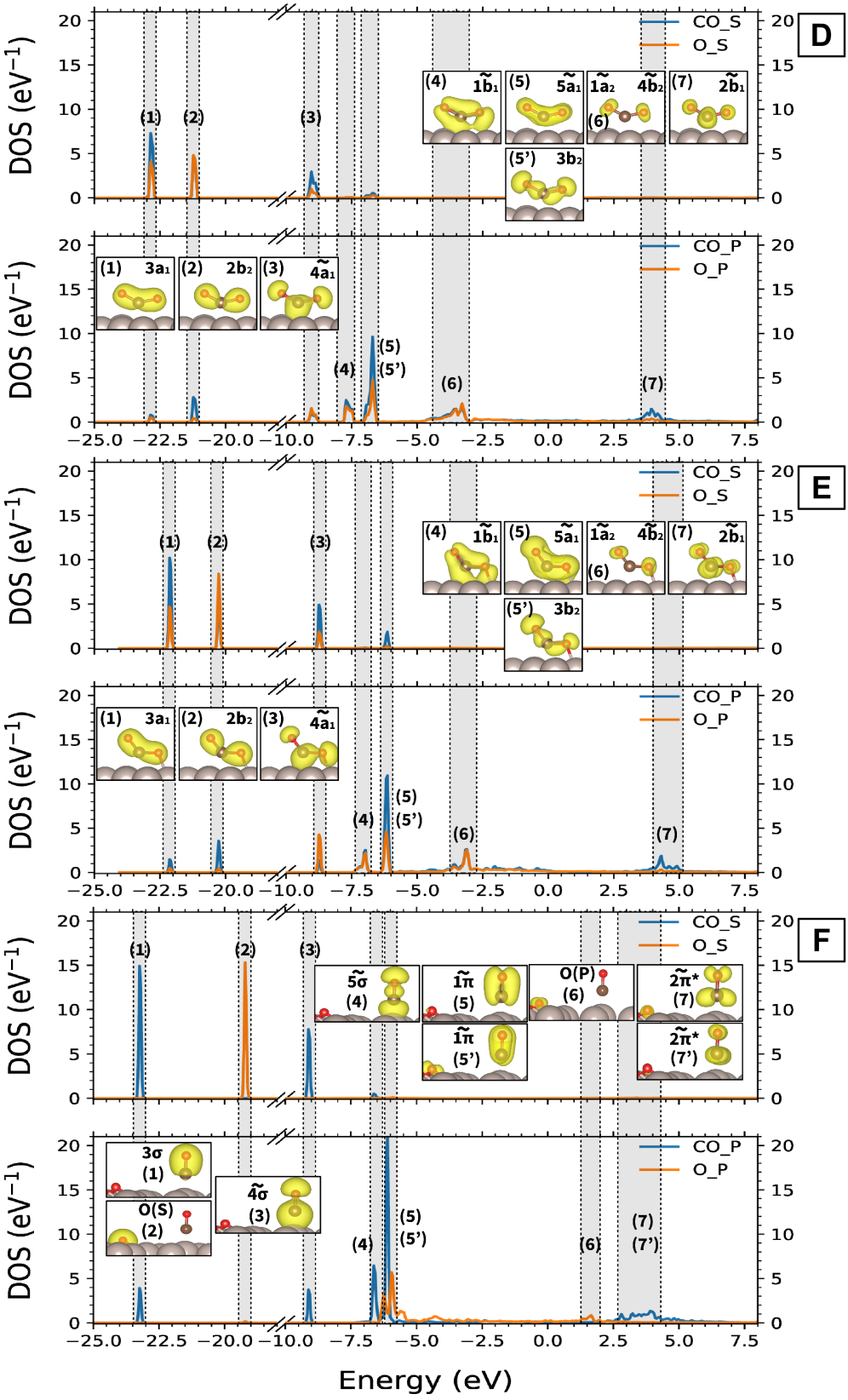

Figure 3.28: Same as Fig. 3.28 for the following states along the MEP: (D) bCO_2, (E) TS1 and (F) IS.

CHAPTER 4

PHOTO-INDUCED CO DESORPTION VERSUS CO OXIDATION: LOW COVERAGE (T_e,T_{ph})-AIMDEF RESULTS

"Que diable allait-il faire dans cette galère?"

— Molière, Les Fourberies de Scapin .[1]

In this chapter we investigate the photo-induced desorption and oxidation of CO on Ru(0001) using ab initio molecular dynamics with electronic friction that account for the non-equilibrated excited electrons and phonons. The chapter starts with a brief description of the experimental findings that had remained unsolved and motivated our study. It follows with a brief section describing the computational details. Next, we discuss the results of our simulations, which have successfully reproduce the main experimental findings: the existence of photo-induced oxidation and desorption, the large desorption to oxidation branching ratio, and the changes in the O K-edge X-ray absorption spectra (XAS) attributed to the initial stage of the oxidation process. An important conclusion of our simulations is that the unexpected inertness to the otherwise energetically favored oxidation is caused by the difficulty in accessing the transition state region that, in fact, does not necessarily guarantee a successful recombination.

4.1 Experimental findings

Early experimental studies carried out for different mixed coverages of O and CO demonstrated that under UHVconditions the oxidation process leading to CO_2 formation cannot be thermally activated.[11] Interestingly, the reaction can be initiated by irradiating the system with near-infrared femtosecond laser pulses[6;12], while thermally only CO desorption is found.[6] Photons in this energy range are efficiently absorbed by the metal electrons that can subsequently transfer energy to the adsorbates directly and also indirectly, via the excited surface phonons that result from electron-phonon coupling. The dependence of the reaction probabilities on the delay between two correlated pulses suggests that the oxidation events are initiated because of direct coupling of the adsorbed O atoms to the laser-excited electrons, thus explaining that the very same reaction cannot be thermally activated.

[1] *"What on earth was he going to do in this galley ?"* —Molière, Les Fourberies de Scapin .

Still, the competing and indirect laser-induced CO desorption mechanism largely dominates over CO_2 desorption, with an observed branching ratio of around 35 between CO desorption and CO oxidation.

This experiment is an emblematic example of a reaction that, being thermally forbidden in ultra-high vacuum, can be activated by femtosecond laser pulse irradiation. Nonetheless, in spite of its relevance, the precise dynamics of the photo-induced CO oxidation process remained unknown. Also the reasons behind the very low probability for CO_2 formation were unclear because density functional theory (DFT) calculations show that CO_2 desorption is energetically favored against CO desorption[12;207], at least for the 0.5 ML O+0.25 ML CO coverage assumed in the experiments of ref.[75] as discussed in Chapter 3. Altogether, the general questions that we intended to answer by performing AIMDEF of this experiment were: How do the ultrafast CO oxidation and CO desorption proceed in the highly-excited and non-equilibrated system? And ultimately, what mechanisms make the photoinduced CO desorption more probable than oxidation?

4.2 Computational details

Photo-induced desorption and oxidation of CO from the (O,CO)-covered Ru(0001) surface is simulated with ab initio classical molecular dynamics using the (T_e,T_{ph})-AIMDEF methodology[7] that accounts for the non-equilibrated excited electrons and phonons created by the laser pulse as explained in Chapter 2. In particular, the laser-excited electrons and concomitant electron-excited phonons are described within the two temperatures model (2TM)[14] as two coupled heat thermal baths, which are characterized by time-dependent electron and lattice temperatures T_e and T_{ph}, respectively. Next, the effect of the excited electrons in the adsorbates dynamics is included by means of Langevin equations of motion, in which electronic friction and random forces model the coupling of the adsorbates to the electronic thermal bath defined by T_e. Furthermore, effects due to the excited phonons are incorporated by coupling the surface atoms in the upper layers to the Nosé-Hoover thermostat,[148;150] assuring that the lattice temperature evolves as T_{ph}. The (T_e,T_{ph})-AIMDEF method as well as variants of it, have been widely used to simulate the femtosecond laser induced dynamics and reactions of adsorbates at metal surfaces.[7;68;69;140;141;142;143;144;208;209] Let us remark that the typical short lifetime of the electronic excited states at metal surfaces (of the order of few fs) justifies employing a Langevin description because the dynamics evolves in the ground potential energy surface most of the time.[91;140;141;209]

As done in Chapter 3, the experimental (2O+CO)/Ru(0001) honeycomb surface,[13] in which CO adsorbs atop a Ru atom and the O atoms occupy the second nearest hcp and fcc sites forming a honeycomb arrangement around the CO, is modeled using a periodic slab with five Ru layers and the adlayer. The employed (4×2) surface cell containing two equivalent adsorbates of each kind is the minimum cell that permits including out of phase movements of the adsorbates and a reliable description of the interadsorbates interactions, that are expected to be relevant at sufficiently large coverages.[7;63;66;68;77;155;210] All (T_e,T_{ph})-AIMDEF simulations are performed with VASP[127;128] and the AIMDEF module[68;93;94;95;211;212;213] using the same computational parameters and the same van der Waals exchange-correlation functional by Dion *et al.*[119] that were used in the structural study of Chapter 3. Electronic friction coefficients are calculated with the Local Density Friction Approximation

(LDFA),[145;214] using the Hirshfeld partitioning scheme to obtain the surface electronic density (see Section 2.4.3).

The O K-edge XAS have been calculated following the theoretical framework explained in Section 2.6.4 that uses the transition potential and Δ-Kohn-Sham methods as implemented in GPAW.[179] Briefly, transition probabilities from the O1s core orbitals are calculated from a Fermi's Golden Rule approach using the core and unoccupied orbitals (a Gaussian broadening of 0.5 eV full-width at half-maximum is used). A shifting method beyond the transition potential method is applied to gauge the lowest-energy peak. For the overall spectrum at a single time step, the approach is applied to all individual oxygen atoms and the final spectrum is obtained by averaging.

4.3 (T_e,T_{ph})-AIMDEF results

Table 4.1 summarizes the results of our simulations for the experimental conditions corresponding to exciting the (2O+CO)/Ru(0001) surface with a 800 nm Gaussian pulse of 110 fs duration and an absorbed fluence F=200 J/m^2.[6] The T_e and T_{ph} curves calculated with the 2TM for these experimental conditions are shown in Figure 4.1 (input parameters as in ref.[68;144;209]). We run 200 (T_e,T_{ph})-AIMDEF trajectories with total simulation time of 4 ps each,[2] being the system initially thermalized at 100 K (see Appendix E for details). The desorption (oxidation) probability per molecule is obtained by dividing the total number of CO (CO_2) desorbing molecules[3] by the total number of trajectories and the total number of CO in the cell. The result of our (T_e,T_{ph})-AIMDEF simulations is clear. As observed in experiments, after photoexcitation both CO desorption and CO_2 formation take place and the former largely dominates over the latter. The corresponding calculated probabilities of 18.25% and 0.5% yield a branching ratio between the two processes in nearly perfect agreement with the experimental values $P_{des}(CO)/P_{des}(CO_2)= 35$[6] and 31.[12] The agreement must be considered as qualitative because of the limited statistics we have for the oxidation process (two oxidation events in 200 trajectories) and our integration time of 4 ps (note that some oxidation and desorption events may occur beyond this interval, as found for CO desorption from Pd(111)[210]), but it remarks already the validity of our non-equilibrium two temperature picture. As shown below, the fact that the XAS features attributed to the oxidation reaction path are also well reproduced makes our simulations all the more reliable.

Simulation	P_{des} (CO)	P_{des} (CO_2)	ratio
(T_e, T_{ph})-AIMDEF	18.25%	0.5%	36.5
refs 6, 12	–	–	35, 31

Table 4.1: AIMDEF desorption and oxidation probabilities, P_{des}(CO) and P_{des}(CO_2), for (2O+CO)/Ru(0001) and F=200 J/m^2. The CO to CO_2 branching ratio is compared to the available experimental values.[6;12]

The results of the (T_e,T_{ph})-AIMDEF simulations provide us with a detailed understanding of the laser-induced oxidation process. The fact that CO desorption dominates over CO oxidation is

[2]The considered number of trajectories and finite integration time make these computationally demanding simulations feasible, while providing us with a reliable understanding on how the photo-induced reactions occur.

[3]A molecule is counted as desorbed if its center of mass crosses the plane z=6.5 Å with positive velocity along the surface normal.

particularly striking considering that our previous DFT calculations of the minimum energy reaction paths showed that desorption requires around 0.38 eV of additional energy compared to oxidation at this coverage[207] (see also Chapter 3). The natural question that arises is whether the laser-induced oxidation dynamics does or does not proceed through that minimum energy oxidation path, in which the less bound O_{fcc} abandons its adsorption well, crosses the bridge site between two Ru atoms, and recombines with the nearby CO that tilts to form the chemisorbed bent CO_2 (hereafter denoted bCO_2). The selected snapshots depicted in Figure 4.2 for one of the trajectories confirm that this is the case. In both trajectories leading to CO_2 desorption, it is an O_{fcc} adsorbate that recombines with CO. During the first picosecond upon arrival of the laser pulse, all the adsorbates become highly vibrationally excited. Thus, the CO molecules, although bound to the Ru atom below, tilt profoundly, while the O_{fcc} and O_{hcp} adsorbates explore the upper part of the wells, approaching the bridge site regions. It is in the interval $t \sim$1580-1600 fs that the recombining O_{fcc} crosses the bridge site and the chemisorbed bCO_2 is formed at $t \sim$1600-1630 fs. From the chemisorbed state the molecule evolves towards the physisorbed linear CO_2 ($t \sim$1820 fs) and finally desorbs at $t \gtrsim 2$ ps. Altogether, the figure remarks the complexity of the oxidation process as compared to the simpler CO desorption dynamics, which do not involve intermediate states and barriers.[207] By analyzing the details of the dynamics, we conclude that it is the reduced configurational space of the former, and particularly the access to the transition state, that explains why the energetically less favorable CO desorption process dominates. This is inferred from the density plot of Figure 4.1 showing the distribution of the instantaneous Ru-$O_{fcc,hcp}$-Ru (in-plane) dihedral angles and the distance between that adsorbed O and the C atoms in the two nearest CO. A successful recombination requires that the adsorbed O reaches the bridge site (characterized by a dihedral angle of 180°) and encounters a CO slightly displaced towards the ahead hollow site and adequately tilted to facilitate the C-O bonds (C-$O_{fcc,hcp}$ distances smaller than 2 Å). These are the properties defining the transition state. As shown in the figure, the access to the bridge site is rather probable, but only on three of these occurrences the excited O finds a CO correctly oriented for recombination. The fact that only two of the three trajectories shown in the figure end as desorbing CO_2 shows that the existence of recrossing events in the transition state makes the oxidation process even more difficult. It is also remarkable to observe that the full oxidation process, which unavoidably involves various intermediate states, lasts a few picoseconds. This is explicitly shown in Figure 4.1, where the instants for desorption and oxidation are plotted together with the time evolution of the electronic and lattice temperatures. Note that only the comparison between the desorption and oxidation time is meaningful because the precise instant at which each process occurs depends on our particular definition of the event.[3] In summary, not only the energetics determines reactivity, but the dynamics plays an important role, too.

Our dynamics simulations confirm the interpretation provided in ref.[13] on the changes observed in the time-resolved XAS experiments. However, that interpretation was based on static DFT calculations under the assumption, questionable under non equilibrium conditions, that the oxidation process follows the minimum energy reaction path with the surface at equilibrium. This approach fully neglects that the reaction proceeds in an extremely dynamically perturbed system. Our dynamics simulations are free of those assumptions and treat explicitly the highly excited environment. As a consequence, they provide an explanation of the measured time-dependent XAS and permit to unravel the mecha-

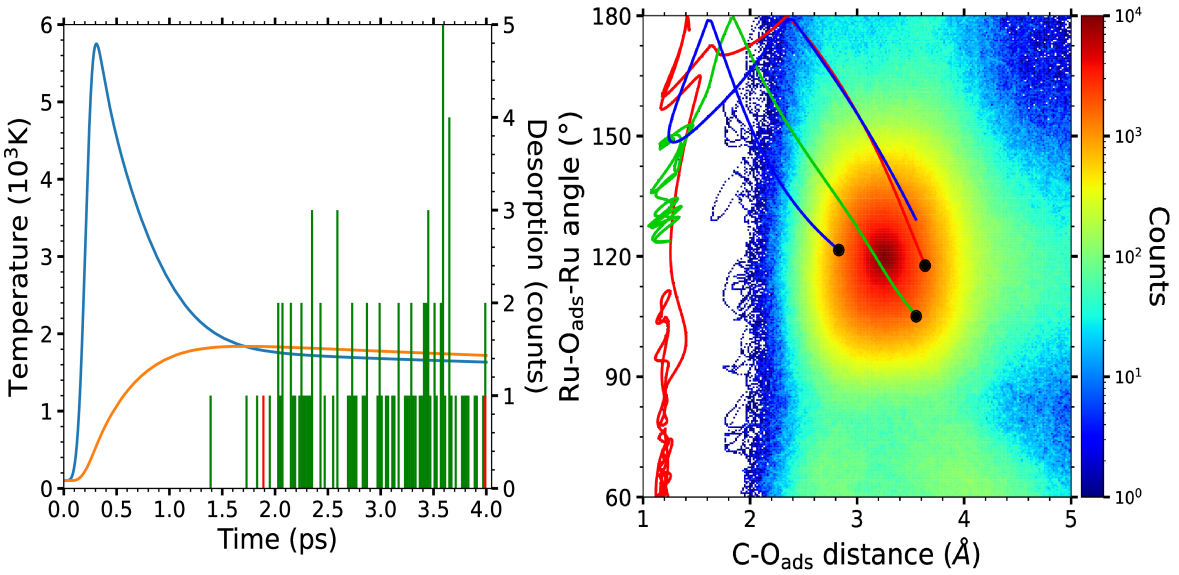

Figure 4.1: Left: Electronic (blue curve) and phononic (orange curve) temperatures (left *y*-axis) used in the simulations. The peak of the pump laser pulse is at 236 fs. The instants at which the desorption and oxidation events occur are respectively plotted by green and red histograms (right *y*-axis), using 20 fs as bin width. Right: Density plot of the instantaneous in-plane dihedral angle Ru-O_{ads}-Ru and the distance between that O_{ads} and the C atom in its nearest CO (see appendix F for calculation details). For clarity, the values of the two oxidation events are shown by a red and a green line, respectively. The blue line corresponds to the third O adsorbate that reaches the transition state, but it cannot recombine. Only the interval of 50 fs before and after reaching the transition state for oxidation is shown by each line. The black circles correspond to the starting points of these three lines.

nisms that govern them. The calculated O K-edge XAS is shown in Figs. 4.2(a)-(c) at selected time intervals characterizing the initial stages in the oxidation dynamics followed by the trajectory shown in the same figure. In agreement with experiments, the absorption peak at ∼530 eV associated to the recombining O_{fcc} shifts and broadens towards lower energies as the adsorbate approaches the Ru–Ru bridge site [compare panels (a) and (b)]. Few tens of fs later, the absorption peak assigned to the CO $2\pi^*$ excitation (∼533 eV) red shifts as the distance between the recombining O_{fcc} and CO decreases and starts to form the chemisorbed bCO_2 [compare panel (c) to (a) and (b)]. Also in agreement to experiments, at this oxidation stage we observe that the initial wide weak peak at ∼539 eV, which is equally contributed by the four O adsorbates [panel (a)], is transformed into a broad structure that extends from about 536 to 540 eV. Comparison of panels (a) and (b) to (c) shows that the change is caused by the reacting O_{fcc} (compare the red curves).

The time-resolved O K-edge XAS spectra plotted in Figure 4.3 for each adsorbate in the simulation cell allow us to track in detail the contribution of each adsorbate to the changes observed in the spectra associated to the trajectory of Figure 4.2. During the first initial femtosecond, the dominant absorption peaks of O_{hcp} and O_{fcc} are slightly shifted from each other because of their minor different chemical environment.

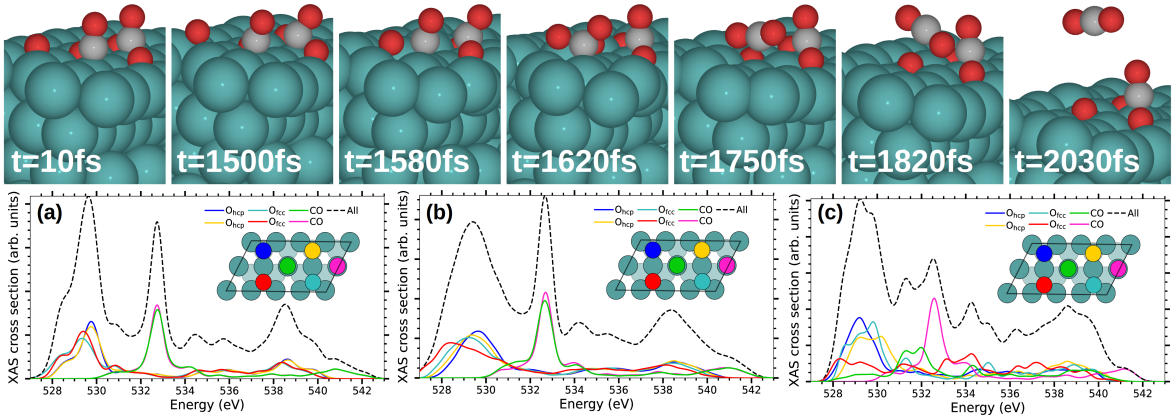

Figure 4.2: Top: Snapshots of a representative CO oxidation dynamics obtained in the (T_e,T_{ph})-AIMDEF simulations (blue, red, and gray spheres correspond to Ru, O, and C atoms, respectively). The AIMDEF simulation time is indicated in each panel (t=0 as in Figure 4.1). Bottom: Time averaged O-K XAS cross section calculated at characteristic time intervals during the oxidative desorption process in the selected trajectory: (a) initial strong excitation of the adsorbates (0-1250 fs), (b) access to the transition state ruling the reaction, in which the recombining O_{fcc} reaches the bridge site that separates it from the nearest CO (1250-1580 fs), and (c) formation of the chemisorbed bent CO_2 (1600-1630 fs). Each color curve shows the contribution of the corresponding colored O atom depicted in the surface unit cell plotted as an inset. Black dashed curves show the total time-averaged XAS.

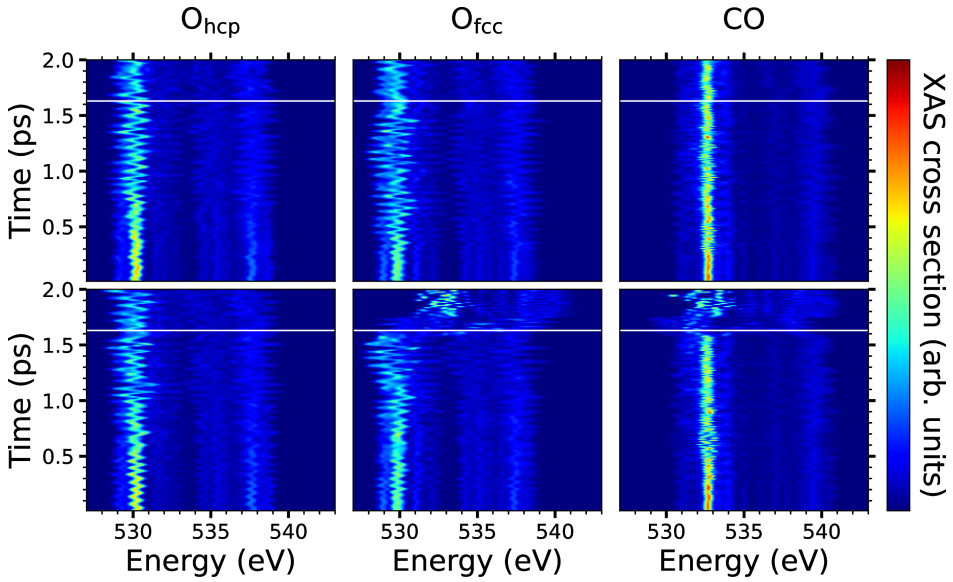

Figure 4.3: Instantaneous O-K XAS of the trajectory shown in Figure 4.2, resolved for each O atom in the simulation cell: O_{hcp} (left panels), O_{fcc} (middle panels), and CO (right panels), with the recombining O_{fcc} and CO being at the bottom. For illustrative purposes, the first instant at which the O_{fcc}-C distance matches the bCO_2 internuclear distance (1.14 Å) is shown by a white line in each plot.

In all cases, the main absorption peak evolves during the first hundreds of fs following a zigzag structure that reflects the small displacements experienced by the adsorbates as a consequence of the electronic and phononic excitations. The observed red (blue) shifts in both O_{hcp} and O_{fcc} correlate with the instants at which adsorbates approach (separate from) the nearby Ru atoms. During the interval

lasting from about 1.25 to 1.6 ps, the recombining O_{fcc} approaches and successfully reaches the bridge position that separates it from the adsorbed CO. This stage is identified in its corresponding spectra by a profound net red shift of the dominant absorption peak from ∼530 eV to ∼528 eV, that is not observed in any of the other O adsorbates. The comparatively small changes (oscillations) in the two CO spectra underlines that the molecules remain firmly bound atop the Ru atom, except for the minor displacements associated to frustrated rotations and translations. At 1.6 ps the absorption peak of the recombining CO vanishes, while a new broaden and less intense peak appears in the range 531-532 eV. This new structure is ascribed to the starting point in the formation of the chemisorbed bCO_2. The nascent molecule stays about 100 fs in this state before definitely breaking the C-Ru bond and reach the physisorbed linear CO_2. Although experimentally inaccessible, note that the absorption spectra in the physisorption state are basically identical for the O atoms, as expected.

Finally, we considered meaningful to confirm the formation of all the bCO_2 orbitals at 1.63 ps with an additional analysis of the partial density of states and partial electron densities. Specifically, the projected density of states (PDOS) is calculated at certain instants along the trajectory shown in Figure 4.2 to follow in more detail the formation of the chemisorbed bCO_2. At 1600 fs, we start to observe hybridization of the more energetic O_{fcc} and CO occupied states, but it is at 1630 fs when we identify all the bCO_2 orbitals. This is shown in Figure 4.4. As noted in Section 2.6, the PDOS is obtained in the VASP implementation by projecting the Kohn-Sham wave function $\phi_{n\mathbf{k}}$ onto spherical harmonics Y^i_{lm} centered at each ion position i. The PDOS shown in the figure corresponds to the sum of the s and p projections centered at the atoms involved in the CO_2 formation. For each of the PDOS peaks we have additionally calculated the corresponding partial electron densities to facilitate the identification of the bCO_2 orbitals.

4.4 Conclusions

Our ab initio molecular dynamics simulations that describe the laser-excited system in terms of non-equilibrated time-dependent electronic and phononic temperatures have successfully reproduced the main features observed in femtosecond laser experiments performed on Ru(0001) covered with a mixed adlayer of O and CO: (i) the photo-desorption of both CO and CO_2, (ii) the large branching ratio between desorption and oxidation that exceeds one order of magnitude and (iii) the changes in the O K-edge X-ray absorption spectra that were associated to the initial stage of the oxidation. Thanks to these simulations we can monitor in detail the elementary steps of the desorption and the oxidation dynamics promoted by the laser and determine the reaction paths in the excited system that explain why CO desorption dominates over the energetically favored oxidation. It is the O adsorbed at fcc sites that primarily recombines with the adsorbed CO, following basically the intermediate extreme states of the minimum energy oxidation path. The reason behind the unexpected inertness to the otherwise energetically favored oxidation is twofold: (i) the difficult access to the transition state region, that requires the O atom crossing the bridge site and finding the CO conveniently close and tilted to form the chemisorbed bent CO_2 and (ii) the fact that this access does not guarantee a successful recombination.

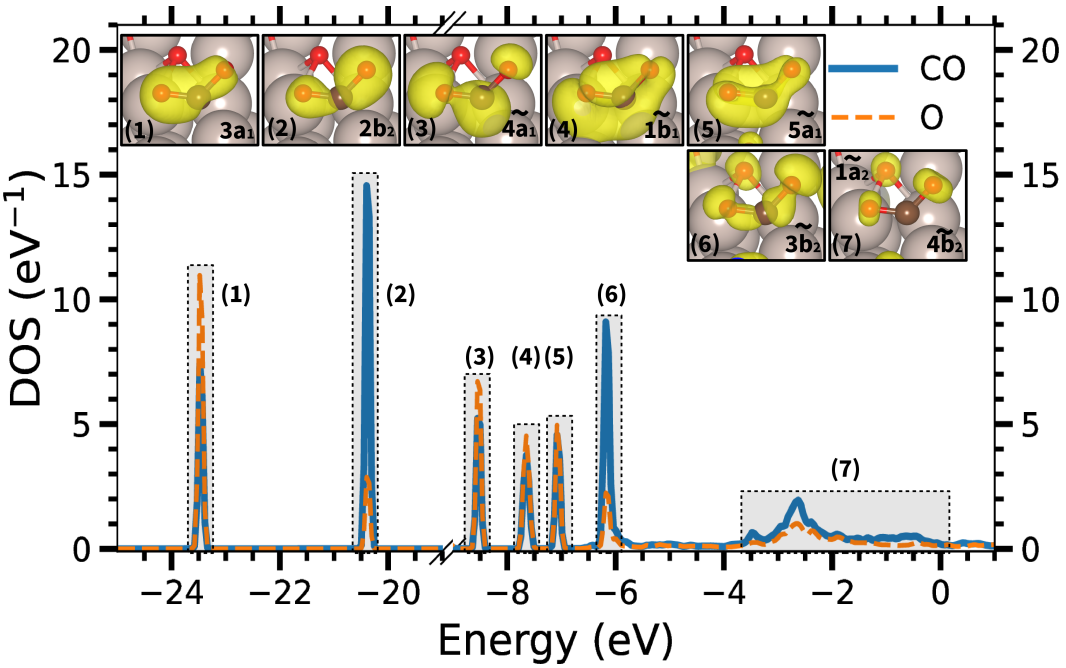

Figure 4.4: Projected density of states and partial electron densities showing that at t=1630 fs the chemisorbed bCO_2 is completely formed in the trajectory depicted in Figure 4.2. In the PDOS plot, the sum of the *s*- and *p*-like projections centered at the atoms forming the recombining CO is depicted by the blue curve, while the dashed orange curve shows the sum of the *s* and *p* projections centered at the recombining O_{fcc} atom. The insets (1) to (7) show the partial electron densities (PED) calculated for each of the (1) to (7) PDOS peaks identified in the main plot. (The energy interval used in each PED calculation is marked by a gray rectangle in the PDOS plot.) The bCO_2 orbital associated to each PED is written in the inset (when applicable, the tilde remarks that the orbital hybridizes with the Ru(0001) states). Note that the PED associated to peaks (6) and (7) also include the contribution in this energy range of the adsorbed O that should not be confused with the bCO_2 orbitals.

CHAPTER 5

AIMDEF SIMULATIONS OF THE PHOTO-INDUCED CO DESORPTION AND OXIDATION ON RU(0001) WITH DIFFERENT COVERAGES

"C'était absurde. Pourquoi se procurer clandestinement des traductions, alors qu'elles aillaient, dans quelques heures, être diffusées dans le monde entier ? La logique conduisait à une réponse effrayante."

— René BARJAVEL, La nuit des temps.[1]

In this chapter we analyze the results of our T_e-AIMDEF and (T_e,T_{ph})-AIMDEF simulations of the CO photo-induced desorption and oxidation on Ru(0001) at low, intermediate, and high surface coverages (described in Chapter 3). First, in Section 5.1, we present and discuss the results of the simulations for the probabilities of desorption of CO and CO_2 molecules. Second, in Section 5.2, we analyze the time evolution of the kinetic energy of the non-desorbed and desorbed species during the AIMDEF simulations. Third, in Section 5.3, we analyze the motion perpendicular to the surface of the adsorbates and the Ru surface layers during the AIMDEF simulations. Fourth, in Section 5.4, we analyze the motion of the adsorbed species parallel to the surface. The results presented in Sections 5.2, 5.3 and 5.4 provide insights into the CO desorption and oxidation processes. Finally, in Section 5.5, we analyze the oxidation dynamics at different coverages, and describe two new CO+O recombination mechanisms that were not found in the low coverage case studied in Chapter 4.

5.1 CO desorption and oxidation probabilities

We start the analysis of our AIMDEF results by providing the obtained CO and CO_2 desorption probabilities. These results can be directly compared to the values reported in experiments.[6;12] Note that if in our simulations we detect CO_2 desorption, it means that previously a CO oxidation took place. The oxidation dynamics are analyzed later in Section 5.5.

Table 5.1 summarizes the results of our simulations for the experimental conditions corresponding to exciting the low, intermediate, and high surface coverages (described in Section 3.3 of Chapter 3) with a femtosecond laser pulse. The laser is a 800 nm Gaussian pulse of 110 fs duration. For all

[1] *"It was absurd. Why smuggle in translations when they were going to be broadcast around the world in few hours? Logic led to a frightening answer."* —René BARJAVEL, La nuit des temps.

coverages and for all kind of simulations the absorbed laser fluence is F=200 J/m^2. Additionally, for the high coverage, an additional T_e-AIMDEF set of simulations was performed with F=300 J/m^2. The time dependence of T_e and T_{ph} for the F=200 J/m^2 case obtained with 2TM were already shown in Fig. 4.1 of Chapter 4 (input parameters as in ref.[68;144;209]). In Fig. 5.1 we show for comparison the time dependence of T_e and T_{ph} for laser fluence F=200 J/m^2 (red and pink) and F=300 J/m^2 (blue and turquoise). We observe that by increasing the laser fluence from F=200 J/m^2 to F=300 J/m^2, the maximum of T_e increases from $\sim$5600 K to $\sim$7200 K. Additionally, T_e reaches its maximum value $\sim$0.1 ps earlier. The maximum of T_{ph} also increases from $\sim$1700 K to $\sim$2400 K. In the (T_e,T_{ph})-AIMDEF simulations, the system was thermalized at 100 K before running the AIMDEF simulations (see Appendix E for details). The time limit for all the simulations is 4 ps. We ran two types of simulations:

T_e-AIMDEF with frozen surface and electronic temperature only.

(T_e,T_{ph})-AIMDEF including both the electronic and lattice temperatures calculated with 2TM.

The number of trajectories is of the order of 100 for the T_e-AIMDEF simulations and of the order of 200 for the (T_e,T_{ph})-AIMDEF simulations.

The CO desorption and oxidation probabilities per CO molecule are calculated for each coverage as

$$P_{\mathrm{des}}(A) = \frac{N_{\mathrm{des}}(A)}{N_{\mathrm{t}} N_{\mathrm{CO}}}, \tag{5.1}$$

where $N_{\mathrm{des}}(A)$ is the number of desorbing molecules (CO or CO_2), N_{t} is the total number of trajectories, and N_{CO} is the number of CO molecules in the simulation cell (2, 3, and 4 for low, intermediate, and high coverages, respectively). A molecule is counted as desorbing if its center of mass crosses the plane z=6.5 Å with positive velocity along the surface normal. In Table 5.1, we also provide the branching ratio (br) between the CO and CO_2 desorption probabilities:

$$\mathrm{br} = \frac{P_{\mathrm{des}}(\mathrm{CO})}{P_{\mathrm{des}}(\mathrm{CO_2})}. \tag{5.2}$$

Obviously, in the cases for which the CO_2 desorption probability is zero, this quantity is undefined.

Calculation type	T_e-AIMDEF				(T_e,T_{ph})-AIMDEF		
Laser Fluence	200 J/m^2			300 J/m^2	200 J/m^2		
surface coverage	low	intermediate	high	high	low	intermediate	high
total CO	200	300	400	400	400	597	556
P_{des}(CO) (%)	0.00%	1.33%	1.00%	15.25%	18.25%	45.06%	34.53%
P_{des}(CO_2) (%)	0.00%	0.00%	0.00%	0.00%	0.50%	0.67%	1.26%
br	/	/	/	/	36.5	67.3	27.4

Table 5.1: T_e-AIMDEF and (T_e,T_{ph})-AIMDEF CO desorption (P_{des}(CO)) and oxidation (P_{des}(CO_2)) probabilities, and desorption to oxidation branching ratio (br), for the low, intermediate, and high surface coverages with absorbed laser fluences F=200 J/m^2 and F=300 J/m^2. The total number of CO molecules used for each kind of simulation (total CO) is also given.

On the left hand side of the table, we present the results of the T_e-AIMDEF simulations. The first observation is that for the nominal F=200 J/m^2 laser fluence, when phononic excitations are not

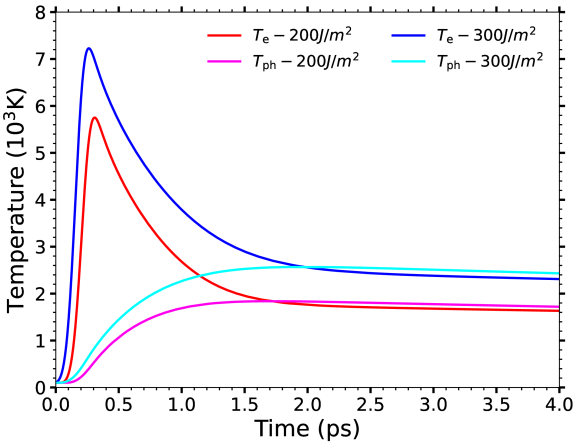

Figure 5.1: Time dependence of T_e and T_{ph} for absorbed laser fluences F=200 J/m^2 (red and pink) and F=300 J/m^2 (blue and turquoise).

included, the CO desorption probability is zero at low coverage, and very low at the other coverages (1.33% at the intermediate and 1% at the high coverage). Interestingly, when increasing the laser fluence to F=300 J/m^2 at the high coverage, the CO desorption probability is 15 times larger than for the lower F=200J/m^2 laser fluence. Finally, for all coverages and both studied absorbed laser fluences, no CO_2 desorption event is obtained in the T_e-AIMDEF simulations.

On the right hand side of the table, we present the results of the (T_e,T_{ph})-AIMDEF simulations. We observe that for all three surface coverages there exist desorption events of both CO and CO_2 molecules. The CO desorption probability is the highest for the intermediate coverage, being 1.3 times larger than for the high coverage and 2.5 times larger than for the low coverage. The CO_2 desorption probability is very low for the three coverages, very similar and below 1% for the low and intermediate coverages, and slightly higher for the high coverage. As a result, we observe that the branching ratio for low and high surface coverages are very close and in a good agreement with experiments (35[6] or 31[75]). In the case of the intermediate coverage, due to the relatively large CO desorption probability, the branching ratio is two times higher than the one found for the other surface coverages.

It is interesting to discuss the above presented results in relation to the CO desorption and oxidation activation energies presented in Chapter 3. We recall that the CO desorption activation energies are 1.57 eV, 0.58 eV, and 0.88 eV for the low, intermediate, and high coverages, respectively. Moreover, the activation energies for CO oxidation are 1.19 eV, 0.80 eV, and 2.01 eV for the low, intermediate, and high coverages, respectively.

Indeed, the dependence of the CO desorption probability on the surface coverage can be understood in terms of the calculated desorption barriers. The largest probability corresponds to the intermediate coverage that presents the lowest energy barrier to desorption, and the lowest probability to the low coverage that presents the highest barrier to desorption. This behavior is not observed for the oxidation process. In this case, the highest probability is unexpectedly obtained for the high coverage, *i.e.*, the coverage for which the activation barrier for CO oxidation is the largest. As it has been already shown in the previous chapter (Chapter 4), the photo-oxidation is a more complex process. CO oxidation reaction is hindered by several surface processes, making the arrival to the configurational space of

reaction very difficult.[57] For these reasons, there exist other properties of the adsorbate-surface system that may affect the reaction probability apart from the activation energy. In our case, although the CO oxidation probabilities are very low, we observe the CO_2 desorption probability increases with the coverage, *i.e.*, with the amount of CO at the surface. Since CO_2 desorption requires the recombination of CO and O at the surface, the initial distance between the recombining adsorbates and/or the specific adsorbate arrangement at the surface may facilitate or hinder the access of the adsorbates to the reaction path. A more detailed description of the CO oxidation dynamics at the different coverages is given in the sections below.

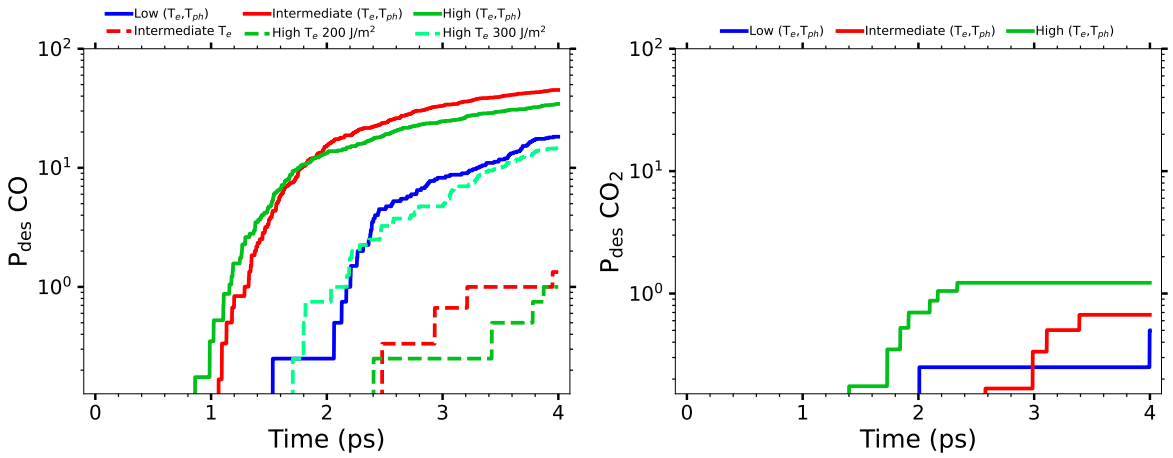

Figure 5.2: Desorption probabilities of CO (left panel) and CO_2 (right panel) as a function of time for the different AIMDEF simulations. Blue, red, and green curves correspond to low, intermediate, and high surface coverages, respectively, and laser fluence F=200 J/m^2. Solid lines and dashed lines are the results of the (T_e,T_{ph})-AIMDEF and the T_e-AIMDEF simulations, respectively. The light green, dashed line corresponds to the T_e-AIMDEF simulations at high surface coverage with laser fluence F=300 J/m^2.

In Fig. 5.2 we show the time evolution of the desorption probability of CO (left panel) and CO_2 (right panel) in all performed simulations. The results for the low, intermediate, and high surface coverages are shown in blue, red, and green, respectively. The solid lines correspond to the (T_e,T_{ph})-AIMDEF simulations and the dashed lines to the T_e-AIMDEF simulations. Finally, the dashed light green curve corresponds to the F=300 J/m^2 T_e-AIMDEF results for the high coverage.

We first observe in the left panel that in T_e-AIMDEF simulations for the coverages where CO desorption exists with F=200J/m^2 (intermediate and high), the first desorption event takes place around 2.4 ps after the laser pulse arrival, although for the high coverage it occurs slightly earlier than for the intermediate coverage. In the case of the high surface coverage with F=300J/m^2 the first CO desorption occurs around 0.7 ps earlier than for F=200J/m^2. This shows that increasing the laser fluence does not only increase the total CO desorption probability but also makes it a faster process.

In the (T_e,T_{ph})-AIMDEF simulations, the first desorptions occur around 1.5 ps, 1 ps, and 0.8 ps after the arrival of the laser pulse, for the low, intermediate, and high coverages, respectively. Briefly, the time for the first desorption event is similar for the intermediate and high coverages. In contrast, the first desorption events in the low coverage occurs about 0.5 ps later and it is not until t=2 ps that the desorption probability starts to increase with time. A rough comparison among the slopes of the curves suggests a faster CO desorption rate in the intermediate coverage as compared to the rather similar

rates obtained in the low and high coverages. It is worth to mention a small difference regarding the time for the first desorption event between the intermediate and the high coverages. As it was the case in the T_e-AIMDEF simulations, the first desorption event takes place earlier and the reaction is slightly faster at short times, when the electronic temperature is high, for the high coverage. The reason for this is probably related to the fact that CO adsorbs on hollow sites in the high coverage case (*i.e.*, very close to the surface) and at near-top and top sites in the intermediate and low coverage cases, respectively. As a consequence, the coupling to the electronic system is stronger in the former which also explains that the desorption probability is initially larger for this coverage and not for the intermediate one.

In the second panel of Fig. 5.2 we show the time evolution of the CO_2 desorption probability in the (T_e,T_{ph})-AIMDEF simulations. The two oxidation events obtained in the low surface coverage occur at well separated instants, t$\sim$2 and t$\sim$4 ps, respectively. In contrast, in the high and intermediate coverages, all the CO_2 desorption events occur within a shorter time interval of about 1 ps. The important difference between these two coverages is that the first event takes place at $t \sim$1.4 ps in the former and at $t \sim$2.6 ps in the latter. Considering that the high coverage has the largest activation energy for CO oxidation, not only it is surprising to find that the oxidation probability is the highest for this coverage but also that the process initiates more rapidly on this surface. There are various reasons that can explain this unexpected result. As it was the case for the CO desorption, the more efficient coupling to the electronic system may imply a more rapid energy gain by the adsorbates at the initial stages of the process in the high surface coverage. Furthermore, the oxidation process in the high coverage is in few cases preceded by other desorption events that contribute to reduce the nominal CO coverage and, concomitantly, the activation energies. Neither we can discard that the energy barriers on the highly excited surface are different from those calculated on the relaxed surface, once more remarking the importance of the dynamics simulations. In this respect, the analysis of the trajectories leading to CO_2 desorption (Section 5.5 below) will show that none of these trajectories in the intermediate and high coverages follow the MEPs calculated in Chapter 3. Finally, CO desorption and oxidation are competing processes. Therefore, a very efficient desorption process in the intermediate coverage may hinder the oxidation process.

5.1.1 Conclusions

We have showed that inclusion of the lattice excitation greatly increases the desorption probability of the photodesorption of both CO and CO_2 at all coverages, and that electronic excitations alone are not sufficient to describe these processes.

CO desorption probabilities at different coverages are directly correlated to the desorption energy barrier. In contrast, CO oxidation is a more complex process and is affected by other properties of the surface. The time of the first CO and CO_2 desorption events are also different at the different coverages. Interestingly, for both reactions, this first desorption is faster at high coverages, which is probably related to the stronger coupling of the CO molecules to the electronic system at this coverage. We have found that the competition between CO oxidation and desorption is significant in the intermediate surface coverage, where the CO desorption is favored, leading to a late CO oxidation comparing to the other surface coverages. Finally, the desorption to oxidation branching ratio obtained in (T_e,T_{ph})-AIMDEF simulations for the low and high surface coverages is in rather good agreement

with the experimental ones (35[6] or 31[75]), while the one for the intermediate surface coverage is two times larger.

5.2 Analysis of the kinetic energy of the adsorbates

In this section we will study the energy gain by the CO and O adsorbates by analyzing the time evolution of their kinetic energy. Results will be presented separately for the adsorbates that are finally desorbed (desorbed species) and the ones that remain adsorbed at the surface at the end of the simulation time (adsorbed species). In the case of the CO molecules we will show results for their mean total kinetic energy, for the mean center-of-mass and mean internal kinetic energies (indistinctly referred to as translational and rovibrational energies along this section). Additionally, the mean center of mass kinetic energies associated to the movements normal and parallel to the surface will be separately analyzed. We show results for the three studied coverages and for the two kinds of simulations (T_e-AIMDEF and (T_e,T_{ph})-AIMDEF). In the case of the T_e-AIMDEF simulations we will not show results for the desorbed species due to the small number of desorption events that do not allow us to perform a meaningful statistical analysis. In all cases, the results refer to the mean kinetic energies per adsorbate type (*i.e.*, O or CO), which are calculated at each instant t as and average over all trajectories and all the atomic or molecular species under consideration.

5.2.1 Low surface coverage

In Fig. 5.3 we show the time evolution of the mean kinetic energy of the adsorbates along the dynamics, for T_e-AIMDEF simulations (left panel) and for (T_e,T_{ph})-AIMDEF simulations (right panel), at low surface coverage. At this coverage there exist two different adsorption positions for atomic O, hcp and fcc (see Fig. 3.10). Therefore, we show separately the results for the species adsorbed on the hcp site (blue curve) and on the fcc site (green curve). For CO molecules we show the mean total kinetic energy (red curve), the mean kinetic energy of the center of mass (orange curve), and the mean kinetic energy of the center of mass associated to the movement normal (pink curve) and parallel (dark red curve) to the surface. Solid lines correspond to the results for adsorbed species and dashed lines to the results for the CO desorbing species.

Regarding the time evolution of the kinetic energy of the O adatoms, it should be remembered that the binding energy in the hcp adsorption site is larger than in the fcc site. In spite of that, we observe, in both T_e-AIMDEF and (T_e,T_{ph})-AIMDEF simulations, that the time evolution of the mean kinetic energy along the dynamics of the O atoms adsorbed in the hcp and fcc adsorption sites is very similar. In (T_e,T_{ph})-AIMDEF simulations the value of the mean kinetic energy of the O adatoms is around 200 meV at the end of the simulation time, and around 40 meV lower in the the T_e-AIMDEF simulations.

Regarding the CO molecules, in the T_e-AIMDEF simulations (Fig. 5.3 left panel) the mean total kinetic energy reaches a value of around 240 meV at the end of the simulation time. The final mean center-of-mass kinetic energy (around 100 meV) is less than one half of this value. In other words, it means that when only electronic excitations are considered, more energy is transferred to the internal rovibrational degrees of freedom of the molecule than to the center of mass kinetic energy. Additionally,

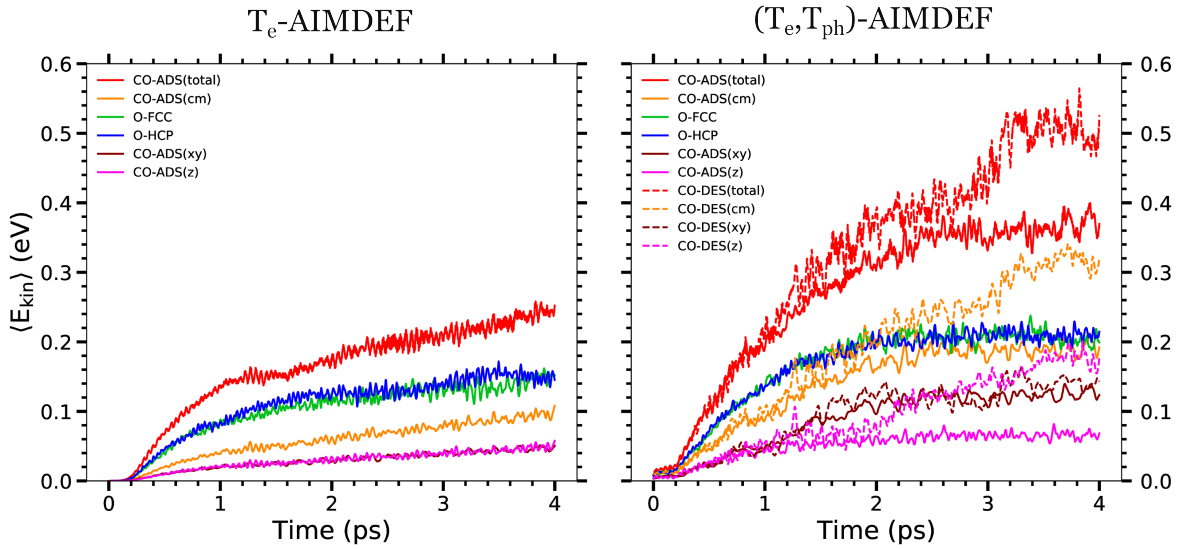

Figure 5.3: Time dependence of different contributions to the kinetic energies of the CO molecules and O adatoms at the low surface coverage for T_e-AIMDEF (left panel) and (T_e,T_{ph})-AIMDEF (right panel) simulations with laser fluence F=200 J/m^2. Solid lines show results for the species that do not desorb at the end of the simulation (adsorbed species), and dashed lines show the results for the species that desorb at the end of the simulation (desorbed species). Results are shown for the mean total kinetic energy of CO molecules (red), the mean CO center of mass kinetic energy (orange), its contributions parallel (brown) and normal (pink) to the surface, and the mean kinetic energy of the O atoms initially adsorbed in fcc sites (green) and hcp sites (blue).

the kinetic energy of the center of mass is equally distributed in its contributions normal and parallel to the surface. Since the former contribution comprises a single degree of freedom and the latter comprises two degrees of freedom, this shows that there does not exist equipartition of the kinetic energy among the different degrees of freedom of the center of mass motion when only electronic excitations are taken into account.

In the analysis of the results of the (T_e,T_{ph})-AIMDEF simulations (right hand panel of Fig. 5.3) for the adsorbates that remain at the surface at the end of the simulations, a first observation is that, as expected, the energy gain is larger than in the T_e-AIMDEF simulations. In those simulations, the time evolution of the kinetic energy of the O atoms is the same irrespective of the initial adsorption site. Interestingly, at the end of the simulation the mean kinetic energy of the center of mass of CO roughly coincides with the mean kinetic energy of the O adatoms. Also, the contribution of the parallel motion to the kinetic energy of the center of mass is roughly twice the value of the normal contribution. Moreover, the mean total kinetic energy is close to twice the kinetic energy of the center of mass, which implies equipartition of the CO kinetic energy among the translational and internal degrees of freedom. Nevertheless, note that these relations between the values of the different contributions to the kinetic energy, that reflect a perfect equipartition among the different degrees of freedom, are not fulfilled during the entire time evolution but just at the end of the simulation. This suggests a system that is slowly arriving to a thermalized or quasithermalized state at the end of the simulation time. Compared to the T_e-AIMDEF simulations, we also observe a clear increase of the contribution of the movement parallel to the surface, which suggests an increased mobility of the adsorbates on the surface when including phononic excitations.

Regarding the desorbed species, we observe that their mean total kinetic energy starts to be larger than the one of the adsorbed species after 1 ps and that the difference increases with the simulation time as the amount of desorbed molecules increases. Interestingly, this energy difference comes mostly from the increase of the contribution corresponding to the normal motion of the desorbed molecules.

5.2.2 Intermediate surface coverage

We show in Fig. 5.4 the time evolution of the mean total kinetic energy of the adsorbates, and its different contributions in case of the CO molecules, in the intermediate surface coverage. As before, the results obtained from T_e-AIMDEF simulations (left panel) and (T_e,T_{ph})-AIMDEF simulations (right panel) are presented.

First, we focus on the atomic O adsorbates. In this case, all O are adsorbed on hcp sites in a O-p(2x1) structure. We observe that in the (T_e,T_{ph})-AIMDEF simulations the value of the mean kinetic energy of the O atoms is around 210 meV at the end of the simulation time, and around 60 meV lower in the the T_e-AIMDEF simulations. Also, in (T_e,T_{ph})-AIMDEF the maximum energy is reached faster (at ∼2.2 ps) than in T_e-AIMDEF (∼2.8 ps).

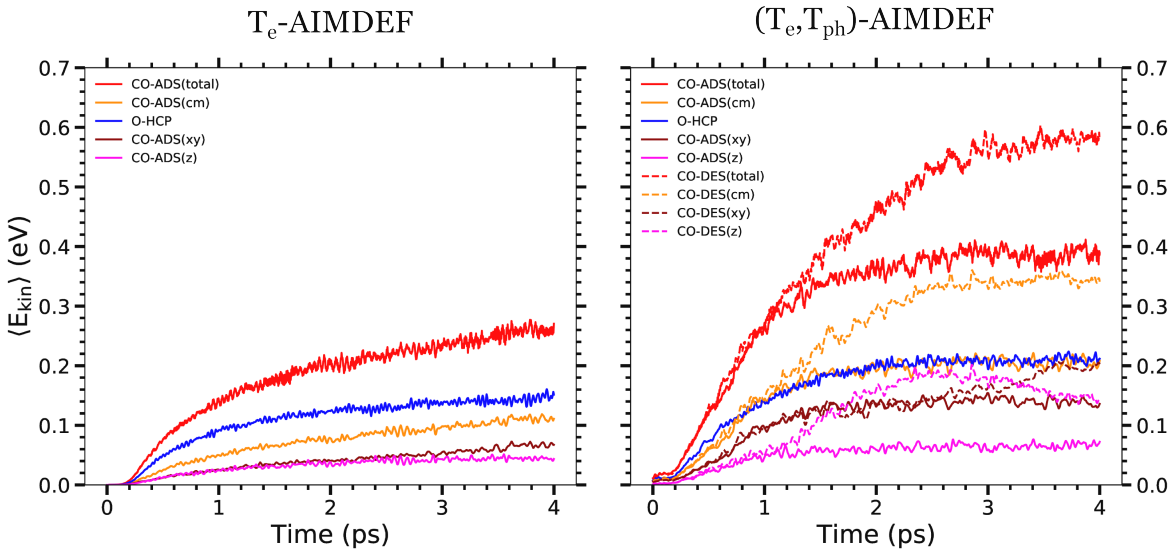

Figure 5.4: Time dependence of different contributions to the kinetic energies of the CO molecules and O atoms at the intermediate surface coverage for T_e-AIMDEF (left panel) and (T_e,T_{ph})-AIMDEF (right panel) simulations with laser fluence F=200 J/m^2. Solid lines show results for the adsorbed species and dashed lines show the results for the desorbed species. Results are shown for the mean total kinetic energy of CO molecules (red), the mean CO center of mass kinetic energy (orange), its contributions parallel (brown) and normal (pink) to the surface, and the mean kinetic energy of the O atoms (blue).

Focusing now on the CO molecules, in the T_e-AIMDEF simulations the mean total kinetic energy reaches a value of around 246 meV at the end of the simulation time. The final center of mass mean kinetic energy (around 110 meV) is, as it was the case for low surface coverage, less than one half of the mean total kinetic energy. Hence, also for the intermediate coverage, electronic excitations transfer more energy to the internal rovibrational degrees of freedom than to the center of mass motion. Regarding the contributions normal and parallel to the surface of the center of mass kinetic energy, they are similar until 2.6 ps. Afterwards, the parallel contribution energy becomes larger than the vertical

one. In any case, at the end of the simulation time the parallel contribution is less than twice the normal contribution. As it was the case for low coverage, it does not exist equipartition of the kinetic energy among the different degrees of freedom of the center of mass motion when only electronic excitations are taken into account.

Regarding the (T_e,T_{ph})-AIMDEF simulations (right hand panel of Fig. 5.4) for the adsorbates that remain at the surface at the end of the simulations, very similarly to the low coverage case, we find equipartion of the energies among the different degrees of freedom of the CO molecules: the mean total kinetic energy is twice the mean kinetic energy of the center of mass, and the contribution of the latter to the lateral motion is twice the contribution to the normal motion. Additionally, the mean kinetic energy of the center of mass of the CO molecules coincides with the kinetic energy of the O adatoms. The main difference with the low coverage case is that for low coverage this thermalized state was only achieved (or was starting to be achieved) at the end of the simulation, *i.e.*, about 4 ps after the arrival of the laser pulse. For the intermediate coverage, this thermalization is much faster as it appears at around 2 ps. Finally, the comparison with the T_e-AIMDEF results shows that, although all the contributions to the kinetic energy increase when including phononic excitations, the contribution of the movement parallel to the surface to the kinetic energy is the one that presents the largest increase.

Regarding the desorbed species, now we observe that their mean total kinetic energy starts to be larger than the one of the adsorbed species after 1.2 ps and that the difference increases with the simulation time as the amount of desorbed molecules increases. For the intermediate coverage this increase does not come uniquely from the increase of the contribution corresponding to the normal motion of the desorbed molecules, since around half of this energy gain goes to the parallel and the rovibrational motions.

5.2.3 High surface coverage

Finally, in Fig. 5.5 we show the results for the high coverage. In this case, we have two T_e-AIMDEF simulations with laser fluences F=200 J/m^2 (left panel) and 300 J/m^2 (center panel) and the (T_e,T_{ph})-AIMDEF simulations with F=200 J/m^2 (right panel).

As it was the case in intermediate surface coverage, in the high surface coverage, all the O adatoms are adsorbed on hcp sites in a O-p(2x1) structure. We observe that in the (T_e,T_{ph})-AIMDEF simulations the value of the mean kinetic energy of the O adatoms at the end of the simulations is very similar to the one achieved in the intermediate coverage, around 210 meV. In the T_e-AIMDEF simulations this maximum value is around 50 meV lower. Interestingly, in the T_e-AIMDEF simulations with F=300 J/m^2 we observe that the energy gain of the O adatoms is very similar to that obtained in the (T_e,T_{ph})-AIMDEF simulations with F=200 J/m^2.

Next, we compare the variations of kinetic energies of the adsorbed CO molecules in the T_e-AIMDEF simulations. As expected, at F=300 J/m^2 the energy gain is larger than at F=200 J/m^2. Apart from that, qualitatively the results are very similar. First, at variance with the results at the other coverages, the mean total kinetic energy is roughly around two times larger than the mean kinetic energy of the center of mass. Also, the value of the parallel contribution to the center of mass kinetic energy is roughly twice the value of the normal contribution. Finally, at the very end of the simulation time the mean kinetic energy of the center of mass roughly coincides with the mean kinetic energy of

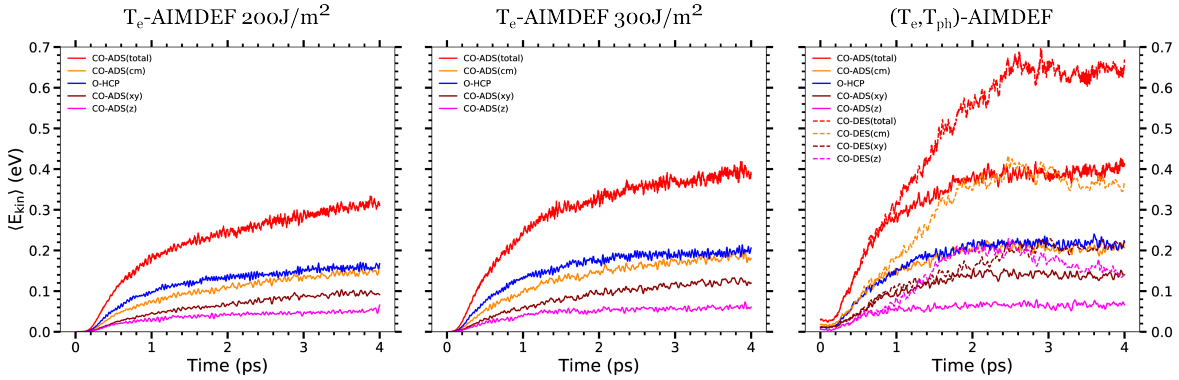

Figure 5.5: Time dependence of different contributions to the kinetic energies of the CO molecules and O adatoms at the intermediate surface coverage for T_e-AIMDEF simulations with F=200 J/m^2 (left panel) T_e-AIMDEF simulations with F=300 J/m^2 (central panel) and (T_e,T_{ph})-AIMDEF simulation with F=200 J/m^2 (right panel). Solid lines show results for the adsorbed species and dashed lines show the results for the desorbed species. Results are shown for the mean total kinetic energy of CO molecules (red), the mean CO center of mass kinetic energy (orange), its contributions parallel (brown) and normal (pink) to the surface, and the mean kinetic energy of the O adatoms (blue).

the O adatoms. All of this suggests that at this high coverage a quasithermalized state is achieved at the end of the simulations even if only electronic excitations are considered. A possible reason for this can be a very efficient interadsorbate energy exchange at this coverage.

As can be expected, in the (T_e,T_{ph})-AIMDEF simulations (right hand panel of Fig. 5.5) for the adsorbates that remain at the surface at the end of the simulations we also observe this thermalized state, the main difference with T_e-AIMDEF being that the thermalization is much faster. As in the intermediate coverage, this thermalization is already achieved at around 2 ps.

For the same laser fluence, the energy gain is much larger in the (T_e,T_{ph})-AIMDEF than in the T_e-AIMDEF. However, we observe that, as it was the case for the O adatoms, the energy gain of the CO molecules as well as its distribution among the different degrees of freedom are very similar at the end of the simulation time in the F=200 J/m^2 (T_e,T_{ph})-AIMDEF and in the F=300 J/m^2 T_e-AIMDEF, although there exist differences in the time evolution. This contrasts to the different CO and CO_2 desorption probabilities obtained in these two different simulations (see Table 5.1). Indeed not only the final energy gain but the different dynamics affect the reaction probabilities.

Regarding the desorbed species, now we observe that their mean total kinetic energy starts to be larger than the one of the adsorbed species after 0.9 ps and that the difference increases with the simulation time as the amount of desorbed molecules increases. As it was the case for the intermediate coverage, this increase does not come uniquely from the increase of the contribution corresponding to the normal motion of the desorbed molecules. In fact, the relative importance of the energy transferred to the parallel and the rovibrational motions is larger at this high coverage.

5.2.4 Comparison between coverages

In Fig. 5.6 we compare the variations of the mean total kinetic energy of O adatoms (left panel) and CO molecules (right panel) in the low, intermediate, and high surface coverages for T_e-AIMDEF and (T_e,T_{ph})-AIMDEF simulations.

For O adatoms, considering T_e-AIMDEF simulations with F=200 J/m^2 for the different surface coverages, we observe that until 0.6 ps the energy gain of the O adatoms is roughly the same at all coverages. Afterwards, at the high coverage the energy gain of the O adatoms starts to be slightly higher than at the other surface coverages. All in all, at the end of the simulation time the mean kinetic energy of the O adatoms at the different coverages are very similar with maximum differences of around 20 meV. For the largest laser fluence F=300 J/m^2, the kinetic energy of the atoms increases faster, almost in the same way as in the F=200 J/m^2 (T_e,T_{ph})-AIMDEF simulations up to 1 ps. Afterwards, its value remains slightly below the one obtained in the (T_e,T_{ph})-AIMDEF simulations but around 50 meV higher than the one obtained in the F=200 J/m^2 T_e-AIMDEF simulations. Regarding (T_e,T_{ph})-AIMDEF simulations, the mean kinetic energy increase is again almost the same at all coverages up to 1 ps. From this time on, the value at high coverage is slightly higher. Finally, at all coverages, the kinetic energy of the O adatoms reaches a plateau around 2.2 ps, with a common mean value of around 210 meV.

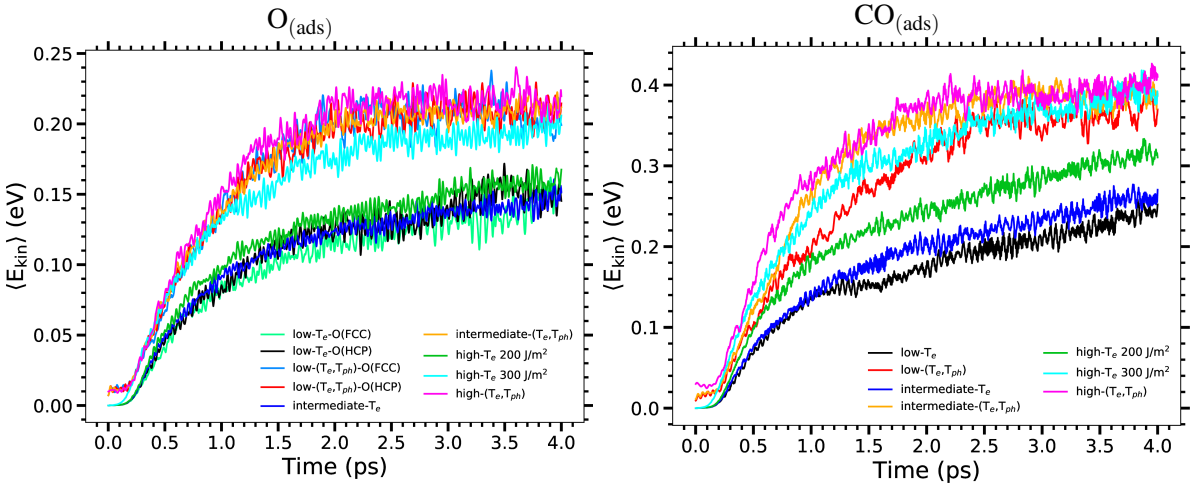

Figure 5.6: Time dependence of the total kinetic energies of O adatoms (left panel) and CO molecules (right panel) in the low, intermediate, and high surface coverages for T_e-AIMDEF and (T_e,T_{ph})-AIMDEF simulations (see insets for the meaning of each curve).

For CO molecules, considering T_e-AIMDEF simulations with F=200 J/m^2 we observe that the final energy increases with the increase of surface coverage. Until 1.2 ps the kinetic energy gain at the low and intermediate surface coverages is the same, but at longer times the kinetic energy at the intermediate surface coverage increases faster. The kinetic energy increase at high coverage is faster than at the other coverages from the beginning of the simulations. As a result of this, at the end of the simulations the mean kinetic energy at the high coverage is around 50 meV larger than in the intermediate coverage and around 60 meV larger than at the low coverage. As expected, with the laser fluence F=300 J/m^2 the kinetic energy increases even faster. The maximum value of the mean kinetic energy in this case reaches similar values than in the (T_e,T_{ph})-AIMDEF simulations with F=200 J/m^2.

In the (T_e,T_{ph})-AIMDEF simulations the kinetic energy gain of the CO molecules is obviously larger than in the T_e-AIMDEF simulations at the same fluence. In spite of that, the results are qualitatively similar. In this case, the mean kinetic energies at low and intermediate coverages are equal up to 0.7 ps. After that time the kinetic energy increases faster at the intermediate coverage until

it reaches a plateau at around 2.5 ps. In contrast, at low coverage the kinetic energy does not seem to arrive to a plateau until the end of the simulations. As in the T_e-AIMDEF simulations the kinetic energy gain at high coverage is the fastest one from the beginning of the simulations until it reaches a plateau at around 2 ps. As a result of all this, at the end of the simulations the mean kinetic energy of the CO molecules is similar for all coverages with a value around 400 meV.

5.2.5 Conclusions

As general conclusion, in the T_e-AIMDEF simulations, the adsorbates gain less kinetic energy than in the (T_e,T_{ph})-AIMDEF calculations. For high coverage, by increasing the laser fluence of 50%, at the end of the T_e-AIMDEF simulations the total kinetic energy of the adsorbates is almost equal to the one of the F=200 J/m^2 (T_e,T_{ph})-AIMDEF calculations, although the time evolution is different. Increasing the amount of CO or changing the adsorption site (in the low coverage case) does not have a particular effect on the kinetic energy of the atomic O. Notwithstanding, the amount of CO does have an effect on the kinetic energy of the CO molecules, where by increasing the amount of CO at the surface, the CO molecules reach higher kinetic energies. Finally in the F=200 J/m^2 (T_e,T_{ph})-AIMDEF simulations, almost independently of the surface coverage, at the end of the simulations the mean total kinetic energy of the O adatoms reaches a value of $\sim$200 meV and the mean total kinetic of the CO molecules reaches a value of $\sim$400 meV.

5.3 Analysis of the vertical motion of the adsorbates and the slab

In the following, we will study the vertical motion of the adsorbates, and of the surface atoms that are allowed to move, during the simulation. For simplicity, only the vertical motion of the adsorbates that remain adsorbed at the end of the simulations will be analyzed.

5.3.1 Low surface coverage

In Fig. 5.7 we show the density plot of the variations of the center of mass height of the CO molecules and the height of the O adatoms as a function of time at the low surface coverage. On the left hand side, the three panels from top to bottom show the results from the T_e-AIMDEF simulations. On the right hand side, the three panels from top to bottom show the results for (T_e,T_{ph})-AIMDEF. Figures 5.10 and 5.12 show the same results for the intermediate and high surface coverages.

For T_e-AIMDEF simulations (left panels of Fig. 5.7), we see that even though the adsorbates initial positions are at different heights (11.3 Å, 10.1 Å, and 9.8 Å for CO, O_{fcc}, and O_{hcp}, respectively) their respective height variations along the dynamics are almost the same, being within a range of $\sim$0.5 Å. For (T_e,T_{ph})-AIMDEF (right panels of Fig. 5.7), the height variations are at least three times larger for CO and two times larger for the majority of the O adatoms (both O_{fcc} and O_{hcp}) than in T_e-AIMDEF. Additionally, some trajectories lead to high (positive $\sim$2 Å) and low (negative $\sim$1.5 Å) positions of the O adatoms in respect to their initial position. This motion is observed in the panels corresponding to the (T_e,T_{ph})-AIMDEF simulations for O_{fcc} and O_{hcp} of Fig. 5.7. As will be explained below, this

behavior is allowed by the motion of the Ru surface atoms that are very mobile, specifically in the z coordinate.

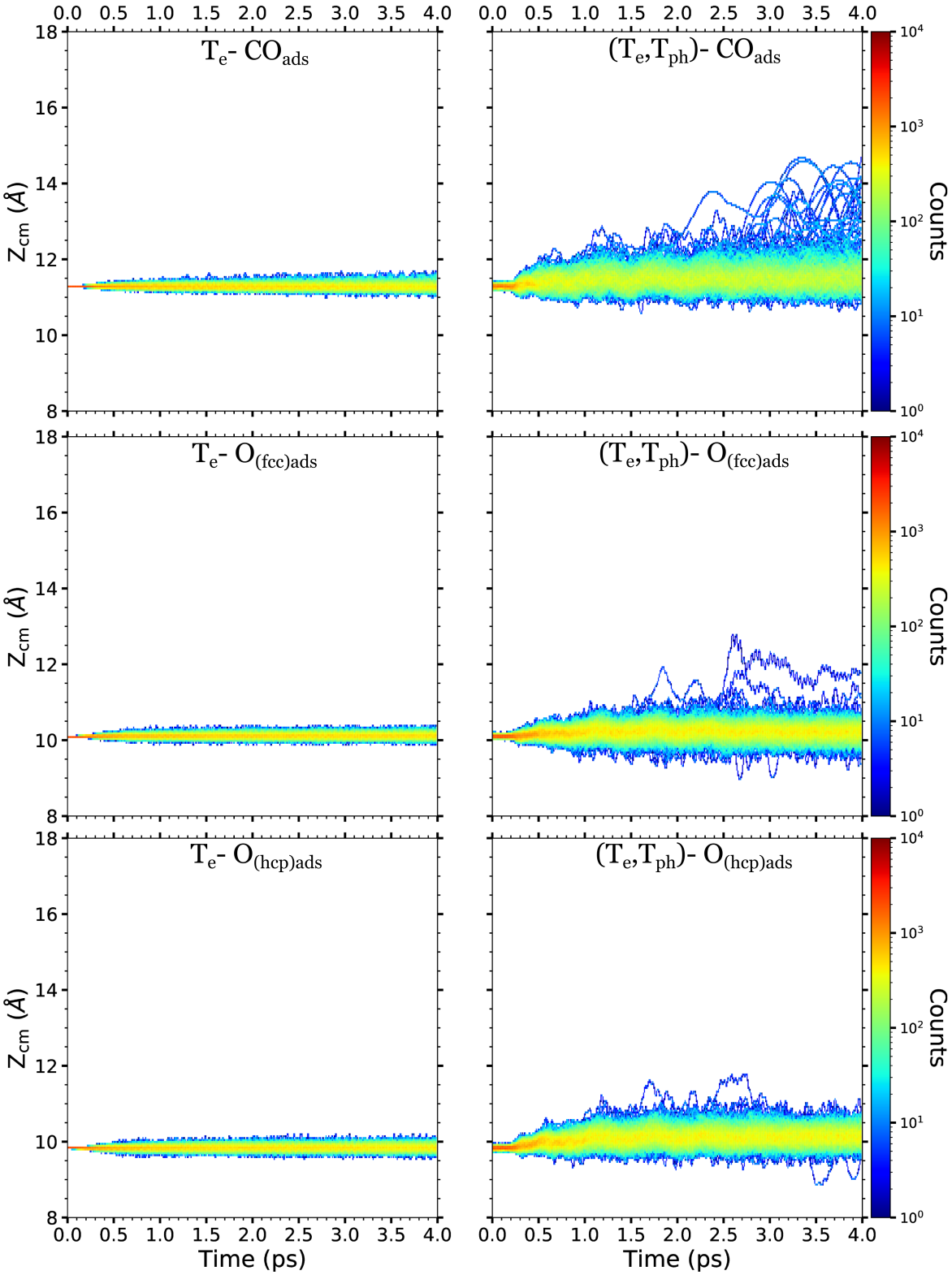

Figure 5.7: Density plots showing the time evolution of the O adatoms height and the CO center-of-mass height in the low surface coverage as obtained from T_e-AIMDEF (left column) and (T_e,T_{ph})-AIMDEF (right column). The color code represents, in a logarithmic scale, the number of adsorbates located at a height Z_{cm} at a given time. Top panels correspond to the CO center of mass height, middle panels to the position of O atoms initially on O_{fcc} sites, and bottom panels to the position of O atoms initially on O_{hcp} sites.

The variations of the positions at low surface coverage of the Ru atoms from the outermost layer, first inner layer and second inner layer are shown as a density plot in the left panel of Fig. 5.8. In this figure we observe that the second inner layer (the lowest one) is less mobile than the first inner layer, which is also less mobile than the outermost layer (the highest one). This behavior was expected since the outermost layer is the layer with the less coordinated Ru atoms. These atoms are less bonded and more free to move than the others. We observe that the majority of the vertical motion of the Ru atoms from the outermost layer is comprised in a range of ∼0.8 Å. However, we observe that several atoms overpass this limit and undergo a vertical motion of almost 2 Å. As last remark, we observe an oscillating behavior of the Ru slab starting around 1 ps with a period of ∼0.5 ps. This oscillation affects also the z coordinate of the adsorbates and induces a collective oscillatory motion of the adsorbates between 0.5 ps to 2.5 ps.

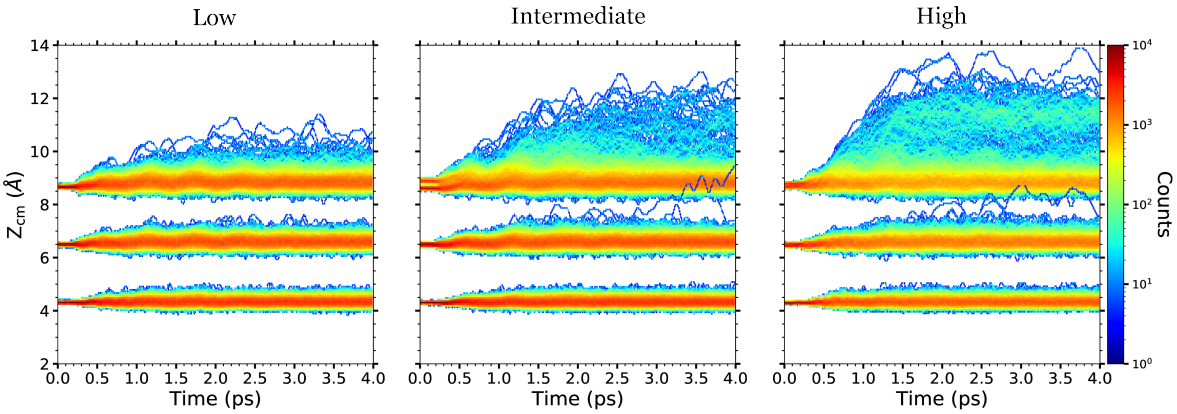

Figure 5.8: Density plots showing the time evolution of the heights of the Ru atoms in the first three topmost layers as obtained from (T_e,T_{ph})-AIMDEF with F=200 J/m^2. The color code represents, in a logarithmic scale, the number of Ru atoms located at a height Z_{cm} at a given time. Results are shown for the low (left panel), intermediate (middle panel), and high (right panel) surface coverages.

Due to the high vertical mobility of some Ru atoms, an O atom can take advantage of this motion and either penetrate the surface, passing below a Ru atom which moves up in the z direction, or remain on the near-top of a Ru atom while the latter is moving upwards. In the same way, a CO molecule can also adsorb on top of a Ru atom that moves upwards, resulting, in practice, in a new CO species. In Figures 5.9 we show the snapshots of the corresponding events in the low surface coverage. In the left hand part of the figure we show the name of the forming species in the series of the snapshots that are in the same line. The nomenclature of those species is taken from ref.[57] and is explained below. The snapshots are presented in rows and show the corresponding species some femtoseconds before and after their creation. In the inset, the time step of the snapshot is written. The central snapshot (third column in Fig. 5.9) shows the formed species. The simulation cell is presented in side view, and to facilitate the identification of the species, we remark the important zone of the snapshot with a white circle and slightly darken the rest of the snapshot. Due to the periodic boundary conditions, in the snapshots we show multiple representations of the unit cell, *i.e.*, we show multiple times the same adsorbates.

In the top row we observe the formation of CO species adsorbing on top of a Ru atom moving upwards (CO^{cus}). We observe that a CO diffuses from its adsorption site at the same time that a Ru

atom is moving up. After 0.6 ps the molecule is at the cus (coordinatively unsaturated site), forming the CO^{cus} species. The adsorbate remains about 0.8 ps at this site, then leaves it by diffusion. Next, in the two middle rows we show the formation of an O atom on top of Ru moving upwards (O^{cus}) and inside the first inner layer (O^{sub}), respectively. The O^{cus} species is formed in a similar way and time step as the CO^{cus} species, although it takes 0.2 ps less to diffuse from its initial adsorption site to the cus site, and remains 0.5 ps there before leaving it by diffusion. Then, the O^{sub} species occurs very late in the simulation, but it cannot be discarded that it may happen before. The present simulation has been chosen only by convenience. In this particular case, we observe that diffusion of one O into the subsurface region is very fast (0.3 ps). This process is a combined motion of a Ru atom going upwards and an O atom diving into the created vacancy. Lastly, in the bottom row, we show the formation of physisorbed (or trapped) CO (CO^{phys}). This process is also very fast ($\sim$0.3 ps), and will be deeply discussed in the following.

Figure 5.9: Snapshots of (T_e,T_{ph})-AIMDEF simulations at low surface coverage in which different species of interest are formed. Each row of snapshots is devoted to the formation of the species named at the left. Each snapshot is labeled with the time step to which it corresponds. The area of interest for the formation of the species is enlightened making darker the rest of the snapshot. The central panel in each row corresponds to the time step in which the specific species is formed.

Although, the creation of the O^{sub} and O^{cus} is rather exceptional (*i.e.*, low probability of occurrence) they have also been theoretically predicted to exist using kinetic Monte Carlo simulations in the RuO_2 surface.[57] Also, experimentally, it has been shown that when performing an O exposure below 850 K on Ru(0001), mobile atomic O species (O^{sub}) are predominantly formed in the subsurface region.[43] Though in our case the O coverage is much lower than the one achieved in that experiment, the lattice temperature reached in our simulations is much higher, which leads to a large mobility of the surface atoms and allows O adatoms to go below the first outermost layer. Regarding O^{cus}, in ref.[46], where the authors relate the activity of Ru to its O stochiometry, it has been demonstrated that O^{cus} can be formed at very low O_2 pressure (10^{-20} atms to 1 atms) and 300 K. Moreover, they also showed that the CO^{cus} species can be formed at room temperature for a wide range of O pressures (10^{-40} atms to 1

atms). Although, this study was conducted for RuO_2, considering the high temperatures reached in our simulations, it is not surprising that the O^{cus} and CO^{cus} species are formed, although they constitute sporadic events.

We remark that in our simulations two CO counted as adsorbed (meaning that they did not went above 6.5 Å from the Ru outermost layer) are in fact caught in a physisorbed well. In the bottom row of Fig. 5.9 we show the snapshots of the dynamics leading to one of those physisorbed CO molecules. If we look at the potential energy curve of the desorption of one CO from the Honeycomb surface (see Fig. 3.11 from Chapter 3), we see that there is no physisorption well when the surface is kept in its equilibrium state. However, as in our dynamics simulations the surface atoms and the adsorbates move so that the surface is not in its lowest energy state. Therefore, the potential energy curve can change in a way that a physisorption well is created where CO molecules can be trapped as they desorb. This behavior has already been experimentally investigated for the CO/Ru(0001) system.[72] The authors find $\sim 30\%$ of the CO molecules trapped in a physisorbed well due to a change of the chemisorption state of the CO molecules on Ru(0001) upon excitation of the substrate by using a femtosecond optical laser pulse. The authors interpret that this precursor state to desorption appears due to the increase of temperature induced by the electron-phonon interactions, and in a time scale superior to 2 ps to the desorption. This precursor state creation has been found to be phonon-mediated, and explains the indirect desorption of CO. In contrast, in a theoretical work,[76] in which independent movement of surface atoms and lattice distortion was not taken into account, the authors did not find physisorbed CO molecules by MD with electronic friction simulations, nor a physisorption well when calculating the potential of mean force with and without vdW correction.

Regarding the CO physisorption well in the presence of O adatoms in the surface, it has not been found under the coadsorption conditions of 0.5 ML of O with CO on Ru(0001), in ref.[77]. No indication of its presence was observed on the CO desorption induced by femtosecond laser pulses, neither in AIMD simulations performed at 2000 K. However, more recently, in ref.[215] the authors found that, with O coadsorbed at the surface, the background pressure of CO directly influences the concentration of CO trapped in the physisorption state although the surface coverage remains unchanged. In fact, they showed that for the low surface coverage, with honeycomb structure, multiplying the CO background pressure by three (from $2x10^{-8}$ to $6x10^{-8}$ Torr) allowed them to detect physisorbed CO. These observations are consistent with our simulations, where over the 200 trajectory calculations, we found 2 CO molecules trapped in physisorption conditions. Therefore, we have a predominance of the direct pathway of desorption of CO for low surface coverage and honeycomb structure in agreement with ref.[77], but we still observe very few trapped molecules in the physisorption well during the dynamics which is consistent with the findings ref.[215]. Finally, we note that concerning the rotational state of the trapped molecules, we find that both trapped molecules rotate parallel to the surface (helicopter rotation) and no trapped molecule rotates perpendicular to the surface (cartwheel rotation) in our simulations.

5.3.2 Intermediate surface coverage

In the following, we study the case of the intermediate surface coverage, where the CO desorption is predominant. We present in Fig. 5.10 the density plot of the variations of the center of mass height of the CO molecules and the height of the O adatoms as a function of time at the intermediate surface

coverage. We recall that in this case all O atoms are initially adsorbed in hcp sites. We observe on the left hand side of Fig. 5.10 that in the T_e-AIMDEF simulations the variations of height of the CO molecules are two times larger than at low surface coverage, while the O_{hcp} experience roughly the same height variations as at low coverage. The reason for this has to be related to the binding energy of the CO molecules. By increasing the CO surface coverage, the dipole-dipole interaction between the CO molecules gets stronger. Moreover, the adsorption site of the CO molecules changes from top to near-top (top-fcc or top-bridge). As a result, their binding energy to the surface diminishes in around $\sim$1eV, resulting in a higher mobility of the CO molecules in the intermediate surface coverage.

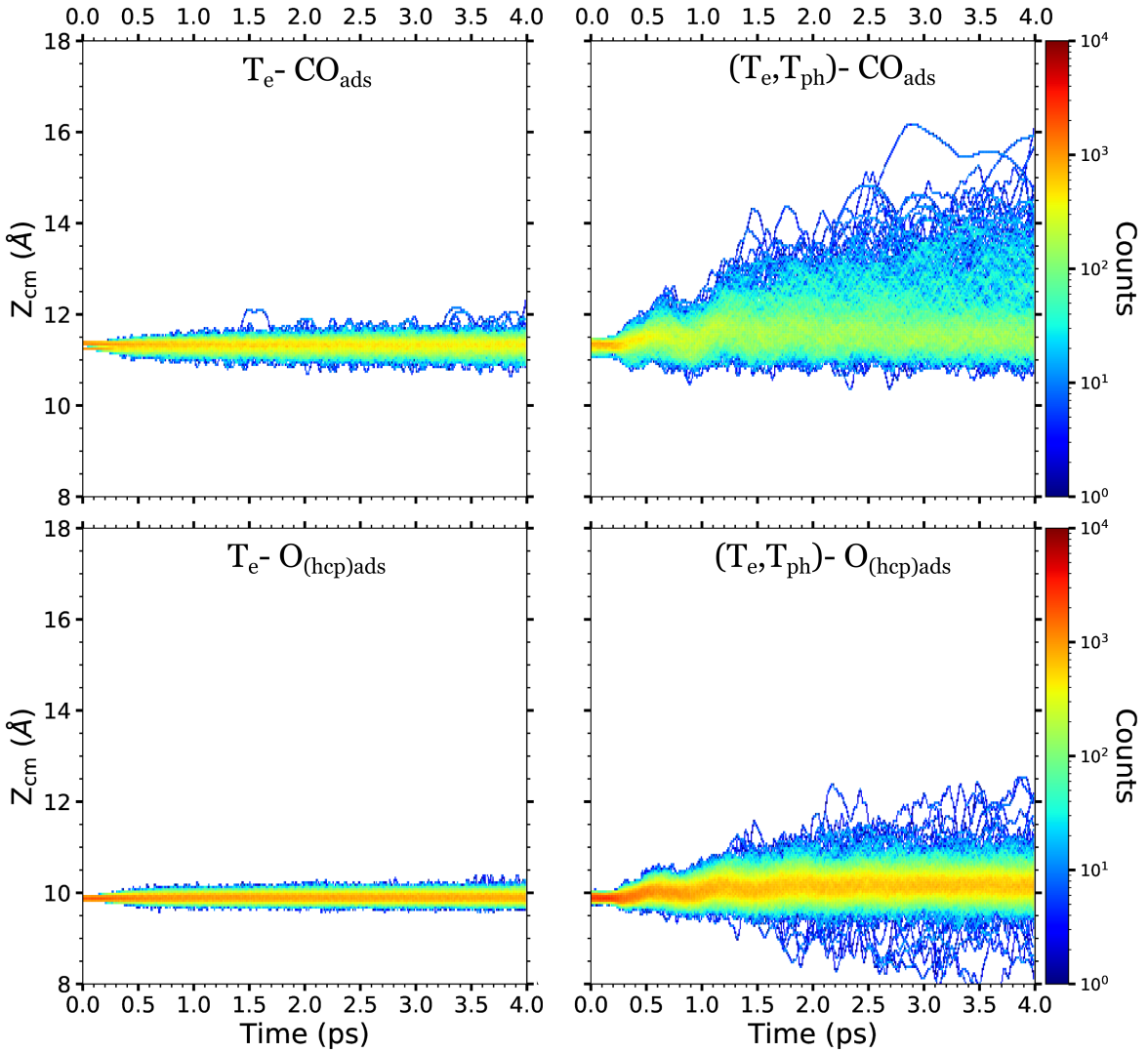

Figure 5.10: Density plots showing the time evolution of the O adatoms height and the CO center-of-mass height in the intermediate surface coverage as obtained from T_e-AIMDEF (left column) and (T_e,T_{ph})-AIMDEF (right column). The color code represents, in a logarithmic scale, the number of adsorbates located at a height Z_{cm} at a given time. Top panels correspond to the CO center of mass height and bottom panels to the height of the O adatoms.

On the right hand side of Fig. 5.10, for (T_e,T_{ph})-AIMDEF simulations, we observe that the height variations of both O and CO is increased. More precisely, this increase amounts to $\sim$3 Å for the CO molecules and to $\sim$1.5 Å for O atoms. Moreover, we see on the middle panel of Fig. 5.8 that the

height variation of Ru atoms in the intermediate surface coverage is much larger than the one in the low surface coverage by almost 2 Å. Additionally, note that in the intermediate surface coverage, at the beginning of the simulations, three Ru atoms of the outermost layer are slightly above the other by $\sim$0.25 Å. These Ru atoms are the ones that are directly binding the CO molecules. As they are less packed than the other surface atoms, we can conclude that the adsorbed CO is weakening the Ru-Ru bond, which could also explain the higher mobility of the O atoms at this coverage. If this hypothesis is true, then in the low surface coverage, Ru atoms with a CO adsorbed on top should experience the same effect. We observe that actually they do, although this effect is much less important than in the intermediate surface coverage. At low coverage these Ru atoms are in a position only $\sim$0.03 Å higher that the rest of Ru surface atoms. The resulting high mobility of the O atoms at the intermediate coverage will allow them to enter below the outermost layer region more easily than in the low surface coverage case.

In the middle panel of Fig. 5.8 we also observe that the trajectory of one of the Ru atoms from the first inner layer shows an exceptionally large vertical motion. This unique behavior is due to the deformation of the outermost layer. First, the outermost layer suffers a great deformation which allows the large vertical displacement of a Ru atom in the first inner layer. Next, this atom from the first inner layer goes up to the outermost layer, creating a vacancy in the first inner layer, and taking a position in the outermost layer. As a result, a Ru atom from the outermost layer is displaced above its normal position. At the same time, an O atom takes advantage of the vacancy created by the Ru atom in the first inner layer to go below the outermost layer.

As for low surface coverage, if we pay attention to the motion of Ru atoms from the outermost layer (middle panel of Fig. 5.8), we observe an oscillatory motion from 0.3 ps to 1.5 ps. We also observe in Fig. 5.10 that this oscillatory motion of the topmost surface layer is transferred to the adsorbates.

Also, we observe that in the intermediate coverage there is a large amount of CO molecules that move in the region of 2 Å to 4 Å above their initial adsorption wells. We have verified that half of these molecules are in fact CO^{cus} species that result from the high vertical mobility of a Ru atom of the outermost layer. The other half consists in molecules trapped in the physisorption well. In the case of the intermediate surface coverage this behavior was expected since we had found a physisorption well in the potential curve of desorption of the CO molecule (see Fig. 3.19). We observe that along the dynamics 10.4% of the total number of CO molecules stay some time trapped in this physisorption well.

Among the trapped CO molecules we observe that several of them have a specific rotational motion (helicopter or cartwheel) as identified in ref.[75]. More precisely, in our simulations we find 12 CO molecules that get trapped during some time in the physisorption well with a cartwheel rotation, 3 of which desorb before the end of the simulation time. In addition, 10 CO molecules get trapped with a helicopter rotation, of which only 1 desorbs before the end of the simulation. Finally, 10 CO molecules get trapped with no clear rotational state, 3 of which desorb before the end of the simulations. As an example, we show in the top panel of Fig. 5.11 the snapshots corresponding to the trajectory of one CO molecule going into the physisorption well state with a cartwheel rotation before desorbing. We observe that the transition from the chemisorbed to the trapped state is fast ($\sim$0.5 ps). Then, the

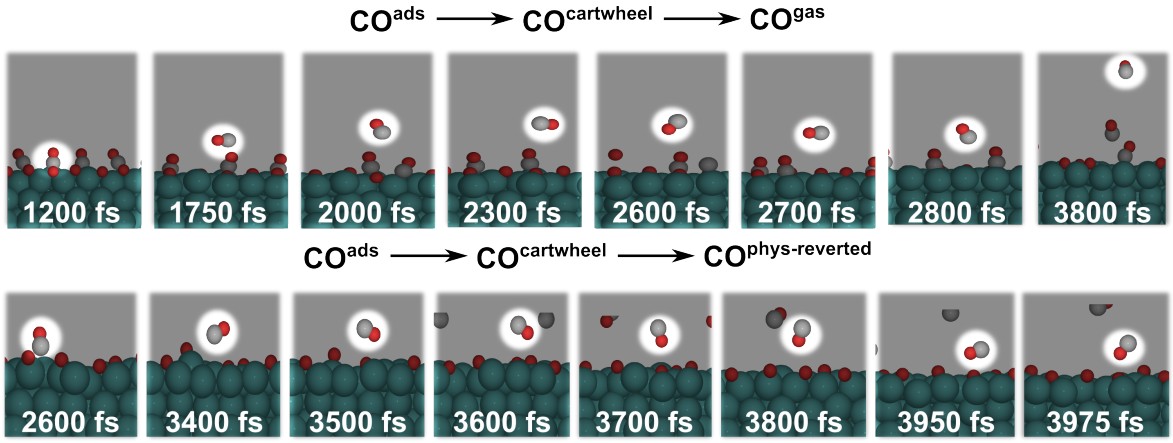

Figure 5.11: Snapshots of the formation of trapped CO molecules and their subsequent evolution in (T_e,T_{ph})-AIMDEF simulations at the intermediate coverage. The first row shows an event in which the molecule is first trapped in the physisorption well in a cartwheel rotation and afterwards desorbs. The second row shows an event in which the molecule is trapped in the physisorption well in a cartwheel rotation and the simulation ends up with the molecule trapped with the oxygen atom pointing to the surface. Each snapshot is labeled with the time step to which it corresponds. The area of interest for the formation of the species is enlightened making darker the rest of the snapshot.

molecule stays more than 1 ps in this trapped state moving parallel to the surface and with a cartwheel rotational motion before desorbing. In the bottom panel we show the snapshots of the trajectory of one CO molecule going into the physisorption well and that remains trapped at the end of the simulation. After its transition to the trapped state the molecule rotates and, interestingly, in the last 0.5 ps of the simulation remains trapped with the O atom pointing downward to the surface. This behavior is very particular and has not been observed for other trapped CO molecules.

5.3.3 High surface coverage

Finally, we study the vertical mobility of the adsorbates and surface atoms in the case of the high surface coverage. Recall that in this case we performed T_e-AIMDEF simulations for two different laser fluences, namely F=200 J/m^2 and F=300 J/m^2. We show in Fig. 5.12 the density plot of the center of mass height of the CO molecules and the height of the O atoms as a function of time for the high surface coverage.

In the case of T_e-AIMDEF simulations with laser fluence F=200 J/m^2 (left panels of Fig. 5.12) the vertical motion of the O atoms and the CO molecules is very similar with height variations of $\sim$0.5 Å. Although there are not CO desorption events in this simulations, we observe one CO that seems to desorb at the end of the integration time in one of the trajectories. However, its height is still below 6.5 Å above the surface, which was the height that we decided the molecules had to reach to be counted as desorbed.

When increasing the fluence to F=300 J/m^2 (central panels of Fig. 5.12) the variations of the adsorbates height is around 0.2 Å larger than with the lower fluence for both CO and O. Also, we note that two CO molecules seem to desorb from the surface, but again they have not been considered as desorbed because they did not reach the height of 6.5 Å above the surface at the end of the simulation. In fact, it looks probable that one of these molecules would end desorbing at a longer time. This

is not the case of the second molecule, for which a closer inspection shows that it gets trapped in a physisorption state with cartwheel rotation.

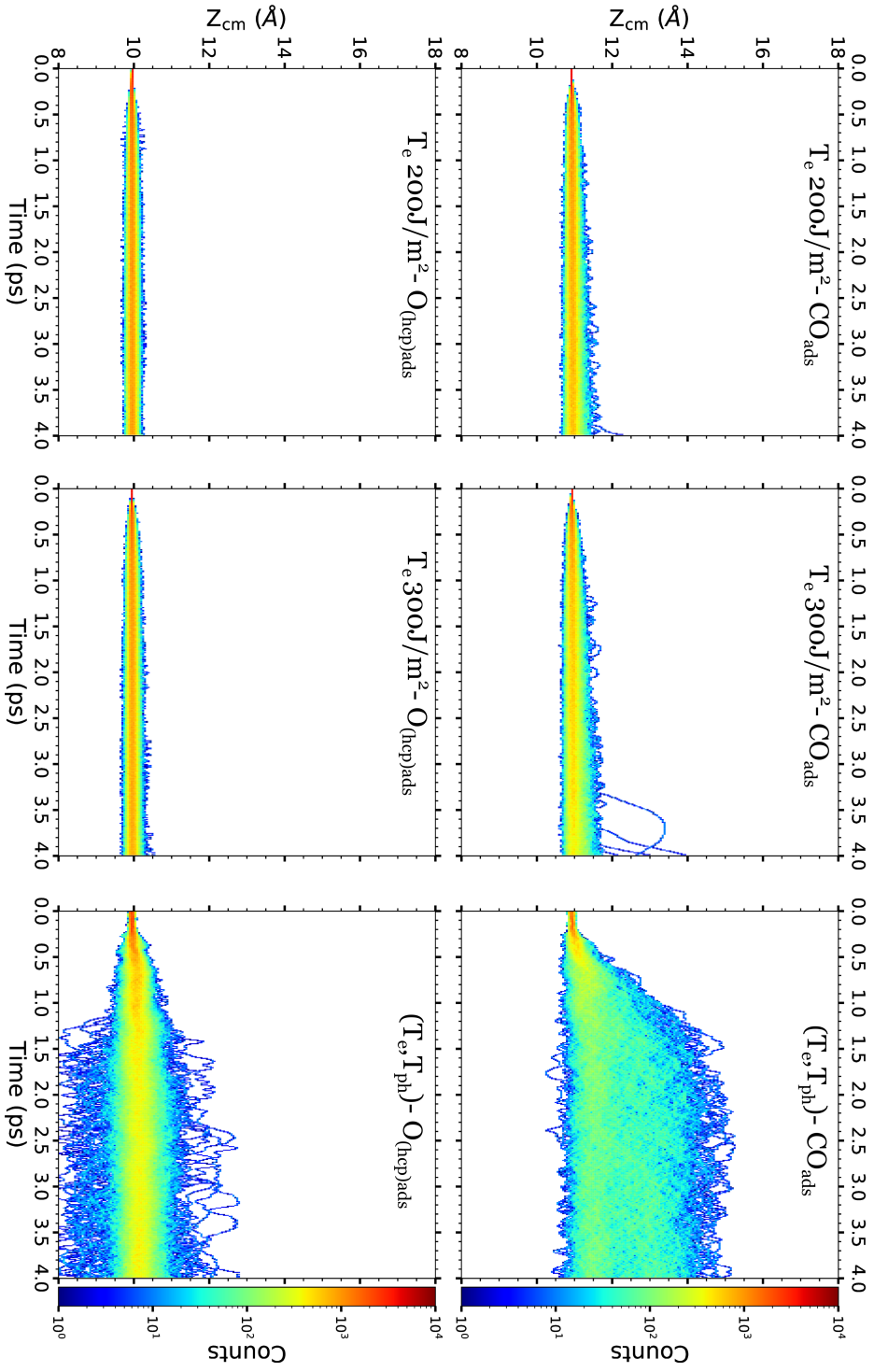

Figure 5.12: Density plots showing the time evolution of the O adatoms height and the CO center-of-mass height in the high surface coverage as obtained from T_e-AIMDEF with F=200 J/m^2 (left column), T_e-AIMDEF with F=300 J/m^2 (middle column) and (T_e,T_{ph})-AIMDEF with F=200 J/m^2 (right column). The color code represents, in a logarithmic scale, the number of adsorbates located at a height Z_{cm} at a given time. Top panels correspond to the CO center of mass height and bottom panels to the height of the O adatoms.

Now, concerning the (T_e,T_{ph})-AIMDEF simulations (right panels of Fig. 5.12) the vertical motion of the O atoms is similar to the results of the intermediate surface coverage. This is consistent with the fact that they are adsorbing in the same adsorption site. In contrast, the vertical displacements of the CO molecules is 0.3 Å larger than the one of the CO molecules in the intermediate coverage.

Although the CO vertical motion is larger at this coverage than in intermediate surface coverage, we observe much less CO molecules trapped in the physisorption well than in the intermediate coverage. We observe only 3 CO molecules trapped with helicopter rotation and other 3 CO molecules trapped with the cartwheel rotation, in contrasts to the hundreds of desorbed CO molecules. This result can be related to the form of the potential energy curve of desorption of CO molecules at this coverage. We see in Fig. 3.17 of Chapter 3 that a physisorption well is present in this curve, as for the intermediate surface coverage. However, this potential energy curve has two major differences. The first one is that the physisorption well is farther from the surface (between 0.7 Å and 1.3 Å). The second one, which is the most important, is that to reach the physisorbed state, the CO molecule has to overpass a barrier of 0.88 eV which implies that the CO molecule reaches the minimum of the physisorbed well with an excess in energy of 0.395 eV. Considering the energy barrier of 0.155 eV to desorption from the physisorbed state, the CO molecules have more than the required energy to desorb in a direct process, rather than being trapped in the physisorbed state.

Furthermore, at high surface coverage, we observe a large number of O^{sub} which are inducing high vertical motion of the outermost layer Ru atoms (see Fig. 5.8). In this way cus sites are created, which are in a great majority occupied by one or two CO molecules. This also explains the larger vertical mobility of the CO molecules in this surface coverage and also the greater amount of CO in the 12-14 Å region as compared to the intermediate coverage.

Finally, we note in Fig. 5.8 very small collective oscillations of the slab, which are almost negligible when comparing them to the oscillations observed in the intermediate and even the low coverages. As a consequence, we do not observe such collective vertical oscillations in the adsorbate motion either.

5.3.4 Conclusions

After the analysis of the vertical mobility of the adsorbates in the different surface coverages, and for the different types of simulations, we draw several conclusions.

First, we discern several species that were found in the literature, such as the O^{cus}, O^{sub}, CO^{cus} and trapped CO (CO^{phys}).[46;57] All those species have been found in all three surface coverages, although in different amounts. The O^{cus} and O^{sub} are present in the low surface coverage, but in lower amount than in the intermediate and high surface coverages. This is specially true for O^{sub} which is very numerous in the high surface coverage. The CO^{cus} and trapped CO are present in low surface coverage also, but trapped CO is present in a much higher amount in the intermediate surface coverage, and CO^{cus} in the high surface coverage The differences between the intermediate and high surface coverages are due to the different forms of the potential energy curve for CO desorption. In the high surface coverage the physisorbed state is disfavored probably due to the activation energy barrier that exist between the chemisorption and physisorption states. In the intermediate surface coverage there is less formation of O^{sub} species than in the high coverage, which leads to a relatively smaller vertical motion of the outermost Ru atoms and, subsequently, to the less formation of the CO^{cus} species.

Second, we observe that several CO molecules when they are trapped at the physisorption well experience cartwheel or helicopter rotational motions. This is an important characteristics of the dynamics specially for the intermediate coverage, which is the surface coverage in which more molecules are trapped. These molecules either remain trapped at the end of the simulation or desorb to the gas phase. In the low and high surface coverages we also observe such species, but as the direct desorption is favored, they are relatively less important.

Finally, in the low and intermediate surface coverages, we observe that between 0.5 ps and 2.5 ps the surface slab shows an oscillatory motion, that is also reflected in the vertical motion of the adsorbates. This motion is more pronounced in the intermediate surface coverage than in the low surface coverage, and not observed in the high surface coverage.

5.4 Analysis of the in-plane motion of the adsorbates

In the following, we will study the in-plane movement of the adsorbed species for the different surface coverages and calculation types. For simplicity, only the diffusion of the non-desorbing species, *i.e.*, the adsorbates that remain on the surface at the end of our simulations, will be discussed.

Colored density plots, that correspond to two-dimensional histograms of the adsorbates (x,y) positions over the surface will be used along this section. For each kind of adsorbate and simulation type, each density plot is constructed using the in-plane positions along the whole trajectory (4 ps, *i.e.,* 4000 steps) of all the adsorbates of that kind, and of all the simulated trajectories. Thus, the density color code gives qualitatively an idea of the amount of time the adsorbates have spent in a given position (higher densities will correspond to longer times). Let us also remark that in each plot the atoms are allowed to go out of the unit cell (enclosed by a black solid line in the figures). The reason is that we are using a extended coordinate representation in order to show the continuous path followed by the adsorbates. The extended coordinates are calculated such that when an adsorbate goes out of the simulation cell, and is forced to stay inside it by the periodic boundary conditions by changing its position to the other border of the unit cell, we sum up the corresponding unit cell basis vector to the adsorbate position. In this way, the adsorbates are allowed to have coordinates that are outside the simulation cell and the figure will provide a better representation of the adsorbates in-plane movement.

5.4.1 Low surface coverage

In Fig. 5.13 we show the density plot of the in-plane center-of-mass position for the whole simulation of the CO molecules and of the in-plane position of the O adatoms in the low coverage. In the left hand side of Fig. 5.13 the three panels from top to bottom show the in-plane motions in the T_e-AIMDEF simulations. In the right hand side, the three panels from top to bottom show the in-plane motions in the (T_e,T_{ph})-AIMDEF simulations. For completeness, density plots showing the time evolution of the in-plane positions of the adsorbates for all three surface coverages, separated in frames of 0.5 ps of simulation time, are also provided in appendix G.

In the T_e-AIMDEF simulations (left panels of Fig. 5.13), the O adatoms stay on their respective adsorption sites. In the same way, the CO molecules remain in top/near-top sites, showing no preference to move neither towards fcc sites nor towards hcp sites. The CO molecules explore an ellipse centered

on the top position with a long axis of ∼1.3 Å and a short axis of ∼1 Å. These movements make impossible the CO oxidation because the CO and O adsorbates cannot get close enough to recombine.

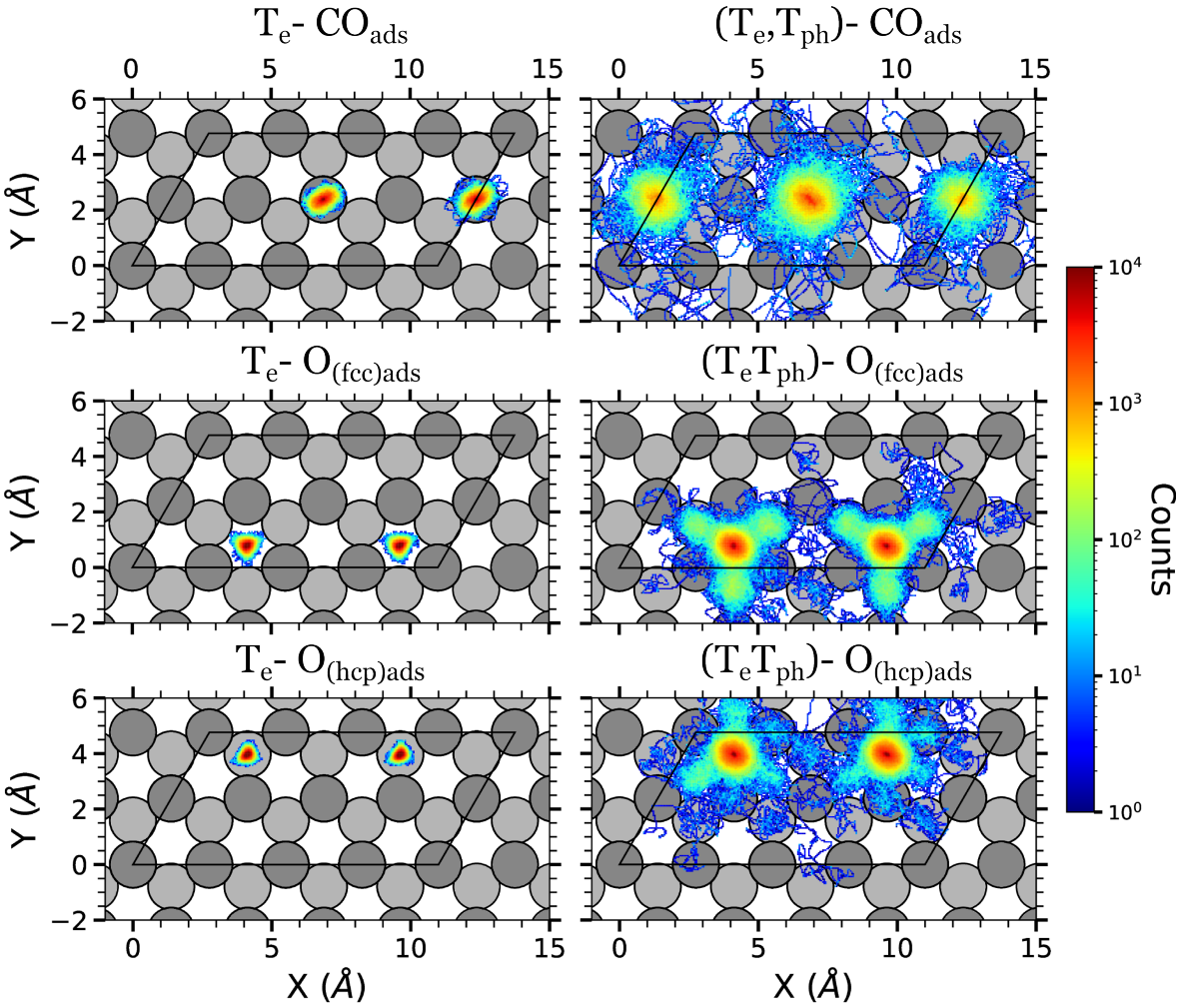

Figure 5.13: Density plots of the (x,y) positions over the surface of the adsorbates at the low surface coverage in the AIMDEF simulations. Only the positions of the adsorbates that remain adsorbed on the surface at the end of the simulation are shown. Left (right) column shows the results of the T_e-AIMDEF ((T_e,T_{ph})-AIMDEF) simulations. Top panels correspond to the center of mass of CO molecules, middle panels to the position of O atoms initially on fcc sites, and bottom panels to the position of O atoms initially on hcp sites. The black line encloses the simulation cell. For clarity, the position of the adsorbates is shown in an extended coordinate representation.

However, in the (T_e,T_{ph})-AIMDEF simulations (right panels of Fig. 5.13), the in-plane mobility of all the adsorbates is tremendously increased when the Ru lattice excitation is incorporated in our simulations. In particular, the O adatoms, even if they spend most of the time in their initial adsorption site, can now abandon it with a rather high probability. More precisely, O atoms initially located at the fcc sites show a tendency to move to the closest hcp sites, whereas the ones initially located at the hcp sites show a tendency to move to the closest fcc sites. We also observe that O atoms initially adsorbed in hcp sites show a slightly smaller mobility than those adsorbed in fcc sites. This is consistent with the larger adsorption energies of atoms in hcp sites. Note that there exist some less probable events in

which the O atoms move beyond the closest neighbor adsorption site (fcc or hcp). Finally, note that for an O adatom to move to the neighbor fcc or hcp sites, it needs to go through a bridge site. This is of great importance for CO oxidation, for which the MEP requires that the O adatom crosses a bridge site.

The mobility of the CO molecules is also much increased in the (T_e,T_{ph})-AIMDEF simulations. Now they explore a circle of $\sim$2.3 Å radius centered in their equilibrium position. We again do not observe that they present any preference to move towards fcc or hcp sites. Additionally, we observe several events in which the CO molecules move beyond their first neighboring site.

5.4.2 Intermediate surface coverage

In Fig. 5.14 we show the density plot of the in-plane center of mass position of the CO molecules and of the in-plane position of the O adatoms on the whole simulation time at the intermediate surface coverage. In the T_e-AIMDEF simulations (left column of Fig. 5.14), we observe that the CO molecules explore an ellipse centered in their adsorption site but which has a larger area than at low coverage. Now, the length of its long axis $\sim$2.5 Å and the one of the short axis $\sim$1.3 Å. Also new features appear. The CO molecule in the left of the simulation cell, even if with low probability, can experience lateral diffusion towards the left. Additionally, and also with low probability, we observe that the CO molecules on the right hand part of the simulation cell can move "upwards" from its initial top-bridge site towards a top-fcc site. The O adatoms mostly remain in their adsorption site, although there exist few events in which they abandon their hcp adsorption site towards the closest fcc site situated close to the row in which the CO molecules are adsorbed. Note that the rightmost O atom is the most mobile one (including the second one from the left which can also abandon its adsorption site towards the "upper" fcc site). This higher mobility is due to the initial configuration of the atoms in the cell, since the O adatom at the right hand side is the one that has not a CO molecule adsorbed on the near-top site above it.

In the (T_e,T_{ph})-AIMDEF simulations (right column of Fig. 5.14), we see that the mobility of both kind of adsorbates is very much larger than in the low coverage. In fact, now there is not any area of the simulation cell that is inaccessible for one kind of adsorbate or the other, and even that there are regions that are accessible for both kind of adsorbates. Still, we observe that in the case of CO molecules, the O row acts as a barrier that prohibits the CO molecules to access the lower part of the simulation cell, except for very few rare events. In contrast, the O adatoms can move all over the cell albeit it is less probable to find them at top sites than in hcp or fcc sites. In any case, as we have seen when studying the vertical mobility of the O atoms (Fig. 5.10), the creation of O^{cus} species implies that the O adatom can adsorb on top of a Ru atom.

5.4.3 High surface coverage

In Fig. 5.15 we show the density plot of the variations of the center of mass in-plane position of the CO molecules and of the in-plane position of the O adatoms on the whole simulation time at the high surface coverage. We recall that in this case, we performed T_e-AIMDEF simulations for two different fluences, namely F=200 J/m^2 and F=300 J/m^2.

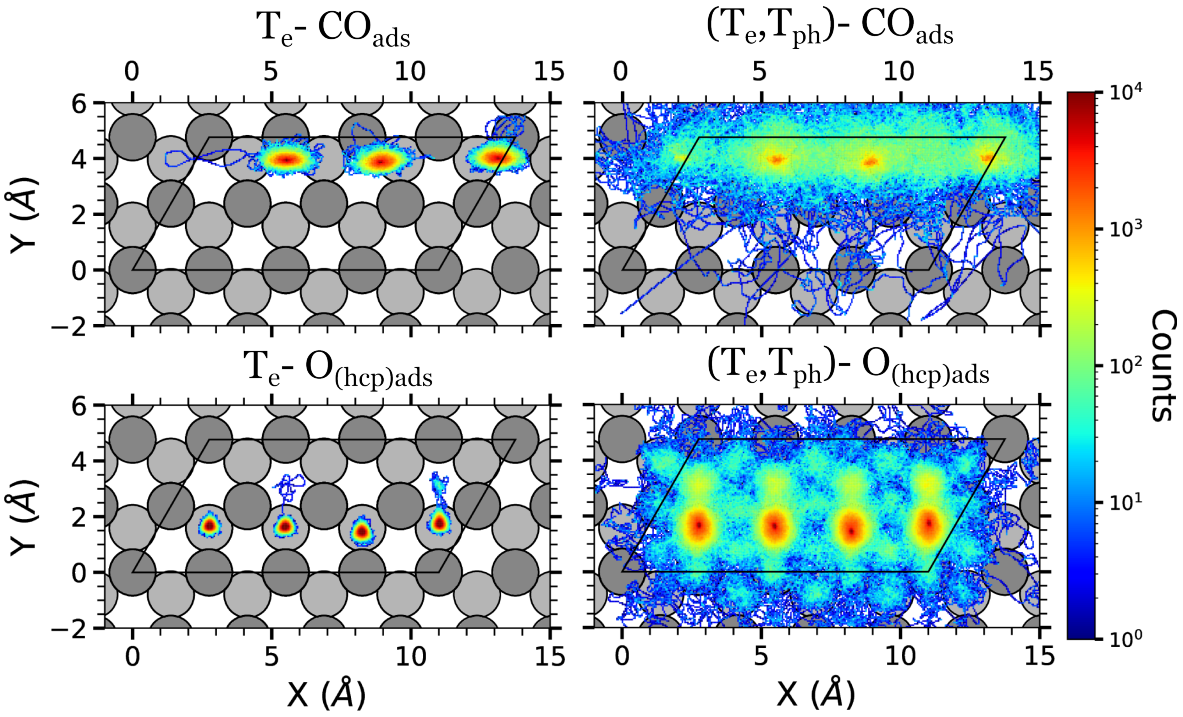

Figure 5.14: Density plots of the (x,y) positions over the surface of the adsorbates at the intermediate surface coverage in the AIMDEF simulations. Only the positions of the adsorbates that remain adsorbed on the surface at the end of the simulation are shown. Left (right) column shows the results of the T_e-AIMDEF ((T_e,T_{ph})-AIMDEF) simulations. Top panels correspond to the center of mass of CO molecules and bottom panels to the position of O atoms. The black line encloses the simulation cell. For clarity, the position of the adsorbates is shown in an extended coordinate representation.

In T_e-AIMDEF simulations with laser fluence F=200 J/m^2 (left column of Fig. 5.15), the in-plane motion of the CO molecules is mostly restricted to a circle of radius $\sim$1 Å. Still, we observe some events that involve lateral displacement of the CO molecules from one hcp site to another along the row in which they are located. Note that at the high surface coverage, when one of the CO molecules in the simulation cell desorbs, the number of atomic and molecular species that remain adsorbed in the simulation cell correspond to the intermediate coverage. As a consequence, the remaining CO adsorbates tend to rearrange into the most stable configuration of the new surface coverage, leading to this lateral displacement. The O atoms remain in their adsorption site, so that CO oxidation cannot take place under these conditions.

In T_e-AIMDEF with laser fluence F=300 J/m^2 (middle column of Fig. 5.15), the in-plane motion of the CO molecules is mostly restricted to a larger circle of radius $\sim$1.2 Å, but now the lateral displacement in the row is much more probable than in the case of the F=200 J/m^2 laser fluence. This can be understood by realizing that the CO desorption probability is 15 times larger than at the lower fluence, which is expected to facilitate the movement of the CO molecules. In the case of the O adatoms, even if they remain mostly at their adsorption site, we observe some events in which they abandon it and move, through bridge sites, towards the fcc sites. Also, we observe in one trajectory that the O adatom at the right hand site of the unit cell moves to a different hcp site after moving to the

fcc site. Clearly, the adsorbates have an increased mobility when the laser fluence is increased that could allow them to eventually recombine, even if there is no motion of the surface.

For (T_e,T_{ph})-AIMDEF simulations (right column of Fig. 5.15), we observe, as for the (T_e,T_{ph})-AIMDEF simulations of the intermediate surface coverage, that the adsorbates move over all the surface. As a general observation we can state that the adsorbates move in a similar way as in the intermediate surface coverage. The CO molecules show mostly a lateral motion along the row in which they are adsorbed, while the O adatoms move all over the surface. The addition of one CO on the surface does not seem to restrict the motion of the CO molecules, as it could have been expected.

5.4.4 Conclusions

The following general conclusions can be extracted of the study on the in-plane motion of the adsorbed species. Regarding the the T_e-AIMDEF simulations, for the low surface coverage the adsorbates do not abandon their adsorption well. In the intermediate surface coverage there is some lateral diffusion of the CO molecules and several O adatoms move toward the fcc adsorption sites. Finally, in the high surface coverage, we observe lateral diffusion of the CO molecules with the F=200 J/m^2 laser fluence, which is much more important with the F=300 J/m^2 laser fluence. In the latter case, we also observe that several O adatoms move to the fcc sites.

Regarding the (T_e,T_{ph})-AIMDEF simulations, for the low surface coverage the O adatoms show a relatively large probability to move towards their first neighboring site in a triangular fashion. With a much lower probability we even observe some trajectories in which the O atoms travel further from their adsorption site. At the same time, the CO molecules explore a circumference of radius 2.3 Å and do not show a tendency to move towards any preferential adsorption site. In intermediate surface coverage, the adsorbates show a larger in-plane motion. This is specially true for the O atoms which now move all over the surface. Although they move preferentially to hcp and fcc sites, they can also access the top sites with the formation of O^{cus} species as we have seen in the study devoted to the vertical movement (see Section 5.3). The CO molecules move preferentially in the lateral direction along the row in which they are adsorbed. Notwithstanding, we still observe that some CO molecules can abandon this row an explore the complete surface. In the high surface coverage the adsorbate motions are very similar to those at the intermediate coverage.

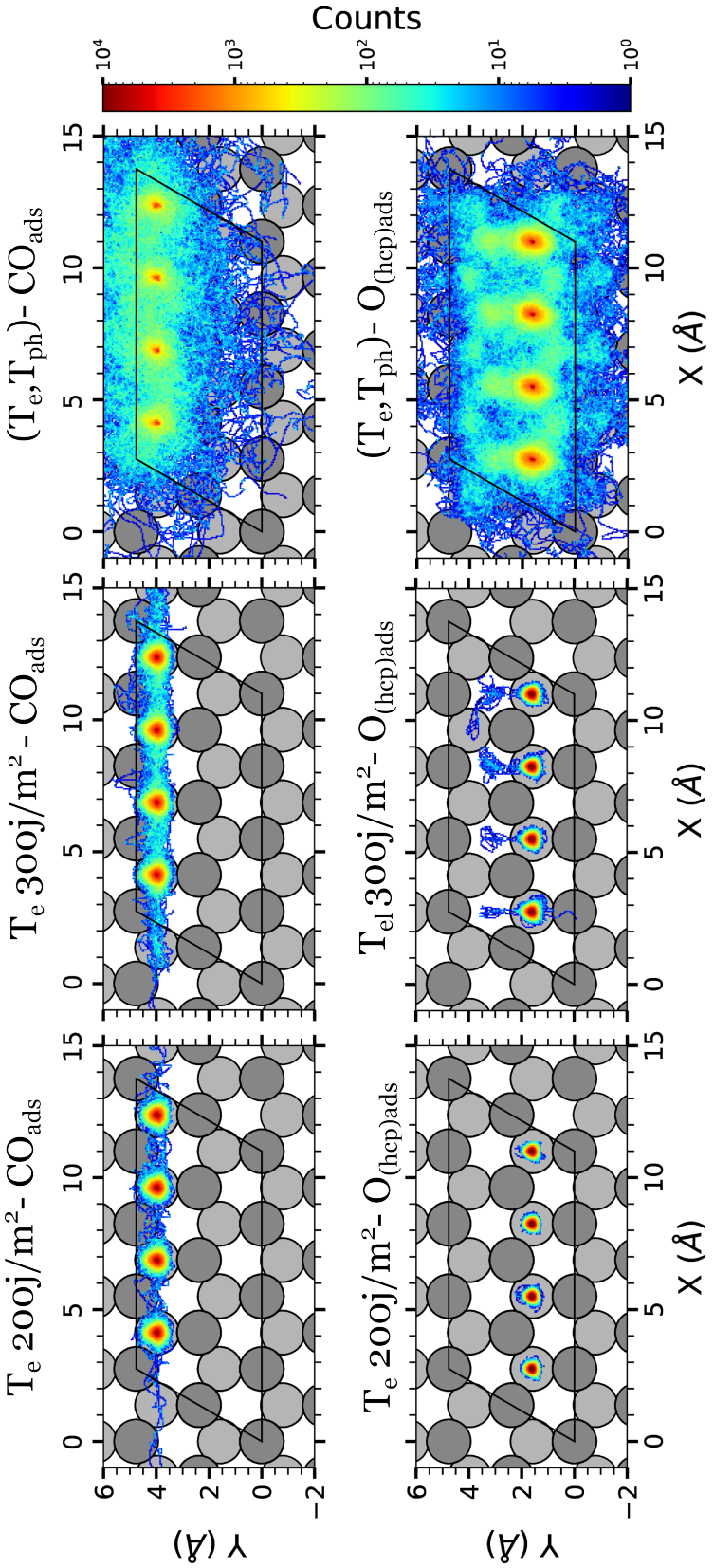

Figure 5.15: Density plots of the (x, y) positions over the surface of the adsorbates at the high surface coverage in the AIMDEF simulations. Only the positions of the adsorbates that remain adsorbed on the surface at the end of the simulation are shown. Left, center, and right columns show the results of the T_e-AIMDEF F=200 J/m^2, T_e-AIMDEF 300 J/m^2, and (T_e,T_{ph})-AIMDEF F=200 J/m^2 simulations, respectively. Top panels correspond to the center of mass of CO molecules and bottom panels to the position of O atoms. The black line encloses the simulation cell. For clarity, the position of the adsorbates is shown in an extended coordinate representation.

5.5 Analysis of the CO oxidation mechanisms

As already discussed in Chapter 4, the two CO oxidation trajectories in the low coverage basically follow the MEP calculated in Chapter 3 for this coverage. However, as discussed in the above sections, compared to the low coverage, not only the adsorbates but also the Ru atoms in the two topmost layers become more rapidly very mobile in the intermediate and high coverages. As a result, none of the oxidation trajectories seem to follow the MEP calculated in Chapter 3 for the equilibrium structures of the intermediate and high coverages. Therefore, considering the variety of reaction paths found in the dynamics simulations, we found useful to classify the CO oxidation trajectories into three different types attending to the different adsorption positions of the reactive O and CO species at the instant of recombination (bridge, near-top, and cus). The three types (denoted in the following as **A**, **B**, and **C**) are defined as follows,

A $CO^{near-top} + O^{bridge}$

B $CO^{cus} + O^{near-top}$

C $CO^{bridge} + O^{bridge}$

where near-top is defined in Section 3.2 of Chapter 3 and cus is defined Section 5.3 of this chapter.

Prior to the oxidation, several events can occur that might affect the reaction dynamics and in some cases they can even help the oxidation process. Since those events are not identified to be mandatory for the reaction, we do not treat them as being a constitutive part of the reaction path. Those events (hereafter denoted by a number in bold) are the following,

1 CO desorption

2 CO_2 desorption

3 CO diffusion on the surface

4 O diffusion on the surface

5 Ru atom moving up creating a cus site

In the following three sections we will describe the mechanisms of CO oxidative recombination observed in our AIMDEF simulations for each surface coverage. For simplicity, the above nomenclature will be used to classify and describe each of the CO oxidation trajectories.

5.5.1 Low surface coverage

In Chapter 3, when studying the MEP of CO oxidative recombination we considered a system close to its equilibrium position. However, when studying the reaction dynamics it is not obvious that the adsorbates will follow the same MEP since the potential energy surface is different. In the case of the oxidative recombination in the low surface coverage, it has already shown in Chapter 4 that the reaction does proceed through the MEP, in which the less bound O_{fcc} abandons its adsorption well, then crosses the bridge site between two Ru atoms, and recombines with the nearby CO on a near-top

site to form the chemisorbed the bCO_2 and desorbs from the surface passing through the physisorbed lCO_2 state described in Chapter 3. The snapshots of one of these trajectories are shown in Fig. 4.2 of Chapter 4. This mechanism where the O adatom and the CO molecule are, respectively, on bridge and near-top site, is the above defined oxidation type **A**.

In summary, the two oxidation trajectories in the low coverage are classified as

94: **A**

163: **A**

where the underlined number denotes the number of the trajectory in the (T_e,T_{ph})-AIMDEF simulation set.

5.5.2 Intermediate surface coverage

In this coverage, the CO is initially adsorbed at near-top sites (top-fcc or top-bridge). Therefore, to recombine, knowing that in the minimum energy path CO is at near-top and O on bridge, the CO is already in the perfect position.

Following the above nomenclature the four oxidizing trajectories can be schematically described and classified as follows,

54: **5** which pushes the reactive CO, then **A**

114: **1**, then **A**

138: **3** of all CO in the row to the left, then **4** to fcc, then **4** to hcp, then **A**

162: **3** of two CO molecules to the right, then **5**, then **B**

We observe that in three out of four trajectories (54, 114 and 138), the oxidation mechanism is **A**. In the four trajectories, one or several events happen prior to oxidation, which was not the case in the low coverage. In trajectory 54 the reactive CO is pushed towards the recombining O by a pronounced vertical motion of the Ru atom on which it adsorbs. In trajectory 114 the oxidation process is preceded by desorption of one of the three CO. The latter allows the other CO molecules on the surface to move more easily, what facilitates the ulterior recombination. In trajectory 138, several diffusion events are occurring prior to oxidation. First, the row of CO molecules diffuse along the *x*-direction, as already observed in the in-plane motion section (see Fig. 5.14). Furthermore, the reacting O adsorbate moves to the nearest fcc site, from where it recombines with CO. Compared to the calculated MEP, diffusion of the recombining CO is rather atypical since it is the recombining O and not the CO the reactant that moves the farthest from the adsorption well.

Surface deformation in which a Ru atom moves upwards is essential to the oxidative reaction in trajectory 162. This new type of recombination that involves a CO^{cus} species is the one denoted **B** above. Obviously, since this mechanism involves CO^{cus} species, the deformation of the surface is mandatory for it to occur. In Fig. 5.16 **A)** we plot selected snapshots of trajectory 162 showing the recombination type **B**. In the time interval 2430 fs to 2500 fs the CO molecule is on a cus site. Therefore, when it approaches the O adsorbate to recombine, it has a vertical position higher than

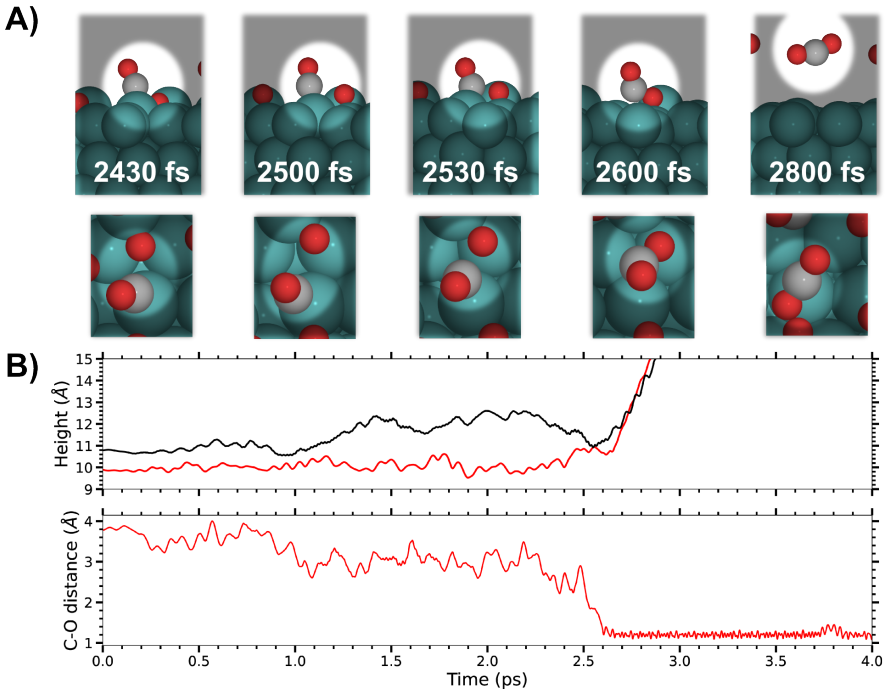

Figure 5.16: A) Snapshots of the AIMDEF trajectory 162 of the intermediate coverage showing type **B** of CO oxidation. For each snapshot, top and bottom panels corresponds to side and top views, respectively. The time of the snapshot (in fs) is written in white. For the sake of clarity, only the recombining O and CO with their periodic images are shown. **B)** Top: Height of the recombining O adsorbate (red) and C in the recombining CO (black) against simulation time. Bottom: distance between these two atoms against simulation time.

when adsorbing on a near-top site. This allows the O adsorbate to recombine being below the CO, and also, not being on a bridge site, but on a near-top site. In Fig. 5.16 **B)** we show the height of the recombining O adsorbate (in red) and the C atom (in black) from the CO molecule as a function of time. The distance between these two atoms are shown in the bottom panel. We observe that prior to recombination ($\sim$ 2.7 ps) the C atom has a vertical position $\sim$2 Å higher than the position of the O atom. Therefore, the specificity of this mechanism is the vertical position of the recombining species, with the O adatom attacking the CO^{cus} from bellow. This mechanism of oxidation resembles the one seen in scattering experiment where the scattered O is attacking the CO hot adsorbate from below due to steric effects.[187] Also, we can compare this mechanism with the one found in ref.[88] where the authors study the CO_2 dissociation on stepped Ru(20$\bar{2}$1) and kinked Ru(11$\bar{2}$1). With calculations of MEP they show that the energy barrier to go from O+CO adsorbed to the CO_2 molecule adsorbed on the surface is lower in the kinked or the stepped surfaces than in the flat Ru(0001) surface. In the case of the stepped Ru(20$\bar{2}$1) surface, the CO is adsorbed on the outermost layer, and the O on the first step, such the O atom is lower in vertical position respect to the CO. During recombination, the CO remains on the near-top position of the outermost layer when the O atom is recombining, being in the bridge site between the step and the upper step of the CO.

5.5.3 High surface coverage

As found in the intermediate surface coverage, none of the CO oxidation trajectories in the high coverage follows the corresponding MEP described in Chapter 3 (see Fig. 3.18). Next, we list the (T_e,T_{ph})-AIMDEF trajectories leading to CO oxidation for the high surface coverage. As previously, the underlined number identifies the number of the trajectory in the simulation set, while the following text is the description of the main recombination steps.

27: **B**

90: **A**

96: **3** of three CO in a row to the left, then **A**

200: **1**, then **B**

359: **C**

368: **B**, then **2**, then **5**, then **4** to fcc then to top site, then **B**

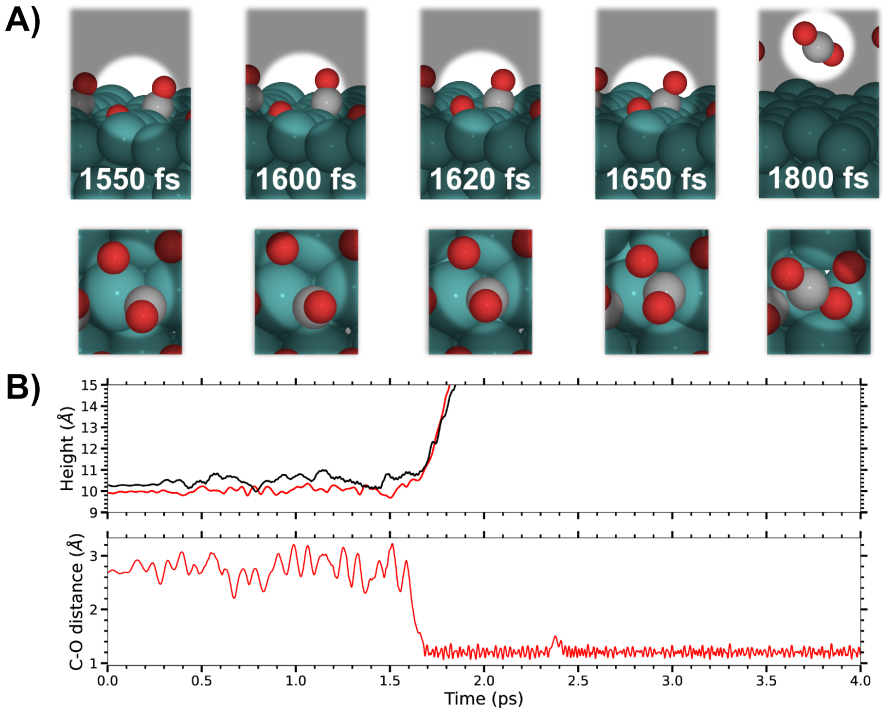

Figure 5.17: **A)** Snapshots of the AIMDEF trajectory 359 of the high surface coverage for which the CO oxidation type **C** is identified. For each snapshot, top and bottom panels correspond to side and top views, respectively. The time of the snapshot (in fs) is written in white. For the sake of clarity, only the recombining O and CO with their periodic images are shown. **B)** Top: Height of the recombining O adsorbate (red) and C in the recombining CO (black) against simulation time. Bottom: distance between these two atoms against simulation time.

In this coverage, we identify the three different types of CO oxidation events, three trajectories with type **B**, two with type **A**, and one with the new type **C** that was not observed in the previous coverages.

The recombinative CO_2 desorption in trajectories 27, 90, and 359, as well as the first desorption in trajectory 368 occur with no prior event. Note that the latter trajectory is the only case in which we observe more than one oxidation processes in the same simulation. In trajectory 96 there is a concert diffusion of all the CO molecules along the *x*-axis, similar to that observed in trajectory 138 of the intermediate surface coverage.

In Fig. 5.17 **A)** we show selected snapshots of the trajectory 359 in which we identify the recombination mechanism **C**. The time evolution of the height of the O adatom (in red) and the C atom (in black) from the CO molecule along the trajectory are shown in panel **B)** of the same figure. As shown in panel **A)**, both species reach a bridge site at 1620 fs. Recombination is already achieved within the next tens of femtoseconds (see also the C–O distance in panel **B)**) and it is rapidly followed by desorption as linear CO_2. In addition, we observe in panel **B)** that the vertical position of the recombining O atom and that of C in the recombining CO molecule are close in height ($\sim$0.4 Å). Although not shown, something similar was observed in the oxidation events of **A**, the only difference between **C** and **A** being that the CO is on bridge in the former and at near-top site in the latter.

5.5.4 Conclusions

As conclusions to this section, we identify three different types of CO oxidation, the first one, denoted **A**, was already shown in Chapter 4. The second one, **B**, has been observed in the intermediate and high surface coverages, which are characterized by large vertical distortions of the Ru topmost layers, and the third one, **C**, has been observed in the high surface coverage.

Mechanism **B** is characterized by the motion of a CO molecule on a cus site, therefore when it approaches to the O adatom to recombine, it has a vertical position higher than when adsorbing on a near-top site. This allows to the O adatom to recombine being below the CO as it could be observed in scattering experiments[187] and on stepped surfaces.[88]

Finally, the **C** mechanism is characterized by the motion of both O and CO species moving to a bridge site, then rapidly recombining and desorbing. Note that, in principle, mechanism **C** could have been observed in all the different surface coverages since it does not require any specificity of the high surface coverage.

CHAPTER 6

MOLECULAR DYNAMICS PERFORMED WITH NEURAL NETWORK POTENTIAL ENERGY SURFACE

"Ce n'est qu'en essayant continuellement que l'on finit par réussir. En d'autres termes, plus ça rate et plus on a de chances que ça marche."

— Jacques ROUXEL, Les Shadoks.[1]

In this chapter we present and describe the construction of two NN-PES using two different data selection methods. We used the EANN architecture presented in Chapter 2.5.3 to generate the NN-PESs. Both NN-PESs are trained using thousands of data provided by the AIMDEF simulations performed in this thesis. These data are used as a reservoir of configurations, henceforth called the Universe. The different data sets that will be used in the NN-PES generation process will consist in subsets of this Universe.

The first and second NN-PESs are constructed using data obtained from the low (0.5 ML O + 0.25 ML CO) and intermediate (0.5 ML + 0.375 ML CO) AIMDEF simulations, respectively. Still, it is expected that though the NN-PESs are calculated for specific coverages, they are transferable, and can be used to describe the dynamics also for other coverages. This will be discussed in Section 6.3.3. Section 6.2 and Section 6.3 are devoted to the first and second NN-PESs, respectively. In those sections, we present the methodology to construct the NN-PESs, analyze their accuracy and use them to perform MD simulations. The conclusions will be presented in Section 6.4.

6.1 Generalities

6.1.1 Overview of the procedures

The general idea to generate a NN-PES can be resumed in the three steps presented in Fig. 6.1. The first step is the selection of data within the whole data set that we have, defined as the Universe (Fig. 6.1 **1.**). Then, we split the Universe into a training set (used to train the NN) and a predict set (used to check the accuracy of the NN-PES). Within the training set, a part of the configurations is reserved

[1] *"It is by continuously making new attempts that we end up succeeding. In other words, more we fail more we increase the probability to succeed."* —Jacques ROUXEL, Les Shadoks

to the test set (usually between 10% and 5%). This test set is used during the training procedure to control the appearance of data overfitting. If the error of the training set decreases, but the error of the test set increases, there is overfitting and the training procedure must be stopped. Since the test set configurations are chosen randomly from those of the training set, when we discuss the process to select the configurations for the training set, one must consider the test set as a part of the training set.

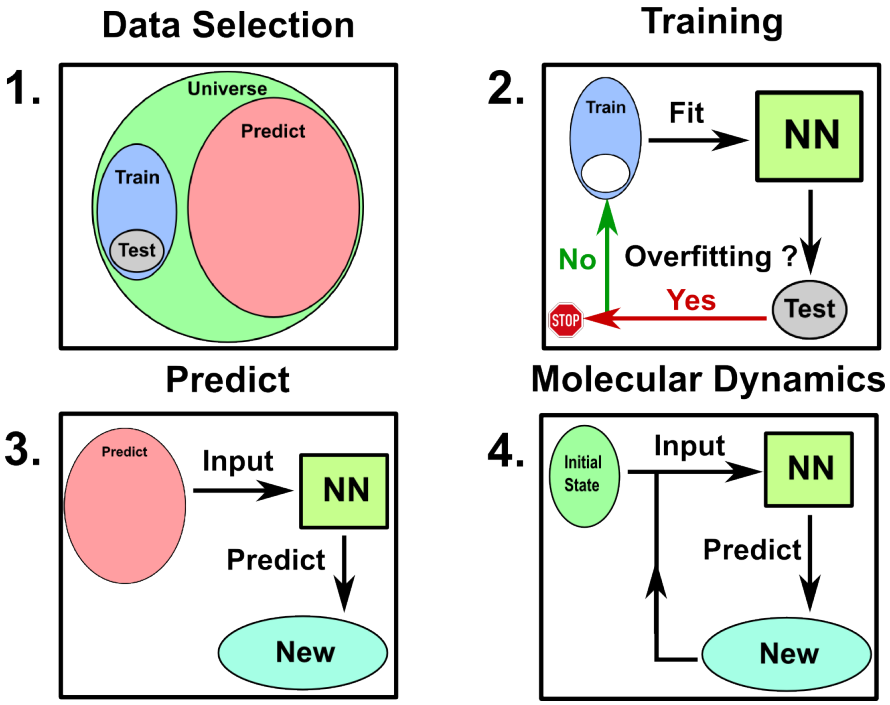

Figure 6.1: Scheme of the three steps to generate a NN-PES and its use in MD. Step 1, called "Data Selection" is the separation of the whole data set in different data subsets. Step 2, called "Training", is the fitting of the weight coefficients to minimize the error in data prediction according to the cost function. The training step stops when either convergence is reached or overfitting takes place. Step 3, called "Predict", is the evaluation of the predict data set with the NN-PES in order to quantify the errors on a non-trained data set. Step 4, called "Molecular Dynamics", consists in performing MD simulations using the trained NN-PES to calculate the adiabatic forces, in which the initial conditions are taken from the Universe.

The second step is the training procedure (Fig. 6.1 **2.**). The generation of the NN can be seen as a multidimensional fitting, in which the weight coefficients are adjusted to minimize the cost function S(**w**) defined as,

$$S(\mathbf{w}) = \sum_{i=1}^{N_{\text{data}}} [w_{\text{E}}(E_i^{\text{NN}} - E_i^{\text{DFT}})^2 + w_{\text{F}} \sum_{j=1}^{N} \sum_{\tau=1}^{3} (F_{\tau_j,i}^{\text{NN}} - F_{\tau_j,i}^{\text{DFT}})^2]/N_{\text{data}}\,, \tag{6.1}$$

where **w** is the collection of the NN weight parameters and N_{data} is the size of the training data set. $F_{\tau_j,i}^{\text{NN}}$ and $F_{\tau_j,i}^{\text{DFT}}$ are the forces of the j^{th} atom in the τ ($\tau = x, y, x$) direction for the i^{th} configuration calculated by NN and DFT, respectively. E_i^{NN} and E_i^{DFT} are the NN and DFT potential energies of the i^{th} configuration, respectively. w_{E} and w_{F} are the weight values to tune the importance of the energy and the forces in the cost function with $w_{\text{E}} = \eta_{\text{E}}$ and $w_{\text{F}} = \sqrt{\frac{\eta_{\text{F}}}{3N_{\text{freeatom}}}}$.

Next, the convergence is reached by repeating the optimization cycle, called epoch. At the end of each fitting cycle, the test set is evaluated in order to check that the NN-PES is not overfitted. If there

is overfitting, then the convergence cycle stops. Otherwise, the convergence cycle continues until the desired accuracy is reached.

The third step is the predict process (Fig. 6.1 **3.**). In this step the converged NN-PES is used to evaluate the energies of the predict data set, which is a data set of completely unknown data, in a sense that the NN-PES has not been trained on it. In this way we check the accuracy of the NN-PES on a larger and different configurational space. If the NN-PES were perfect, the error regarding to the value of DFT data would be zero.

Finally, the fourth step (Fig. 6.1 **4.**) consists in performing MD with the calculated NN-PES. In our case, the initial configuration for the dynamics is picked from a thermalization at 100 K of a random configuration from the Universe data set. Next, the NN-PES is used to calculate at each integration step the adiabatic forces acting on each moving atom in the simulation cell. The MD simulation stops when the desired number iterations is reached.

6.1.2 Data selection of the two methodologies used

As we said previously, we used two different methodologies to generate two different NN-PES. These methodologies affect the data selection and training steps.

The first methodology that we used to generate the NN-PES presented in section, 6.2 is to classify the whole data set of AIMDEF simulations, into different subsets depending on the types of events that have occurred at the end of the trajectory (*i.e.*, no CO desorption events, CO desorption, CO oxidation). The list of those events is presented in Section 6.2. Next, we select from each subset a number of configurations taking care of maintaining in the training set the same proportion that each event has in the Universe set. This process will be denoted binning henceforth. To do so, we choose the total number of configurations that we want to have in the training set. Next, using the calculated proportion respect to the Universe data set, we calculate how many configurations we need to extract from each subset of events. The NN-PES resulting from this methodology will be called "Direct-NN-PES".

The second methodology consists in selecting from the Universe an initial training set with a very small number of configurations and train the NN-PES with it. This small initial subset is selected with a binning process, such we take 800 configurations of each event subsets. Next, we evaluate the configurations of the Universe data set with the NN-PES and select the configurations for which the NN-PES prediction is worse. Finally, we incorporate these configurations into the training set and retrain the NN-PES. We perform this process recursively until we reach a selected maximum of configurations in the training set, or a selected maximum number of retraining cycles. The NN-PES resulting from this methodology will be called "Cycle-NN-PES".

In this chapter, several data sets are created. As they are created in different ways and contain different types of data, it is crucial to differentiate them and understand their content. Therefore, we give to each set a name formed by three words linked by hyphens according to the methodology used for data selection, the surface coverage from which the data were selected, and the function of the data set. For instance, Direct-Low-Train is the training data set obtained from the low coverage data using the direct methodology.

6.2 Direct-NN-PES based on low surface coverage data

6.2.1 Training of the Direct-NN-PES

The first methodology to construct the NN is to carefully select the data of the training set. We need it to be not too large but at the same time to represent adequately the whole configurational space. In order to decide whether the data set were large enough, we proceeded by a trial and error procedure and concluded that 50000 configurations are sufficient to reach an acceptable accuracy. In our case, we consider acceptable accuracy when the absolute errors in the potential energy per moving atom are of the order of the meV. Since the different surface coverages have different numbers of atoms in the system, the total energy in not directly comparable. Therefore, by dividing the energies by the number of moving atoms, we can compare the errors for different surface coverages. The evaluation of the errors will be performed by the evaluation of two different quantities, the root mean square error (RMSE) and the maximum absolute error (MAE). The RMSE is defined by the following expression:

$$\mathrm{RMSE} = \sqrt{\frac{1}{N_{\mathrm{struct}}} \sum_{i=1}^{N_{\mathrm{struct}}} (E_{i,\mathrm{ref}} - E_{i,\mathrm{NN}})^2}\,, \tag{6.2}$$

where N_{struct} is the total number of configurations, and $E_{i,\mathrm{NN}}$ and $E_{i,\mathrm{ref}}$ the energies of the configuration evaluated with the NN-PES and calculated using DFT (reference), respectively. The MAE is defined as:

$$\mathrm{MAE} = \sum_{i=1}^{N} \frac{|E_{\mathrm{nnpes}} - E_{\mathrm{dft}}|}{N}\,. \tag{6.3}$$

As said above, the training set is constructed by maintaining the proportion of the different events existing in the Universe data set. The idea behind this method is to try to represent adequately the configurational space explored by the dynamics. However, this method has several drawbacks. First, it does not exist a guarantee that this procedure really samples adequately the relevant configurational space. Second, the aim is to perform NN-PES based molecular dynamics simulation with much longer integration times than the ones used in the AIMDEF simulations from which we extract the training set data. As a result it may happen that the simulations reach configurations that are not well represented by the sampled configurational space. This can introduce important errors in the MD simulations.

Now we will explain the details of the training procedure. As said, we sampled data by separating the different trajectories in categories depending on the events that arise during each trajectory. Here, we will only focus on the (T_e,T_{ph})-AIMDEF calculations simulations, because they sample a wider configurational space than the T_e-AIMDEF simulations. The event groups that we consider are summarized in the following list:

Adsorbed Trajectories in which no desorption event is observed.

1CO Trajectories in which only one CO desorption is observed.

2CO Trajectories in which two CO desorptions are observed.

1CO_2 Trajectories in which one CO_2 desorption is observed.

In Figure 6.2 we represent the processes of categorization and selection of the data. On the left panel (Fig. 6.2 **1.**), we present the organization of the full Universe of data. The Universe is composed of all the AIMDEF calculations, those obtained from (T_e,T_{ph})-AIMDEF simulations (red) and those obtained from T_e-AIMDEF simulations (blue). Afterwards, we split the Direct-Low-(T_e,T_{ph}) data set into subsets according to the event taking place in the trajectory. Next, on the right panel (Fig. 6.2 **2.**) we show the representation of the different data sets that will be used to train, or to evaluate the Direct-NN-PES. The so called Cycle-Low-Predict-β set is formed by taking randomly 95% of the Universe. The construction of the training set (Direct-Low-Train) and of the so called Direct-Low-Predict-α set is more complicated and will be described in the following.

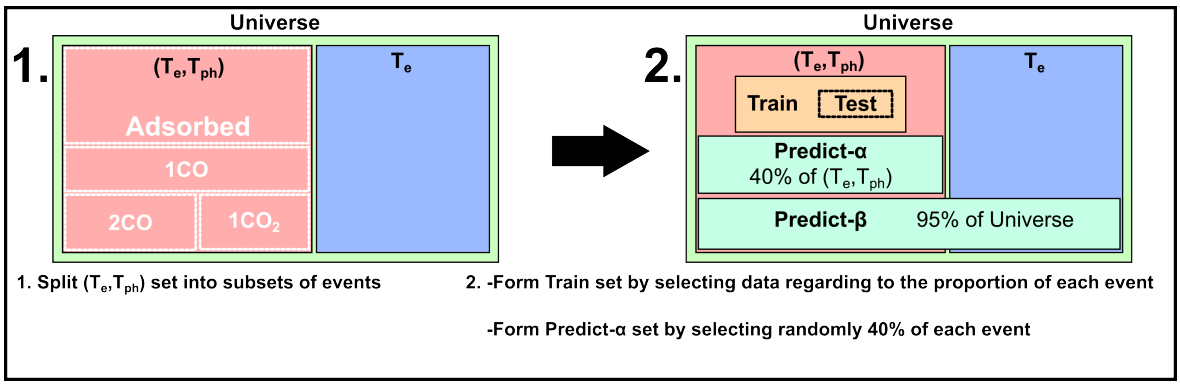

Figure 6.2: Representation of the data sets used for the training and predict procedures for Direct-NN-PES generation (see text).

First, we decide to set the number of configurations in the Direct-Low-Train set to 50000. As already stated, the hypothesis in which this data selection methodology is based is that a subset (Direct-Low-Train) of the Direct-Low-(T_e,T_{ph}) set that keeps the same proportions of the considered events as the complete Universe is enough to represent the whole configurational space. However, following this procedure the number of configurations in the training set coming from the $1CO_2$ and 2CO sets will be very small. For this reason, we have increased the number of configurations coming from the $1CO_2$ and 2CO in the training set, their number being 8 and 5 times larger, respectively, than the number that will correspond to them if the correct proportions were chosen. The remaining configurations are taken from the 1CO and Adsorbed sets, fulfilling the above discussed proportion rule. Note that the test set (Direct-Low-Test) is constituted by choosing randomly a 10% of the configurations in the Direct-Low-Train set. Finally, the Direct-Low-Predict-α set is constituted by selecting randomly 40% of the configurations in the Direct-Low-(T_e,T_{ph}) set, excluding the configurations that are already included in Direct-Low-Train set.

The number of configurations of each group in the training set (Direct-Low-Train), the Direct-Low-Predict-α set and the Direct-Low-(T_e,T_{ph}) sets are given in Table 6.1. We also give the proportion of the configurations in each group relative to the total number of configurations in the Direct-Low-(T_e,T_{ph}) set. The left panel of Fig. 6.3. shows the distribution of potential energies corresponding to all the configurations obtained in the (T_e,T_{ph})-AIMDEF simulations at low coverage. The distributions of potential energies for the different subsets of events are also shown. The right panel of Fig. 6.3 shows the potential energy distributions of the configurations in the Direct-Low-Train set and in its subsets

Event	Train ($\times 10^3$)	Predict-α($\times 10^3$)	(T_e,T_{ph})($\times 10^3$)
Adsorbed	22.424 (2.8%)	174.4 (21.9%)	436 (54.8%)
1CO	17.076 (2.1%)	132.8 (16.7%)	332 (41.7%)
2CO	6.5 (0.8%)	13.5 (1.7%)	20 (2.5%)
$1CO_2$	4 (0.5%)	4 (0.5%)	8 (1%)
sum	50 (6.3%)	324.7 (40.8%)	796 (100%)

Table 6.1: Number of configurations in the Direct-Low-Train, Direct-Low-Predict-α and Direct-Low-(T_e,T_{ph}) sets separated in the contributions extracted from the different groups of events. In parenthesis we give the percentage of configurations in each subset relative to the total number of configurations present in the Direct-Low-(T_e,T_{ph}) set.

corresponding to the different events. We show that it reasonably reproduces the distribution of the complete set of available configurations.

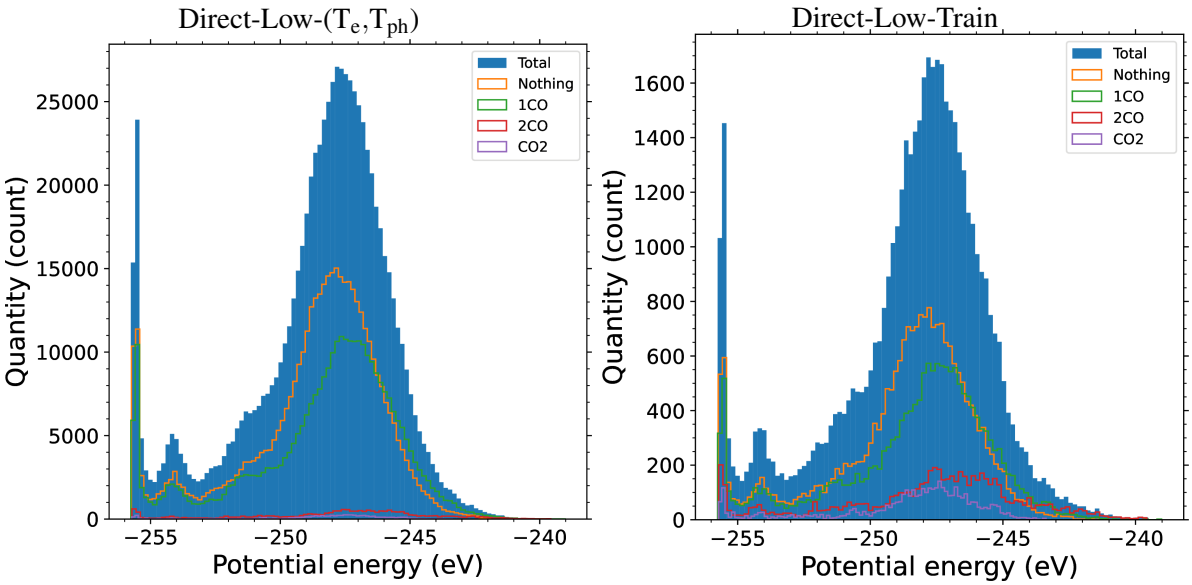

Figure 6.3: Distribution of the potential energy of the different events of low surface coverage AIMDEF calculation with electronic and phononic temperature. Left panel is the distribution of all the DFT configurations in the Direct-Low-(T_e,T_{ph}) set. Right panel is the distribution of the 50000 configurations selected for the Direct-Low-Train set.

As it was explained in the chapter devoted to the theoretical methods, the NN-PES has been constructed using the EANN method[10]. The structure of the NN chosen for each atomic species is 60-60-1 ttl. We use 15 GTOs and $l = 0, 1, 2, 3$ in eq.2.67 with $\alpha = 0.93 \text{Å}^{-2}$, r_s varying in the interval [0, r_c] in increments $\Delta r_s = 0.46$ Å and cut-off radius $r_c = 6.5$ Å. The energy and force weights in the loss functions are obtained using $\eta_E = 1$ and $\eta_F = 0.5$, that result in $w_E = 1$ eV^{-2} and $w_F = 0.102$ Å^2/eV^2.

After the training process the RMSEs per moving atom are 1.7 meV and 2.4 meV in the training and test sets, respectively. As shown in Fig. 6.4 this accuracy is obtained after 70 iterations and there is not overfitting.

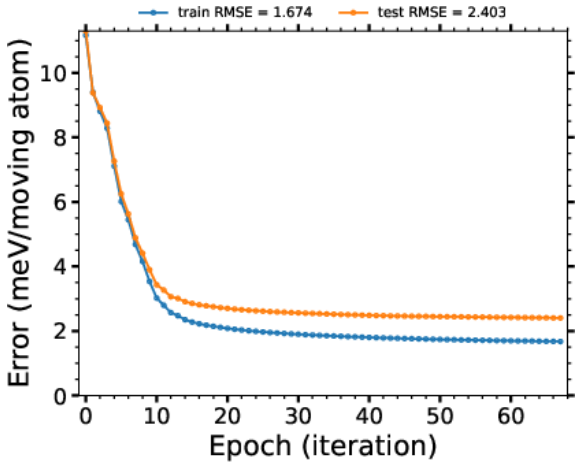

Figure 6.4: Convergence plot of the RMSE on the energy per moving atom of the training and test data sets during the training procedure of the Direct-NN-PES. The final RMSE-s of training and test sets are given at the top of the figure.

6.2.2 Accuracy check of the Direct-NN-PES

To confirm the accuracy of the NN-PES before performing MD, we evaluate using the NN-PES energies of configurations that have not been used in training process. This data set is much larger than the training set to ensure that we are sampling well a wider configurational space. The composition of this data set is described in table 6.1. This set is named Direct-Low-Predict-α and is more than six times larger than the training set.

The results of this analysis are shown in the left panel of Fig. 6.5. The figure shows the values of the potential energy obtained with the Direct-NN-PES for the configurations in the predict set versus the corresponding energy values obtained using DFT. If both results matched perfectly, the graphic would be a straight line $y = x$. To show the distribution of configurations that are not on the line, we display a density plot. In the following sections, we will present the same type of graphics but for different surface coverages. We remind that in order to compare the values of those graphics, the errors are given in energy per moving atoms. This allows to compare the accuracy achieved for the different surface coverages for which the number of atoms in the simulation cell is different. In the left panel of Fig. 6.5, we observe that the RMSE amounts to 2.6 meV per moving atom which is already an acceptable value. Although, the maximum error is ten times larger than the RMSE, there are very few configurations for which the error is close to this value. Indeed, the density plot shows that most of the configurations are close to the y=x line.

Subsequently, we have checked the accuracy of this NN-PES evaluating its predictions for 95% of the configurations available for the low surface coverage, which amounts to 756200 configurations. This data set (called Cycle-Low-Predict-β) contains data from T_e-AIMDEF and (T_e,T_{ph})-AIMDEF simulations. The results of this analysis are shown in the right panel of Fig. 6.5. First, we remark that there are several configurations for which the maximum error is large. Second, we observe that the RMSE is 13 times larger than the one corresponding to the Direct-Low-Predict-α set. More precisely, the RMSE is 35.1 meV, which is too large to perform accurate MD simulations. This means that there

is a part of the configurational space, which is accessible by AIMD, that the Direct-NN-PES is not describing well.

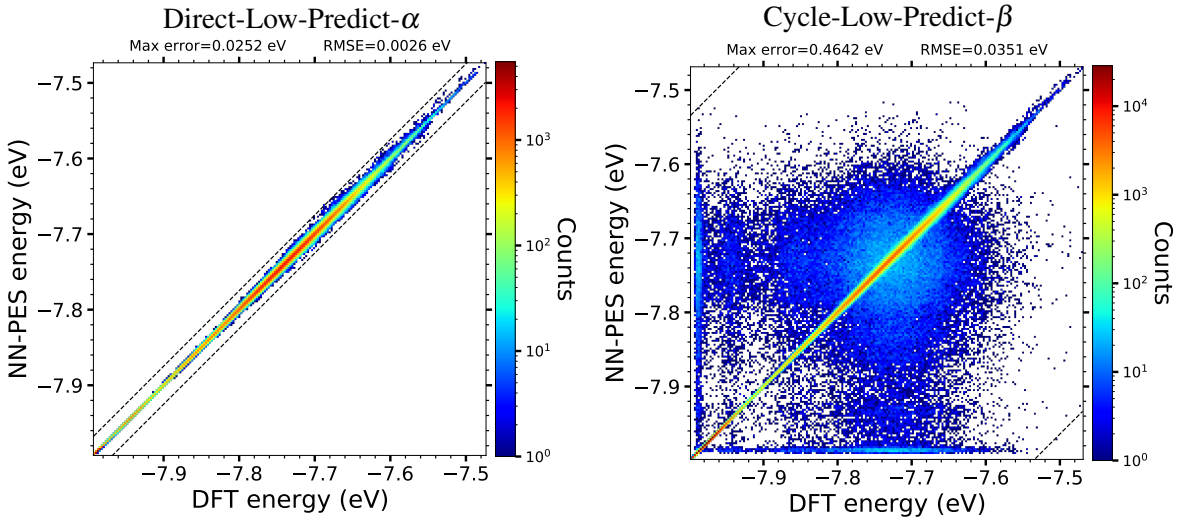

Figure 6.5: Density plot of the energy values obtained by the NN-PES vs the DFTenergy data. Left (right) panel corresponds to the evaluation of the energies of the configurations on the Direct-Low-Predict-α (Cycle-Low-Predict-β) data set.

In Fig. 6.6 we present a deeper analysis of the distribution of errors. Here we describe the general scheme to create this figure. First, we compute the absolute error of the NN-PES prediction for each DFT energy. Then, we divide the range of DFT energy in bins of 0.5 meV width to draw an histogram. For each bin we calculate the MAE and represent it as a point in the top panel. In the bottom panel, we represent the amount of configurations in each bin. This allows to show the weight of each bin in the total histogram. Since the data originate from *ab-initio* calculations, the weight of each bin can also be seen as the probability to reach this region of the configurational space. Therefore, the larger the number of configurations in a bin, the more important it is that this bin is accurately fitted. We show results corresponding to the Direct-Low-Predict-α set (red points and lines) and to the Cycle-Low-Predict-β set (green points and lines). Black points and curves correspond to the results obtained for the training set data. These results will serve as a reference in the forthcoming analysis.

First, the top panel shows that the errors in the evaluation of the Direct-Low-Predict-α data are very low and very similar to those obtained in the evaluation of the Direct-Low-Train data set. An exception to this are the errors obtained for energies higher than -7.7 eV. Notwithstanding, the MAEs in this energy region is still lower than 10 meV per moving atom, which is quite satisfactory. The bottom panel show that the energy distribution of the data is very similar for in these two data sets. In this respect, it must be remembered that in the training data set there are ten times less configurations than the Direct-Low-Predict-α.

Second, we observe that in general the MAE for the Direct-Low-Predict-α data is lower than the MAE of the Cycle-Low-Predict-β data. In fact, in most of the cases, the MAE of the data in the Cycle-Low-Predict-β set is one or two orders of magnitude larger than the MAE of the data of the Direct-Low-Predict-α and training sets. There are two exceptions to these general rule. On the one hand, in the very high energy region there exist some bins for which the MAE of the data of the

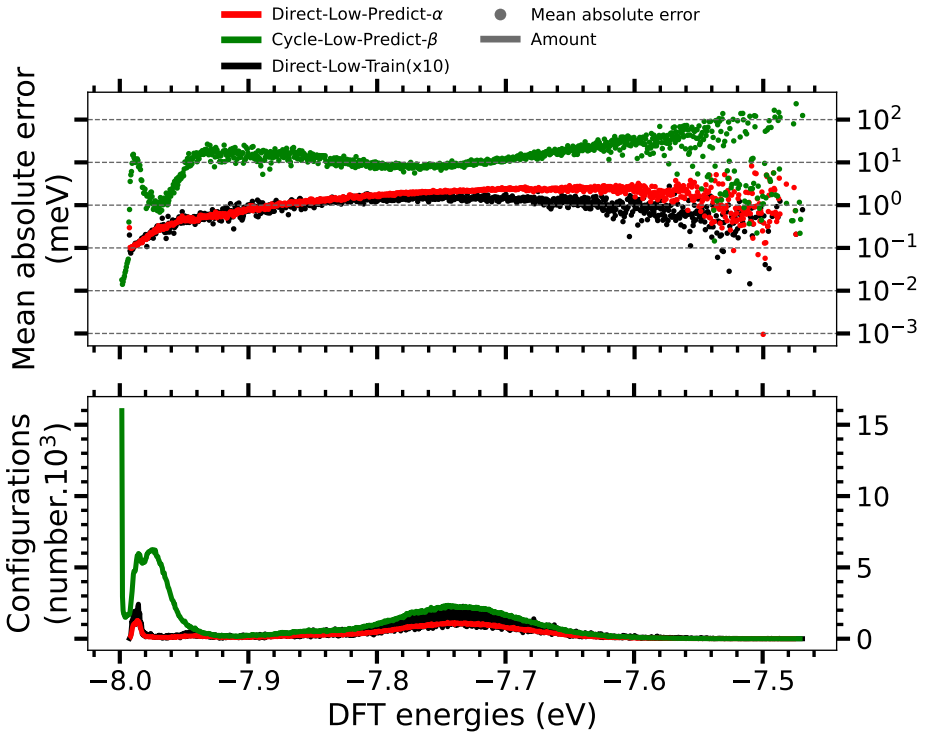

Figure 6.6: Top panel: MAE distributions of the NN-PES energies as a function of the corresponding DFT energies. Bottom panel: Distributions of the numbers of configurations as a function of the energy. The bin used is 0.5 meV for both distributions. Results are shown for the Direct-Low-Predict-α data set (red), Cycle-Low-Predict-β data set (green) and the Direct-Low-Train data set (black). In the bottom panel the number of configurations of the Direct-Low-Train data set is multiplied by ten to fit the scale.

Cycle-Low-Predict-β set is lower. Nevertheless, note that the number of configurations in this energy region is very small (see bottom panel). On the other hand, in the low energy region, close to the -8.0 eV energy value, there also exist some bins of energy for which the MAE of the Cycle-Low-Predict-β data is also lower. In this case, the errors for the Cycle-Low-Predict-β data are surprisingly low, considering that these configurations are not present in the Direct-Low-Train set. This means that the Direct-NN-PES extrapolates very well this region of energy.

Third, comparing the energy distributions of the configurations of the two predict data sets, we observe that the Direct-Low-Predict-α set represents adequately the region of energy between -7.8 eV and -7.66 eV. However, the region between -8.0 eV and -7.94 eV is not well represented in this data set. Finally, note that energy regions for which the errors are larger are mostly the ones for which the number of configuration is smaller. We can conclude that although the errors in these energy regions are high, their relative importance is probably not that large because it is less probable that the system visits this part of the configurational space. In other words, event though the MAE is high, it does not mean that the NN-PES is not accurate in the majority of the accessible configurational space.

As a way to improve the Direct-NN-PES, we could add the configurations for which the energy prediction is worse to the training set. Also, we can investigate these configurations to see if they have a common factor that could trigger the bad prediction of the NN-PES, *e.g.* desorbed molecule far from the surface.

Anyhow, we computed MD simulations with this NN-PES. In the next section, we analyze the results of these dynamics simulations and check whether the bad prediction for the energies of the Cycle-Low-Predict-β data set constitutes a red flag, and whether it is necessary to build a better NN-PES in order to perform accurate MD simulations.

6.2.3 Molecular dynamics simulations based on the Direct-NN-PES

Using the Direct-NN-PES we have performed molecular dynamics simulations for the low surface coverage (see Fig. 3.10 in Chapter 3) system under femtosecond laser irradiation. The characteristics of the laser pulse and the time dependence of the electronic and phononic temperatures are the same as in the (T_e,T_{ph})-AIMDEF simulations presented in Chapter 4 and 5. We have calculated 200 trajectories with a time step of 0.2 fs. The total integration time for each trajectory is 4 ps. The initial configurations are the same as the ones used in the AIMDEF simulations in the previous chapters, which are obtained from an initial thermalization of the system at 100 K. The friction forces are introduced in the NNP-MD as described in Section 2.4.3. More technical details concerning the NN-PES based molecular dynamics (NNP-MD) are discussed in appendix H. Additionally, in appendix I we present how the analytical function used to calculate the electronic density of the Ru slab is constructed. This function is necessary to compute the non-adiabatic forces during the NNP-MD simulations.

	AIMDEF	NNP-MD
P_{des} CO	18.25%	19.50%
P_{des} CO_2	0.50%	0.50%
br	36.5	39

Table 6.2: CO desorption and oxidation probabilities in AIMDEF and Direct-NN-PES MD simulations. The branching ratio between desorption and oxidation (br) is defined in eq.(5.2).

In Table 6.2 we present the CO desorption and oxidation probabilities during the dynamics (as definied in eq.(5.1)), and compare it with the same observable obtained using AIMDEF. For both kind of simulations, the CO and CO_2 molecules are considered as desorbed when they reach a distance of 6.5 Å from the surface. We observe few more desorptions of CO in the case of NNP-MD (5 more desorption events) than in the case of AIMDEF, while the amount of oxidation is the same (2 oxidation events). Therefore the branching ratio (defined in eq.(5.2)) is slightly modified in the case of NNP-MD and increases to 39.

To conclude this section, in Figure 6.7 we show the time evolution of the CO desorption (in red) and CO_2 desorption (in blue) probabilities as a function of time. We also show the time evolution of the branching ratio in green. Note that the branching ratio cannot be defined when there is no oxidation.

We see that there is no desorption of CO before 1.8 ps and that the first CO_2 desorption occurs at 2.6 ps, when around 3% of the CO molecules have already been desorbed. Those results are very similar to those obtained in the AIMDEF simulations. Moreover, after the analysis of the trajectories in which CO_2 formation takes place, we find that the recombination follows the minimum energy path for oxidation obtained by the CI-NEB calculations shown in Section 3.3.2.These results suggest that the above discussed errors of the NN-PES at some range of energies are not serious enough to prevent the use of this PES to perform reasonable MD simulations, at least for the conditions in which

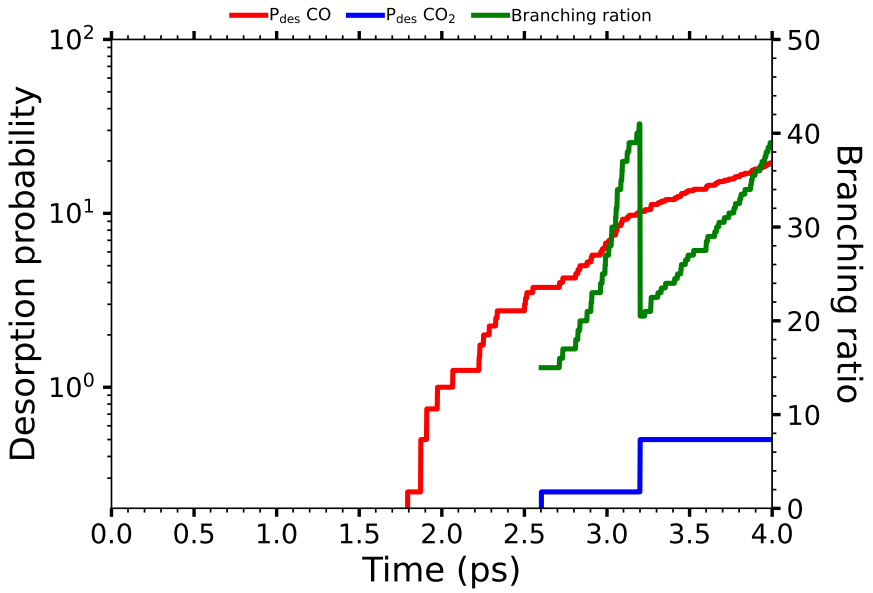

Figure 6.7: Variation of the CO and CO_2 desorption probability during the NNP-MD simulations as a function of time. In green (right axis) we show the time evolution of the branching ratio.

the AIMDEF data were obtained. Still, a further comparative analysis of the time evolution of the kinetic energies of the adsorbates and of the movement of the atoms would be desirable to reach a more definite conclusion on this matter.

6.3 Cycle-NN-PES based on the intermediate surface coverage data

6.3.1 Training of the Cycle-NN-PES

We propose a different approach to select the data and to train the NN-PES in order to automatize the selection of configurations. The NN-PES presented in this section has been generated using the intermediate surface coverage data. In Figure 6.8 we show a representation of those data, and the construction of the different data sets. We first construct an initial training set. To do so first we separate the complete Universe data set into two subsets: the subset that includes all the configurations obtained in the T_e-AIMDEF simulations and the subset that includes all the configurations obtained in the (T_e,T_{ph})-AIMDEF simulations. Subsequently, as shown in Fig. 6.8 **1.**, we separate these two subsets into another 4 subsets according to the event taking place on the simulation (no desorption, one CO desorption, two CO desorptions, $1CO_2$ desorption). Finally, from each of the resulting 8 subsests we take randomly 800 configurations to form the initial training set that comprises a total of 6400 configurations. As will be explained below, the training data set will be increased in different cycles in order to improve the quality of the PES. In all cycles, 90% of the configurations of the training set will be actually used to train the PES and the remaining 10%, chosen randomly, will be used for test purposes (test data set).

In Figure 6.8 **2.** the different data sets are schematically represented. Note that the area of the rectangles is not proportional to the amount of data in each data set. The Predict-β set that will be

used to test the accuracy of the PES has been constructed by selecting randomly 95% of the data of the Universe. In order to train the NN-PES and increase its accuracy, we will use an "active learning" scheme. To do so, after training the PES with the selected data set and checking its accuracy with the Predict-β data set, we increase the training set with the configurations in the Predict-β set for which the errors in the forces are larger. Therefore, we recursively perform the following actions:

1. Train the NN with the Train data set.
2. Evaluate the Predict-β data set with the converged NN-PES.
3. Select the 100 configurations with the worse force predictions of each atom.
4. Add them in the Train data set.
5. Go to first step except if a limiting condition is reached.

The limiting conditions are the following: we stop the iterations if 15 iterations have been performed or if the number of configurations in the training set is larger than 50000. This scheme leads us to form a training data set much bigger than the initial one, and also to converge the accuracy of the prediction of the NN-PES to a better value. Finally, note that the training set contains configurations from the Predict-β set. However, the configurations that are common to the training set and the Predict-β set are so few compared to the total number of configurations in the Predict-β set that this does not affect the results.

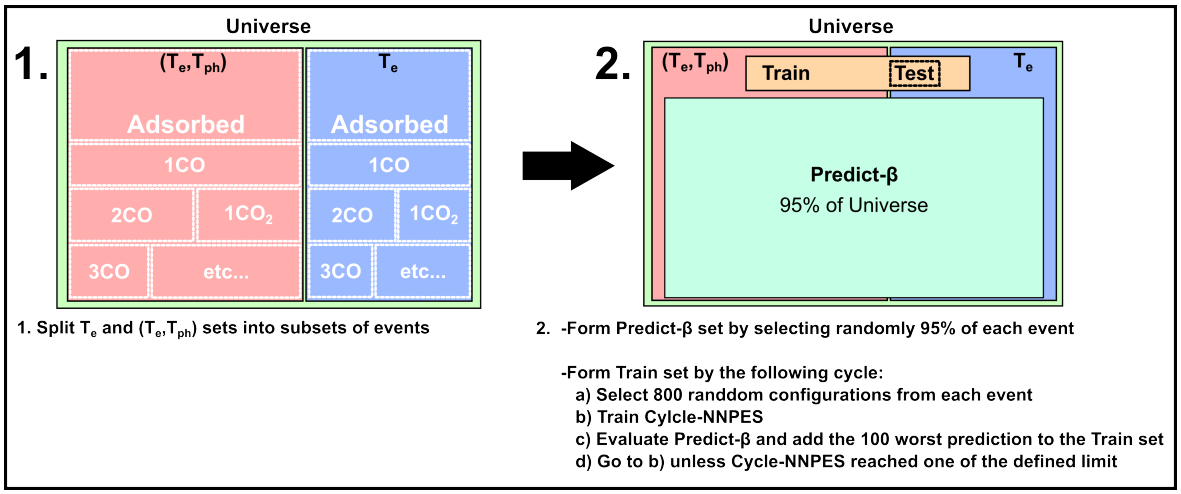

Figure 6.8: Representation of the data set used for the predict and train procedures during the second NN-PES generation procedure.

Additionally, we have also tested how the weights attributed to the the energy and the forces in the cost function, defined as is eq.(6.1), affect the accuracy of the NN-PES. The sets of pairs of parameters analyzed are the following:$\{\eta_E = [0.5;1], \eta_F = [0.5;1]\}$ and $\{\eta_E = 1, \eta_F = [2;4;8;16;24;32]\}$. We have found that the most accurate PES is obtained with the pair of parameters $\{\eta_E = 1, \eta_F = 0.5\}$, although similar accuracy is obtained with the pairs of parameters $\{\eta_E = 1, \eta_F = 1\}$ and $\{\eta_E = 1, \eta_F = 2\}$. Therefore, the NN-PES discussed from here on has been trained using the pair of parameters

$\{\eta_E = 1,\ \eta_F = 0.5\}$, that result in $w_E = 1$ eV^{-1} and $w_F = 0.070$ Å^2/eV^2. The architecture of the PES and the parameters describing the descriptors are the same as those used in the Direct-NN-PES presented in the previous section.

In the left panel of Fig. 6.9 we show the evolution of the RMSE during the training process described above. We see on the retraining process that, each time we introduce new configurations in the training data set, the RMSE of the training set increases. However, at the end of each new loop we reduce RMSE of the test set, which is a manifestation of the improvement of the accuracy of the PES. At the end of the training process the RMSE of the training set is of 1.3 meV per moving atom, and the RMSE of the test set is 2.1 meV per moving atom. These result are very acceptable, and already better than the ones obtained for the Direct-NN-PES.

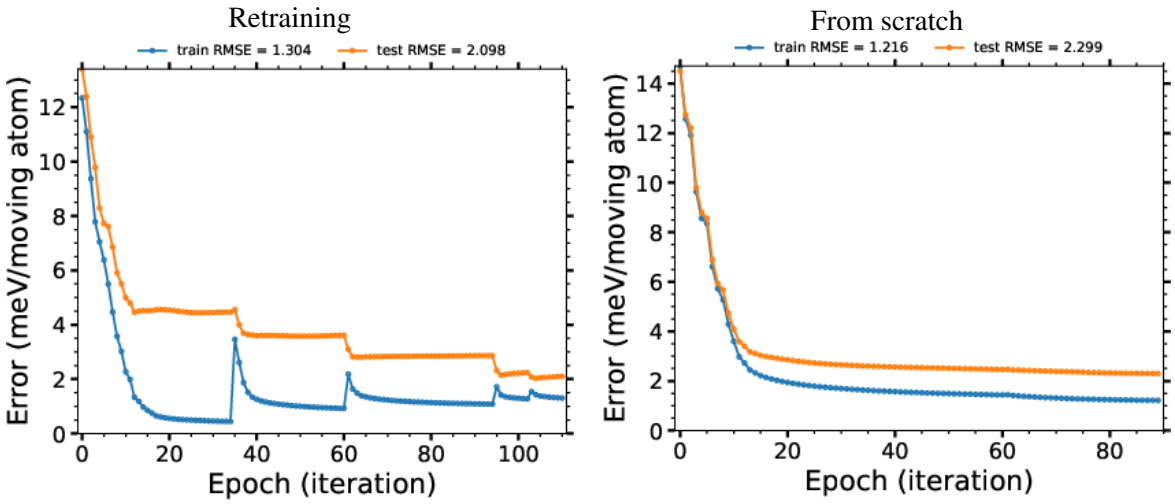

Figure 6.9: Convergence plots of the RMSE of the training and test data sets during the training procedure of the Cycle-NN-PES. The final RMSE values at the end of the training process are show at the top of the figure. The left panel corresponds to the retraining scheme. The right panel corresponds to a training produced from scratch (without retraining cycles) but using the Cycle-Intermediate-Train data set as the training set.

After this training process one question arises. When we train the NN-PES for certain configurations, we tune the weight coefficients. Therefore, when we retrain after adding new configurations, we restart the training with the old weight coefficients. However, we are not sure that these old coefficients are the best to reach the convergence. Maybe if we re-initialize the weight coefficients randomly, as training from scratch, we would reach a better convergence. Therefore, to check this hypothesis we retrained the NN-PES from scratch using the final training set obtained at the end of the "active learning" process as the training set. In the following this data set will be called Cycle-Intermediate-Train set. Right panel of Fig. 6.9 shows the evolution of the RMSE for the training and data sets during the training process when this procedure is followed. We find that even if the RMSE of the training set improves compared to the previous case, this is not the case for the RMSE of the test set.

However, as we mentioned before, the best test to see which training procedure is the best, is to test the NN-PES predictions for a large number of different configurations. Thus we have evaluated the two mentioned NN-PES on the Cycle-Intermediate-Predict-β data set that comprises 1100000 configurations and present the results in Fig. 6.10. On the left panel we show the results obtained

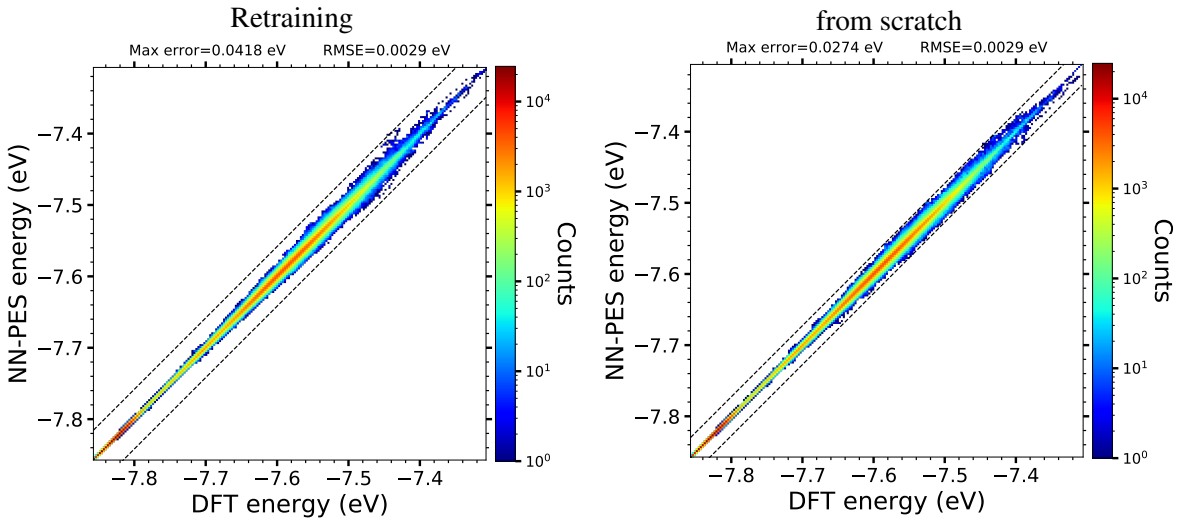

Figure 6.10: Density plot of the energy values obtained by the NN-PES vs the DFT energy data. Left panel corresponds to the NN-PES obtained after the retraining process. Rifgt panel correponds to the PES obtained by training from scratch and using as a training set the Cycle-Intemerdiate-Tain set. In both cases configurations from the Cycle-Intermdiate-Predict-β data set are evaluated.

with the NN-PES obtained at the end of the retraining process, and on the right hand side the results obtained with the the NN-PES trained from scratch with Cycle-Intermediate-Train set. We can see that the RMSE is exactly the same for both NN-PES, but that the maximum error of NN-PES trained from scratch is 40% lower than the other. Thus, we conclude that this NN-PES is the most accurate. For this reason, from now on we will consider exclusively this last PES and it will be also the only PES for which we will perform MD simulations. We will name this PES as Cycle-NN-PES. Also, note that the error is comparable to the one achieved in the case of the low surface coverage NN-PES for the Direct-Low-Predict-α data set.

6.3.2 Accuracy check of the Cycle-NN-PES

To get a better insight on the accuracy of the Cycle-NN-PES we have analyzed separately how it performs on the configurations extracted from the T_e-AIMDEF simulations and the (T_e,T_{ph})-AIMDEF simulations. These results are shown in Fig. 6.11. In the left panel we show the results for the configurations obtained from the T_e-AIMDEF simulations. We observe that the accuracy is very high with a RMSE lower than 1 meV and a max error of only $\sim$5 meV. In the right panel, we show the results for the configurations obtained from the (T_e,T_{ph})-AIMDEF simulations. In this case the errors are larger, but still the accuracy is rather good with a RMSE of 3.5 meV and a max error of 27 meV. The errors are very similar to the errors obtained with the Direct-NN-PES (Section 6.2.2).

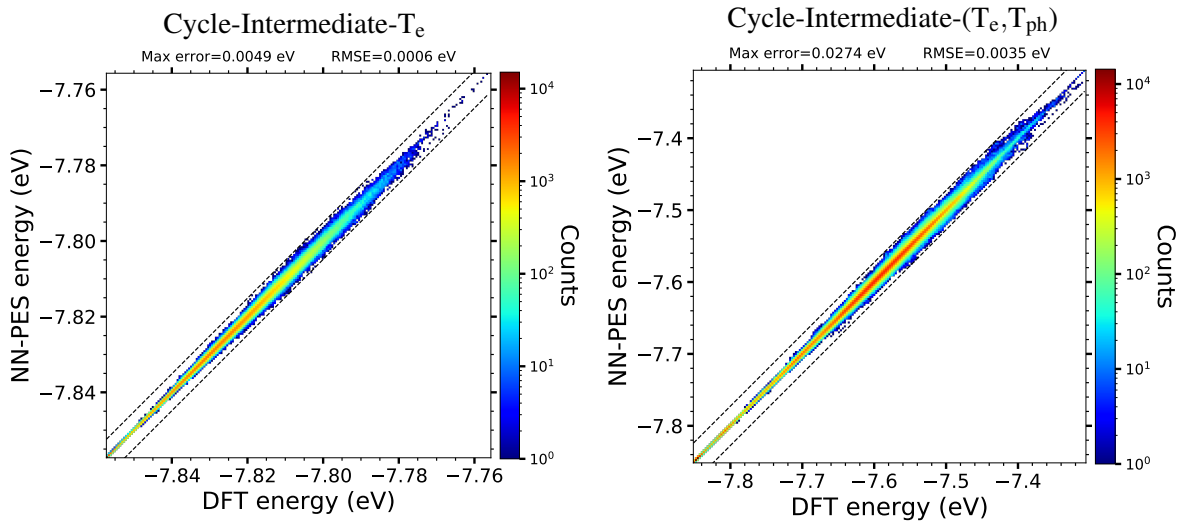

Figure 6.11: Density plot of the energy values obtained by the Cycle-NN-PES vs the DFT energy data. Left panel corresponds to the evaluation of the energies of the configurations obtained from the T_e-AIMDEF simulations. Right panel corresponds to the evaluation of the energies of the configurations obtained from the (T_e,T_{ph})-AIMDEF simulations.

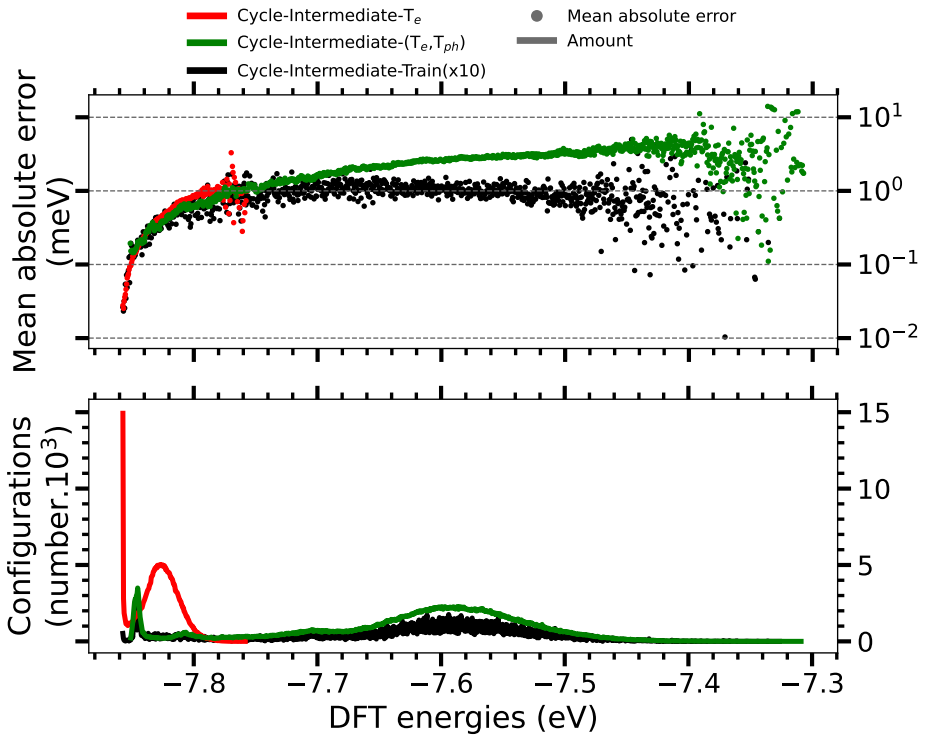

Figure 6.12: In top panel is represented with scatter points, in logarithmic scale, the histograms of MAE of the NN-PES energy prediction compared to the DFT energies. In bottom panel is represented with solid lines, the histogram of the amount of configuration in each bin of 0.5 meV energy. In red is represented Cycle-Intermediate-T_e data set, in green Cycle-Intermediate-(T_e,T_{ph}) data set, and in black Cycle-Intermediate-Train data set. The amount of point of the latter is multiplied by 10 to fit in the scale of the bottom pane.

In Fig. 6.12 we present a deeper analysis of the error distribution. To this aim, we show results obtained by evaluating the Cycle-NN-PES on the the Cycle-Intermediate-Train, the Cycle-Intermediate-

T_e and Cycle-Intermediate-(T_e,T_{ph}) data sets. The first observation is that the Cycle-NN-PES is very accurate in the evaluation of the data that are in the [-7.86; -7.70] eV energy region, with MAEs of 1 meV or lower. We also observe that the data from the Cycle-Intermediate-T_e set (red curve) are concentrated in the small energy range of [-7.86; -7.78] eV. This shows that this data set samples a relatively reduced configurational space. A closer analysis shows that in the range of energies [-7.86; -7.78] eV the MAE is slightly higher for the data of the Cycle-Intermediate-T_e set than for the data of the Cycle-Intermediate-(T_e,T_{ph}). In all cases, the larger errors occur for the higher energy configurations. This suggest that to give a larger weight in the cost function to these configurations might be a way to improve the NN-PES.

6.3.3 Analysis of the accuracy of the Cycle-NN-PES for different surface coverages

Since we trained the Cycle-NN-PES with configurations extracted from the intermediate surface coverage, it does not have any information from the other surface coverages. However, we expect that the NN-PES should be able to describe also other surface coverages because the EANN method is based in an atomstic NN framework in which the total energy of the system is evaluated as a sum of atomic contributions that depend on the specific atomic environments. Therefore, if the atomic environments that constitute the configurations at the intermediate coverage are not that different to those encountered at the other coverages, our Cycle-NN-PES should be also accurate for the low and intermediate coverages. In the following, we will analyze whether this is the case.

Cycle-NN-PES based evaluation of the minimum energy path for CO oxidation

First, we will analyze the accuracy of the Cycle-NN-PES regarding the MEP for CO oxidation at the different coverages. The MEP and its more important configurations are presented in Chapter 3. More precisely, in Fig. 3.21 we present the MEP for CO oxidation at the four studied surface coverages: minimum, low, intermediate and high. In order to see how accurately the Cycle-NN-PES describes the MEP at the different surface coverages, we evaluate the energy of the image configurations of the CI-NEB calculations and present the results in Fig. 6.13.

First, we focus on the intermediate surface coverage, from which the training set of this PES was constructed. These results are shown in the bottom-left panel of Fig. 3.21. We observe that the predictions of the PES are very good for the configurations in which the reactants are close to the surface, where the CO_2 is formed (IS, TS1, bCO_2, TS2) and that the absolute errors increase in the physisorbed and desorbed CO_2 region.

In the top-right panel of Fig. 3.21 for low surface coverage, we observe that The Cycle-NN-PES is surprisingly accurate in the evaluation of the energy of the FS, with an error of 2.7 meV, almost two orders of magnitude lower than the error in the energy of the FS at the intermediate surface coverage. However, it does not describe correctly the profile of the energy variations in the MEP, and in particular the energy barriers to escape the bCO_2 state. Also, the description of the physisorption region is rather inaccurate with errors as large as 403 meV.

For the high surface coverage (bottom-right panel of Fig. 3.21) the results are very similar to the intermediate coverage case. In fact, although the predicted energy of the bCO_2 is a little bit too high,

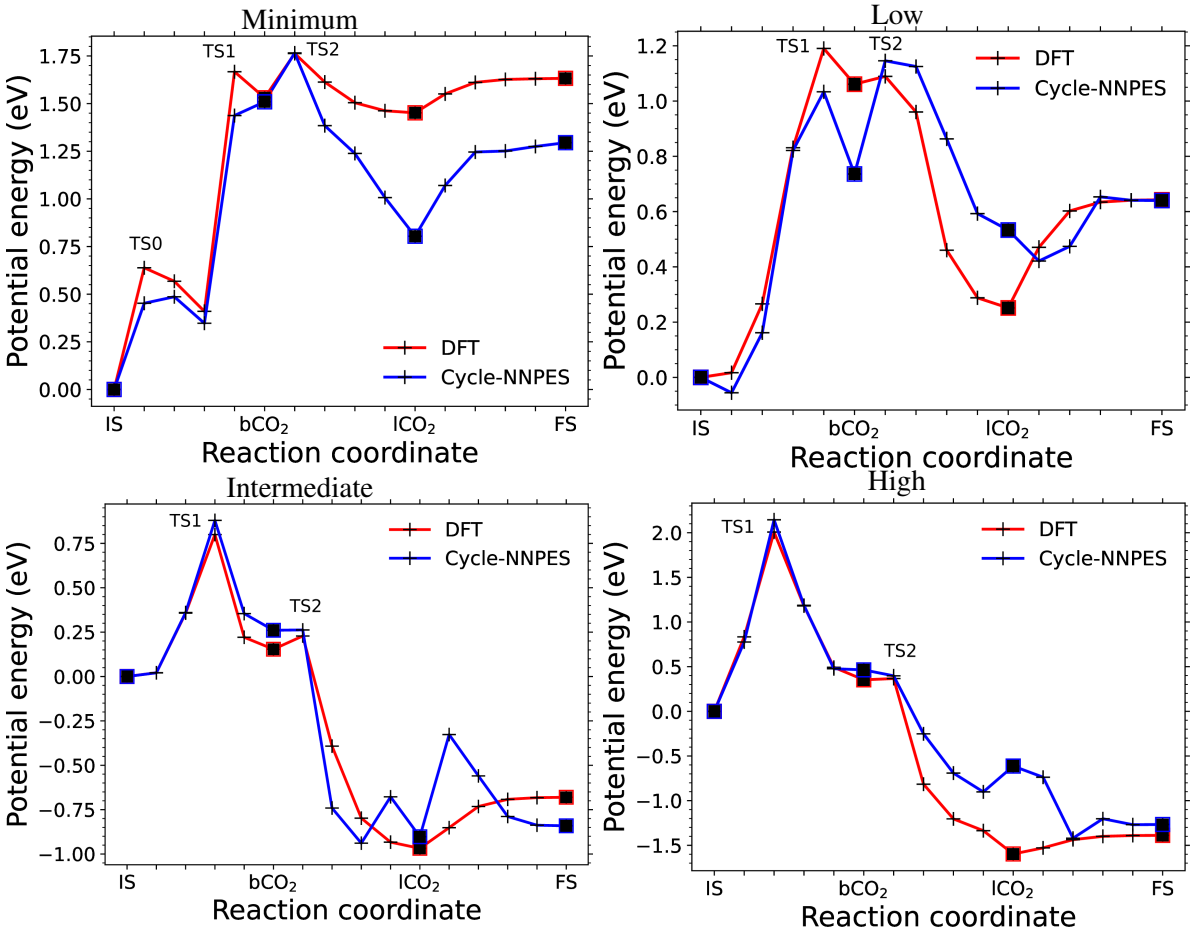

Figure 6.13: Potential energy of the configurations in the MEP for CO oxidation. DFT energies are joined by red lines, and Cycle-NN-PES energies by blue lines. Top-left panel corresponds to the minimum coverage, top-right panel to the minimum coverage, bottom-left panel to the intermediate coverage and bottom-right panel to the maximum coverage.

the results are quite accurate for configurations between IS and TS2. This is interesting considering that the PES was not trained with configurations of this coverage. Again, as in the intermediate coverage case, the results worsen at the physisorption region and for gas CO_2.

Finally, in the top-left panel of Fig. 3.21 we analyze the results for the so-called minimum surface coverage in which we have one CO molecule and one O atom in the simulation cell. In this case, although some characteristics of the MEP are captured by the NN-PES predictions, there are some features that are completely lost. For instance, the NN-PES does not predict the TS1 configuration to be a transition state. Moreover, the errors at the physisorption region and for CO_2 gas are very large. All in all, this is the coverage for which the NN-PES predictions are worse though, maybe accidentally, the errors for the bCO_2 and TS2 states are extremely low.

In conclusion, the Cycle-NN-PES, although trained for the intermediate coverage, reproduces rather accurately the energy values in the MEP for oxidation for the low and high surface coverages. This is mostly true for configurations in which the reactants are close to the surface and where the CO_2 is formed. The errors are larger in the physisorption region and for gas-phase CO_2. Note that this also

happens for the intermediate surface coverage. This suggests that configurations for desorbed species should be added to the training set in order improve the accuracy of the Cycle-NN-PES.

Accuracy of the Cycle-NN-PES for the low and high coverages

Now, as we did for the intermediate coverage case, we check the accuracy of the Cycle-NN-PES taking all the Universe data for the low and high coverages. We start our analysis with the low coverage. We analyze separately the accuracy of the PES for the configurations obtained from the T_e-AIMDEF simulations (Cycle-Low-T_e data set) and the ones obtained (T_e,T_{ph})-AIMDEF simulations (Cycle-Low-(T_e,T_{ph}) data set). In Fig. 6.14 we plot the energies calculated with the Cycle-NN-PES versus the DFT energies obtained both in the T_e-AIMDEF simulations (left panel) and the (T_e,T_{ph})-AIMDEF simulations (right panel).

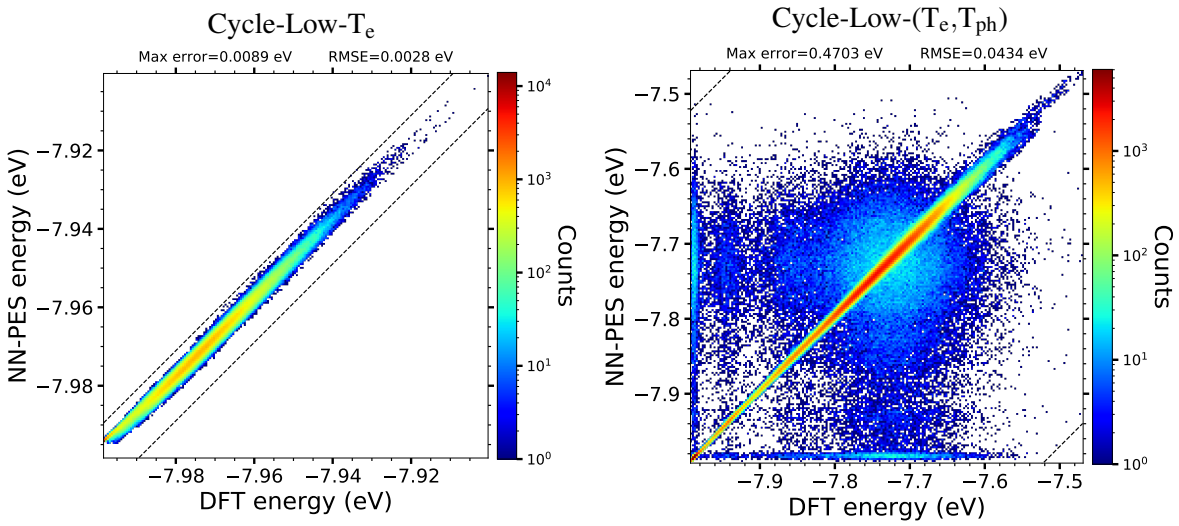

Figure 6.14: Density plot of the energy values obtained by the Cycle-NN-PES vs the DFT energy data. Left panel corresponds to the evaluation of the energies of the configurations obtained from the low coverage T_e-AIMDEF simulations. Right panel corresponds to the evaluation of the energies of the configurations obtained from the low coverage (T_e,T_{ph})-AIMDEF simulations.

The first observation is that the PES is reasonably accurate reproducing the T_e-AIMDEF results with a RMSE below 3 meV and a maximum error of around 9 meV. However, in the case of the (T_e,T_{ph})-AIMDEF results the agreement is not that good and both the RMSE and maximum error are too large. Nevertheless, it is worth to mention that similar error were obtained for this data set when using the Direct-NN-PES that was trained with the low coverage data. This means that the errors that we find with the Cycle-NN-PES are not necessarily due to the fact that this PES was trained with data for a different coverage.

In Figure 6.15 we check the accuracy of the Cycle-NN-PES on different data sets provided by AIMDEF calculations on the high surface coverage. In this case we have available data from two types of T_e-AIMDEF simulations, one with a 200 J/m^2 laser fluence and the other with a 300 J/m^2 laser fluence. We therefore evaluate them separately. The corresponding data sets are names Cycle-High-T_e-200 J/m^2 and Cycle-High-T_e-300 J/m^2, respectively. We observe that the RMSE for the data obtained from both T_e-AIMDEF simulations and also for the data obtained from (T_e,T_{ph})-AIMDEF simulations

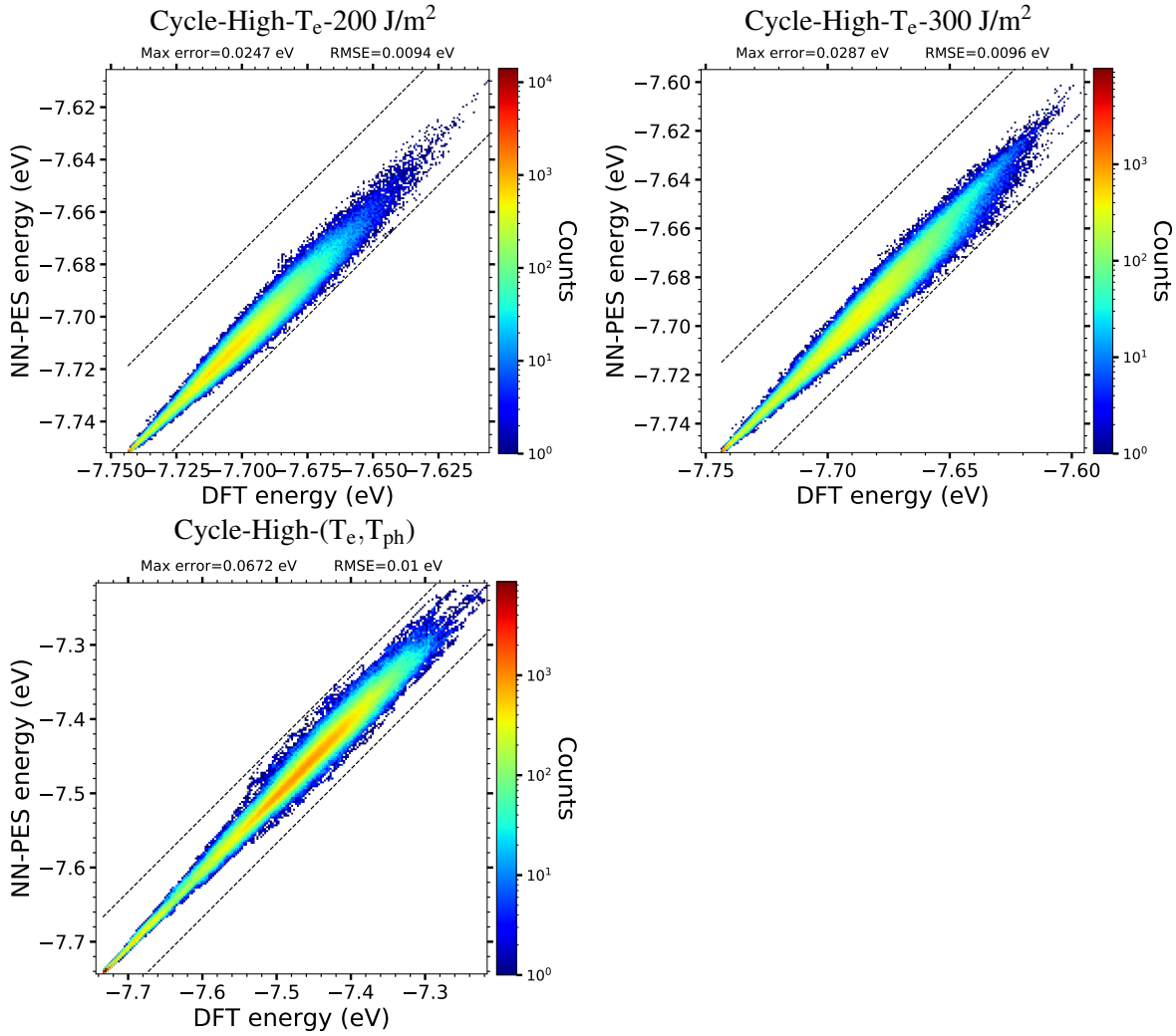

Figure 6.15: Density plot of the energy values obtained by the Cycle-NN-PES vs the DFT energy data. Top-Left panel corresponds to the evaluation of the energies of the configurations obtained from the high coverage T_e-AIMDEF simulations with a 200 J/m^2 laser fluence. Top-Right panel corresponds to the evaluation of the energies of the configurations obtained from the high coverage T_e-AIMDEF simulations with a 300 J/m^2 laser fluence. Bottom panel corresponds to the evaluation of the energies of the configurations obtained from high coverage the (T_e,T_{ph})-AIMDEF simulations with a 200 J/m^2 laser fluence.

are of the order of 10 meV. Regarding the maximum error, for the T_e-AIMDEF results it is of the order of that obtained for the intermediate coverage (T_e,T_{ph})-AIMDEF data. The maximum error for the high coverage (T_e,T_{ph})-AIMDEF data is around 3 times larger. All in all, we consider that the results are quite reasonable considering that the PES was not trained for the high coverage.

A more detailed analysis of the performance of the Cycle-NN-PES for different coverages is presented in Appendix K.

6.3.4 Molecular dynamics simulations based on the Cycle-NN-PES

We have performed MD simulations using the Cycle-NN-PES for the femtosecond laser induced dynamics for the (O, CO)/Ru(0001) system at the low, intermediate and high surface coverages (see

Figs. 3.10, 3.13, 3.16 in Chapter 3). The laser fluence is 200 J/m^2. We have calculated 5000 trajectories for each surface coverage and the integration time is 15 ps. Due to the lack of accuracy of the PES for some configurations along the dynamics, there exist some problems with the simulations that are discussed in Appendix J. Still, we think that at least qualitatively, the obtained results are still interesting and we show them here.

In Fig. 6.16 we show the CO desorption probability (left panel) and the CO_2 desorption probability (right panel) as a function of time for the three different studied coverages. In the bottom panel we show the calculated branching ration (br) between CO desorption and oxidation as defined in eq.(5.2). We remind that, before the first CO_2 molecule is desorbed this quantity is not defined.

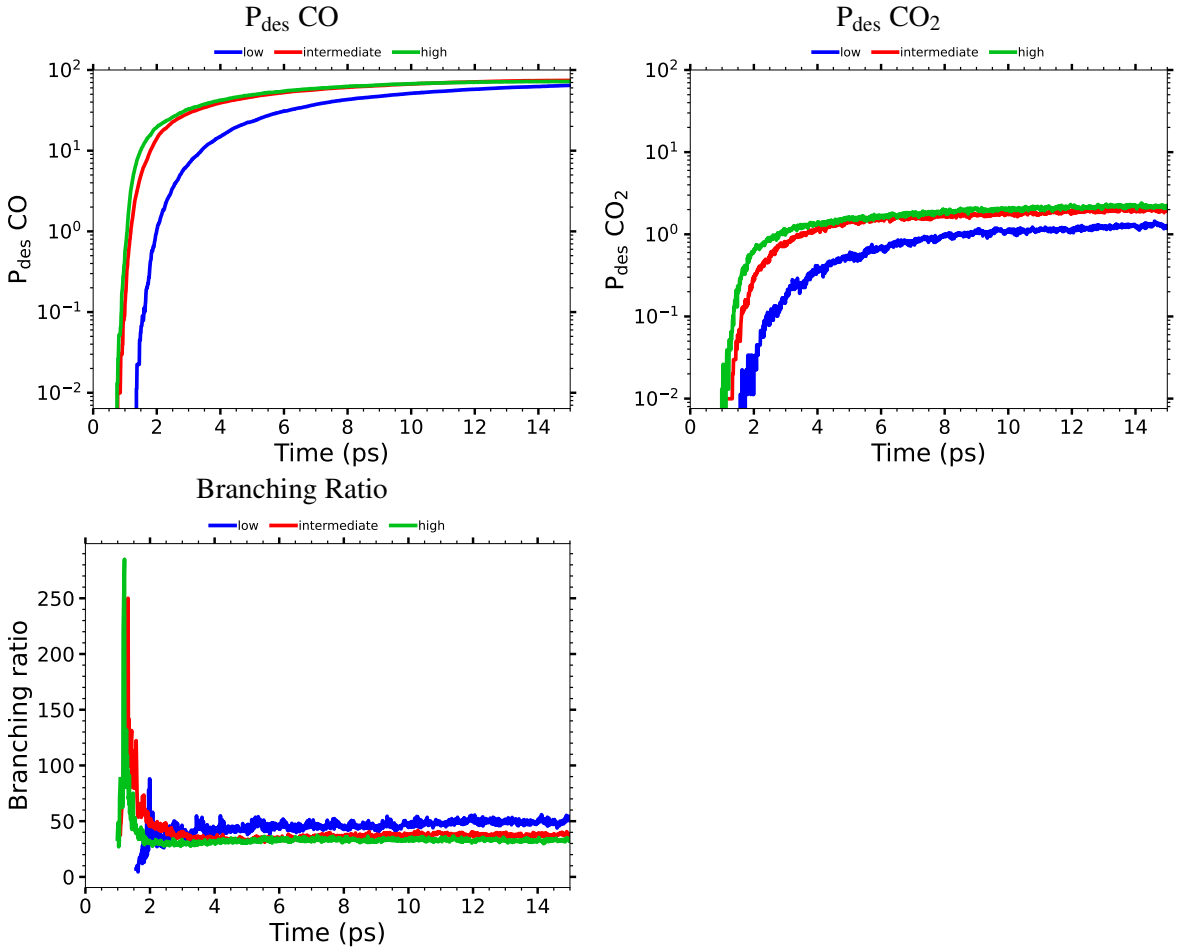

Figure 6.16: CO desorption probability (top left panel), CO_2 desoprtion probability (top right panel) and branching ratio between CO desorption and oxidation (bottom panel) as a function of time obtained from molecular dynamics simulations based on the Cycle-NN-PES. The results for the low, intermediate and high coverage are shown in blue, red and green, respectively.

Regarding the CO desorption, we observe that both the desorption probability and the desorption rate are similar for the intermediate and high coverages, though the process is slightly faster at high coverage. For low surface coverage, the first CO desorption takes place 0.5 ps after the first desorption of the other surface coverages. Afterwards, the desorption probability increases also more slowly than for the other surface coverages, and after the 15 ps of simulation time it seems that it has not yet

surface coverage	low	intermediate	high
desorbed CO	64.49%	74.25%	72.08%
desorbed CO_2	1.19%	1.94%	2.18%
br	54.21	38.25	33.06

Table 6.3: Amount of desorption and oxidation of CO molecules during Cycle-NN-PES MD calculations. The branching ratio (br) is defined in eq.(5.2).

completely converged to its maximum value. The time evolution of the CO_2 desorption probability presents a similar behavior, though with much smaller values.

On the bottom panel, we observe that the branching ration between CO desorption and oxidation remains roughly constant after 3 ps for the high and intermediate coverages. In the case of the low surface coverage, the value obtained for the branching ratio is somewhat higher than for the other coverages and is still slowly increasing at the end of the simulation.

The final values of the CO desorption and oxidation probabilities and of the branching ratio at the end of the 15 ps of the simulation are given in Tab. 6.3. Interestingly, the results are similar for the different coverages, though the branching ratio between desorption and oxidation is somewhat larger for the low coverage case.

However, in order to compare the results from those simulations to the ones from AIMDEF simulations we need to show the values of the probabilities and branching ratio at 4 ps. In Table 6.4 we gather those values together with the one of AIMDEF simulations (which originate from Tab. 5.1) in parenthesis to facilitate the comparison.

surface coverage	low	intermediate	high
desorbed CO	14.88% (18.25%)	39.20% (45.06%)	42.20% (34.53%)
desorbed CO_2	0.41% (0.50%)	1.19% (0.67%)	1.32% (1.26%)
br	35.84 (36.5)	32.8 (67.3)	32.02 (27.4)

Table 6.4: Amount of desorption and oxidation of CO molecules during Cycle-NN-PES MD calculations at 4 ps to compare with AIMDEF simulations. In the cells we show the results for Cycle-NN-PES MD calculations, while in parenthesis we show for comparison the results of AIMDEF simulations. The branching ratio (br) is defined in eq.(5.2).

Comparing to the values extracted at the end of the 15 ps of simulation time, we observe that the amount of desorbed CO decreases drastically, as the amount of desorbed CO_2, although in less proportion than the latter. This leads us to the conclusion that if we increase the simulation time, we favored the desorption of CO and not the oxidation, meaning that a large simulation time, the CO desorption is predominant. This has a great effect on the branching ratio of intermediate and specifically low surface coverage. Therefore, we see that the values at 4 ps of simulation time, are closer to the experimental values than the one observed at the end of the 15 ps.

Now, comparing the values of Cycle-NN-PES MD with the ones of AIMDEF. In low surface coverage, we see that the CO desorption probability is lower, but in the same proportion, as the one of CO_2, leading to a branching ratio very close to the one find in AIMDEF simulation. In intermediate surface coverage, the CO desorption probability is lower, while the one of CO_2 is higher, leading to a branching ratio in agreement with the experiment, contrasting with the AIMDEF simulations we made.

Finally, in the high surface coverage, the CO desorption probability is higher while the one of CO_2 is almost equal, leading to a higher branching ratio, but still in agreement to the experimental results. We note that the branching ratio of high and intermediate surface coverage are surprisingly very close.

6.4 Conclusions and improvements

In this chapter we have constructed two different NN-PES based in the previously used AIMDEF data. The first one was trained with the low coverage data. The training set consisted of 50.000 data points. The data selection criteria were based on maintaining the proportion of events taking place in the AIMDEF simulations. The second PES was trained with the intermediate coverage data. The training was started with a small training of 6400 configurations selected maintaining the proportion of events taking place in the AIMDEF simulations. Subsequently, the PES was improved by retraining it with the configurations for which it was less accurate in the calculation of the forces. We found that this second procedure was more efficient to get an accurate PES. In any case, none of the PES was able to represent accurately all the configurations encountered along the molecular dynamics simulations. Still, even being aware of this problem, the analysis of the final results of the MD simulations, regarding the probabilities of CO desorption and oxidation, shows that they are not that different from those obtained in the AIMDEF simulations. In any case, further work is necessary to obtain a NN-PES accurate enough to perform MD simulation for which adequate active learning techniques should be implemented.

CHAPTER 7

CONCLUSIONS

"Yo hice lo que pude. Creo que tan mal no me fue."
— Diego Armando MARADONA, "Yo soy EL DIEGO" Diego Armando Maradona.[1]

The problem of photo-induced desorption and oxidation of CO coadsorbed with O atoms on Ru(0001) in ultra high vacuum condition, has been extensively studied in the end of the XXth [6] century, and beginning of XXI^{rst} [12;13;89;90;215] thanks to the advent of two-pulse correlation experiments with femtosecond laser pulses. Nonetheless, to complement the experimental studies, theoretical methods were insufficient, as for instance, the lack of integration of the hot phonons and electrons effects in the *ab-initio* molecular dynamics. This thesis inscribes in this problematic, and aims to fill the theoretical hole left in the literature.

In the present knowledge, several experimental studies with use of two-pulse correlation experiment, or X-Ray adsorption/desorption spectroscopy proposed an understanding of the problematic around CO desorption and oxidation, such as the mechanism of oxidation itself, the role of the hot electron and phonon in the mechanisms, and the competition between desorption and oxidation.

In this thesis we began with the characterization of three (O, CO) mixed surface coverages on Ru(0001). According to literature,[6;11;75] two of them had been experimentally observed. The third one has not yet been observed in experiments but we found it to be stable. The systems considered are 0.5 ML of O adatoms adsorbed on Ru(0001), with different CO coverages of 0.25 ML, 0.375 ML and 0.5 ML, named low, intermediate and high surface coverages, respectively. Our DFT study was performed with the GGA rev-PBE functional, including vdW long range interactions correction as presented bi Dion *et al.* [119] in order to give a deeper understanding of the interactions in the system, comparing to the traditional use of PBE in literature. We first found the adsorption configuration of minimum energy for each surface coverage. This allowed us to compute the desorption potential of a CO molecule from those coverages and find the minimum energy path to CO oxidation on all three surface coverages by making use of CINEB.[8;9] We also computed the variation of the molecular orbitals of the CO_2 when adsorbing on the Ru(0001) surface.

[1] *'J'ai fait ce que j'ai pu. Je ne crois pas m'en être si mal sorti."* —Diego Armando Maradona, "Yo soy EL DIEGO" Diego Armando MARADONA.

With the systems well characterized we then investigated the dynamical properties of them. Therefore, in the framework of recently developed AIMDEF,[93;94;95] we computed hundreds of multidimensional nonadiabatic *ab-initio* molecular dynamics of photo-induced reactions at the DFT level[7;68;69] of the three (O, CO) mixed surface coverages on Ru(0001). This advanced theoretical method allowed to study in great depth the dynamical properties of the systems, and to answer one of the major question of the topic, as the complexity of the CO oxidation in such system and its mechanisms. Indeed, with the AIMDEF simulations ran for the low surface coverage with the specific honeycomb arrangement, and in regard to the energetic informations collected in our characterization study, we have been able to show the complexity of the reaction path to oxidize CO molecule, and explain its low probability of occurrence. This shown, we pursued the investigation in the dynamical studies for the three surface coverages, by showing the importance of surface deformations on the desorption and oxidation probabilities of CO, on the kinetic energy of the adsorbates, and on their vertical and in-plane motion. Finally, we have shown in detail and characterized the different mechanisms of CO oxidation, which answer another of the question raised in literature.

The AIMDEF simulations are high precision calculations that have a high computational cost. Due to this cost, a limited amount of simulation are tractable which conducts to obtain rather high uncertainties when considering very low probable events. To tackle this problem, we used a cutting edge technology in our days, and create a potential energy surface based on neural network (NN-PES). We used the framework of embedded atom neural network[10] to investigate the best of two methods to produce NN-PES based on our previously acquired AIMDEF data. Afterward, we analyzed the data predictions of our NN-PES and ran thousands of molecular dynamics with electronic frictions, for the three surface coverages under study. The results of those dynamics are consistent with the AIMDEF simulations, although improvement of the accuracy of the NN-PES can be done. This preliminary result is a very promising answer to solve one of the biggest issue in *ab-initio* calculations.

Summarizing, in this thesis, we used novel theoretical methods to answer hot topic questions in heterogeneous catalysis and photo-induced reactions. The advance provided by this work closes open questions and unlock new path of reflection, which brings new questions.

REFERENCES

[1] X. Xie, Y. Li, Z. Q. Liu, M. Haruta, and W. Shen, Nature **458**, 746 (2009).

[2] H. C. Wu, L. C. Liu, and S. M. Yang, Appl. Catal. A Gen. **211**, 159 (2001).

[3] J. Szanyi and D. W. Goodman, J. Phys. Chem. **98**, 2972 (1994).

[4] H.-I. Lee and J. White, J. Catal. **63**, 261 (1980).

[5] T. E. Madey, H. A. Engelhardt, and D. Menzel, Surf. Sci. **48**, 304 (1975).

[6] M. Bonn, S. Funk, Ch. Hess, D. N. Denzler, C. Stampfl, M. Scheffler, M. Wolf, and G. Ertl, Science **285**, 1042 (1999).

[7] M. Alducin, N. Camillone, S.-Y. Hong, and J. I. n. Juaristi, Phys. Rev. Lett. **123**, 246802 (2019).

[8] G. Henkelman, B. P. Uberuaga, and H. Jónsson, J. Chem. Phys. **113**, 9901 (2000).

[9] G. Henkelman and H. Jónsson, J. Chem. Phys. **113**, 9978 (2000).

[10] Y. Zhang, C. Hu, and B. Jiang, Journal of Physical Chemistry Letters **10**, 4962 (2019).

[11] K. L. Kostov, H. Rauscher, and D. Menzel, Surf. Sci. **278**, 62 (1992).

[12] H. Oberg, J. Gladh, K. Marks, H. Ogasawara, A. Nilsson, L. G. M. Pettersson, and H. Ostrom, The Journal of Chemical Physics **143**, 074701 (2015).

[13] H. Öström, H. Öberg, H. Xin, J. b. LaRue, M. b. Beye, M. Dell'Angela, J. Gladh, M. L. Ng, J. A. a. Sellberg, S. Kaya, G. Mercurio, D. Nordlund, M. Hantschmann, F. Hieke, D. Kühn, W. F. Schlotter, G. L. Dakovski, J. J. Turner, M. P. Minitti, A. Mitra, S. P. Moeller, A. d. Föhlisch, M. Wolf, W. e. Wurth, M. Persson, J. K. b. Nørskov, F. Abild-Pedersen, H. Ogasawara, L. G. M. Pettersson, and A. a. Nilsson, Science **347**, 978 (2015).

[14] S. Anisimov, B. Kapeliovich, and T. Perel'Man, Soviet Journal of Experimental and Theoretical Physics **39**, 776 (1974).

[15] J. E. Lennard-Jones, Trans. Faraday Soc. **28**, 333 (1932).

[16] A. Zangwill, *Physics at Surfaces* (Cambridge University Press, 1988).

[17] K. Oura, M. Katayama, A. V. Zotov, V. G. Lifshits, and A. A. Saranin, *Surface Science* (Springer, Berlin, Germany, 2003).

[18] E. Q. Michele Aresta, Angela Dibenedetto, *Reaction Mechanisms in Carbon Dioxide Conversion*.

[19] L. G. P. Anders Nilsson and J. K. Norskov, *Chemical Bonding at Surfaces and Interfaces*, edited by Elsevier (2008).

[20] J. de la Figuera, J. M. Puerta, J. I. Cerda, F. El Gabaly, and K. F. McCarty, Surf. Sci. **600**, L105 (2006).

[21] H. Pfnür, P. Feulner, and D. Menzel, J. Chem. Phys. **79**, 4613 (1983).

[22] A. B.M.Smirnov, *Reference Data on Atoms, Molecules, and Ions*, edited by Springer-Verlag (1985).

[23] X. Wu, J. Lang, Z. Sun, F. Jin, and Y. H. Hu, Appl. Catal. B Environ. **295**, 120312 (2021).

[24] B. Qiao, J. Liu, Y. G. Wang, Q. Lin, X. Liu, A. Wang, J. Li, T. Zhang, and J. Liu, ACS Catal. **5**, 6249 (2015).

[25] J. Saavedra, T. Whittaker, Z. Chen, C. J. Pursell, R. M. Rioux, and B. D. Chandler, Nat. Chem. **8**, 584 (2016).

[26] S. Dey, G. C. Dhal, D. Mohan, and R. Prasad, Adv. Compos. Hybrid Mater. **2**, 501 (2019).

[27] C. H. Peden and D. W. Goodman, J. Phys. Chem. **90**, 1360 (1986).

[28] C. H. F. Peden, D. W. Goodman, M. D. Weisel, and F. M. Hoffmann, Surf. Sci. **253**, 44 (1991).

[29] F. M. Hoffmann, M. D. Weisel, and C. H. F. Peden, Surf. Sci. **253**, 59 (1991).

[30] I. Langmuir, Transactions of the Faraday Society **17**, 607 (1922).

[31] C. Stampfl, M. Veronica Ganduglia-Pirovano, K. Reuter, and M. Scheffler, Surf. Sci. **500**, 368 (2002).

[32] A. Böttcher, M. Rogozia, H. Niehus, H. Over, and G. Ertl, J. Phys. Chem. B **103**, 6267 (1999).

[33] M. Lindroos, H. Pfnür, G. Held, and D. Menzel, Surf. Sci. **222**, 451 (1989).

[34] H. Pfnür, G. Held, M. Lindroos, and D. Menzel, Surf. Sci. **220**, 43 (1989).

[35] C. Stampfl and M. Scheffler, Phys. Rev. B **54**, 2868 (1996).

[36] C. Stampfl, S. Schwegmann, H. Over, M. Scheffler, and G. Ertl, Phys. Rev. Lett. **77**, 3371 (1996).

[37] C. Stampfl and M. Scheffler, Phys. Rev. Lett. **78**, 1500 (1997).

[38] C. Stampfl and M. Scheffler, Surf. Sci. **433-435**, 119 (1999).

[39] A. Böttcher, H. Niehus, S. Schwegmann, H. Over, and G. Ertl, J. Phys. Chem. B **101**, 11185 (1997).

[40] A. Böttcher and H. Niehus, Phys. Rev. B **60**, 14396 (1999).

[41] F. Gao, Y. Wang, Y. Cai, and D. W. Goodman, Surf. Sci. **603**, 1126 (2009).

[42] J. Q. Cai, H. Ning, H. J. Luo, X. M. Tao, and M. Q. Tan, Comput. Mater. Sci. **122**, 210 (2016).

[43] A. Böttcher, H. Conrad, and H. Niehus, J. Chem. Phys. **112**, 4779 (2000).

[44] H. Over, Y. D. Kim, A. P. Seitsonen, S. Wendt, E. Lundgren, M. Schmid, P. Varga, A. Morgante, and G. Ertl, Science **287**, 1474 (2000).

[45] H. Over and M. Muhler, Prog. Surf. Sci. **72**, 3 (2003).

[46] K. Reuter and M. Scheffler, Phys. Rev. Lett. **90**, 4 (2003).

[47] B. Narloch, G. Held, and D. Menzel, Surf. Sci. **317**, 131 (1994).

[48] S. S. Sung and R. Hoffmann, J. Am. Chem. Soc. **107**, 578 (1985).

[49] A. Föhlisch, M. Nyberg, P. Bennich, L. Triguero, J. Hasselström, O. Karis, L. G. Pettersson, and A. Nilsson, J. Chem. Phys. **112**, 1946 (2000).

[50] A. Nilsson and L. G. M. Pettersson, Surf. Sci. Rep. **55**, 49 (2004).

[51] N. Dimakis, F. A. Flor, N. E. Navarro, A. Salgado, and E. S. Smotkin, J. Phys. Chem. C **120**, 10427 (2016).

[52] B. Huang, H. Kobayashi, T. Yamamoto, T. Toriyama, S. Matsumura, Y. Nishida, K. Sato, K. Nagaoka, M. Haneda, W. Xie, Y. Nanba, M. Koyama, F. Wang, S. Kawaguchi, Y. Kubota, and H. Kitagawa, Angew. Chem. Int. Ed. **58**, 2230 (2019).

[53] N. Dimakis, N. E. Navarro, T. Mion, and E. S. Smotkin, J. Phys. Chem. C **118**, 11711 (2014).

[54] G. Blyholder, J. Phys. Chem. **68**, 2772 (1964).

[55] C. Stampfl and M. Scheffler, J. Vac. Sci. Technol. A Vacuum, Surfaces, Film. **15**, 1635 (1997).

[56] C. Stampfl and M. Scheffler, Phys. Rev. B **65**, 155417 (2002).

[57] K. Reuter and M. Scheffler, Phys. Rev. B - Condens. Matter Mater. Phys. **73**, 1 (2006).

[58] J. E. Sutton, J. M. Lorenzi, J. T. Krogel, Q. Xiong, S. Pannala, S. Matera, and A. Savara, ACS Catal. **8**, 5002 (2018).

[59] S. Sakong, A. K. Henß, J. Wintterlin, and A. Groß, J. Phys. Chem. C **124**, 15216 (2020).

[60] J. Wu, Y. Huang, W. Ye, and Y. Li, Adv. Sci. **4**, 1 (2017).

[61] F. Budde, T. F. Heinz, M. M. T. Loy, J. A. Misewich, F. de Rougemont, and H. Zacharias, Phys. Rev. Lett. **66**, 3024 (1991).

[62] S. Funk, M. Bonn, D. N. Denzler, Ch. Hess, M. Wolf, and G. Ertl, J. Chem. Phys. **112**, 9888 (2000).

[63] D. N. Denzler, C. Frischkorn, C. Hess, M. Wolf, and G. Ertl, Phys. Rev. Lett. **91**, 226102 (2003).

[64] P. Szymanski, A. L. Harris, and N. Camillone, J. Phys. Chem. A **111**, 12524 (2007).

[65] P. Szymanski, A. L. Harris, and N. Camillone, J. Chem. Phys. **126**, 214709 (2007), https://doi.org/10.1063/1.2735594 .

[66] S.-Y. Hong, P. Xu, N. R. Camillone, M. G. White, and N. Camillone III, J. Chem. Phys. **145**, 014704 (2016).

[67] M. Beye, T. Anniyev, R. Coffee, M. Dell'Angela, A. Föhlisch, J. Gladh, T. Katayama, S. Kaya, O. Krupin, A. Møgelhøj, A. Nilsson, D. Nordlund, J. K. Nørskov, H. Öberg, H. Ogasawara, L. G. Pettersson, W. F. Schlotter, J. A. Sellberg, F. Sorgenfrei, J. J. Turner, M. Wolf, W. Wurth, and H. Öström, Phys. Rev. Lett. **110**, 186101 (2013).

[68] J. I. Juaristi, M. Alducin, and P. Saalfrank, Phys. Rev. B **95**, 125439 (2017).

[69] R. Scholz, S. Lindner, I. Lončarić, J. C. Tremblay, J. I. Juaristi, M. Alducin, and P. Saalfrank, Phys. Rev. B **100**, 245431 (2019).

[70] J. A. Prybyla, H. W. K. Tom, and G. D. Aumiller, Phys. Rev. Lett. **68**, 503 (1992).

[71] L. M. Struck, L. J. Richter, S. A. Buntin, R. R. Cavanagh, and J. C. Stephenson, Phys. Rev. Lett. **77**, 4576 (1996).

[72] M. Dell'Angela, T. Anniyev, M. Beye, R. Coffee, A. Föhlisch, J. Gladh, T. Katayama, S. Kaya, O. Krupin, J. LaRue, A. Møgelhøj, D. Nordlund, J. K. Nørskov, H. Oberg, H. Ogasawara, H. Öström, L. G. M. Pettersson, W. F. Schlotter, J. a. Sellberg, F. Sorgenfrei, J. J. Turner, M. Wolf, W. Wurth, and A. Nilsson, Science **339**, 1302 (2013).

[73] J. Gladh, T. Hansson, and H. Öström, Surf. Sci. **615**, 65 (2013).

[74] E. Diesen, H. Y. Wang, S. Schreck, M. Weston, H. Ogasawara, J. Larue, F. Perakis, M. Dell'Angela, F. Capotondi, L. Giannessi, E. Pedersoli, D. Naumenko, I. Nikolov, L. Raimondi, C. Spezzani, M. Beye, F. Cavalca, B. Liu, J. Gladh, S. Koroidov, P. S. Miedema, R. Costantini, T. F. Heinz, F. Abild-Pedersen, J. Voss, A. C. Luntz, and A. Nilsson, Phys. Rev. Lett. **127**, 16802 (2021).

[75] H. Öberg, J. Gladh, M. Dell'Angela, T. Anniyev, M. Beye, R. Coffee, A. Föhlisch, T. Katayama, S. Kaya, J. Larue, A. Møgelhøj, D. Nordlund, H. Ogasawara, W. F. Schlotter, J. A. Sellberg, F. Sorgenfrei, J. J. Turner, M. Wolf, W. Wurth, H. Öström, A. Nilsson, J. K. Nørskov, and L. G. Pettersson, Surf. Sci. **640**, 80 (2015).

[76] R. Scholz, G. Floß, P. Saalfrank, G. Füchsel, I. Lončarić, and J. I. Juaristi, Phys. Rev. B **94**, 165447 (2016).

[77] H. Xin, J. LaRue, H. Öberg, M. Beye, M. Dell'Angela, J. J. Turner, J. Gladh, M. L. Ng, J. A. Sellberg, S. Kaya, G. Mercurio, F. Hieke, D. Nordlund, W. F. Schlotter, G. L. Dakovski, M. P. Minitti, A. Föhlisch, M. Wolf, W. Wurth, H. Ogasawara, J. K. Nørskov, H. Öström, L. G. M. Pettersson, A. Nilsson, and F. Abild-Pedersen, Phys. Rev. Lett. **114**, 156101 (2015).

[78] C. Liu, T. R. Cundari, and A. K. Wilson, J. Phys. Chem. C **116**, 5681 (2012).

[79] I. V. Chernyshova and S. Ponnurangam, Phys. Chem. Chem. Phys. **21**, 8797 (2019).

[80] J. Ko, B. K. Kim, and J. W. Han, J. Phys. Chem. C **120**, 3438 (2016).

[81] L. Zhou, A. Kandratsenka, C. T. Campbell, A. M. Wodtke, and H. Guo, Angew. Chem-Ger Edit **58**, 6916 (2019).

[82] A. Álvarez, M. Borges, J. J. Corral-Pérez, J. G. Olcina, L. Hu, D. Cornu, R. Huang, D. Stoian, and A. Urakawa, ChemPhysChem **18**, 3135 (2017).

[83] M. Zhang, M. Dou, and Y. Yu, Appl. Surf. Sci. **433**, 780 (2018).

[84] C. Zhang, P. Hu, and A. Alavi, J. Am. Chem. Soc. **121**, 7931 (1999).

[85] C. J. Zhang, P. Hu, and A. Alavi, J. Chem. Phys. **112**, 10564 (2000).

[86] B. Y. Liu, J. M. Jin, C. Hardacre, P. Hu, and W. F. Lin, Journal of Electroanalytical Chemistry **688**, 216 (2013).

[87] P. Zhao, Y. He, S. Liu, D. B. Cao, X. Wen, H. Xiang, Y. W. Li, and H. Jiao, Appl. Catal. A Gen. **540**, 31 (2017).

[88] P. Zhao, Y. He, X. Wen, and H. Jiao, Surf. Sci. **715** (2022), 10.1016/j.susc.2021.121936.

[89] J. L. Larue, T. Katayama, A. b. Lindenberg, A. S. Fisher, H. Öström, A. a. Nilsson, and H. a. Ogasawara, Phys. Rev. Lett. **115**, 036103 (2015).

[90] S. Schreck, E. Diesen, J. LaRue, H. Ogasawara, K. Marks, D. Nordlund, M. Weston, M. Beye, F. Cavalca, F. Perakis, J. Sellberg, A. Eilert, K. H. Kim, G. Coslovich, R. Coffee, J. Krzywinski, A. Reid, S. Moeller, A. Lutman, H. Öström, L. G. M. Pettersson, and A. Nilsson, J. Chem. Phys. **149**, 234707 (2018).

[91] P. Saalfrank, Chem. Rev. **106**, 4116 (2006).

[92] J. C. Tully, M. Gomez, and M. HeadGordon, J. Vac. Sci. Technol. A Vacuum, Surfaces, Film. **11**, 1914 (1993).

[93] D. Novko, M. Blanco-Rey, J. I. Juaristi, and M. Alducin, Phys. Rev. B **92**, 201411 (2015).

[94] D. Novko, M. Blanco-Rey, M. Alducin, and J. I. Juaristi, Phys. Rev. B **93**, 245435 (2016).

[95] D. Novko, I. Lončarić, M. Blanco-Rey, J. I. Juaristi, and M. Alducin, Phys. Rev. B **96**, 085437 (2017).

[96] G. J. Kroes, *Prog. Surf. Sci.*, Vol. 60 (1999) pp. 1–85.

[97] A. C. Van Duin, S. Dasgupta, F. Lorant, and W. A. Goddard, J. Phys. Chem. A **105**, 9396 (2001).

[98] J. Behler, Journal of Chemical Physics **134**, 74106 (2011).

[99] N. Ashcroft and N. Mermin, *Solid state physics*, edited by S. College (1976).

[100] B. Bransden and C. Joachain, *Physics of atoms and molecules*, edited by Longman (1983).

[101] A. Groß, *Theoretical Surface Science: A Microscopic Perspective*, edited by Springer (2009).

[102] M. Born and J. Oppenheimer, **84**, 457 (1927).

[103] L. H. Thomas, Math. Proc. Cambridge Philos. Soc. **23**, 542 (1927).

[104] E. Fermi, Rend. Accad. Naz. Lincei **6**, 32 (1927).

[105] P. Hohenberg and W. Kohn, Physical Review **136**, B864 (1964).

[106] W. Khon, "nobel-lecture.pdf," (1999).

[107] G. Baym, *Lectures on Quantum Mechanics* (1973).

[108] W. Kohn and L. J. Sham, Physical Review **140**, A1133 (1965).

[109] J. P. Perdew and K. Schmidt, AIP Conf. Proc. **577**, 1 (2001).

[110] R. M. Martin, *Electronic Structure: Basic Theory and Practical Methods* (Cambridge University Press, Cambridge, England, UK, 2004).

[111] D. M. Ceperley and B. J. Alder, Physical Review Letters **45**, 566 (1980).

[112] S. H. Vosko, L. Wilk, and M. Nusair, Canadian Journal of Physics **58**, 1200 (1980).

[113] J. P. Perdew and A. Zunger, Physical Review B **23**, 5048 (1981).

[114] J. P. Perdew and Y. Wang, Physical Review B **45**, 13244 (1992).

[115] A. D. Becke, Physical Review A **38** (1988), 10.1063/1.1749835.

[116] C. Lee, W. Yang, and R. G. Parr, Physical Review B **37**, 785 (1988).

[117] J. P. Perdew, K. Burke, and M. Ernzerhof, Physical Review Letters **77**, 3865 (1996).

[118] S. Grimme, J. Antony, S. Ehrlich, and H. Krieg, Journal of Chemical Physics **132**, 10089 (2010).

[119] M. Dion, H. Rydberg, E. Schroder, D. C. Langreth, and B. I. Lundqvist, Physical Review Letters **92**, 246401 (2004).

[120] D. C. Langreth, B. I. Lundqvist, S. D. Chakarova-Kack, V. R. Cooper, M. Dion, P. Hyldgaard, A. Kelkkanen, J. Kleis, L. Kong, S. Li, P. G. Moses, E. Murray, A. Puzder, H. Rydberg, E. Schroder, and T. Thonhauser, Journal of Physics Condensed Matter **21** (2009), 10.1088/0953-8984/21/8/084203.

[121] Y. Zhang and W. Yang, "Comment on "generalized gradient approximation made simple"," (1998).

[122] F. Bloch, Zeitschrift für Phys. **52**, 555 (1929).

[123] P. E. Blöchl, Phys. Rev. B **50**, 17953 (1994).

[124] H. J. Monkhorst and J. D. Pack, Phys. Rev. B **13**, 5188 (1976).

[125] M. Methfessel and A. T. Paxton, Phys. Rev. B **40**, 3616 (1989).

[126] G. Kresse and D. Joubert, Phys. Rev. B **59**, 1758 (1999).

[127] G. Kresse and J. Furthmüller, Comp. Mater. Sci. **6**, 15 (1996).

[128] G. Kresse and J. Furthmüller, Phys. Rev. B **54**, 11169 (1996).

[129] P. Ehrenfest, Zeitschrift fur Physik **45**, 455 (1927).

[130] W. H. Press, S. A. Teukolsky, W. T. Vetterling, B. P. Flannery, and M. Metcalf, *Numerical recipes in Fortran 90: Volume 2, volume 2 of Fortran numerical recipes: The art of parallel scientific computing* (Cambridge university press, 1996).

[131] P. Schofield, Computer Physics Communications **5**, 17 (1973).

[132] L. Verlet, Physical Review **159**, 98 (1967).

[133] M. Lisowski, P. A. Loukakos, U. Bovensiepen, J. Stahler, C. Gahl, and M. Wolf, Applied Physics A: Materials Science and Processing **78**, 165 (2004).

[134] W. S. Fann, R. Storz, H. W. Tom, and J. Bokor, Phys. Rev. B **46**, 13592 (1992).

[135] R. H. Groeneveld, R. Sprik, and A. Lagendijk, Phys. Rev. B **45**, 5079 (1992).

[136] T. Juhasz, H. E. Elsayed-Ali, G. O. Smith, C. Suãrez, and W. E. Bron, Phys. Rev. B **48**, 15488 (1993).

[137] C. Springer, M. Head-Gordon, and J. C. Tully, Surf. Sci. **320**, L57 (1994).

[138] C. Springer and M. Head-Gordon, Chem. Phys. **205**, 73 (1996).

[139] T. Vazhappilly, T. Klamroth, P. Saalfrank, and R. Hernandez, J. Phys. Chem. C **113**, 7790 (2009).

[140] G. Füchsel, T. Klamroth, J. C. Tremblay, and P. Saalfrank, Phys. Chem. Chem. Phys. **12**, 14082 (2010).

[141] G. Füchsel, T. Klamroth, S. Monturet, and P. Saalfrank, Phys. Chem. Chem. Phys. **13**, 8659 (2011).

[142] I. Lončarić, M. Alducin, P. Saalfrank, and J. I. Juaristi, Phys. Rev. B **93**, 014301 (2016).

[143] I. Lončarić, M. Alducin, P. Saalfrank, and J. I. Juaristi, Nucl. Instrum. Methods B **382**, 114 (2016), the 21st International Workshop on Inelastic Ion Surface Collisions (IISC-21).

[144] R. Scholz, G. Floß, P. Saalfrank, G. Füchsel, I. Lončarić, and J. I. Juaristi, Phys. Rev. B. **94**, 165447 (2016).

[145] J. I. Juaristi, M. Alducin, R. D. Muiño, H. F. Busnengo, and A. Salin, Phys. Rev. Lett. **100**, 116102 (2008).

[146] M. Alducin, R. Díez Muiño, and J. I. Juaristi, Prog. Surf. Sci. **92**, 317 (2017).

[147] D. Novko, M. Blanco-Rey, M. Alducin, and J. I. Juaristi, Physical Review B **93**, 1 (2016).

[148] W. G. Hoover, Physical Review A **31**, 1695 (1985).

[149] S. Nosé and S. Nosi, An Int. J. Interface Between Chem. Phys. Mol. Phys. **52**, 255 (1984).

[150] S. Nosé, J. Chem. Phys. **81**, 511 (1984).

[151] P. H. Hünenberger, Adv. Polym. Sci. **173**, 105 (2005).

[152] H. Hellmann, *Einführung in die Quantenchemie* (1937).

[153] R. Feynman, Physical Review **56**, 340 (1939).

[154] F. L. Hirshfeld, Israel Journal of Chemistry **16**, 198 (1977).

[155] A. Serrano-Jiménez, A. P. S. Muzas, Y. Zhang, J. Ovčar, B. Jiang, I. Lončarić, J. I. Juaristi, and M. Alducin, J. Chem. Theory Comput. **17**, 4648 (2021).

[156] J. Behler, Journal of Physics Condensed Matter **26** (2014), 10.1088/0953-8984/26/18/183001.

[157] W. S. McCulloch and W. Pitts, The Bulletin of Mathematical Biophysics **5**, 115 (1943).

[158] F. Rosenblatt, Psychological Review **65**, 386 (1958).

[159] M. Minsky and S. A. Papert, *Perceptrons: An Introduction to Computational Geometry*, edited by M. Press (1969).

[160] J. Behler and M. Parrinello, Phys. Rev. Lett. **98**, 146401 (2007).

[161] T. Hammerschmidt, R. Drautz, and D. G. Pettifor, Int. J. Mater. Res. **100**, 1479 (2009).

[162] R. H. Byrd, P. Lu, J. Nocedal, and C. Zhu, SIAM J. Sci. Comput. (2006).

[163] D. W. Brenner, Phys. Status Solidi B **217**, 23 (2000).

[164] S. Manzhos, X. Wang, R. Dawes, and T. Carrington, Journal of Physical Chemistry A **110**, 5295 (2006).

[165] P. M. Agrawal, L. M. Raff, M. T. Hagan, and R. Komanduri, Journal of Chemical Physics **124** (2006), 10.1063/1.2185638.

[166] J. Behler, R. Martoňak, D. Donadio, and M. Parrinello, Physica Status Solidi (B) Basic Research **245**, 2618 (2008).

[167] M. S. Daw and M. I. Baskes, Physical Review Letters **50**, 1285 (1983).

[168] M. S. Daw and M. I. Baskes, Physical Review B **29**, 6443 (1984).

[169] M. J. Stott and E. Zaremba, Physical Review B **22**, 1564 (1980).

[170] S. F. Boys, Proceedings of the Royal Society of London. Series A. Mathematical and Physical Sciences **200**, 542 (1950).

[171] M. Gastegger, L. Schwiedrzik, M. Bittermann, F. Berzsenyi, and P. Marquetand, Journal of Chemical Physics **148**, 1 (2018).

[172] H. Jonsson, G. Mills, and K. W. Jacobsen, *Classical and Quantum Dynamics in Condensed Phase Simulations* (WORLD SCIENTIFIC, Singapore, 1998) pp. 385–404.

[173] H. Group, "convergence of saddle point," ().

[174] R. F. Bader, Accounts of Chemical Research **18**, 9 (1985).

[175] R. F. W. Bader, *Atoms in molecules : a quantum theory*, The International series of monographs on chemistry ; 22 (Clarendon Press, Oxford).

[176] W. Tang, E. Sanville, and G. Henkelman, J. Phys-Condes. Mat. **21**, 084204 (2009).

[177] G. Henkelman, A. Arnaldsson, and H. Jónsson, Comp. Mater. Sci. **36**, 354 (2006).

[178] H. Group, "Code: Bader charge analysis," ().

[179] J. Enkovaara, C. Rostgaard, J. J. Mortensen, J. Chen, M. Dułak, L. Ferrighi, J. Gavnholt, C. Glinsvad, V. Haikola, H. A. Hansen, H. H. Kristoffersen, M. Kuisma, A. H. Larsen, L. Lehtovaara, M. Ljungberg, O. Lopez-Acevedo, P. G. Moses, J. Ojanen, T. Olsen, V. Petzold, N. A. Romero, J. Stausholm-Møller, M. Strange, G. A. Tritsaris, M. Vanin, M. Walter, B. Hammer, H. Häkkinen, G. K. H. Madsen, R. M. Nieminen, J. K. Nørskov, M. Puska, T. T. Rantala, J. Schiøtz, K. S. Thygesen, and K. W. Jacobsen, J. Phys.: Condens. Mat. **22**, 253202 (2010).

[180] J. J. Mortensen, L. B. Hansen, and K. W. Jacobsen, Phys. Rev. B **71**, 035109 (2005).

[181] J. P. Perdew, K. Burke, and M. Ernzerhof, Phys. Rev. Lett. **78**, 1396 (1997).

[182] C. Ehlert and T. Klamroth, J. Comput. Chem. **41**, 1781 (2020).

[183] B. Hammer, L. B. Hansen, and J. K. Nørskov, Phys. Rev. B **59**, 7413 (1999).

[184] S. Grimme, S. Ehrlich, and L. Goerigk, J. Comput. Chem. **32**, 1456 (2011).

[185] Y. URASHIMA, T. WAKABAYASHI, T. MASAKI, and Y. TERASAKI, Mineralogical Journal **7**, 438 (1974).

[186] P. Zhao, Y. He, D.-B. Cao, X. Wen, H. Xiang, Y.-W. Li, J. Wang, and H. Jiao, Phys. Chem. Chem. Phys. **17**, 19446 (2015).

[187] Q. Wu, L. Zhou, and H. Guo, J. Phys. Chem. C **123**, 10509 (2019).

[188] S. Y. Liem and J. H. R. Clarke, J. Chem. Phys. **121**, 4339 (2004).

[189] P. Légaré, Surf. Sci. **580**, 137 (2005).

[190] G. Michalk, W. Moritz, H. Pfnur, and D. Menzel, Surf. Sci. **129**, 92 (1983).

[191] I. Lončarić, G. Füchsel, J. I. Juaristi, and P. Saalfrank, Phys. Rev. Lett. **119**, 146101 (2017).

[192] T. K. Shimizu, A. Mugarza, J. I. Cerdá, M. Heyde, Y. Qi, U. D. Schwarz, D. F. Ogletree, and M. Salmeron, J. Phys. Chem. C **112**, 7445 (2008).

[193] J.-Q. a. Cai, H.-J. a. Luo, X.-M. Tao, and M.-Q. Tan, ChemPhysChem **16**, 3937 (2015).

[194] S. Liu, Y.-W. Li, J. Wang, and H. Jiao, J. Am. Chem. Soc. (2016), 10.1021/acs.jpcc.6b06649.

[195] A.-K. Henß, S. Sakong, P. K. Messer, J. Wiechers, R. Schuster, D. C. Lamb, A. Groß, and J. Wintterlin, Science **363**, 715 (2019).

[196] G. E. Thomas and W. H. Weinberg, J. Chem. Phys. **70**, 954 (1979).

[197] D. Loffreda, D. Simon, and P. Sautet, Surf. Sci. **425**, 68 (1999).

[198] B. Shan, Y. Zhao, J. Hyun, N. Kapur, J. B. Nicholas, and K. Cho, J. Phys. Chem. C **113**, 6088 (2009).

[199] G. T. K. K. Gunasooriya and M. Saeys, ACS Catal. **8**, 10225 (2018).

[200] J. A. Steckel, A. Eichler, and J. Hafner, Phys. Rev. B **68**, 085416 (2003).

[201] N. M. Martin, M. Van den Bossche, H. Grönbeck, C. Hakanoglu, F. Zhang, T. Li, J. Gustafson, J. F. Weaver, and E. Lundgren, J. Phys. Chem. C **118**, 1118 (2014).

[202] A. P. G. P. G. P. Andrew Burrows, John Holman, *Chemistry*^{3}*: Introducing inorganic, organic and physical chemistry* (2022).

[203] G. Herzberg, *Molecular spectra and molecular structure: III. Electronic spectra and electronic structure of polyatomic molecules*.

[204] R. H. Crabtree, *The organometallic chemistry of the transition metals*.

[205] G. Blyholder, J Vac Sci Technol **11**, 865 (1974).

[206] B. Mondal, J. Song, F. Neese, and S. Ye, Curr. Opin. Chem. Biol. **25**, 103 (2015).

[207] A. Tetenoire, J. I. Juaristi, and M. Alducin, J. Phys. Chem. C **125**, 12614 (2021).

[208] C. Springer, M. Head-Gordon, and J. C. Tully, Surf. Sci. **320**, L57 (1994).

[209] T. Vazhappilly, T. Klamroth, P. Saalfrank, and R. Hernandez, J. Phys. Chem. C **113**, 7790 (2009).

[210] A. P. S. Muzas, A. Serrano-Jiménez, J. Ovčar, I. Lončarić, M. Alducin, and J. I. Juaristi, Chem. Phys. **558**, 111518 (2022).

[211] M. Blanco-Rey, J. I. Juaristi, R. Díez Muiño, H. F. Busnengo, G. J. Kroes, and M. Alducin, Phys. Rev. Lett. **112**, 103203 (2014).

[212] P. Saalfrank, J. I. Juaristi, M. Alducin, M. Blanco-Rey, and R. Díez Muiño, J. Chem. Phys. **141**, 234702 (2014).

[213] D. Novko, M. Blanco-Rey, J. I. Juaristi, and M. Alducin, Nucl. Instrum. Methods B **382**, 26 (2016).

[214] M. Alducin, R. Díez Muiño, and J. I. Juaristi, Prog. Surf. Sci. **92**, 317 (2017).

[215] J. Larue, B. Liu, G. L. Rodrigues, C. Liu, J. A. Garrido Torres, S. Schreck, E. Diesen, M. Weston, H. Ogasawara, F. Perakis, M. Dell'Angela, F. Capotondi, D. Ball, C. Carnahan, G. Zeri, L. Giannessi, E. Pedersoli, D. Naumenko, P. Amann, I. Nikolov, L. Raimondi, C. Spezzani, M. Beye, J. Voss, H. Y. Wang, F. Cavalca, J. Gladh, S. Koroidov, F. Abild-Pedersen, M. Kolb, P. S. Miedema, R. Costantini, T. F. Heinz, A. C. Luntz, L. G. Pettersson, and A. Nilsson, J. Chem. Phys. **157** (2022), 10.1063/5.0114399.

[216] R. Heid and L. Pintschovius, Phys. Rev. B - Condens. Matter Mater. Phys. **61**, 12059 (2000).

Appendices

APPENDIX A

VIBRATIONAL FREQUENCIES

We have calculated the vibrational stretch mode frequencies of CO in the different structures found for each coverage. Note that the number of stretch modes is different for each coverage and equal to the number of CO molecules in the simulation cell. As a result, in the low coverage case there exist one symmetric and one antisymmetric mode, in the intermediate coverage one symmetric and two asymmetric modes, and in the high coverage limit one symmetric and three asymmetric modes. The values obtained for the frequencies are giving in Table A.1 and the different structures named as in the main text. Recall that the label CO-Ru(0001) refers to the minimum coverage that corresponds to one CO molecule adsorbed in the bare Ru(0001) surface atop a Ru atom.

Coverage	Structure	$E(\mathrm{cm}^{-1})$	E(meV)	Mode
$CO_{(gas)}$	–	2099.55	260.31	ω
CO-Ru(0001)	CO_{top}	1922.726	238.388	ω_s
0.5ML O+0.25ML CO	Honeycomb	2001.149	248.111	ω_s
		1976.206	245.018	ω_a
	$p(2\times1)O_{hcp}$+$p(2\times2)CO_{top-fcc}$	1994.081	247.235	ω_s
		1968.878	244.110	ω_a
	$p(2\times1)O_{hcp}$+$p(2\times2)CO_{hcp}$	1791.965	222.175	ω_s
		1769.214	219.355	ω_a
0.5ML-O+0.375ML-CO	Structure A	2005.546	248.656	ω_s
		1960.762	243.104	ω_a
		1951.654	241.974	ω_a
	Structure B	1841.713	228.343	ω_s
		1789.780	221.905	ω_a
		1783.340	221.106	ω_a
0.5ML-O+0.5ML-CO	Structure C	1874.877	232.455	ω_s
		1820.599	225.726	ω_a
		1820.598	225.725	ω_a
		1791.564	222.126	ω_a
	Structure D	2034.621	252.261	ω_s
		1976.180	245.015	ω_a
		1976.178	245.015	ω_a
		1949.778	241.742	ω_a

Table A.1: Vibrational frequency of the symmetric (ω_s) and asymmetric (ω_a) CO stretch modes for the different coverages and structures, including the minimum coverage denoted as CO-Ru(0001) and the gas-phase value to be compared to the experimental frequency ω_{exp}=2169.81cm^{-1} [22]. Energies E given in cm^{-1} and meV.

APPENDIX B

GEOMETRY ANALYSIS

In Table B.1 we give all the intra and inter coordinates of the different CO_2 states for the different coverages. Labels O1, O2, C, and Ru are defined in Fig. 3.4.

	Bare slab + CO_2			0.5ML O + 0.25 ML CO		
	bCO2	lCO2	CO2(gas)	bCO2	lCO2	CO2(gas)
O1-C	1.245	1.180	1.179	1,209	1,171	1,179
O2-C	1.264	1.180	1.179	1,377	1,187	1,179
Ru-C	2.091	3.878	10.908	2,114	3,523	10,844
Ru-O1	2.407	3.669	10.840	2,948	4,584	10,910
Ru-O2	3.101	4.401	11.101	2,905	2,570	10,909
$\widehat{O1-C-O2}$	137.80	179.88	179.98	126,45	178,47	179,83
$\widehat{O1-C-Ru}$	88.59	71.09	83.62	122,65	151,16	90,11
$\widehat{O2-C-Ru}$	133.61	108.79	96.36	110,90	30,37	90,05
	0.5 ML O + 0.375 ML CO			0.5 ML O + 0.5 ML CO		
	bCO2	lCO2	CO2(gas)	bCO2	lCO2	CO2(gas)
O1-C	1,207	1,177	1,179	1.210	1.180	1.132
O2-C	1,355	1,182	1,179	1.293	1.179	1.133
Ru-C	2,138	4,168	10,787	2.282	5.237	9.851
Ru-O1	3,047	4,786	10,858	3.098	4.604	9.706
Ru-O2	2,803	3,812	10,877	2.923	6.037	10.128
$\widehat{O1-C-O2}$	126,32	179,54	178,38	130.64	179.78	179.70
$\widehat{O1-C-Ru}$	129,15	115,01	90,34	121.98	51.93	79.35
$\widehat{O2-C-Ru}$	104,52	64,54	91,28	106.36	128.20	100.95

Table B.1: Intra and Inter coordinates of the different CO_2 states for the different coverages. Labels O1, O2, C, and Ru are given as in Fig. 3.4. Distances are given in Å and angles in degrees.

APPENDIX C

FINDING INTERMEDIATE STATE

In the appendixC, we precise the research of the intermediate states bCO_2 and lCO_2 for covered surface. As for the explication of the protocol in section 3.2, we focus on the bCO_2, since the lowest energy state lCO_2 is the one with the same orientation than bCO_2. Before to read this appendix, we recommend to read the section 3.3 where the surface coverages are detailed.

In the following, for the sake of clarity, each state will bear as name its initial φ orientation The φ orientation is given as shown in Fig. 3.5 such as the origin of the cartesian system of coordinates is the center of the top ruthenium atom where the CO_2 adsorbs. The angle $\varphi = 0$ is given along the right direction of the x axis. Finally, we turn around the circle following the anticlockwise rotation direction with a step of $\varphi = \frac{\pi}{6}$. After some calculation, and so, by experience, we note that concerning the surfaces with adsorbates, the bCO_2 that are along a bridge site (meaning bCO_2 along a bridge), are unstable such they do not converge to a bCO_2 state, or slide down to another calculated direction such fcc or hcp. Hence, so for some positions we did not calculate such orientation.

In Figures C.1, C.2, and C.3 we show the studied recombining adsorbate combinations, and the corresponding bCO_2 initial adsorption sites and orientations for the low, intermediate, and high surface coverages, respectively.

For low surface coverage we computed four different φ orientations. Two of them with the oxygen from the hcp site that correspond to $\varphi = 0$ and $\varphi = \frac{\pi}{6}$ (represented in blue on the left panel of Fig. C.1), and two of them with the oxygen from the fcc site that correspond to $\varphi = 0$ and $\varphi = -\frac{\pi}{6}$ (represented in green on the right panel of Fig. C.1). The orientation that converges to the lowest energetic bCO_2 state is $\varphi = -\frac{\pi}{6}$ with an energy of 1.06 eV . Both $\varphi = 0$ with fcc or hcp oxygen converged to lCO_2. The other orientations lead to a bCO_2. All calculated lCO_2 converged to lCO_2.

For the identification of intermediate states for intermediate surface coverage, we had to test a larger number of states involving different adsorption sites for the recombining CO and O and different azimuthal φ orientations of the CO-O bond. Nevertheless, the followed strategy is the same as for the other surface coverages. In the first place, we used the lowest energy desorbed CO_2 state to select the recombining CO and O. We thus tried to find the intermediate state for the CO2 + O1 (or equivalently CO3 + O2) recombination which has an exothermic desorption energy of -0.81 eV. The CO2+O1 recombination, with its corresponding tested orientations, is represented in pink in the top-left panel of Fig. C.2. The CO3+O2 recombination, with its corresponding tried orientations, is depicted in yellow in the top-right panel of Fig. C.2. However, we were not able to find any bCO_2 state with

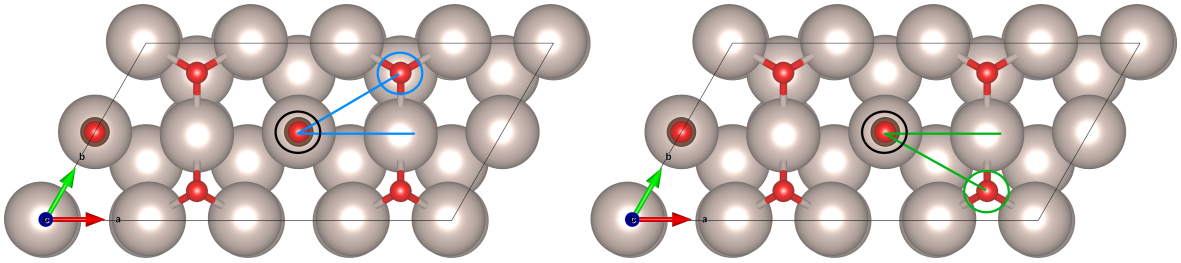

Figure C.1: Sketch of the different azimuthal orientations tested to find the bCO_2 and lCO_2 states in the low surface coverage honeycomb structure. Black circles show the CO used. Blue and green circles show the oxygen used for recombination. Blue and green lines show the corresponding azimuthal φ orientations of the CO-O bond.

these recombining species. Therefore, we studied the next two less energetic CO_2 desorption that involves the CO1 + O2 recombination which has a desorption energy of -0.68 eV and the CO2+O4 recombination desorption energy of -0.58 eV. The CO1+O2 recombination, with its corresponding tested orientations, is illustrated in red in the bottom-left panel of Fig. C.2. The CO2+O4 recombination, with its corresponding tried orientations, is represented in blue in the bottom-right panel of Fig. C.2. In this way, we found that the lowest energy bCO_2 state for the intermediate surface coverage is obtained from the CO1 + O2 recombination with $\varphi = -\frac{\pi}{2}$ and that its energy is 0.15 eV measured from the dissociative adsorption state ($O_{(ads)}$ + $CO_{(ads)}$). The corresponding lCO_2 with the same φ angle also converged to a stable lCO_2 state.

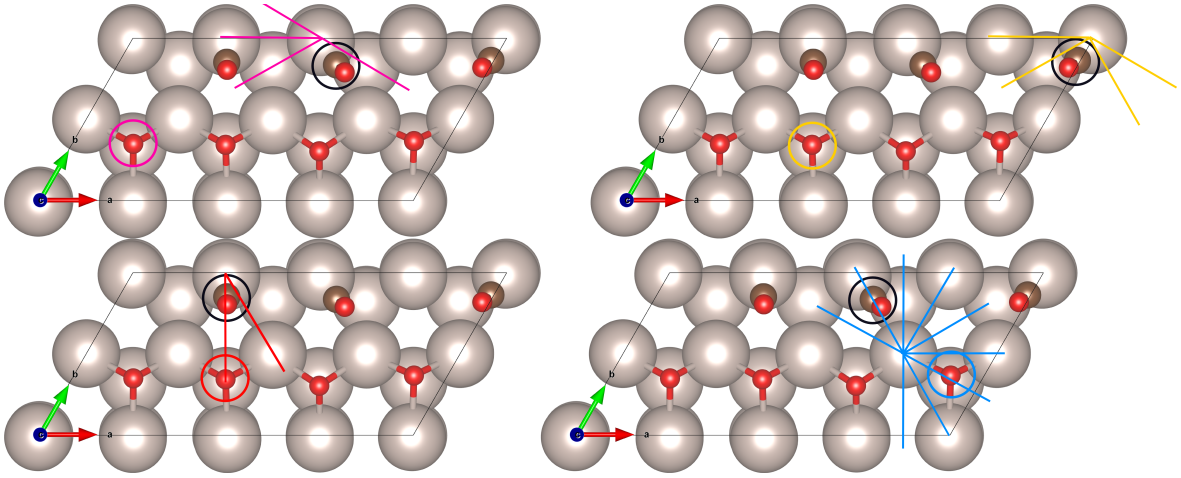

Figure C.2: Sketch of the different azimuthal orientations tested to find the bCO_2 and lCO_2 states at the intermediate surface coverage. Black circles show the CO used. Pink, yellow, red and blue circles show the oxygen used for recombination. Pink, yellow, red and blue lines show the corresponding azimuthal φ orientations of the CO-O bond.

Finally, for the high surface coverage, for which all the CO and O adsorbates are, respectively, equivalent by symmetry, we have tried recombination between nearest neighbors CO and O with the orientations sketched in Fig. C.3. We found the lowest energy bCO_2 state for the orientation $\varphi = \frac{2\pi}{3}$ with an energy 0.35 eV measured from the dissociative adsorption state ($CO_{(ads)}$+$O_{(ads)}$). The lCO_2 with corresponding φ angle, as for the lower surface coverages, also converged to a stable lCO_2 state.

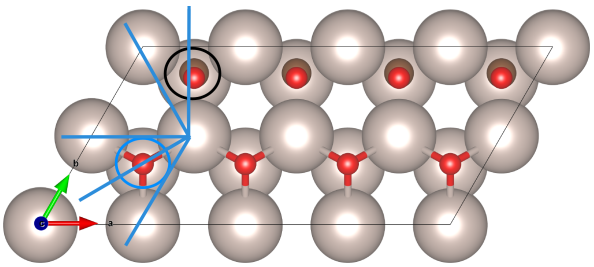

Figure C.3: Sketch of the different azimuthal orientations tested to find the bCO_2 and lCO_2 at the high surface coverage. The black circle shows the CO used. The blue circle shows the oxygen used for recombination. The blue line shows the corresponding azimuthal φ orientation of the CO-O bond.

Appendix D

Full relaxation figure

In this appendix we are showing the six possible adsorption sites of the adsorbates before and after the relaxation of the forces. In Figure D.1 we show on the left panel a top view of the position of the adsorbates before relaxation of the forces, and on the right panel after the relaxation. In black is given the label of the configuration, and in red is given the final energy in eV compared to the lowest energy configuration (hcp). Concerning the top configuration, the CO atoms desorbed, therefore the energy in not given. Here we observe that although we tried six different initial configurations, we end with only three where the adsorbates are adsorbed on the surface. The hcp being the most stable configuration, then the ones from bridge-b and bridge-c, and finally the ones of fcc and bridge-a.

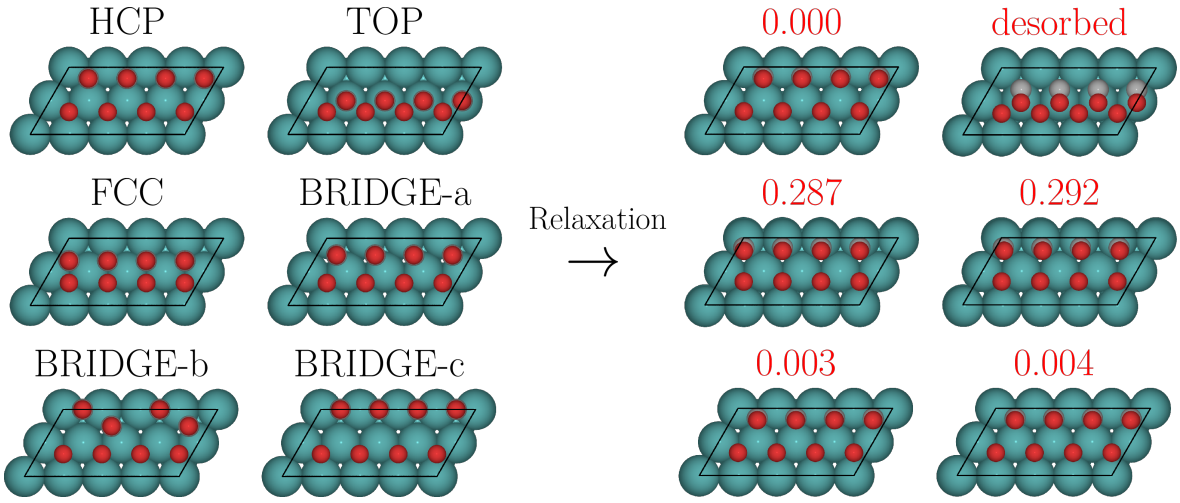

Figure D.1: Initial(left) and final(right) positions of the adsorbates before and after relaxation of the forces for the 0.5 ML O + 0.5 ML CO coverage. The name of the initial configurations are written in black (right panels). The energy differences with respect to the lowest energy configuration in eV are written in red (right panels).

APPENDIX E

THERMALIZATION

During the experiments of refs. 6;13, the ruthenium surface has been heated to 100 K. Therefore, prior to run AIMDEF simulations, we had to thermalize the system to 100 K. To do so, for each surface coverage, we start from the lowest energy configuration as initial step, then run a dynamic with the three outermost layer of the surface coupled to a Nosé-Hoover (NH) thermostat. The adsorbate should also thermalize at 100 K by exchange of energy with collision with the surface. However, before to run this dynamic, we must select the mass coupling constant of the NH thermostat, between the real and fictitious systems. We investigate for the high surface coverage which is the best mass coupling constant, and use it for all the surface coverages. Next, we run the full thermalization of the systems, and show how we selected the configurations that will be used in AIMDEF simulations.

E.1 Selection of the mass coupling constant

The mass coupling constant must be select to reflect a canonical ensemble. In VASP framework, the parameter defining the mass coupling constant of the NH thermostat has units of $[eV][fs]^{-2}[]^2$. Therefore, we chose three values of this parameter, and run a simulation of ten thousands steps with the high surface coverage. The distribution of energy of this simulation is shown in Fig. E.1. The temperature has been calculated using the kinetic energy of the system. This definition comes from the total energy, that can be calculated as the product of the degrees of freedom of the system with the Boltzmann constant and the temperature. Then, assuming the equipartition of energies in the system, the kinetic energy is thus half of the total energy. Therefore, the kinetic temperature in function of time is defined as

$$T(t) = E_{\text{kin}}(t)/(3Nk_{\text{B}}), \tag{E.1}$$

where $E_{\text{kin}}(t)$ is the kinetic energy of the system at time t, N is the number of moving atoms considered in the system and k_{B} the Boltzmann constant.

In Figure E.1 we show in **a)**, **b)** and **c)** the kinetic temperature distribution of the adiabatic dynamics with different mass coupling constants corresponding to the parameters equal to 0.01, 0.05 and 0.1, respectively. As general comment, the shape of the distribution is respecting the Maxwell-Boltzmann distribution, although the center of the distribution is not centered at 100 K, the target temperature.

Also, for coupling constant equal 0.01, the distribution is worse than the two others. The distribution with the mean value the closest to the target temperature is the one in panel **b)** with a value of 96.41 K. Therefore, we conclude that the best mass coupling constant is the one with parameter equal to 0.05.

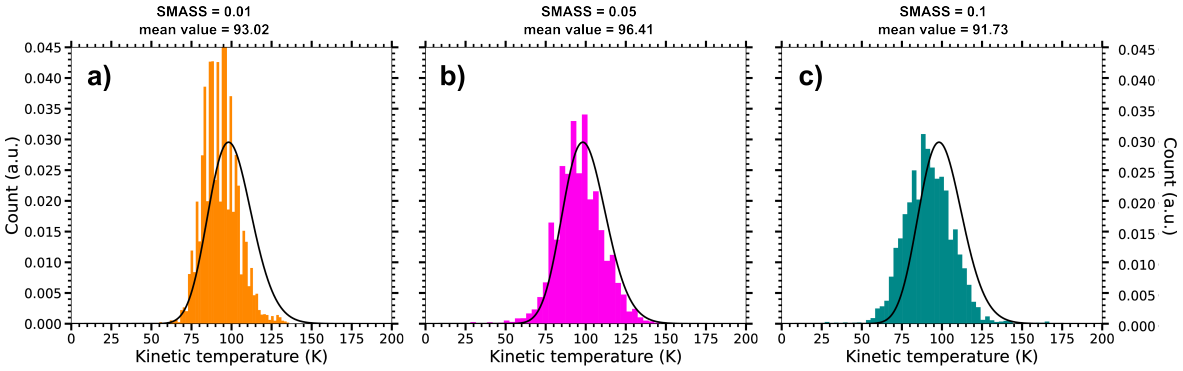

Figure E.1: Distribution of kinetic temperatures during the 10000 steps of thermalization for the different parameters defining the mass coupling constants.

E.2 Thermalization of the surface coverages

Now that we identified the best mass coupling constant to thermalize the system, we will see how after 20 ps of thermalization we select the configurations that we will use as starting point for the AIMDEF simulations. We still use the high surface coverage as reference to establish the protocol of configuration selection.

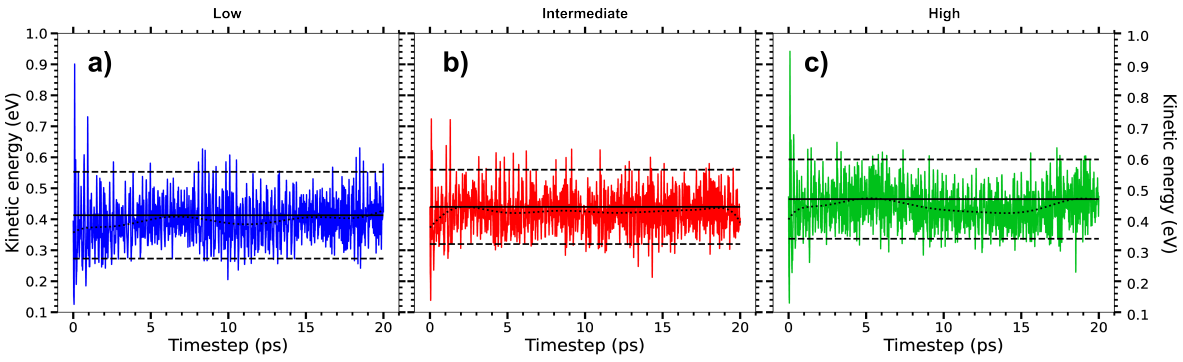

Figure E.2: Variation of the kinetic energy of the thermalization simulation regarding to the time step, for the different surface coverages.. The black lines represent in solid, the theoretical value, in dashed, the trend line and in dotted, pus or minus two times the standard deviation of the thermalization regarding to the theoretical value.

In Figures E.2 and E.3 we present the variation of kinetic and potential energy of the system along the thermalization for the three different surface coverages. In the panels **a)**, **b)**, **c)** are represented the energies of low, intermediate and high surface coverages, respectively. In in black solid line is the theoretical value of the energy, in black dotted line a trend line and in black dashed line the high and low limits of selection for the configuration. Those limits are equal to plus/minus two times the standard deviation of the energy variation with respect to the theoretical value. We use those conditions

for the selection of configurations because we want to get rid of the configurations that have extreme behavior. This way, we do not include the extreme configurations. We separately use this condition for kinetic and potential energy, and not on total energy, because it happens that a configuration with very high kinetic energy is compensated by a configuration with very low potential energy. Therefore this configuration seems good regarding to total energy, but bad regarding to kinetic or potential energy.

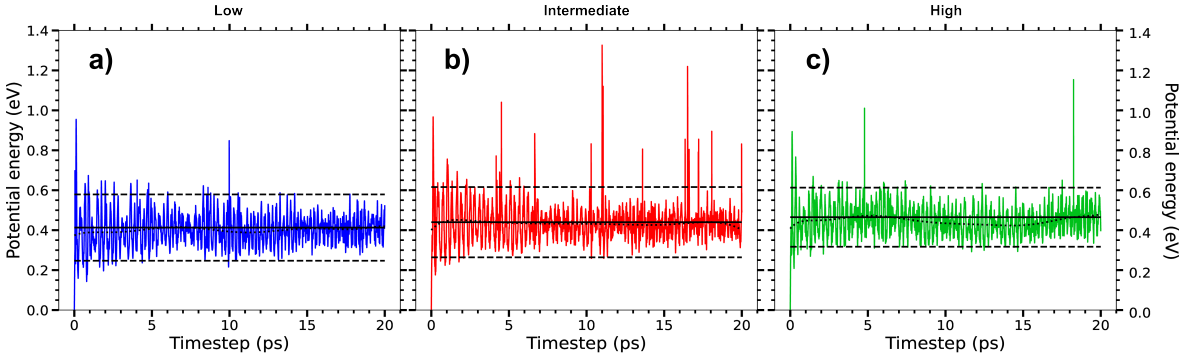

Figure E.3: Variation of the potential energy of the thermalization simulation regarding to the time step, for the different surface coverages.. The black lines represent in solid, the theoretical value, in dashed, the trend line and in dotted, pus or minus two times the standard deviation of the thermalization regarding to the theoretical value.

We see on the panel **c)** of Figures E.2 and E.3 that the kinetic and potential energies trend lines are close to the theoretical value between 4 and 6 ps and after 17 ps. Before 10 ps we assume that the system is not really thermalized although the mean value of the temperature is close to the theoretical one. In fact, since the adsorbates are not connected to the NH thermostat, they act as a third bath (considering the fictitious bath of NH and the real bath containing the ruthenium atoms). This bath must be also thermalized to 100 K, but before several picoseconds this bath is under the target temperature of 100 K. Therefore, we consider the system as thermalized after 17.5 ps, and select this time step as criterion for the selection of configuration. As summary, we select the configurations that respect the following rule:

- time step $t \geq 17.5$ ps
- $E_{\text{kin}}(\text{th}) - 2\sigma_{\text{kin}} \leq E_{\text{kin}}(t) \geq E_{\text{kin}}(\text{th}) + 2\sigma_{\text{kin}}$
- $E_{\text{pot}}(\text{th}) - 2\sigma_{\text{pot}} \leq E_{\text{pot}}(t) \geq E_{\text{pot}}(\text{th}) + 2\sigma_{\text{pot}}$

where t is the time step, $E_{\text{kin}}(\text{th})$ and $E_{\text{pot}}(\text{th})$ the theoretical values of kinetic and potential energies, σ_{kin} and σ_{pot} the calculated standard deviation of kinetic and potential energy of the simulation, and, $E_{\text{kin}}(t)$ and $E_{\text{pot}}(t)$ the kinetic and potential energies at time t.

In Figure E.4 we present the kinetic temperature distribution of the selected configurations. In black is represented the Maxwell-Boltzmann distribution according to the target temperature 100 K and the degrees of freed of the system. We observe in panel **c)** that the high surface coverage is the best distribution, close to the Maxwell-Boltzmann, and a mean value of 100 K exactly. In the case of the other surface coverage, their mean value of kinetic temperature is lower than target temperature, with the one of intermediate surface coverage almost 5 K higher than the one of the low surface coverage.

We observe that the distribution of the low and the intermediate surface coverages have a maximum peak shifted to the low temperature. Since the selection criteria were not designed for those lower surface coverage, we assume that they could have been better chosen, although in practice it will not be a problem for the AIMDEF simulations. Indeed, we will not run a dynamic for all the selected points, but simply a subset of 200 points from the thousands selected.

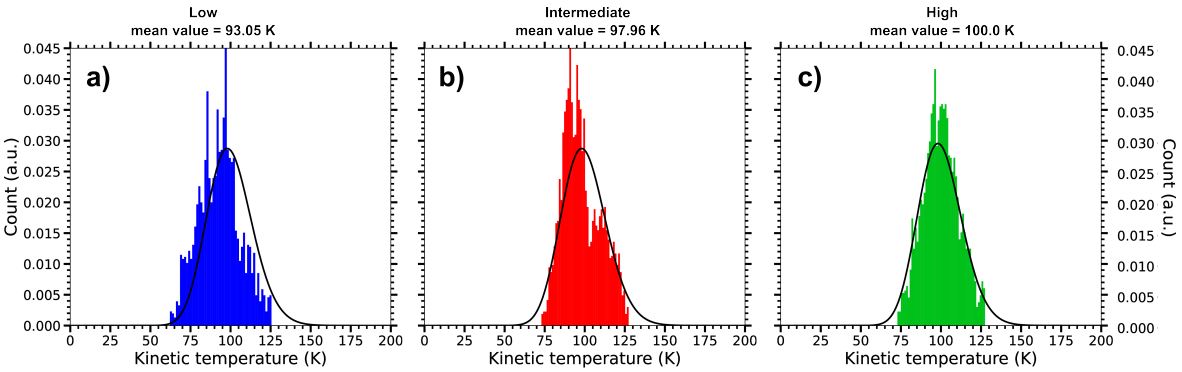

Figure E.4: Distribution of kinetic temperatures of the selected points for AIMDEF initial configuration, for the different surface coverages.

APPENDIX F

DENSITY PLOT CALCULATION

In this appendix we detail how we calculated the values presented in the density plot of Chapter 4, and 5. Here we use the low surface coverage as example, but the way to calculate is the same for the other surface coverages. The density plot showing the distribution of the instantaneous Ru-$O_{fcc,hcp}$-Ru (in-plane) dihedral angle and the distance from that adsorbed O to the C atom in the nearest CO (right panel of Figure 1 in the main text) is calculated as follows.

First, for each instantaneous configuration extracted from the data set formed by the (T_e,T_{ph})-AIMDEF trajectories and each integration step (4000 points per trajectory), we calculate for each O adsorbate (O_{ads}) in the unit cell the three Ru-O_{ads}-Ru (in-plane) dihedral angles Θ that the adsorbate forms with the three (initially) nearest Ru atoms in the topmost layer (i.e., the three Ru atoms that were the nearest neighbors to the corresponding O_{ads} in the initial configuration), see Figure F.1.

Next, for the same instantaneous configuration and the same O_{ads}, we calculate the minimum distances $d_{O\text{-}C1}$ and $d_{O\text{-}C2}$ from O_{ads} to any of the images of the two nonequivalent C atoms in our unit cell (labeled C1 and C2 in Figure F.1). In practice, we generate eight periodic images of the C1 and C2 atoms in the unit cell by applying $\pm\vec{a}$ and/or $\pm\vec{b}$ translations. Subsequently, we calculate the distances from O_{ads} to C1 and C2 in the unit cell and to their 8 images in adjacent cells, and the minimum distance for each nonequivalent atom is selected. This process is repeated for each of the four nonequivalent O_{ads} in the unit cell. Note that for each instantaneous configuration and each O_{ads} we extract six pairs of points (Θ,$d_{O\text{-}C}$) corresponding to three dihedral angles and two distances ($d_{O\text{-}C1}$ and $d_{O\text{-}C2}$).

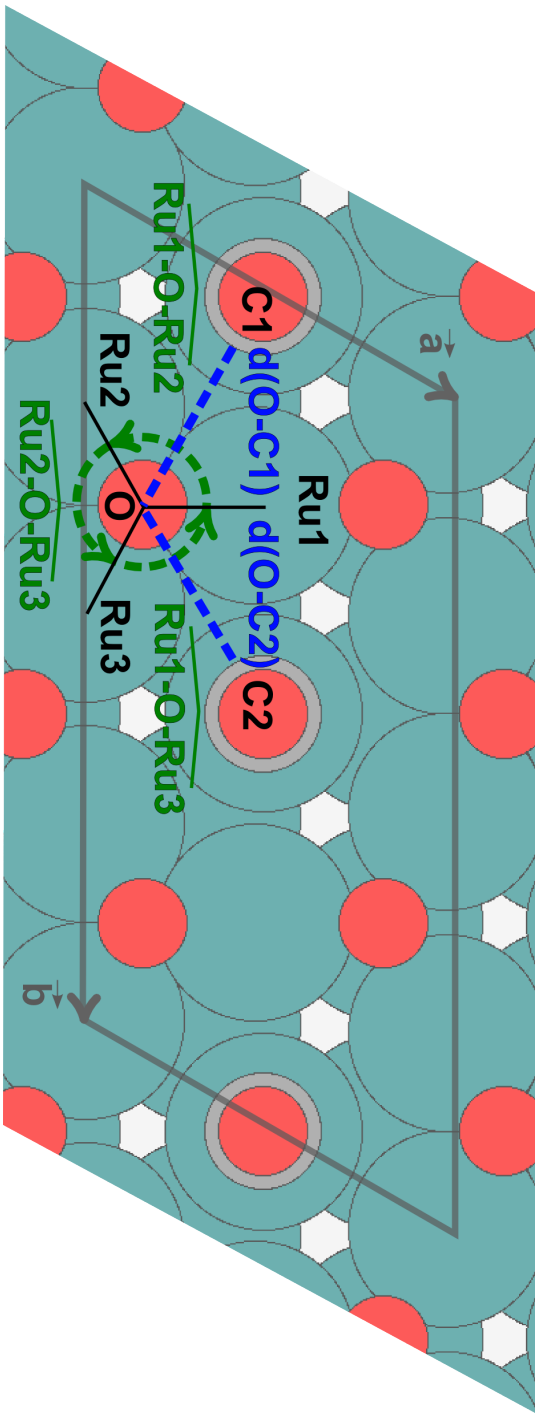

Figure F.1: Scheme showing, as an example, the three Ru-O_{ads}-Ru in-plane dihedral angles (in green) and the two O_{ads}-C distances (in blue) calculated for one of the four O adsorbates in the unit cell.

APPENDIX G

IN PLANE VARIATION OF THE ADSORBATES

In this appendix we are presenting a complementary analysis to the in-plane displacement of the adsorbates over the surface during the simulations. In Figure G.1 we re showing the density plots of the variations of the in-plane positions of the adsorbates during a range of time. We recall that the position of the adsorbates are the extended positions, not the actual one during the dynamics. Because of the periodic boundary condition which enforce the atoms the remain inside the simulation cell, the position of the adsorbates is may not be continuous in time. However, we perform a post-treatment analysis allowing to follow the position of the adsorbate in continuous way, allowing the adsorbate to move outside of the unit cell. In order to show the evolution of the displacement of the adsorbates during the dynamics, we split the graphics in frames of 500 fs, allowing us to show the evolution in time. The columns represent the range of time in which the variation of in-plane position of the adsorbates is depicted. The rows represent the different surface coverages. The colorbars represent the amount of time this *x*-*y* coordinate has been accessed by the adsorbates during the range of time. In warm colors (red to pink) are represented the variations of the center of mass of the CO molecules, while in cold colors (blue to green) are represented the variations of O adatoms. The variations of the positions of the O adatoms are drawn above the one of the CO molecules.

We observe that in the first 500 fs the adsorbates are mostly concentrated in their adsorption sites. The CO molecules from low and intermediate surface coverages are the ones having the largest largest in-plane displacement. Then, in the 500-1000 fs time range, although we observe that the O adatoms are escaping their initial adsorption site in all surface coverages, we see differences between the surface coverages. First, the low surface coverage is the one observing the smallest in-plane displacement of its abdsorbates, with the O adatoms and the CO molecules mostly staying in their adsorption site. Second, in the high surface coverage, we observe that the CO molecules are escaping their adsorption site, and in proportion more than the O adatoms that are adsorbing on the same adsorption site. Finally, in the intermediate surface coverage, we observe that the adsorbates have the largest in-plane displacement comparing to the two other surface coverage. We observe an in-row horizontal displacement of the CO molecules. As mentioned in Chapter 5, the O adatoms in $p(2 \times 1)$ arrangement are forming a barrier preventing the CO molecules to displace vertically.

Next, in the 1000-1500 fs time range, we observe that still, the low surface coverage is the one showing the smallest adsorbate in-plane displacement. The O adatoms are mostly confined in their adsorption site, although the ones from fcc adsorption site have are crossing more bridge site than the

ones in hcp site. Then, the CO molecules are still mostly moving on the top and near-top adsorption site, showing very few encounters with the O adatoms. In the case of the intermediate surface coverage, the CO molecules continue with their in-row motion, although the O adatoms now can access the CO molecules, escaping mostly throughout the bridge site on toward the CO molecules. In the high surface coverage, the in-plane displacement of the CO is the largest in this time frame, comparing to the other, as the one of the O adatom. The latter are moving as in the intermediate surface coverage, and even go farther. The large motion of the adsorbates in intermediate and high surface coverage is leading to encounter between the atoms, eventually inducing CO oxidation, as observed for the high surface coverage at $\sim$1400 fs.

In the 1500-2000 fs time range, we observe for low surface coverage that the radius of in-plane displacement of the CO molecules is larger, and that the motion of the O adatoms is also larger, allowing both species to encounter more frequently. We remind that the first CO oxidation in low surface coverage occurred at $\sim$2 ps. Concerning the intermediate and high surface coverage, we observe and increase of the diffusion of the O adatoms through the bridge site, being slightly larger in the case of high surface coverage. In the case of the CO diffusion, it already covers most of the available areas as seen in the Figure 5.14 and 5.15 of Chapter 5.

Finally, in the time range going from 2 ps to 4 ps, we do not have further comment regarding to the ones made in Chapter 5, and leave the figure as informative purpose.

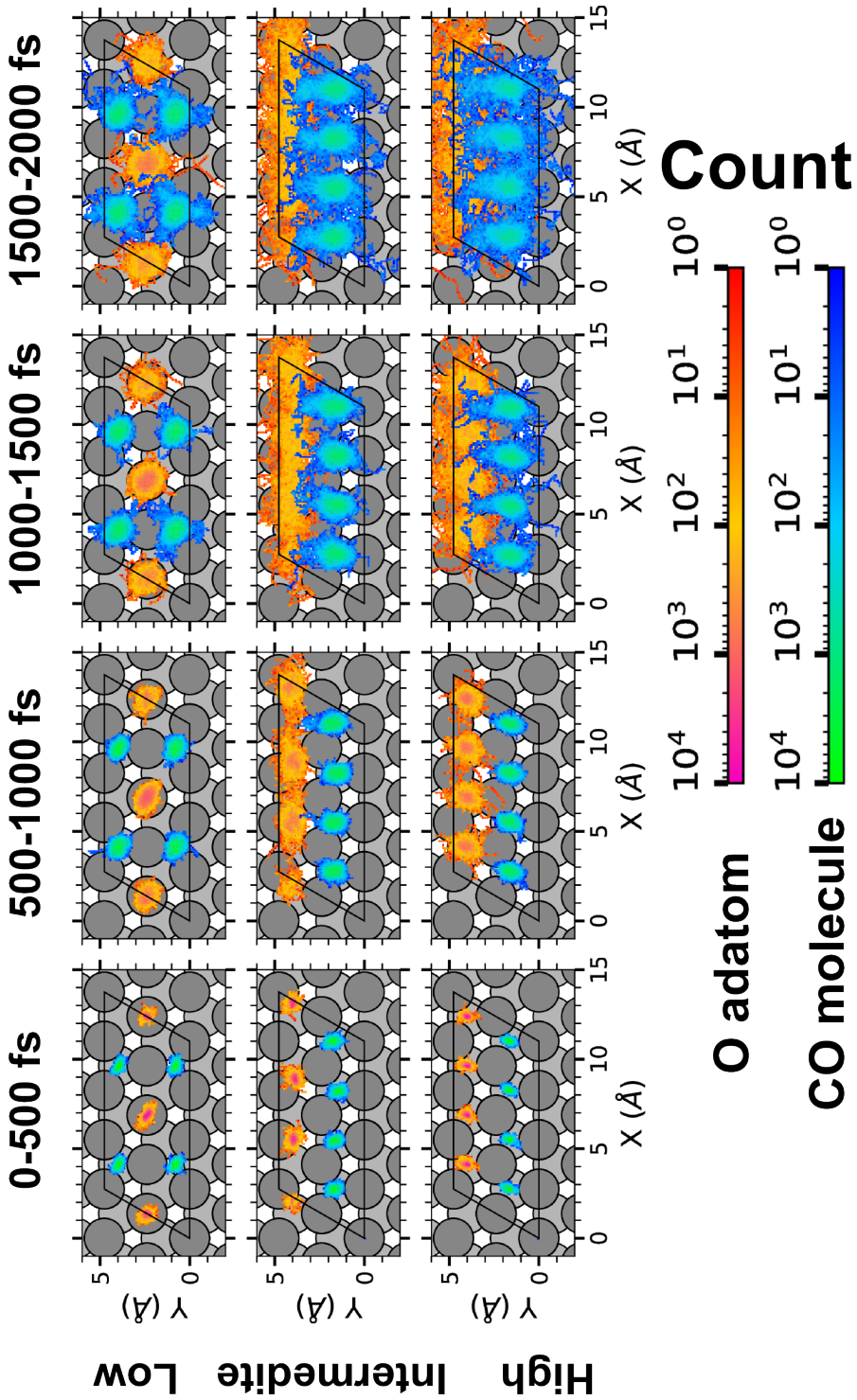

Figure G.1: Density plots of the (x, y) positions over the surface of the adsorbates at low, intermediate and high surface coverages. Only the position of the adsorbates that remain adsorbed on the surface at the end of the simulation are shown. We show the results of (T_e,T_{ph}) simulations only. The rows represent the different surface coverages. The colorbars represent the amount of time this (x, y) coordinate has been accessed by the adsorbates during the range of time. In warm colors (red to pink) are represented the variations of the center of mass of the CO molecules. In cold colors (blue to green) are represented the variations of O adatoms. The black line encloses the simulation cell. For clarity, the position of the adsorbates is shown in extended coordinate representation.

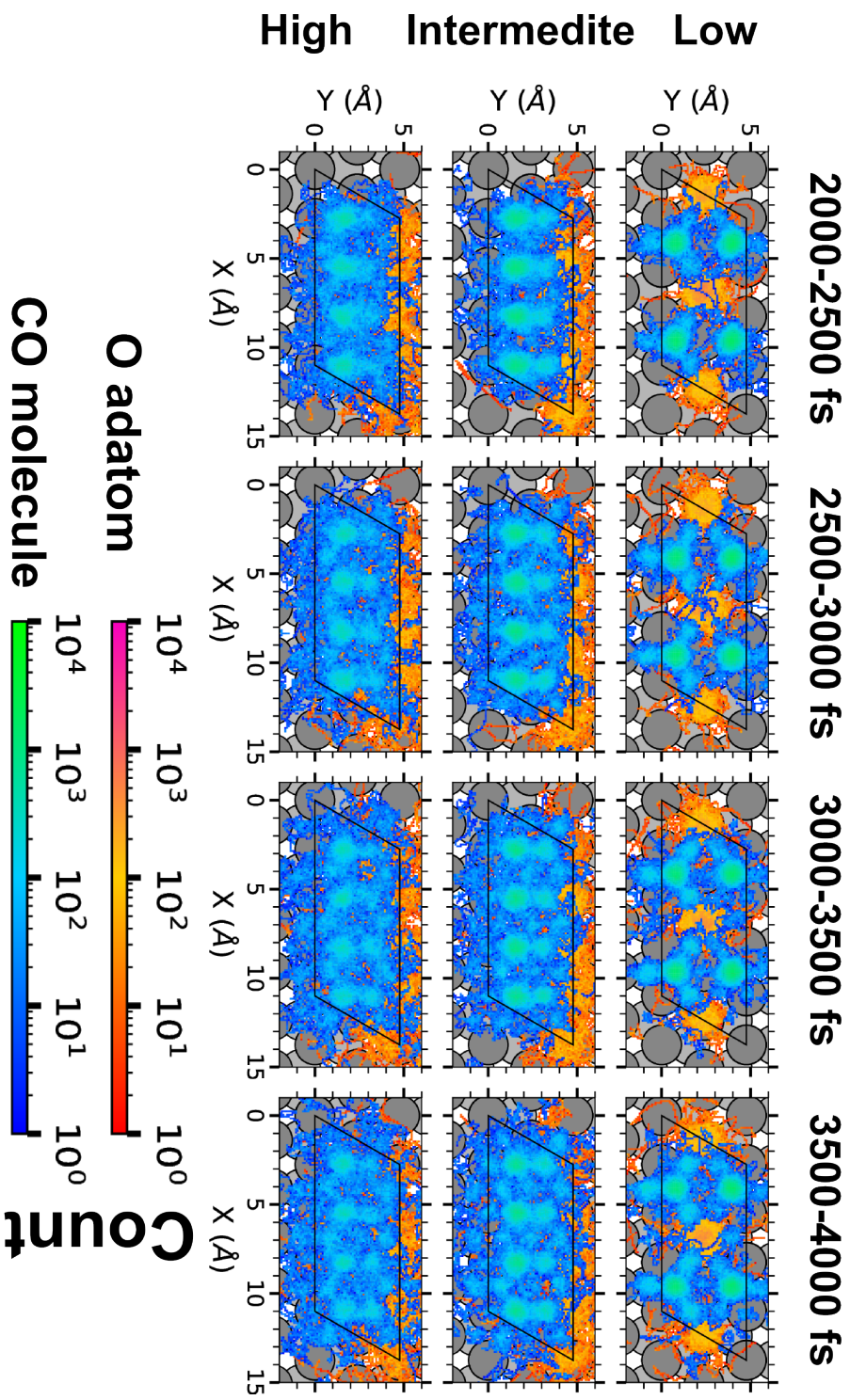

Figure G.1: Density plots of the (x, y) positions over the surface of the adsorbates at low, intermediate and high surface coverages. Only the position of the adsorbates that remain adsorbed on the surface at the end of the simulation are shown. We show the results of (T_e,T_{ph}) simulations only. The rows represent the different surface coverages. The colorbars represent the amount of time this (x, y) coordinate has been accessed by the adsorbates during the range of time. In warm colors (red to pink) are represented the variations of the center of mass of the CO molecules. In cold colors (blue to green) are represented the variations of O adatoms. The black line encloses the simulation cell. For clarity, the position of the adsorbates is shown in extended coordinate representation.

APPENDIX H

CHECK OF MD PARAMETERS

Before computing MD simulation, one must perform a systematic study of the parameters that influence the simulation in order to avoid artifacts and to optimize the simulation. In our simulations we use a NH thermostat which includes a parameter coupling the fictitious and real systems. Also, the integration time step of the MD is a crucial parameter since if it is very small, it increases the time of calculation, while if it is too high it lost information of the forces and introduces artifacts. Therefore, those parameters musts be optimized, and in this appendix we present the systematic study of those two parameters.

H.1 Check of temperature variation and canonical distribution for fictitious mass parameter

As we mentioned in section 2.4.2 when using the NH thermostat, the fictitious mass used to couple the real and extended bath must be chosen with good care. In ref.[151] the authors advice to parameterize the value of the fictitious mass to have the frequency vibration of the extended system adjust within the frequencies of the phonons of the surface. We can find the phonons frequencies in ref.[216]. To compute the exact value of the fictitious mass we use the following equation[149] with the phonon frequency of the above reference

$$Q = \frac{2f \times k_{\mathrm{B}} T}{\omega^2 < s >^2}\,. \tag{H.1}$$

In the equation the degrees of freedom $f = 3N$ with N the number of atoms in the NH thermostat, k_{B} is the Boltzmann constant, T the target temperature, and ω the phonon frequency. The parameter s is a time which rescale the velocities between the real and fictitious bath. Note this equation uses two approximations. It assumes that the frequency is a harmonic oscillator, and that s is equal to 1. By doing the latter, one considers that the rescaling of the bath temperature is in average one. We calculate that the fictitious mass Q must be within [612.70; 2451.06] $\mathrm{eV}^{-1}.\mathrm{s}^{-2}$.

In order to verify the effect of the two different values of the fictitious mass on the simulation, we compute with the NN-PES several thermalization of MD with NH thermostat applied on the two outermost layer of the slab surface. For each of the two values of fictitious mass, we computed 14 different MD of 10 ps each but with different temperatures. The temperatures go from 100 K to 1000 K

with steps of 100 K, and from 1000 K to 3000 K with steps of 500 K. The initial position of each of the 28 MD is the same. It is a random position extracted from 100 K thermalization made for AIMDEF of honeycomb structure of low coverage (section 3.3.2).

For each MD we represent in Fig. H.1 the variation of the temperature along the dynamic, and in Figure H.2 the different histograms of the temperature along the dynamic compared with Maxwell-Boltzmann distribution (in black). The temperature has been calculated using the kinetic energy of the atom composing the two outermost layer of the slab. This is why we are calling it the kinetic temperature. If we represent the variation of the temperature between each simulation in the same graphic, the curves are over imposing, giving an unreadable figure. To tackle this problem we represent the graphic in four subgraphics, and plot the temperature variation in decimal logarithmic scale. To help the comprehension, the temperature is written as inset close to each curve in both Figure H.1 and H.2. In the top panel of each target figure are represented the graphics for $Q = 612\text{eV}^{-1}.\text{s}^{-2}$ and in the bottom panel for $Q = 2451\text{eV}^{-1}.\text{s}^{-2}$.

Firstly, we observe in Figure H.1 that the variation of the temperature in the first picosecond for $Q = 612\text{eV}^{-1}.\text{s}^{-2}$ is very high, specifically at high temperature. Secondly, we observe that the temporal fluctuation of the temperature is lower in the case of $Q = 2451\ \text{eV}^{-1}.\text{s}^{-2}$ than for the latter. This feature is due to the type of coupling with the extended bath which is weaker in the case of $Q = 2451\ \text{eV}^{-1}.\text{s}^{-2}$ than in the other, because phonons of lower frequency have been used to calculate the fictitious mass.

In Figure H.2 we see that $Q = 612\ \text{eV}^{-1}.\text{s}^{-2}$ is sampling good the canonical ensemble except for 200 K where they are too many states close to 200 K. The sampling is also not appropriate for 300 K, 2000 K and 3000 K where there are too many states in the lower energy tail of the Maxwell-Boltzmann distribution. Both behaviors are explained by the huge variation of temperature seen in the beginning of the thermalization as shown in Figure H.1. In the case of $Q = 2451\ \text{eV}^{-1}.\text{s}^{-2}$ the canonical ensemble is well sampled for 700 K to 3000 K. For the temperatures below 700 K, we observe on Figure H.2 that there are too many states in the lower and higher tail of the Maxwell-Boltzmann distribution. This behavior demonstrates a fluctuation of energy for these temperatures below 700 K that is greater than at higher temperature.

As remarked in the precedent section, since in our molecular dynamics we will reach lattice temperature close to 2000 K, we select the value of $Q = 2451\ \text{eV}^{-1}.\text{s}^{-2}$ because it samples better the canonical ensemble at higher temperature than $Q = 612\ \text{eV}^{-1}.\text{s}^{-2}$, and have a more stable behavior at the beginning of the thermalization.

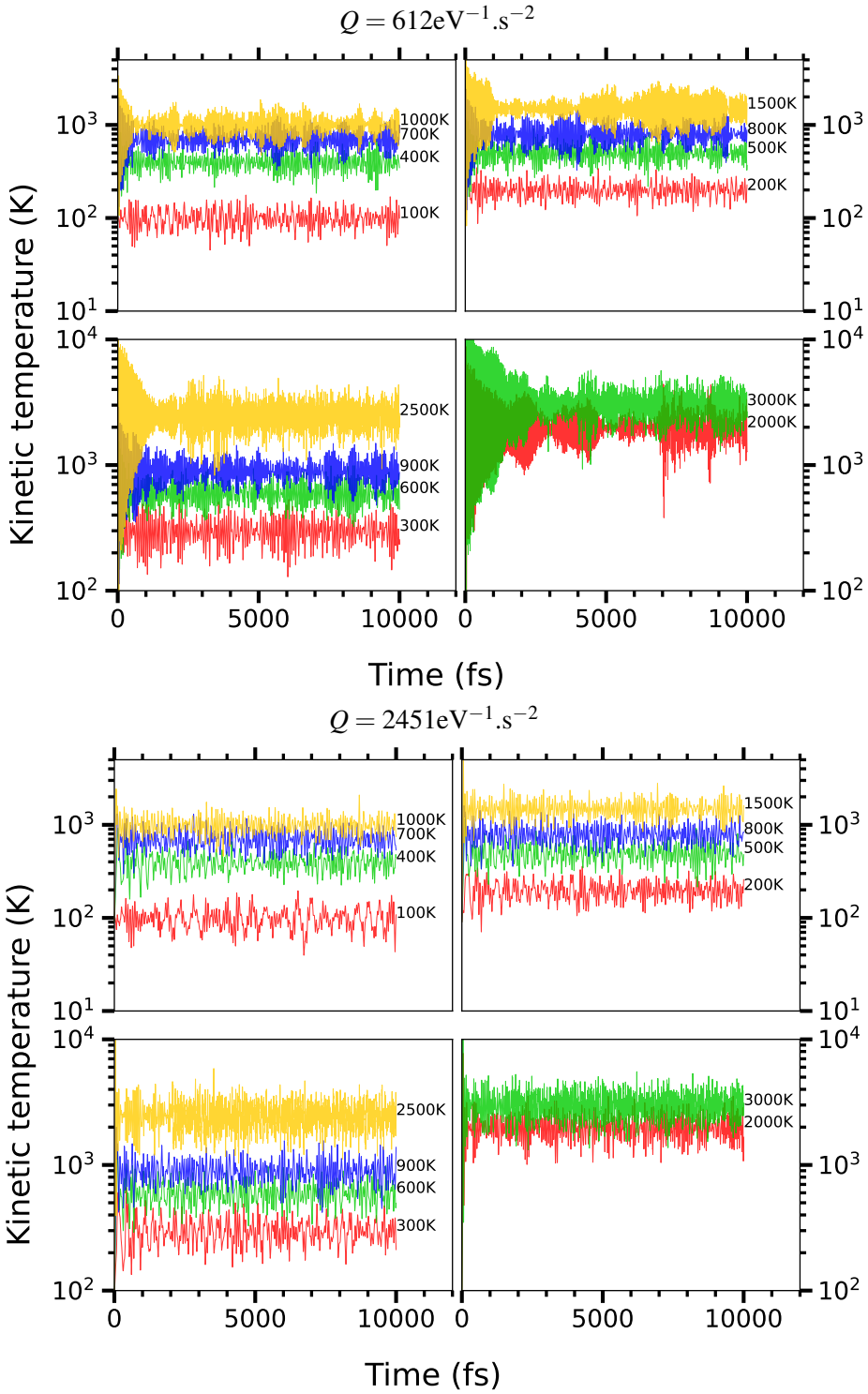

Figure H.1: Variation of the total kinetic temperature during 10ps dynamics with fictitious mass of 612.70 and 2451.06 $\text{eV}^{-1}.\text{s}^{-2}$ and various temperature: 100, 200, 300 ,400, 500, 600 ,700, 800, 900, 1000, 1500, 2000, 2500, 3000 K.

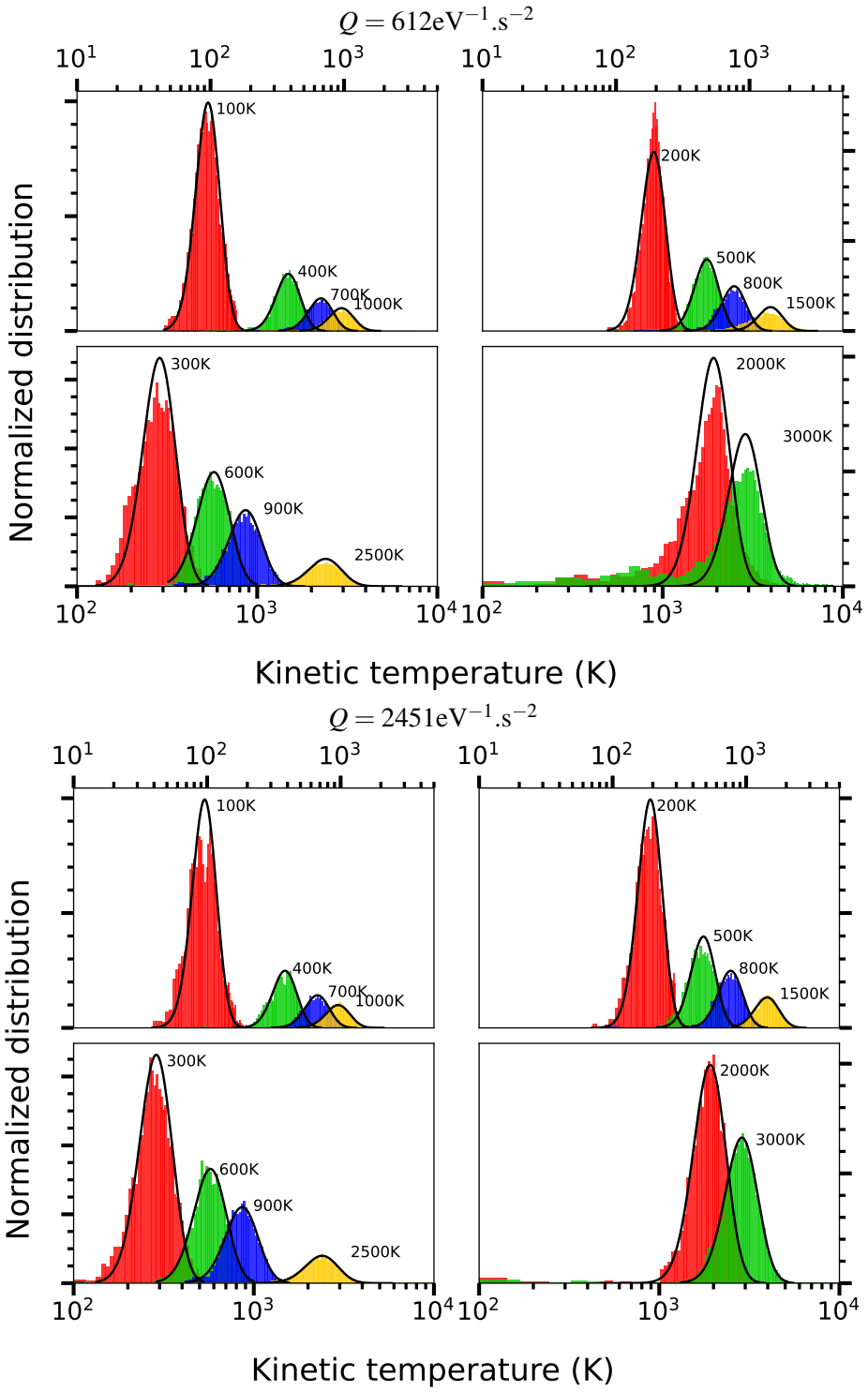

Figure H.2: Distribution of kinetic temperature compared to the Maxwell-Boltzmann distribution, of the 10 ps dynamics with fictitious mass of 612.70 and 2451.06 $\text{eV}^{-1}.\text{s}^{-2}$ and various temperature: 100, 200, 300 ,400, 500, 600 ,700, 800, 900, 1000, 1500, 2000, 2500, 3000 K. In black is represented the Maxwell-Boltzmann distribution for the target temperature.

H.2 Check of the conservation of energy for integration time step parameter

In order to check the effect of the value of the integration time step parameter on the molecular dynamics, one has to run various MD (long enough, at least 10 ps) to check the conservation of the energy. In Figure H.3 we show the variation of the total energy during several MD with respect to the first step, to show the dispersion of energy. On top panel we show the variation of MD at 100 K and as inset give the respective integration time step. We see that until 1 fs the energy dispersion is below meV, while for 5 fs it has error greater than a few meVs. The bottom panel of Figure H.3 shows the same MD as the top panel but for 2000 K. In this case, what is striking is the huge increase after 6 ps for the integration time step of 5 fs which amounts of several keV. We also note that for 0.1 fs, the error amounts to about 10^{-5}eV as for 100 K. Also until 1 fs of time step, the error is below the meV. Since in our MD we will reach lattice temperature close to 2000 K, we would like to ensure that there will be no dispersion of the total energy. Thus we will use 0.2 fs as integration time step.

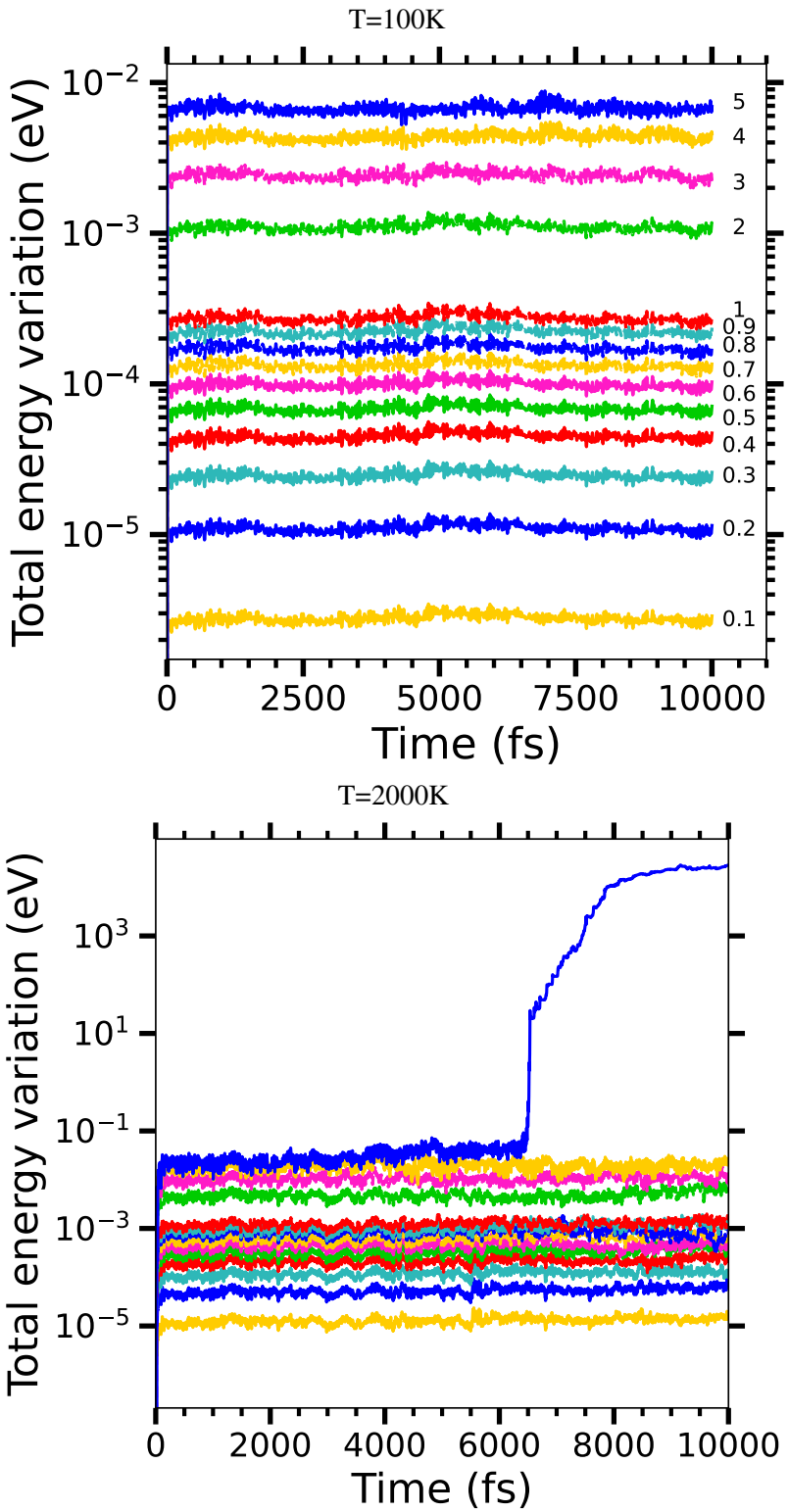

Figure H.3: Variation of the total energy during dynamics for different integration time steps (0.1, 0.2, 0.3, 0.4, 0.5, 0.6, 0.7, 0.8, 0.9, 1, 2, 3, 4, 5 fs) at T=100 K (left pane) and T=2000 K (right pane).

APPENDIX I

FITTING PARAMETERS FOR RU ELECTRONIC DENSITY

In this appendix we are showing the details of the fitting procedure of the electronic density of the ruthenium surface. We used data from AIMDEF calculations in order to have an analytical function, usable in NNP-MD calculations.

We used the AIMDEF data points of $\rho(\mathbf{r}_A)$, in eq.(2.56) to adjust the four parameters: a, b, c, and d which results in $a = 4.178222$ au, $b = 4.022414$ Å^{-1}, $c = 0.061987$ au, and $d = 1.876455$ Å^{-1} (au stands for atomic units). Once the analytical function of the density is known, the friction coefficients are calculated within the LDFA as it was also done in the AIMDEF simulation.

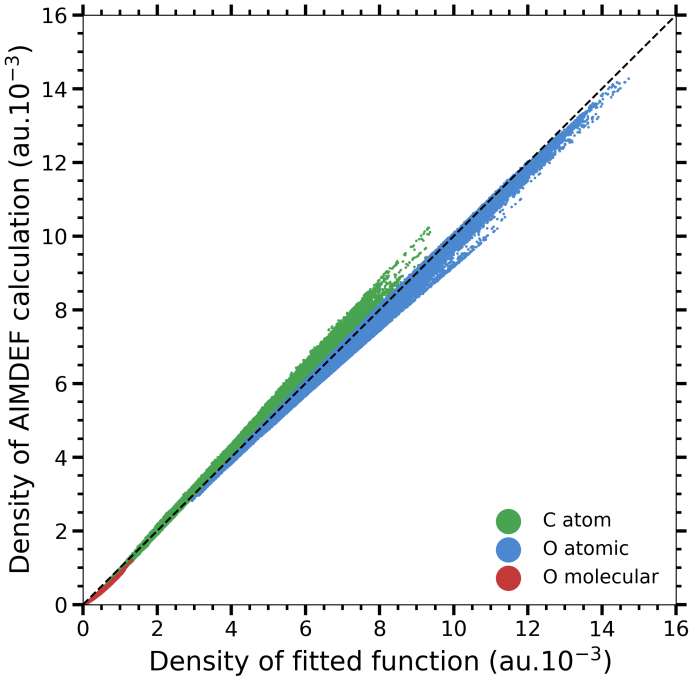

Figure I.1: Comparison of the fitted electronic density with the one extracted from AIMDEF calculation. The density is in atomic units. The atomic oxygen, molecular oxygen and carbon atom are at different distances from the surface, thus feels different electronic densities. Therefore, they are shown in three different colors. In red, green and blue are represented the density of the molecular oxygen, carbon atom and atomic oxygen, respectively. The black dashed line represent the curve y=x.

Figure I.1 represents the values of the electronic density felt by the atoms extracted from AIMDEF versus the value of the fitted coefficient. We plotted in three different colors the type of atomic species. In red, green and blue are represented the density of the molecular oxygen, carbon atom and atomic oxygen, respectively.

The molecular oxygen is far from the surface, thus does not feel the friction force, except when the CO molecule is tilting. Therefore the errors on this species are high in percentage but very low in effective value. The mean error of this specie amount to 1.110^{-4} au and a max error to 2.210^{-4} au. The values of the coefficient for atomic oxygen are very well fitted, with a mean error of 4.610^{-5} au and a max error of 1.210^{-3} au. However, the values for the carbon atom are not as exact as the one of atomic oxygen. Indeed they present a mean error of 1.510^{-4} au and a max error of 1.110^{-3} au. Also, we can see that the fitting is not working well between the values [5;11], because the points have a great dispersion regarding to the x=y line. However, the error is still very low, amounting to 43.0%, 0.6% and 3.8% of the mean value of molecular oxygen, atomic oxygen and carbon atoms, respectively. In order to confirm that this function is suitable to perform molecular dynamics, we will run 200 simulations of NNP-MD and compare the mean friction coefficients obtained this way with the mean friction coefficients obtained with AIMDEF simulations.

In Figure I.2 we compare for each of the atoms of the cell (except the molecular oxygens that are too far from the surface to feel friction forces) the variation of the mean value of the friction force during the AIMDEF simulations of NNP-MD simulations. We can see that in mean value, the friction force giving by the fitted function from the AIMDEF calculation gives result in a very good agreement with the forces calculated *ab initio*. Although, we see that for the carbon atom, the fitted friction coefficient is lower than the one from AIMDEF, the errors are reasonable and amount to $\sim$4%. We conclude that the analytical function we fitted is accurate enough to run AIMDEF simulation, and safely reproduce *ab initio* calculation.

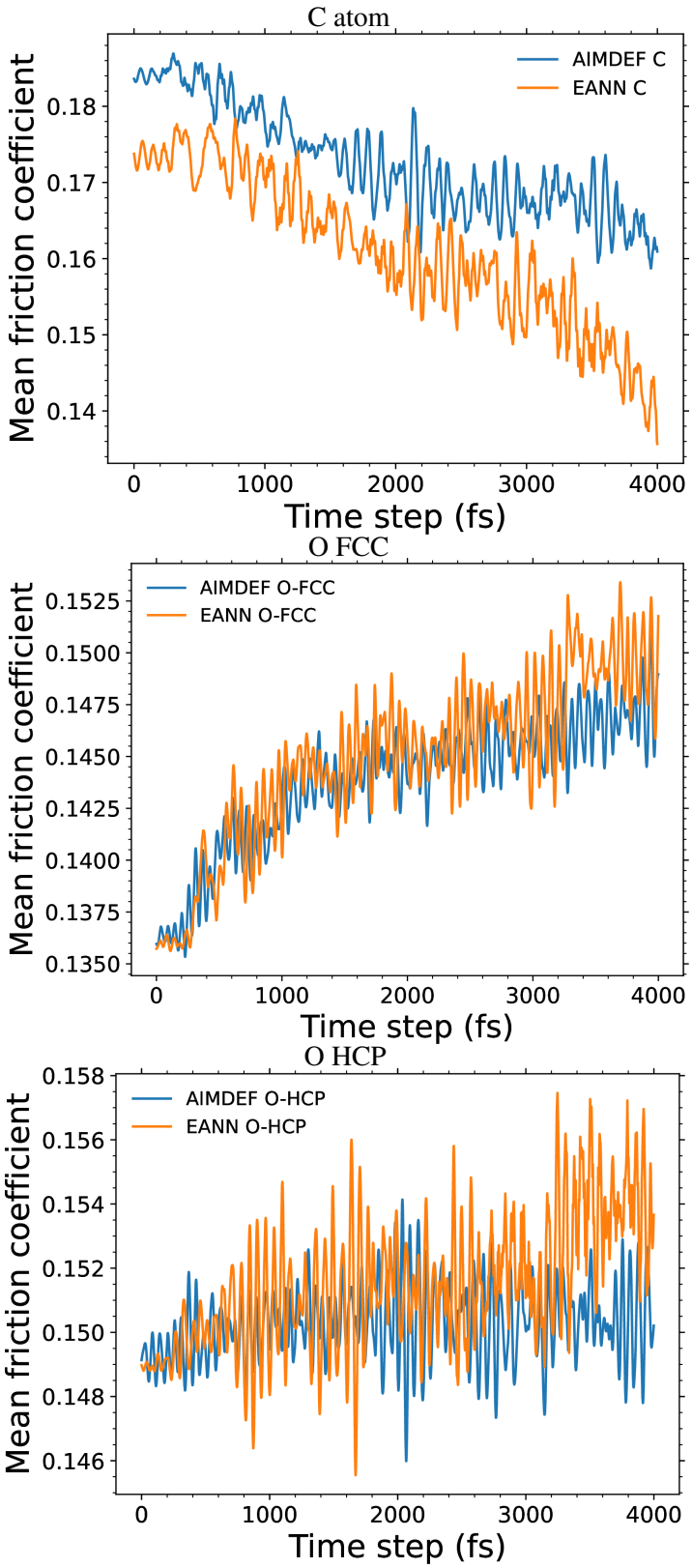

Figure I.2: Comparison of the AIMDEF with NNP-MD extracted mean friction coefficient experienced by the carbon atom, and atomic oxygen from HCP and FCC adsorption site during the 200 trajectory dynamics. In blue (orange) is represented the mean value of the friction coefficients for AIMDEF (NNP-MD) calculation.

APPENDIX J

POTENTIAL ENERGY STUDY OF THE NNP-MD OF THE SECOND NN-PES

In this appendix we are showing the study of the potential energy of the NNP-MD of Cylce-NN-PES.

Although in non-adiabatic dynamics the forces are not conservative, the decrease of potential energy should be balanced by an increase of the kinetic energy. However, we observed that it happens to several dynamics to have a potential energy lowering be several eV until several tens of eV. Thus, this demonstrates an issue in the NNP-MD. Although we selected a fictitious mass and integration time step to avoid energy drifts (see Appendix H), it happens. Later, we realized that some of the simulation were leading to configurations with vaporized ruthenium. Here we investigate the impact of those configurations on the potential energy.

In Figure J.1 we present a density plot of the potential energy of the NNP-MD at the different times of the dynamics, for the low, intermediate and high surface coverages, respectively. This way we visualize in this 2D space the concentration of the accessed potential energies by the system along dynamics. The density plots are in logarithmic scale. On the left panel we present the density plots of the potential energy for all the simulations of the surface coverage. On the right panel we present the density plots of the potential energy for the simulations that do not have vaporized ruthenium.

On the left panels of Figure J.1 we observe that after $\sim$2.5 ps of simulation, the potential energy of several trajectories already decreased bellow the initial one. We investigate the trajectories, and find out that for several trajectories, after this time step one or several atoms of ruthenium were vaporized from the surface. This process seems to follow the step:

1. A ruthenium atom of the outermost layer get z momentum toward vacuum.
2. An oxygen atom takes advantage of the space left by the uprising ruthenium atom to go inside the empty space.
3. A combined movement of the ruthenium going up and the oxygen going down, with repulsive forces between both increase this behavior.
4. The ruthenium atom is vaporized, and continue to receive energy from the thermostat. The oxygen atom is stuck below the outermost layer of ruthenium surface.

Thus, after identifying this behavior, we decided to create the same graphic, but, removing the points with vaporized ruthenium. This is presented in the right-hand side of the Figure J.1. We clearly

see that it removes the majority of the points that were below the initial potential energy. This behavior appears for all the three coverages, but is increased as we increase the coverage.

To understand more about this behavior, we decided to run, less but some, NN-PES-MD with a laser fluency lower than before (140 J/m^2) in order to see if, by providing less energy to the system, we can prohibit this behavior. It can be assimilated as restricting the configurational space of the surface, by lowering the quantity of high energetic state. However, we observe in Fig. J.1 bottom panels, that even with lower laser fluency, and less amount of trajectory, there are still some points that are below the initial potential energy.

If we look at the trajectories that contain a value below the initial potential energy, we do find extraneous behaviors as: CO dissociation, formation of C_2O, bad description when CO is far from surface (<35A), and excessive movements of inner ruthenium atoms. Further investigation could be done to understand where this problem comes from. Although, we know that the NN are bad when extrapolating, thus it is not extraneous that such behavior occurs. This is the manifestation of "holes" between the points of configurational space that have not been provided during the training process.

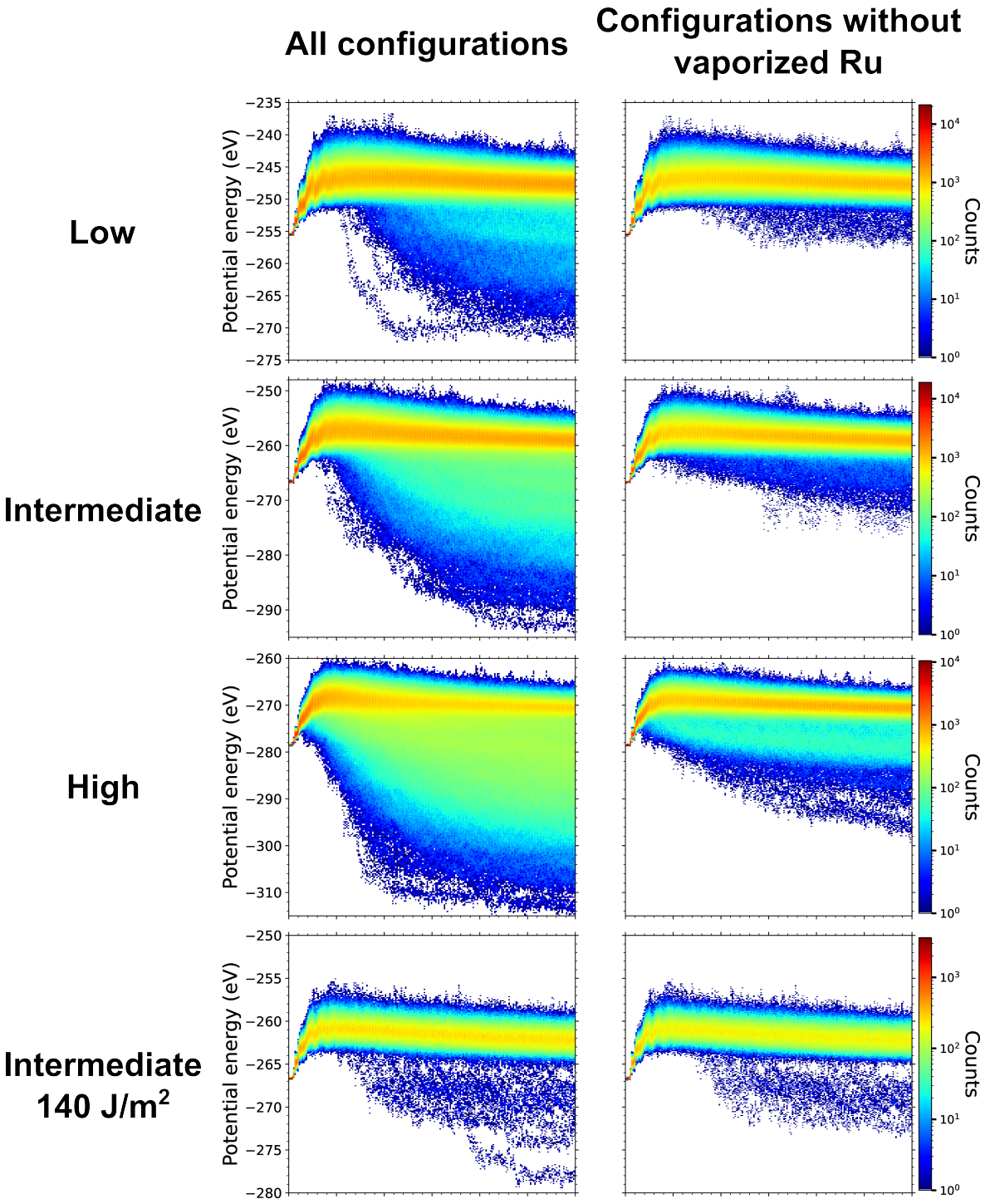

Figure J.1: Density plots of the potential energy of the NNPMD calculated configurations depending on simulation time for low, intermediate and high surface coverages. The colorbars show the amount of configuration in this area of the graphic. On the left panels are shown the graphics with all the configurations. On the right panels are shown the graphics without the configurations containing a vaporized ruthenium atom.

APPENDIX K

EVALUATION OF LOW AND HIGH SURFACE COVERAGE BY CYCLE-NN-PES

In this appendix we are showing the study of the evaluation by Cylce-NN-PES of data set from low and high surface coverages. In order to compare the density plots presented in Figures 6.14 and 6.15 where we present in Figures K.1 and K.2 the evaluation by Cycle-NN-PES of the different data sets of low and intermediate coverages. We present an histogram of the DFT energies of the configurations from each data set, and the result of the evaluation by Cycle-NN-PES. In the bottom panel we show the amount of configuration in each bin (of 0.5 meV width) of the histogram, and in the top panel we display theMAE associated to this bin.

In Figure K.1 we present the results for data set deriving from low surface coverage AIMDEF calculations. For comparison, we show in black the data of Cylcle-Intermediate-Train data set that Cycle-NN-PES has been trained with. In red, green and blue are presented the results for Cycle-Low-T_e, Cycle-Low-(T_e,T_{ph}) and Direct-Low-Predict-α data set, respectively.

Firstly we see that the MAEs of the data set that are not from intermediate surface coverage are higher than the ones of Cycle-Intermediate-Train data set. This was expected since those points corresponds to extrapolation of the Cycle-NN-PES with respect to the configurations used for the training. Secondly, we observe that the data set of T_e calculations (red line and points) have an energy range five times smaller than the other data sets that contains (T_e,T_{ph}) calculations. It was shown in Chapter 5 that the T_e calculations explore a smaller configurational space than with (T_e,T_{ph}) calculations, allowing access to smaller range of energy. Also, the MAEs of this data set are the lowest for data set derived from low surface coverage. Thirdly, the MAEs of Direct-Low-Predict-α data set are bellow 10 meV, except for the highest energies. If we compare this result to the one of Fig. 6.6 we see that the MAEs here are higher, but by less than one order of magnitude. This is already reasonable, considering the difficulties that NNs have to extrapolate. Finally, we see that for the evaluation of (T_e,T_{ph}) configurations, the errors are at least of 10 meV and go to 100 meV. However, the configurations that have the highest MAEs are the less representatives ones since there is very few amount of them comparing to the ones in [-7.80;-7.68] eV energy range.

In Figure K.2 we present the histogram of configurations from High surface coverage and their MAEs projected on the DFT energy axis as already explained above. For comparison, we also show in black the histogram of Cylcle-Intermediate-Train data set. The T_e calculations data sets are represented in red for 200J/m^2 laser fluence, and green for 300J/m^2 laser fluence. In blue we depict the (T_e,T_{ph})

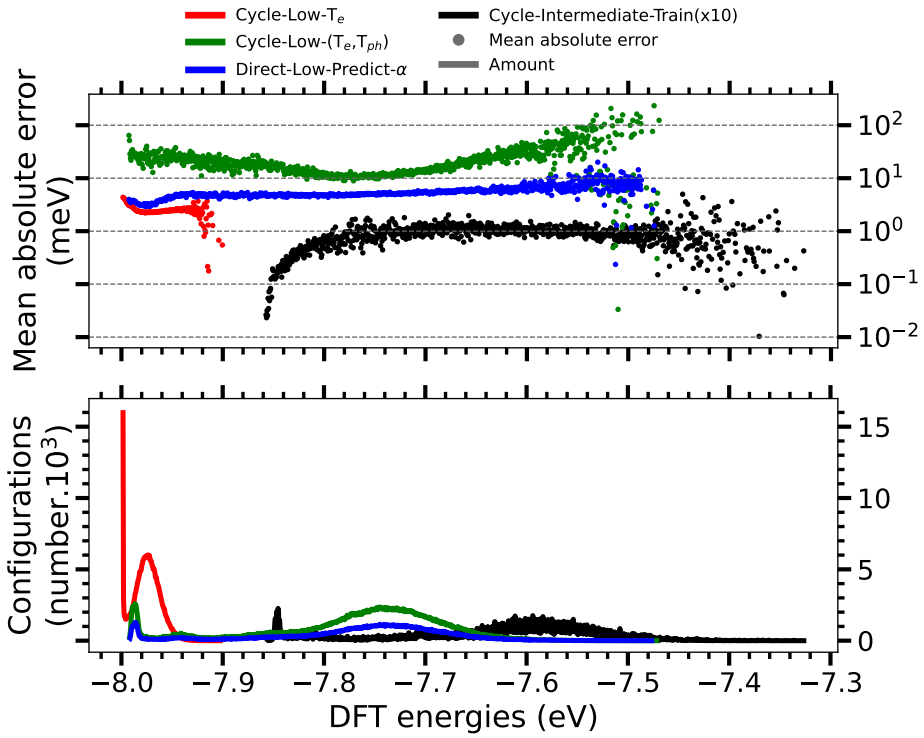

Figure K.1: In top panel is represented with scatter points, in logarithmic scale, the histograms of MAE of the NN-PES energy prediction compared to the DFT energies. In bottom panel is represented with solid lines, the histogram of the amount of configuration in each bin of 0.5 meV energy. In red is represented Cycle-Low-T_e data set, in green Cycle-Low-(T_e,T_{ph}) data set, in blue Direct-Low-Predict-α data set, and in black Cycle-Intermediate-Train data set. The amount of point of the latter is multiplied by 10 to fit in the scale of the bottom panel.

calculations data set. We see in bottom panel that the two data sets of T_e calculations do not coincide exactly in energy, except for the first energies. For the first energies, this is a consequence of the AIMDEF simulation which started all from the equilibrium position. The difference comes from the change in laser fluence. With higher laser fluence, the system can explore a broader configurational space. In the case of (T_e,T_{ph}) calculations, we clearly see that this data set is sampling a larger configurational space, since the energy range of the configurations is $\sim$4 time larger.

As we expected, Cycle-Intermediate-Train does not coincide in the energy range with the other data sets. Remarkably, in the [-7.7; -7.6] eV energy range, the Cycle-NN-PES is describing better the configurations of the (T_e,T_{ph}) set than the T_e data sets. This is remarkable because in the case of low surface coverage, it was more accurate to predict the T_e calculations and here the tendency is the opposite. We conclude that the configurations from T_e calculations data sets must be fundamentally different to the one from (T_e,T_{ph}) calculations, although they have the same potential energy. The evident difference is the distortion of the surface. Finally, we see that the worse MAE of this data set comes from the configurations that have energy higher than -7.5 eV. This corresponds to the majority of the (T_e,T_{ph}) configurations. However, the error being close to 10 meV, it is still an acceptable result considering that Cycle-NN-PES is extrapolating data.

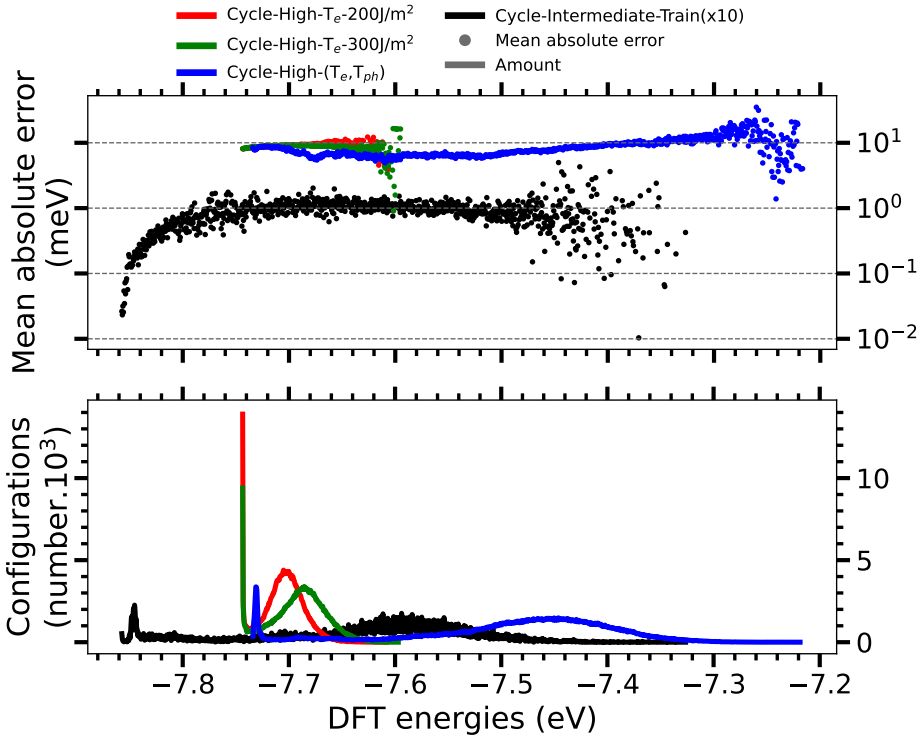

Figure K.2: In top panel is represented with scatter points, in logarithmic scale, the histograms of MAE of the NN-PES energy prediction compared to the DFT energies. In bottom panel is represented with solid lines, the histogram of the amount of configuration in each bin of 0.5 meV energy. In red is represented Cycle-High-T_e data set for calculation with laser fluence of 200 J/m^2, in green Cycle-High-T_e data set for calculation with laser fluence of 300 J/m^2, in blue Cycle-High-(T_e,T_{ph}) data set, and in black Cycle-Intermediate-Train data set. The amount of point of the latter is multiplied by 10 to fit in the scale of the bottom panel.

INDEX

Carbon monoxide (CO) is a neurotoxic gas emitted for instance in combustion reaction. Therefore, it has been sought for air treatment solutions, where CO oxidation is a straight forward choice. In ultra high vacuum conditions the ruthenium has been found to be very inactive for CO oxidation. Experimentally, it has been shown the opening of a new reaction path for CO oxidation on ruthenium surfaces by means of femtosecond laser irradiation. Accurate simulations of the photo-reaction dynamics are required to give a proper characterization of this kind of experiments.

This thesis is dedicated to the study of the photo-induced desorption and oxidation of CO molecules, coadsorbed with oxygen (O) adatoms on Ru(0001) with different surface coverages.
We began with the characterization of three (O, CO) mixed surface coverages on Ru(0001). We first found the adsorption configuration of minimum energy for each surface coverage, then we computed the desorption potential of a CO molecule, and found the minimum energy path to CO oxidation on all three surface coverages.
Then, we ran *ab-initio* molecular dynamics with electronic friction simulations, and we have been able to show the complexity of the reaction path to oxidize the CO molecule, and explain its low probability of occurrence.
Next, we showed the importance of surface deformations on the desorption and oxidation probabilities of CO, and on the adsorbate motion. Then, we presented in detail and characterized the different mechanisms of CO oxidation.
Finally, we created a potential energy surface based on neural networks and showed that it is a very promising tool to solve the problem of the computational cost of *ab-initio* molecular dynamics simulations.

CSIC
GOBIERNO DE ESPAÑA
MINISTERIO DE CIENCIA, INNOVACIÓN Y UNIVERSIDADES
CFM Materials Physics Center